

Curvature Manipulation of Photomasks

Enhancing the imaging performance of
immersion lithography systems

Christiaan L. Valentin

Curvature Manipulation of Photomasks

Enhancing the imaging performance of immersion lithography equipment

PROEFSCHRIFT

ter verkrijging van de graad van doctor
aan de Technische Universiteit Delft,
op gezag van de Rector Magnificus prof.ir. K.C.A.M. Luyben,
voorzitter van het College voor Promoties,
in het openbaar te verdedigen
op woensdag 22 mei 2013 om 12:30 uur

door

Christiaan Louis VALENTIN

werktuigbouwkundig ingenieur
geboren te Seria, Brunei.

Dit proefschrift is goedgekeurd door de promotoren:

Prof. ir. R.H. Munnig Schmidt
Prof. dr. ir. D.J. Rixen

Samenstelling promotiecommissie:

Rector Magnificus	voorzitter
Prof. ir. R.H. Munnig Schmidt	Technische Universiteit Delft, promotor
Prof. dr. ir. D.J. Rixen	Technische Universität München, promotor
Prof. dr. ir. D. Trumper	Massachusetts Institute of Technology
Prof. dr. ir. J. Benschop	ASML
Prof. dr. ir. H. Butler	Technische Universiteit Eindhoven
Prof. dr. ir. G. Schitter	Vienna University of Technology
Prof. dr. ir. M. Verhaegen	Technische Universiteit Delft
Prof. dr. ir. J. Herder	Technische Universiteit Delft, reservelid

ASML

This research was financed and supported by ASML. B.V. in Veldhoven, the Netherlands.

ISBN 978-94-6186-128-3

Copyright © 2013 by C.L. Valentin.

All rights reserved. No part of the material protected by this copyright notice may be reproduced or utilized in any form or by any means, electronic or mechanical, including photocopying, recording or by any information storage and retrieval system, without the prior permission of the author.

Author email: chris.valentin@asml.com

Printed by Wöhrmann Print Service, Zutphen.

Voorwoord

Ongeveer vijf jaar geleden ben ik begonnen aan een onderzoek naar het actief vervormen van maskers in immersielithografiemachines. Deze technologie faciliteert een focusverbetering in de machines wat nodig is om kleinere geïntegreerde schakelingen te kunnen realiseren. Dit proefschrift beschrijft de resultaten van het onderzoek. Hierin komen onderwerpen als de te verwachten focusverbetering, de technische haalbaarheid, de ontworpen manipulator en de experimentele validatie aan bod.

Net zoals alle anderen die mij voor gingen is er met het afronden van het proefschrift tijd gekomen voor reflectie. Terugkijkend op de periode ben ik van mening dat het onderzoek me veel heeft gebracht. Allereerst heeft het me de mogelijkheid gegeven om mezelf te ontwikkelen op het gebied van Mechatronica. Het multidisciplinaire karakter van dit vakgebied zorgt ervoor dat je continu leert van anderen op zowel technisch als persoonlijk vlak. Dit werd grotendeels versterkt door de intensieve samenwerking met het bedrijfsleven. Hoewel ik hierdoor niet altijd de meest wetenschappelijk benadering heb gekozen, heeft het me er wel van doen doordringen dat je kritisch moet zijn op de haalbaarheid en toepasbaarheid van je onderzoek. Dit hielp met name bij het definiëren van de onderzoeksrichtingen en organisatie van het onderzoek.

Naast de vele positieve ervaringen kent een promotietraject ook zijn dieptepunten. Dit heb ik met name ervaren tijdens het schrijven van dit proefschrift. Hiervoor is flink wat doorzettingsvermogen nodig. Hoewel dit als een karaktereigenschap gezien kan worden had ik het nooit af kunnen ronden zonder de inhoudelijke en mentale ondersteuning van een groot aantal mensen.

Allereerst wil ik mijn promotoren prof. Rob Munnig Schmidt en prof. Daniel Rixen bedanken voor de mogelijkheid om mijn promotieonderzoek te verrichten binnen de afdeling Precision Engineering and Microsystems Engineering (PME). Rob, naast je vakinhoudelijke ondersteuning ben ik je ook zeer erkentelijk voor de introductie bij ASML, je coaching, humor en het doorgeven van je industriële ervaringen. Ik heb hier veel profijt van gehad gedurende mijn onderzoek en weet zeker dat ik hier in de toekomst ook veel aan zal hebben. Daniel, je inzet, sterke analytische en didactische vaardigheden hebben mij zowel tijdens mijn afstudeerperiode als mijn promotietraject geïnspireerd. Ook je scherpe feedback heeft veel bijgedragen aan dit proefschrift.

Ten tweede wil ik graag ASML en haar medewerkers bedanken voor het faciliteren en ondersteunen van dit promotieonderzoek. Theo Cadee, ik ben dankbaar dat je mij de kans hebt gegeven om het onderzoek te verrichten binnen de ASML Research Mecha-

tronics groep. Ook je persoonlijke ondersteuning en coaching heb ik erg gewaardeerd. Wat betreft de technische en organisatorische begeleiding ben ik altijd goed ondersteund door Hans Vermeulen. Ondanks je erg drukke agenda maakte je altijd ruimte om advies te geven en het onderzoek verder te brengen. Jos Benschop wil ik bedanken voor het beschikbaar stellen van budget voor het onderzoek, de inhoudelijke discussies en vooral zijn prikkelende vragen ten aanzien van de motivatie voor het onderzoek. Verder zijn mijn collegas binnen de ASML Research groep altijd bereid geweest om mee te denken met het onderzoek. Met name Ton de Groot, Bas van de Ven, Marijn Kessels, Wouter Aangenent, Iwan Akkermans, George Clijsen, Jeroen de Boeij, Marc van der Wal, Stan van der Meulen, Jan Huang, Nico ten Kate en Laurens van Bokhoven stonden voor mij klaar. Dit gold ook voor Jan Baselmans, Andre Jeunink, Marc Zellenrath, Haico Kok, Dirk-Jan Bijvoet, Ralf Brinkhof, Erik Koop, Martin Verhoeven en Christopher Ward van de System Engineering en de Development & Engineering afdelingen.

Op het praktische vlak heb ik samengewerkt met Jansen Precision Engineering (JPE). Mijn dank gaat met name uit naar Bart van Bree, Richard Albers en Huub Janssen die een belangrijke rol hebben gespeeld in het ontwerp en de realisatie van de testopstellingen. Daarnaast wil ik ook IBS Precision Engineering bedanken voor hun technische ondersteuning bij de metrologieopstelling die is gebruikt voor de validatie metingen.

Ik heb tijdens mijn promotietraject twee studenten mogen begeleiden die allebei een deelstuk van het onderzoek voor hun rekening namen. Bas van Wuijkhuijse en Bart Festen wil ik dan ook bedanken voor hun bijdrage aan het onderzoek. Ik hoop dat jullie, net als ik, veel geleerd hebben in die periode en dat jullie er met plezier naar terugkijken.

Naast mijn werkplek bij ASML had ik ook een plek binnen de Mechatronic System Design vakgroep aan de TU Delft. Dit gaf mij de mogelijkheid om de ASML hectiek te ontvluchten wanneer er geschreven moest worden. Ook gaf het de gelegenheid tot inhoudelijke gesprekken met de stafleden Jo, Ron en Anton. Hiervoor mijn dank. Verder wil ik mijn medepromovendi Jan, Rudolf, Phuc, Ruijun, Oscar, Johan, Arjan, Pablo, Patrice, Sander, Maarten, Jeroen, Jeroen, Jasper, Guido, Marc, Walter, Jon, Friedjof, Eric, Ki-Nam, Alexander, Sven, Paul en Jodi bedanken voor de technische discussies en de prettige sfeer op de TU, tijdens uitjes of op conferenties.

Twee andere groepen mensen die een belangrijke rol hebben gehad zijn mijn huisgenoten en vrienden. Jullie brachten de benodigde afleiding wanneer ik daar behoefte aan had. Frank en Marijn, jullie weten als geen ander hoeveel avonden er in dit proefschrift zitten. De spaarzame avonden uit in Eindhoven en discussies waren dan ook een welkome ontspanning. Hetzelfde geldt ook voor mijn vrienden vlakbij Den Haag wanneer ik ieder weekend in de buurt was.

De laatste personen die ik wil bedanken voor hun steun en toeverlaat tijdens deze vijf jaar zijn mijn familie en vriendin Nancy. Mijn proefschrift wil ik dan ook graag aan jullie opdragen! Ik ben mijn ouders erg dankbaar voor de opvoeding die ze mij gegeven hebben in zowel Nederland als het buitenland. Daarnaast hebben jullie mij altijd ondersteund in mijn keuzes. Dit geldt ook voor mijn zus Stephanie en broer Casper die ik helaas weinig zie omdat ze in het buitenland wonen. De persoon waar ik echter de meeste steun aan gehad heb tijdens de laatste twee-en-een-half jaar is mijn vriendin Nancy. Het is niet altijd even leuk om met een promovendus samen te zijn omdat hij altijd 'moet' werken en wel eens een dipje heeft. Ik heb dan ook respect voor je geduld tijdens deze periode en hoop dat we nog vele mooie jaren samen mogen beleven.

Summary

The semiconductor industry is constantly improving Integrated Circuits (IC) in order to provide society with the latest information technology at an affordable price. The improvements are realized by reducing the IC's minimum feature size or Critical Dimensions (CD). The CD is defined by the photolithography process which transfers a geometric image from a photomask to a photosensitive layer on a silicon wafer by light. The Depth-of-Focus (DOF) during the lithography imaging process influences the achieved CD and CD Uniformity in an IC. Immersion lithography equipment manufacturers are currently pursuing a DOF of 65 – 70 [nm] and an overlay error of 2 [nm] in order to manufacture 20 [nm] feature sizes [15]. The focus and overlay requirements will become more stringent if smaller CDs are manufactured with these kind of tools.

This thesis investigates the benefit and feasibility of a photomask curvature manipulator as focus improvement technology in immersion lithography systems. The concept consists of applying bending moments to the photomask edges in order to control its curvature during its exposure. The curved photomask surface results in a curved aerial image at wafer level. Analyses have demonstrated that a reticle curvature of $\kappa = \pm 0.4 \times 10^{-3}$ [1/m] is able to reduce the defocus by lens heating deformation and wafer topology non-flatness by 10 [nm] each. Alternative curvature correction concepts like a manipulator in the lithographic lens or active control of the wafer surface are considered infeasible because they are too complex or have a detrimental effect on the lithographic imaging process.

The curvature manipulator boundary conditions and system specifications are identified from literature. The transmissive nature of the reticle makes it necessary to apply the bending moments at the reticle's edges. Furthermore, the current reticle clamping configuration suitable for photomask bending because it contributes to the bending stiffness to the reticle. It also has the risk of slip between the reticle and clamping surface during bending. Other parasitic effects that are caused by bending and that need to be minimized are the optical aberrations, photomask stress-birefringence and overlay. The latter should not exceed 0.1 [nm].

The initial feasibility of photomask curvature manipulation is investigated with simplified opto-mechanical models of the photomask and lithographic imaging system. Analytical and numerical models are used to describe the reticle bending behaviour. A bending moment of ± 0.1 [Nm] is needed in order to achieve the desired curvature correction of $\kappa = \pm 0.4 \times 10^{-3}$ [1/m]. The 0.1 [nm] overlay specification can be satisfied if the reti-

cle pattern deformations by bending are corrected by the lithographic lens. The induced stress-birefringence and optical aberrations by bending are also negligible. It can therefore be concluded that photomask curvature manipulation is conceptually feasible.

The next steps consist of the design, modelling and experimental validation of a specific curvature manipulator concept. Design specifications are first derived from the lithography specifications and used to design the preferred manipulator concept. The concept consists of two opposing arrays of piezoelectrically driven bending mechanisms that are preloaded onto the reticle via a leaking vacuum clamp. The piezoelectric actuators are selected because of their low power dissipation, volume and mass. Each actuator is integrated into a mechanism which is able to generate the bending moment whilst keeping the manipulator's parasitic stiffness and forces at acceptable levels. Local feedback is applied across each piezoelectric actuator in order to counteract its hysteresis and creep. Strain gauge sensors are used to measure the actuator elongation for the feedback loop.

The performance of the curvature manipulator is further evaluated with linear mechanical, control and thermal models. The mechanical model demonstrates that the system eigenfrequencies, photomask deflection, reticle pattern distortions and stress-birefringence specifications are satisfied by the manipulator design. The control model is used to investigate the manipulator's curvature tracking performance for different control strategies and to perform more detailed servo error budgeting. The analysis demonstrates that the manipulator design is able to achieve the desired tracking performance for 100 [Hz] curvature setpoints. An outer curvature feedback loop is nevertheless proposed as addition because of the unobservability of the photomask curvature in the strain gauge measurement information. The thermal model highlights that the reticle thermal expansion by the piezoelectric actuator and leaking vacuum clamp heat loads are within specification but that the strain gauge configuration requires further optimization.

The performance of the photomask curvature manipulator is finally experimentally validated. The setup consists of a curvature manipulator assembly and external metrology system that measures the photomask's out-of-plane deflection. In-plane pattern distortions cannot be measured with the setup but need to be estimated from the out-of-plane photomask deflection. Measurements for static setpoints demonstrate that the photomask deflection correlates to the theoretically modelled shape but that a higher order deflection shape is also present. Errors in the curvature manipulator setup and the external metrology system are the cause of the higher order out-of-plane deformation. The achieved curvature amplitude was limited to 0.11×10^{-3} [1/m] because the photomask out-of-plane constraints were not properly integrated in the manipulator design. The curvature manipulator nevertheless showed to have a linear behaviour across this actuation range. Measurements were also performed for dynamic curvature setpoints. It was difficult to quantify the system's performance however because of the absence of a real-time curvature sensor in the measurement setup.

The modelling and experimental results that are obtained in this thesis demonstrate the conceptual feasibility of a photomask curvature manipulator. The concept has not been validated with respect to all high-level lithography specifications however because of the measurement setup limitations. A lithography tool is considered as the only environment in which the concept can be fully validated. Future work should focus on further validation and evolution of the manipulator so that it can be used as a field curvature correction manipulator in immersion lithography tools.

Contents

Voorwoord	iii
Summary	v
Nomenclature	1
I Motivation	9
1 Introduction	11
1.1 IC manufacturing	11
1.2 Photolithography equipment	13
1.2.1 System architecture	13
1.2.2 Performance parameters	15
1.3 Depth-of-Focus	17
1.4 Focus limiting factors	18
1.4.1 Lens heating	19
1.4.2 Wafer topology	20
1.5 Reticle bending as focus enabler	20
1.6 Study of similar systems	21
1.6.1 Direct reticle curvature manipulation	23

1.6.2	Indirect reticle curvature manipulation	23
1.7	Research objectives	24
1.8	Outline of thesis	25
2	Curvature manipulator requirements analysis	27
2.1	Introduction	27
2.2	Field curvature correction by reticle bending	28
2.2.1	Simplified model of reticle bending	28
2.2.2	Relation between wafer and reticle curvature	30
2.3	Focus improvement analysis	32
2.3.1	Lens heating	32
2.3.2	Wafer topology	34
2.4	Boundary conditions	38
2.4.1	Reticle properties	38
2.4.2	Reticle clamping configuration	39
2.5	Specifications	42
2.5.1	Imaging	42
2.5.2	Overlay	46
2.5.3	Throughput	49
2.6	Summary & Conclusions	53
3	Conceptual analysis of photomask curvature manipulation	55
3.1	Introduction	55
3.2	Reticle bending strategies	56
3.3	Mechanical modelling of photomask bending	57
3.3.1	Analytical modelling	57
3.3.2	Numerical modelling	61

3.4	Pattern distortion estimation	65
3.5	Induced stress birefringence	67
3.6	Generated optical aberrations	71
3.7	Summary & Conclusions	75
4	Design of the curvature manipulator	77
4.1	Introduction	77
4.2	Design specifications	78
4.2.1	Parasitic loads	78
4.2.2	Manipulation range	80
4.2.3	Parasitic stiffnesses	84
4.2.4	Added mass	85
4.2.5	Mechanical resonance frequencies	88
4.2.6	Volume claim	88
4.2.7	Power dissipation	88
4.3	Conceptual design	91
4.3.1	Actuation mechanism	92
4.3.2	Metrology	97
4.3.3	Control	99
4.4	Final design	102
4.4.1	Kinematic analysis	104
4.4.2	Mechanical design	106
4.4.3	Electrical design	107
4.5	Summary & Conclusions	110
5	Performance estimation of the manipulator design	113
5.1	Introduction	113

5.2	Models of the manipulator	114
5.2.1	Mechanical model	114
5.2.2	Control oriented model	115
5.3	Mechanical performance	116
5.3.1	System eigenfrequencies	118
5.3.2	Photomask deflection	119
5.3.3	Reticle pattern distortions	120
5.3.4	Photomask stress-birefringence	121
5.3.5	Reticle gravity deflection	121
5.4	Control performance	122
5.4.1	System dynamics	122
5.4.2	Piezoelectric actuator elongation feedback control	125
5.4.3	Curvature feedback control	128
5.4.4	Curvature tracking performance	131
5.4.5	Effect of disturbances on curvature manipulation	133
5.5	Thermal performance	137
5.5.1	Piezoelectric actuator dissipation	137
5.5.2	Induced heat load by leaking vacuum clamp	138
5.5.3	Strain gauge heat load	147
5.6	Summary & Conclusions	147
 II Experimental Analysis of the Curvature Manipulator		151
 6 Experimental validation of the full actuator array		153
6.1	Introduction	153
6.2	Experimental setup	154
6.2.1	Objectives	154

6.2.2	Setup description	154
6.2.3	Realization	158
6.3	Measurements	159
6.3.1	Calibration	159
6.3.2	Controller implementation	167
6.3.3	Curvature control performance	174
6.3.4	In-plane pattern distortion estimation	180
6.4	Summary & Conclusions	181
III Closing		185
7	Conclusions and Recommendations	187
7.1	Conclusions	187
7.2	Recommendations	192
Bibliography		197
A	Lithographic lens correction model	209
A.1	Optical aberrations	209
A.2	Describing optical aberrations in Zernikes	210
A.3	Lens correction calculation procedure	213
A.3.1	Translation of pattern distortions to optical aberrations	213
A.3.2	Calculation of lens manipulator setpoints	213
A.3.3	Calculation of residual pattern distortions	214
A.3.4	Average distortions and fading penalty	214
A.4	Overview of correctable pattern distortions	215
B	Modelling the photomask as a Kirchhoff plate	219
B.1	The Kirchhoff plate model assumptions	219

B.2	Strain-curvature relations	220
B.3	Stress-curvature relations	222
B.4	Internal bending moment relations	223
B.5	Governing equation of photomask deflection	223
B.6	Photomask undergoing pure bending	224
C	Number of discrete moments for photomask bending	227
C.1	Introduction	227
C.2	Model with discrete bending moments	227
C.3	Analysis results for discrete actuation	229
D	Piezoelectric actuator power dissipation model	231
D.1	Introduction	231
D.2	Linear model of a piezoelectric actuator	231
D.3	Relation for actuator power dissipation	232
E	Experimental validation of a single actuator unit	235
E.1	Experimental setup	235
E.1.1	Objectives	235
E.1.2	Setup design	236
E.1.3	Realization	239
E.2	Measurements	241
E.2.1	Calibration	241
E.2.2	Controller implementation	244
E.2.3	Curvature tracking performance	248
	Samenvatting	253
	Curriculum Vitae	255

Nomenclature

Acronyms

3D	Three-dimensional
AA	Anti Aliasing
AD	Analog-to-Digital
ADC	Analog-to-Digital Converter
AI	Analog Input
AO	Analog Output
CAS	Cumulative Amplitude Spectrum
CD	Critical Dimensions of an Integrated Circuit
CDU	Critical Dimensions Uniformity of an Integrated Circuit
CPS	Cumulative Power Spectrum
CTE	Coefficient of Thermal Expansion
Ctrl	Control
DA	Digital-to-Analog
DAC	Digital-to-Analog Converter
DCO	Dedicated Chuck Overlay
DEB	Dynamic Error Budgeting
DOF	Depth-of-Focus
DoF	Degree-of-Freedom
DoFs	Degrees-of-Freedom
DUV	Deep Ultraviolet
DP	Double Patterning
EDM	Electro Discharge Machining
ERO	Edge Roll Off
ESD	Electrostatic Discharge
EUV	Extreme Ultraviolet
FC	Field Curvature
FCC	Field Curvature Correction
FE	Finite Element
FEM	Finite Element Method; Finite Element Model

FUMO	Functional Model
GND	Ground
HV	High Voltage
HVM	High Volume Manufacturing
H-line	Horizontal line
IC	Integrated Circuit
L	Loop gain
MA	Moving Average
MAC	Modal Assurance Criteria
MIMO	Multi Input Multi Output
MSD	Moving Standard Deviation
MMO	Matched Machine Overlay
NA	Numerical Aperture of a lens
NI	National Instruments
NTU	Number of Transfer Units
OL	Overlay
OPA	Operational Amplifier
OPD	Optical Path Differ
OPL	Optical Path Length
PI	Physik Instrumente
PSD	Power Spectral Density
Qgrid	Qualification grid
RGA	Relative Gain Array
RMS	Root Mean Square
RS	Reticle Stage
S	Sensitivity
SE	Single Exposure
SEBS	Styrene Ethylene Butylene Styrene
SEMI	Semiconductor Equipment and Materials International
SG	Strain Gauge
SISO	Single Input Single Output
SMO	Single Machine Overlay
SNR	Signal-to-Noise ratio
T	Complementary Sensitivity
TE	Transverse Electric
TM	Transverse Magnetic
TPT	Throughput
UEI	Universal Electronics
ULE	Ultra Low Expansion
V-line	Vertical line
WPH	Wafers Per Hour

WS	Wafer Stage
ZOH	Zero-Order-Hold

Greek symbols

α	Coefficient of thermal expansion;	[1/K]
	Asymmetric magnification	[−]
δ	Retardation of light beam along its path when it traverses an optical material;	[−]
	Loss factor of piezoelectric actuator	[−]
ε	Strain	[−]
$\varepsilon_x, \varepsilon_y, \varepsilon_z$	Strains in the Cartesian coordinate system	[−]
ϕ	Angle in the circular pupil	[−]
φ_i	Angle of incidence of a light ray	[−]
φ_o	Angle of reflection of a light ray	[−]
κ	Curvature	[1/m]
κ_x, κ_y	Curvature in x - and y -direction	[1/m]
λ	Wavelength;	[nm]
	Characteristic locus	[−]
μ	Dynamic viscosity;	[Ns/m ²]
	Friction coefficient;	[−]
	Average, mean	
ν	Poisson ratio	[−]
ρ	Density;	[kg/m ³]
	Normalized pupil radius	[−]
σ	Stress;	[N/m ²]
	Standard deviation	
$\sigma_x, \sigma_y, \sigma_z$	Stress in the Cartesian coordinate system	[N/m ²]
σ_1, σ_2	Principal stresses	[N/m ²]
τ_x, τ_y, τ_z	Shear stresses in the Cartesian coordinate system	[N/m ²]
θ	Angle of incidence;	[rad]
	Principal angle	[rad]
$\theta_x, \theta_y, \theta_z$	Rotations around the axis of the Cartesian coordinate system	[rad]
ω	Frequency	[rad/s]
ω_c	Cross-over frequency	[rad/s]
ω_n	Excitation frequency of piezoelectric actuator	[rad/s]

Matrices

I	Identity matrix	[−]
J	Actuator selection matrix	[−]
K	Stiffness matrix	[N/m]

M	Mass matrix;	[kg]
	Jones matrix	[–]
R	Rotation matrix	[–]
X	Anticlastic curvature fitting matrix	

Vectors

c	Fit coefficients of anticlastic curvature model	[–]
E, E₁, E₂	Electric fields	[V/m]
H	Magnetic field	[A/m]
T_i	Input decoupling vector	[m ²]
u, v, w	Vectors containing reticle deformation in the Cartesian coordinate system	[m]

Large symbols

A	Area	[m ²]
A_i	Amplitude of <i>i</i> th Zernike polynomial	[m]
A_m	Mounting or clamping area	[m ²]
C	Stress-optic-coefficient	[m ² /N]
C₁, . . . , C₅	Fit coefficients of anticlastic curvature model	
C_l	SISO controller of the piezoelectric actuator elongation feedback loop	
C_p	Capacitance of piezoelectric actuator	[F]
D	Flexural rigidity	[Nm ²]
D_h	Hydraulic diameter	[m]
E	Elasticity modulus;	[m]
	Efficiency	
F	Force	[N]
F_a, F_{act}	Actuator force	[N]
F_b	Force from applied bending moment	[N]
F_p	Preload force;	[N]
	Internally generated force by piezoelectric actuator	[N]
F_{ix}, F_{iz}	Force in <i>x</i> - and <i>z</i> -direction through interface rods	[N]
F_{zx}, F_{zz}	Force in <i>x</i> - and <i>z</i> -direction through z-support	[N]
G_{sg}	Strain gauge gain	[m/V]
H_a	Dynamics of piezoelectric actuator amplifier	[V/V]
H_f	Dynamics of anti aliasing filter	[V/V]
H_s	Dynamics of strain gauge sensor	[V/m]
H_κ	Dynamics of curvature sensor	[V/(1/m)]
I	Moment area of inertia	[m ⁴]
J_r	Rotational inertia of reticle	[kgm ²]
K_l	SISO piezoelectric actuator feedforward	

	controller	[V/m]
L	Length	[m]
ΔL	Reticle length tolerance	[m]
ΔL_p	Piezoelectric actuator elongation	[m]
ΔL_{pi}	Elongation of i^{th} piezoelectric actuator	[m]
M	Moment;	[Nm]
	Lens magnification	[–]
M_b	Bending moment	[Nm]
M_c	Counteracting bending moment by single bending actuator	[Nm]
N	Normal force	[N]
P	Plant;	
	Power	[W]
P_m	Dynamics of manipulator	[W]
P_p	Dynamics of reticle	[W]
P_{diss}	Power dissipation	[W]
P_{loss}	Piezoelectric actuator power loss	[W]
P_{cum}	Cumulative power	[W]
P_{tot}	Total power	[W]
Pr	Prandtl number	
PSD_{ad}	PSD of analog-to-digital converter noise	[V]
PSD_{amp}	PSD of piezoelectric actuator amplifier noise	[V]
PSD_{da}	PSD of digital-to-analog converter noise	[V]
PSD_{sg}	PSD of strain gauge sensor noise	[V]
PSD_{κ}	PSD of curvature sensor noise	[V]
Q_a	Quantization interval	
\dot{Q}	Thermal load	[W]
\dot{Q}_{air}	Thermal load by flowing air	[W]
\dot{Q}_g	Thermal load by flowing air at one discrete actuator	[W]
R	Electrical resistance;	[Ω]
	Thermal resistance;	[K/W]
	Voltage range;	[V]
	Ideal gas constant;	[J/(mol · K)]
	Stress-optic-coefficient;	[m ² /N]
	Coefficient of regression	
R_1, \dots, R_4	Electrical resistances in Wheatstone bridge	[Ω]
R_p	Leakage resistance of piezoelectric actuator	[Ω]
R_x, R_y	Rotation around the x - and y -axis of the Cartesian coordinate system	[rad]
R_{gas}	Thermal resistance of gas	[K/W]
R_{solid}	Thermal resistance of solid	[K/W]

S	Actuator-to-reticle deflection sensitivity	[m/V]
S_b	Wheatstone bridge sensitivity	[V/ Ω]
ΔS	Squareness of reticle	[m]
T	Temperature	[K]
	Time	[s]
T_a	Temperature of ambient air	[K]
T_w	Temperature of wall in flow restriction	[K]
T_z	Translation in z -direction	[m]
U	Voltage	[V]
V	Shear force;	[N]
	Volume	[m ³]
W	Friction force	[N]
	Slit width	[m]
Z_i	i^{th} Zernike polynomial	[–]

Small symbols

a	Acceleration	[m/s ²]
a	Pitch between applied bending forces in y -direction	[m]
b	Reticle length	[m]
c	Specific heat	[J/(kgK)]
c_p	Specific heat at constant pressure	[J/(kgK)]
d	Diameter;	[m]
	Distance	[m]
d_b	Distance between deformed reticle and reference flat in metrology tool	[m]
d_c	Height of chamber in vacuum clamp	[m]
d_e	Pitch between applied bending forces at reticle edge	[m]
d_e	Pitch between applied bending forces at reticle bottom	[m]
d_r	Height of flow restriction;	
	Distance between undeformed reticle and reference flat in metrology tool	[m]
e	Control error	[m]
e_l	Piezoelectric actuator elongation error	[m]
e_κ	Reticle curvature error	[m]
f, f_1, f_2	Focal lengths	[m]
f_{bw}	Bandwidth	[Hz]
f_n	Excitation frequency of piezoelectric actuator	[Hz]
f_N	Nyquist frequency	[Hz]
f_p	Mechanical resonance of piezoelectric actuator	[Hz]
f_r	Mechanical resonance of reticle	[Hz]
f_s	Sample frequency	[Hz]

f_x, f_y, f_z	Mechanical resonance in the directions of the Cartesian coordinate system	[Hz]
g	Gravitational constant ($g = 9.81$)	[m/s ²]
h	Height;	[m]
	Enthalpy;	[m]
	Wafer topology	[m]
h_c	Convection coefficient	[W / (m ² K)]
\bar{h}_c	Average convection coefficient	[W / (m ² K)]
h_s	Height of positioning stage in metrology tool	[m]
l	Length	[m]
l_c	Length of vacuum chamber in x -direction	[m]
l_r	Length of flow restriction in x -direction	[m]
k	Conductivity;	[W / (mK)]
	Stiffness;	[N/m]
	Boltzmann constant	[m ² kg/s ²]
k_m	Manipulator stiffness	[N/m]
k_p	Photomask stiffness;	[N/m]
	Piezoelectric actuator stiffness;	[N/m]
k_1, k_2	Lithography process parameters	[–]
k_s	Stiffness in series with piezoelectric actuator	[N/m]
k_θ	Rotational stiffness of curvature manipulator	[Nm/rad]
m	Mass	[kg]
\dot{m}	Mass flow	[kg/s]
m_a	Actuator mass	[kg]
m_p	Payload mass	[kg]
n	Index of refraction	[–]
n_1, n_2	Principal directions	
Δn_{12}	Stress-birefringence	[nm/cm]
o	Overlay	[nm]
o_n	n^{th} Contributor to the overlay budget	[nm]
p	Pressure	[N/m ²]
p_a	Pressure of ambient air	[N/m ²]
p_r	Clamp pressure	[N/m ²]
p_x, p_z	Reticle edge rotational pole location	[m]
q	Generalized coordinate;	[m]
	Heat flux;	[W/m ²]
	Distributed load	[N/m ²]
r_κ	Reticle curvature setpoint	[1/m]
r_l	Piezoelectric actuator elongation setpoint	[m]
s	Pitch between horizontal leaf spring and piezoelectric actuator in manipulator mechanism;	[m]

	Number of bits	[–]
s_1, s_2	Measured distance by capacitive sensors	[m]
s_v	Position uncertainty	[m]
t	Time;	[s]
	Thickness	[m]
Δt	Reticle thickness tolerance	[m]
u, v, w	Deflections in the Cartesian coordinate system	[m]
Δu	Reticle thermal elongation in x -direction	[m]
v_{scan}	Scan speed	[m/s]
\bar{v}	Average scan speed	[m/s]
w	Width	[m]
w_r	Reticle deflection at RS level	[m]
w_w	Reticle deflection at WS level	[m]
Δw_g	Reticle deflection at WS level	[m]
x, y, z	Cartesian coordinate system	[m]
x_i, y_i, z_i	Dimensions of the image in the Cartesian coordinate system	[m]
x_o, y_o, z_o	Dimensions of the object in the Cartesian coordinate system	[m]
y_κ	Reticle curvature output	[1/m]
y_{slit}	Slit length in y -direction	[m]
y_r	Reticle or Reticle stage position in y -direction	[m]
y_w	Wafer or wafer stage stage position in y -direction	[m]
z	Out-of-plane distance to neutral bending axis	[m]
Δz	Defocus	[m]
Δz_o	Object position change along the optical axis	[m]
Δz_i	Image position change along the optical axis	[m]

Dimensionless parameters

Ma	Mach number
Nu	Nusselt number
Pr	Prandtl number
Re	Reynolds number
Re _H	Reynolds number for hydraulic diameter

Operators

\dot{y}	First time derivative of variable y
\ddot{y}	Second time derivative of variable y
$ \cdot $	Absolute value
$\max(\cdot)$	Maximum value
$\text{diag}(\cdot)$	Diagonal of matrix

Part I

Motivation

Chapter 1

Introduction

The research of the thesis is motivated in this chapter. State-of-the-art immersion lithography equipment that is used for the Integrated Circuit manufacturing is first introduced. The Depth-of-Focus requirements and focus limiting factors for the lithography process are thereafter explained. It is shown that a field curvature correction in the lithography system can improve focus and that this correction can be achieved by manipulating the curvature of the photomask. The latter corresponds to the topic of this thesis. The chapter ends with the definition of the thesis objectives and a thesis outline.

1.1 IC manufacturing

Modern society has seen an explosive growth of novel products that contain information and communication technology at an affordable price. This is especially illustrated by the larger demand for mobile devices such as MP3 players and Smart-phones in the last years where storage capacity and functionality are the main product drivers. The increase in functionality is facilitated by the presence of faster, more affordable and energy efficient Integrated Circuits (ICs) in consumer electronics. The global \$302-billion semiconductor industry [38] is considered as a key player in the electronics supply chain because it is responsible for providing ICs to the electronics industry.

ICs are miniaturized electronic circuits that are manufactured on a silicon wafer. Like conventional electronic circuits, they contain a number of electrical components such as transistors and capacitors to achieve a desired electrical functionality. The architecture is obtained by stacking and interconnecting patterned layers of conducting or insulating channels on top of one another. Figure 1.1 provides an example of an IC architecture. It clearly shows structured channels of varying dimensions. The dimension of a structure in an IC is referred to as *feature size*.

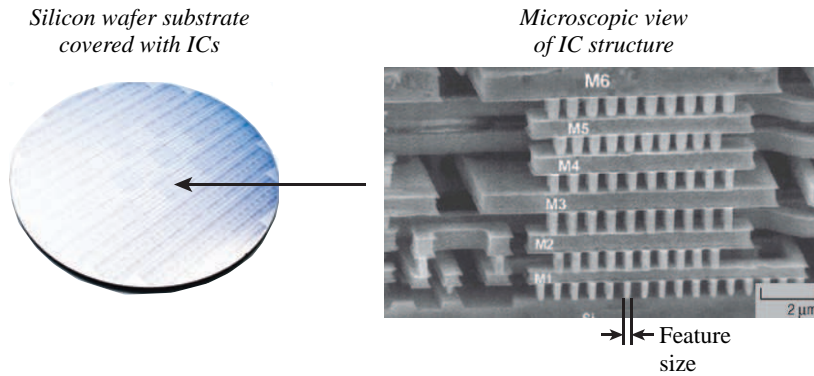


Figure 1.1: An example of the IC structure on a silicon wafer. The left picture shows a silicon substrate that is covered with ICs. The right picture shows a microscopic view of an IC with its layered structure of channels. The smallest channel dimension corresponds to the ICs feature size. The letters *M1* to *M6* indicate different metal layers in the IC structure.

It is well known in the semiconductor industry that the performance of ICs improve for smaller feature size. This scaling law was originally identified in 1965 by Gordon Moore who stated that the number of transistors per chip double every 18 – 24 months [75]. The semiconductor industry has followed this trend ever since by continuously improving the IC manufacturing process.

Figure 1.2 provides an overview of the IC manufacturing steps. The process starts by chemically modifying or doping the silicon wafer such that it acquires semiconductor properties. It is thereafter covered by a layer of metal and photoresist. The next IC manufacturing step consists of the projection of a pattern onto the photoresist with an exposure process. This changes the chemical properties of the resist in the exposed area on the wafer. The exposed or non-exposed area is thereafter removed in a development step in order to uncover areas of the metal layer. The desired features in the metal layer are finally obtained by the removal of the uncovered metal and the remaining photoresist with respectively an etching and washing step. Repetition of the deposition, patterning and etching steps makes it possible to manufacture the desired IC structure.

The exposure step in the IC manufacturing process is known as *photolithography* and is considered as the most critical step in realizing smaller feature size of ICs. The accuracy and cost of the imaging process is largely dominated by the performance of the equipment that is used during the lithography process. Lithography equipment manufacturers are therefore continuously pursuing improvement of their tools in order to facilitate the shrink of ICs and reduction of manufacturing cost.

This thesis focusses on the investigation of a technology that facilitates a further reduction of IC feature size by improving the imaging depth-of-focus in state-of-the-art lithography tools. A further clarification of the thesis topic and objectives are provided in this chapter. Section 1.2 provides an introduction to the lithography equipment by discussing the system architecture and its performance parameters. Section 1.3 provides an explanation of the required Depth-of-Focus for the lithography process. Two focus limiting factors are introduced in Section 1.4. Section 1.5 proposes a method to correct for these focus errors. The state-of-the-art technology of that method is provided in 1.6. The research objectives and the thesis outline are finally provided in Sections 1.7 and 1.8.

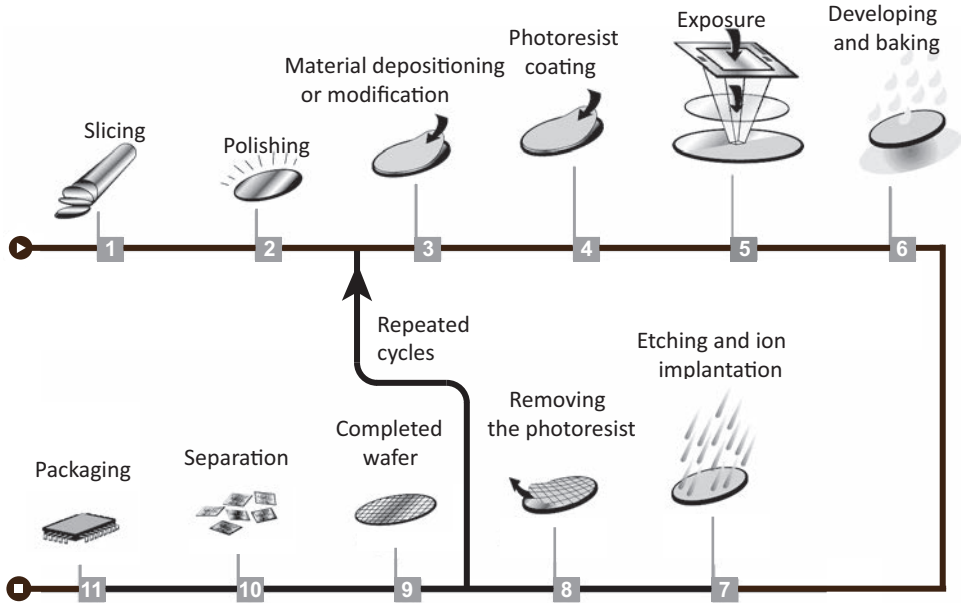


Figure 1.2: The process steps that are used for the production of ICs. Multiple ICs are generated on a Silicon wafer substrate bulk material by different chemical and imaging process steps. The ICs are finally separated from each other and packaged for use in electronic products.

1.2 Photolithography equipment

Immersion photolithography scanners are state-of-the-art production equipment that are used for the High Volume Manufacturing (HVM) of ICs. The equipment performance impacts the achieved feature size as well as the cost effectiveness of production. Section 1.2.1 introduces the system architecture of these immersion scanners whilst Section 1.2.2 provides an explanation of the impact of the machine performance on the lithography process.

1.2.1 System architecture

Figure 1.3 provides a schematic representation of an immersion lithography scanner [20, 21]. It is essentially a large projector that exposes an image onto a Silicon substrate. The imaging process is facilitated by a number of modules in the system. The laser source and illuminator respectively supply and shape the exposure beam into a rectangular slit before it reaches the *photomask* or *reticle*. This is a square piece of glass which has a Chrome pattern on its bottom surface. The exposure beam diffracts at the Chrome pattern, propagates through the projection lens and reaches the Silicon substrate where a four times smaller image is formed. Only the zeroth and first orders of the diffracted light are captured by the lens and used for the imaging process.

Current state-of-the-art lithography systems expose the photomask by scanning the rect-

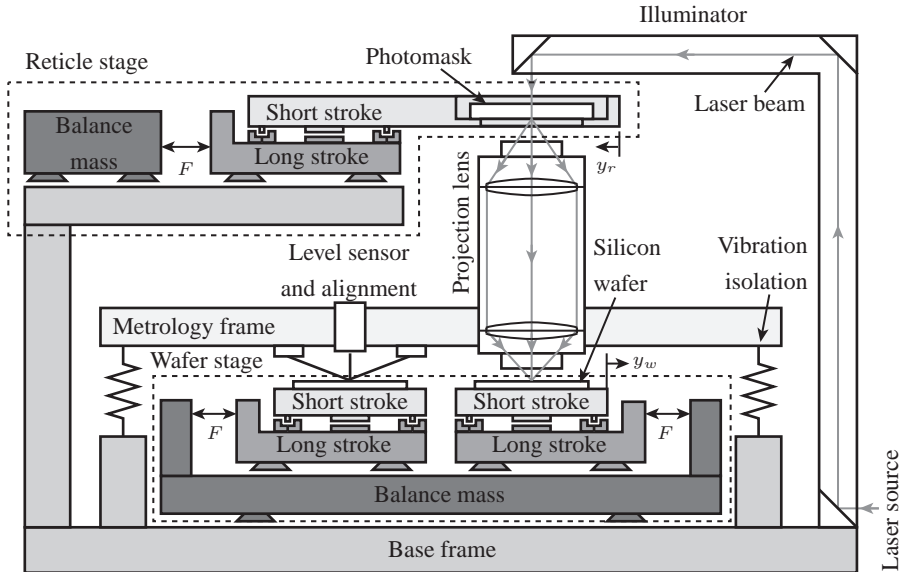


Figure 1.3: A schematic representation of the lithography machine architecture as presented in [20]. For specific details on the machine metrology architecture, see [26].

angular slit along the photomask length instead of exposing the full pattern in one instance. This is schematically shown in Figure 1.4. The main driver for the scanning process is the lower lens cost because a projection lens with smaller diameter can be used [122]. Other advantages are the reduced impact of wafer and reticle unflatness on the exposure process. Note that the reticle and wafer stage have to move in opposite direction because the lens mirrors the image [59].

The scanning motion introduces a number of challenges to the exposure process [20]. The main challenge is the nanometre positioning accuracy requirement of the photomask with respect to the Silicon substrate during the exposure trajectory of both the wafer and reticle. The positioning functionality is facilitated by the reticle and wafer stage module [79, 101]. Both modules consist of a balance mass, long stroke and short stroke. The short stroke or stage holds either the reticle or wafer and is positioned to nanometre accuracy with respect to the lens in six-degrees-of-freedom. Encoders are used for the position measurement of the stage whilst Lorentz actuators apply the required forces for the stage positioning. These actuators are selected because they have low transmission of long stroke position errors and a motor constant which is position independent. The limited range of the short stroke actuators makes it necessary to include a long stroke positioning system. It is positioned within ± 0.1 [mm] with respect to the short stroke and therefore has less stringent positioning requirements than the short stroke. The balance mass absorbs the reaction forces of the long stroke motors and subsequently reduce the amount of disturbance forces that are introduced in the base frame.

The choice of the lithography scanner architecture is driven by the required performance that must be satisfied for the lithography process. The next section discusses the high level system specifications that state-of-the-art scanners have to satisfy. Furthermore, it also introduces the performance requirements for future lithography processes.

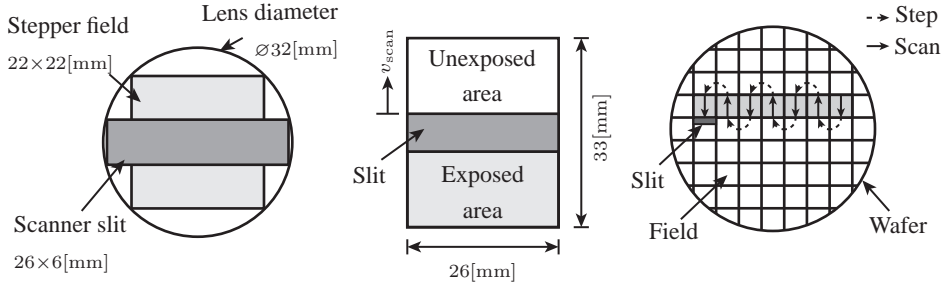


Figure 1.4: The scanning nature of the exposure process in a lithography scanner. The left figure shows that a wider field can be exposed with a scanner instead of a stepper for the same lens diameter. The centre figure provides a schematic representation of a slit scanning across the length of a field. The right figure shows part of the step-and-scan exposure profile across the fields on a wafer [20, 79].

1.2.2 Performance parameters

The performance of a lithography scanner is normally quantified with respect to three parameters. These are *Critical Dimension (Uniformity)*, *Overlay* and *Productivity*. An explanation of the parameters and the future specifications are provided below.

The first performance parameter which is discussed is Critical Dimension (CD) and Critical Dimension Uniformity (CDU). CD is defined as the absolute minimum feature size that is realized in an Integrated Circuit whilst CDU corresponds to the variation of the CD as is graphically shown in Figure 1.5. The former has an influence on the overall device performance whilst the CDU affects the device yield. The realizable CD or resolution in a lithography system is defined by the resolution scaling equation [68]:

$$CD = k_1 \frac{\lambda}{NA} \quad (1.1)$$

where λ is the wavelength, NA is the Numerical Aperture of the lens¹ and k_1 is a process parameters that varies between 0.25 and 1. The latter coefficient indicates the process complexity because it is dependent on resolution enhancement techniques and resist properties [68]. The state-of-the-art immersion lithography scanners that are used for High-Volume Manufacturing (HVM) employ a Deep Ultraviolet (DUV) laser source with $\lambda = 193$ [nm] wavelength and a Numerical Aperture of $NA = 1.35$ [21, 77]. The high NA is achieved by the presence of water between the last lens and the Silicon wafer, hence the name immersion lithography.

Immersion lithography systems are theoretically able to pattern CDs up to 36 [nm] when a Single Exposure process is used [33]. Today's costs and technical challenges of HVM lithography systems with Extreme Ultraviolet laser wavelength of $\lambda = 13.5$ [nm] has pushed IC manufacturers to look to alternative methods to achieve the required reduction in CD. Double Patterning (DP) techniques have been developed for this purpose

¹The Numerical Aperture of the lens is defined by $NA = n \sin \theta$ where n is the index of refraction of the medium between the lens and the wafer and θ is the collected angle of light by the lens.

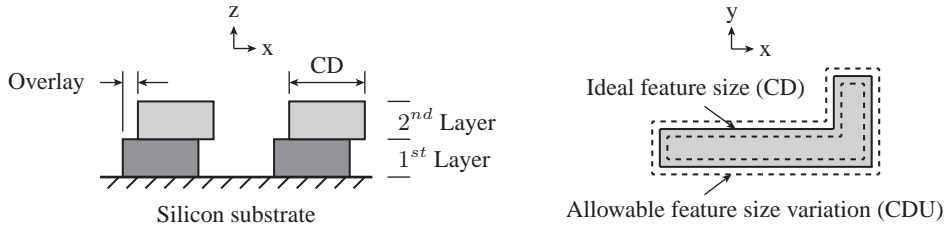


Figure 1.5: Schematic representation of the different performance parameters of the lithography process. The left figure shows the overlay error which is the placement error between two subsequent layers on the Silicon substrate. It also shows the Critical Dimension (CD) which correspond to the smallest feature size on the substrate. The right figure shows the allowable variation on the feature size which is known as Critical Dimension Uniformity (CDU).

[6, 32, 77]. They consist of using two exposures and a number of process steps before etching and can facilitate the aggressive shrink down to CD values of 18 [nm] with immersion lithography systems. Figure 1.6 shows the CDU requirements as a function of technology node for both the SE and DP processes which were identified at the start of this thesis project. The CDU requirements of the SE process corresponds to 7% of the half pitch as a rule of thumb [6]. The graph shows that CDU values below 1 [nm] were initially estimated for the 30 [nm] node although recent publications show that the value has been relaxed to 1 [nm] for the 20 [nm] node [78]. The trend in the reduction of CDU as a function of technology node nevertheless highlights that tighter process control is needed. Parameters such as machine focus and dose control during the imaging process are therefore become more stringent. Furthermore, more effort is put into the optimization of the imaging process and settings [37, 78].

The second performance parameter is *overlay*. It is defined by the alignment error of a layer in the IC with respect to a previously printed layer as is schematically shown in Figure 1.5. Overlay errors have an impact on the electrical performance of the integrated circuit. Short circuits might occur if the overlay specification is not satisfied. Furthermore, it also has an influence on the achievable CD for DP processes [6]. Figure 1.6 provides the overlay specifications as a function of technology node that was identified at the start of the thesis project in 2008. It shows that the overlay budget is approximately 20% of the half pitch value for SE processes [6] and more stringent for DP processes. Recent publications have confirmed that the immersion machine overlay requirements that are used for the DP process must be below 2 [nm] for the 20 [nm] node [15, 21].

The final performance parameter is *Productivity*. It is a measure of the economic value of the machine which is influenced by items like the machine reliability and throughput. The latter is defined as the number of wafers per hour that can be exposed by a machine. An increase in productivity facilitates a cost reduction of Integrated Circuits [68]. State-of-the-art lithography machines are currently running at 175 wafers-per-hour and are expected to increase to more than 200 wafers-per-hour in future [15, 21].

The above discussion highlights that the lithographic processes and equipment need to be constantly improved to facilitate a cost effective shrink of feature size. This is especially the case for the achieved Depth-of-Focus (DOF) of the imaging process in the lithographic machine. A further explanation of DOF and its requirements for future feature size are provided in Section 1.3.

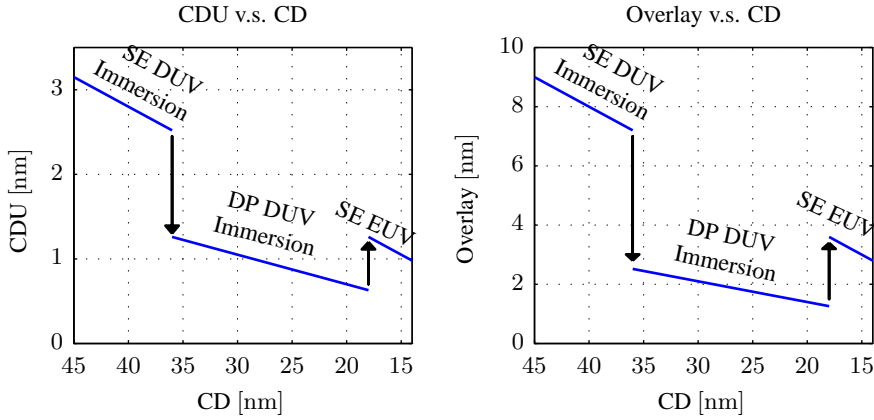


Figure 1.6: The high-level overlay and CDU performance specifications as a function of CD and applied lithography process. SE and DP respectively stand for Single Expose and Double Patterning processes whilst DUV Immersion and EUV correspond to the machine architecture that is used for the exposure process. Values were obtained from [10].

1.3 Depth-of-Focus

One of the parameters that facilitates the reduction of CD and CDU is the achieved Depth-of-Focus (DOF) during the exposure process [68, 78]. The DOF can be considered as the range of defocus of the aerial image with respect to the best focal plane which still gives satisfactory lithography results. A graphical representation of DOF in the lithography imaging system is provided in the right picture of Figure 1.7.

Several mathematical expressions exist to describe the lithography scaling relation for DOF. The most straightforward relation can be obtained by taking a paraxial approximation² of the lithography imaging system. This gives [68]:

$$\text{DOF} = k_2 \frac{\lambda}{\text{NA}^2} \quad (1.2)$$

where λ is the wavelength of the exposure beam, NA is the Numerical Aperture of the lithographic lens and k_2 is a process parameter. The latter is dependent on several factors, such as the k_1 -coefficient, and varies between 0.5 and 1. Equations (1.1) and (1.2) highlight the general trend that a smaller CD requires a reduction in DOF. This observation also holds for the immersion lithography case where both equations change to account for the larger angles in the imaging system [67, 68].

The influence of focus on CD and CDU is caused by two effects. It not only changes the image intensity profile in the resist layer but also affects the sensitivity of the process to other imaging parameters. This is especially the case for exposure dose. Focus and exposure dose are therefore considered to be coupled in the imaging process. Lithographers

²The paraxial approximation is a small-angle approximation of light rays that travel through an optical system such that $\sin \theta \approx \theta$ [47].

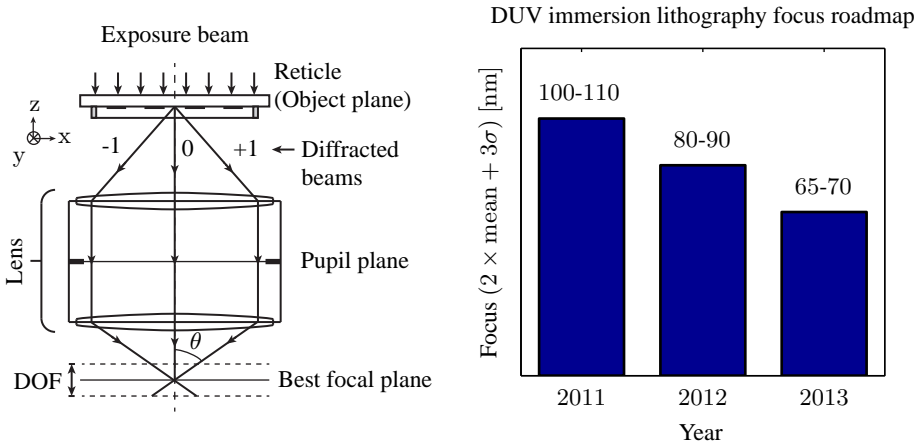


Figure 1.7: A graphical explanation of Depth-of-Focus (DOF). The left picture provides a simplified schematic of DOF in a lithographic imaging system. The right graph shows the roadmap for focus control in immersion lithography systems as provided in [15]. A 70 [nm] focus control is needed for the manufacturing of 22 [nm] feature size.

are able to determine their effect on CD and CDU with simulations or measurements. Furthermore, they define a range of dose and focus variation known as an *exposure-defocus window* that provides the desired pattern fidelity [67]. Such methods have been used to identify focus requirements of about 70 [nm] for the 22 [nm] node [8, 34].

The above discussion indicates that lithography tool manufacturers must continuously improve focus control in their machines in order to facilitate the required DOF for the IC manufacturing process. This is demonstrated by the right graph of Figure 1.7 which shows the focus roadmap for immersion lithography systems as a function of time. The 70 [nm] focus control in 2013 has the objective to facilitate device shrink below 20 [nm] and is enabled by several new technologies [15]. The focus requirements beyond 20 [nm] has uncertainty however because the manufacturing technology and processes are still under development. This has triggered the investigation of other focus limiting factors and a potential improvement technology in lithography machines. They are explained in respectively Section 1.4 and 1.5.

1.4 Focus limiting factors

The overall machine focus budget consists of several high-level contributors. These are lens heating induced defocus, wafer topography, process dependency, focus stability and focus uniformity during the exposure process [15]. Simulations and machine focus measurements are normally used to determine their contributors [95, 135].

This thesis focuses on a method to reduce the effect of two contributors to the overall focus budget, namely lens heating and wafer topology induced defocus because these can be reduced by the same correction mechanism. They are schematically shown in the left drawing of Figure 1.9. These contributors are explained in Section 1.4.1 and 1.4.2.

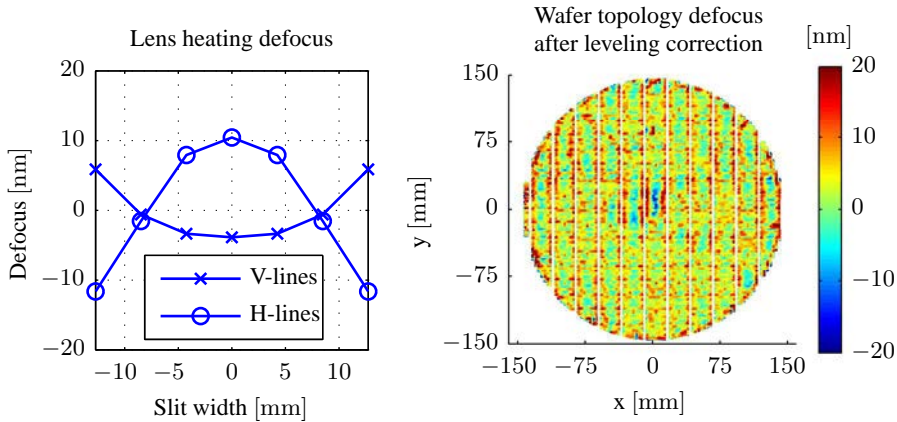


Figure 1.8: Examples of two defocus contributions in lithography systems. The left graph shows the curved focal plane for vertical (V-line) or horizontal (H-line) oriented patterns that is caused by lens heating at high machine throughput. The right graph shows the residual focus error after subtracting ideal wafer stage scanner corrections from the initial wafer topology.

1.4.1 Lens heating

Lens heating changes the optical characteristics (focus, optical aberrations) of the lens. It has a number of causes. First, laser source power has seen a steady increase over the years in order to deliver the necessary exposure energy at wafer level for the demanded throughput increase. Part of the laser energy is absorbed by the lens elements in the optical column. This causes a thermal expansion of the optical elements and subsequently a change of the lens characteristics. Second, resolution enhancement techniques like off-axis illumination are used for the manufacturing of the critical IC nodes [68, 71]. These lead to more localized lens heating and thermal expansion of the optics [9, 84].

Lithography equipment manufacturers have developed several ways to counteract lens heating such as non-absorptive coatings on lens elements [84] and active optical columns. The latter are realized by the integration of position controlled lens elements [77, 81] and deformable lenses or mirrors in the lithography projection optics [84, 102, 111]. They reduce the contribution of lens heating to the lithography tool focus budget [15].

Simulations can be performed in order to estimate the lens heating induced defocus. The left graph in Figure 1.8 provides an example of such a simulation. It shows the residual focus error across the slit width at wafer level for vertical and horizontal oriented lines in a 42 [nm] Flash memory device [7]. Specific details of the simulation are provided in Section 2.3.1. The curves in the graph show a quadratic defocus term in both the horizontal and vertical lines which cannot be corrected by the present lithography lens. The effect is commonly known as *field curvature* which was identified as a focus budget contributor in [133]. Section 2.3.1 will show that the lens heating induced defocus can be eliminated by an ideal curvature correction in the lithography machine. This cancels the 6 [nm] lens heating contribution from the overall focus budget based on numbers in [15].

1.4.2 Wafer topology

Another contributor to the overall focus budget is the wafer topology [68]. In a perfect imaging system, the wafer surface must conform to the lens focal plane or aerial image across the exposure field in order not to have a contribution to the DOF budget. This is not the case in practice because of wafer chuck flatness, wafer thickness variations, wafer flatness, wafer edge effects and device topography [66, 104]. These components contribute to the wafer topography and focus uniformity in the overall focus budget.

Wafer topology has always been a major contributor to the focus budget [36, 48, 116]. Its influence has been relaxed in the past by the introduction of lithography scanners. These made it possible to optimally position the wafer surface with respect to the lens focal plane during the scanning exposure process by continuously adapting the wafer stage translation and rotations [14]. The industry also adopted double sided polished wafers with improved wafer flatness and thickness variations for IC production [130].

The International Roadmap for Semiconductor of 2011 has identified that the wafer site flatness across the exposure area must be improved to approximately 20 [nm] for the 18 [nm] node [49]. The same roadmap stresses that technologies to improve wafer site flatness have not yet been identified. The flatness and therefore defocus are especially an issue at the wafer edge. This phenomenon is known as edge-roll-off [104].

The above has triggered the analysis of lithography tool correctables on measured wafer topology data. The right graph in Figure 1.8 shows an example of the residual wafer defocus after subtracting optimal wafer stage setpoints from the initial wafer topology. The graph demonstrates that the largest defocus occurs at the wafer edge. This confirms the above described edge-roll-off effect. The wafermap also shows another trend. Each field has a negative defocus in its centre and a positive defocus at its edges. This is especially visible for the field in the centre of the wafer. It corresponds to a remaining defocus with a curved shape which was also observed for the lens heating induced defocus. The result indicates that an additional field curvature correction by the lithography tool can potentially facilitate a further reduction of the residual focus error. Section 2.3.2 will show that the focus improvement across the wafer varies between ± 10 [nm] if a field curvature correction is applied.

1.5 Reticle bending as focus enabler

The discussion on the focus limiting factors in Section 1.4 has indicated that an additional and ideal field curvature correction in the lithography system reduces two focus budget contributors. It eliminates the lens heating contribution from the total focus budget and reduces the wafer unflatness contribution to the focus uniformity and wafer topography items. This leads to an estimated focus budget reduction of approximately 10 [nm] based on the values that are provided in [15].

The possible focus improvement has triggered the idea to investigate the feasibility of a field curvature correction in lithography machines. Such a curvature correction mechanism should be placed in any plane that is conjugate to the focal plane at wafer level. This is because a formed image in a focal plane is equally well imaged in its conjugate plane for an ideal imaging system [47, 79]. Trying to achieve the correction outside con-

jugate planes, as is shown in the top-middle picture of Figure 1.9, will result in an image deterioration across the field [53]. These errors are known as *optical aberrations* which have a detrimental effect on the lithography imaging process [18, 71].

The lithographic system has only two conjugate focal planes in the optical column. These are the object plane at the reticle level and the image or focal plane at wafer level as shown in Figure 1.7. No intermediate focal plane exists in the lens column itself [52, 112]. Achieving the desired curvature correction in the lens will therefore require a complete new lens design with an intermediate focal plane as is shown in the top-right drawing of Figure 1.9. This is undesired because of the large costs that are involved for this activity. An alternative solution is to adapt the curvature of the wafer surface to the lens focal plane during the exposure process. This is schematically shown in the bottom-left drawing of Figure 1.9. The proposed method has several difficulties. First, a large number of actuators are needed below the silicon wafer in order to achieve the required spatial correction of the wafer unflatness per exposure field. This increases the complexity of the wafer stage architecture. Second, wafer deformations translate into parasitic in-plane distortions and potentially overlay errors if they are uncorrectable by the lithographic system [108, 109]. This effect is undesired because of increasingly stringent overlay requirements for the lithography process as was explained in Section 1.2.2.

The final alternative consists of actively adapting the curvature of the reticle during the exposure process as is shown in the bottom-right drawing of Figure 1.9. The curvature adaptation of the reticle directly leads to a curved aerial image at wafer level because the reticle and wafer are located in conjugate image planes. It can also lead to an overlay error if the in-plane reticle pattern distortions by bending are left uncorrected. The concept has advantages though. First, the reticle stage architecture is less complex in comparison to the wafer stage and therefore has more design freedom. Second, one reticle curvature manipulator can achieve the same effect as a large number of actuators that would be needed at wafer level. Finally, any manipulation error at reticle level results in smaller errors at wafer level because of the lens reduction factor. This helps relax design specifications for a curvature manipulator when it is designed at reticle level.

The above discussion indicates that the adaptation of the reticle curvature during the exposure process is the preferred way to achieve the desired curvature correction in a lithography machine if the overlay penalty can be resolved. This thesis investigates the potential, feasibility and design of a field curvature correction for an immersion lithography system by adaptation of the reticle curvature. The state-of-the-art of reticle curvature manipulation is provided in Section 1.6 by giving an overview of similar systems. The thesis research objectives are thereafter summarized in Section 1.7

1.6 Study of similar systems

It is clear that an additional field curvature correction in a lithography machine can facilitate a reduction of the focus budget and that this correction can be achieved by adaptation of the reticle curvature. A literature study has shown that others in the lithographic industry have also studied this technology. This section provides an overview of their work. The identified technologies can be categorized into two different classes, namely direct and indirect curvature manipulation. They are treated in Sections 1.6.1 and 1.6.2.

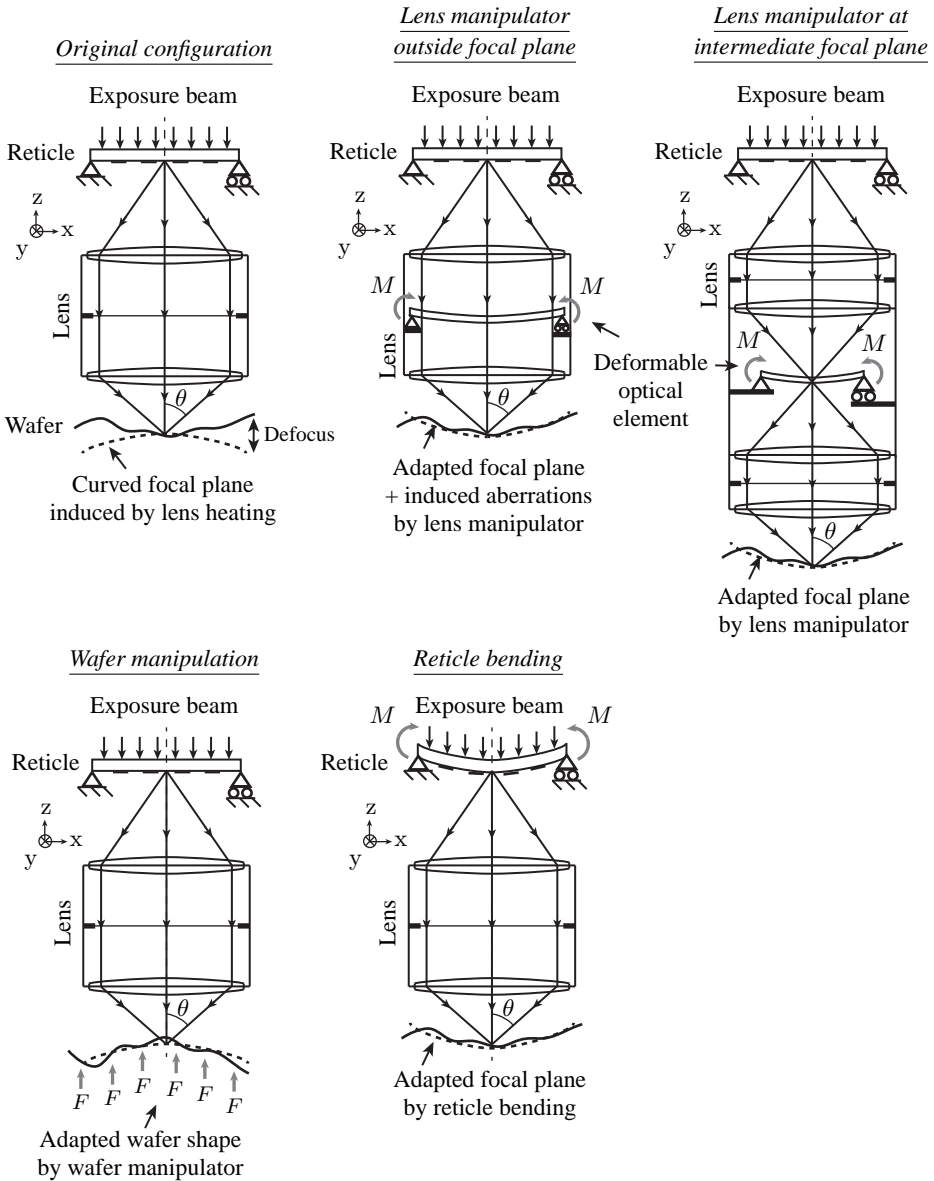


Figure 1.9: Potential ways to resolve a field curvature error in a lithography system. The top-left drawing shows the defocus in the lithography system by a non-flat wafer and curved focal plane due to lens heating. The top-middle and top-right configurations respectively have a lens manipulator outside a lens focal plane or at an intermediate focal plane in order to resolve the defocus. The bottom-left configuration provides a way to account for the defocus by adaptation of the wafer surface with actuator forces F . The bottom-right configuration shows an alternative where bending moment M are applied to the reticle in order to adapt the focal plane at wafer level.

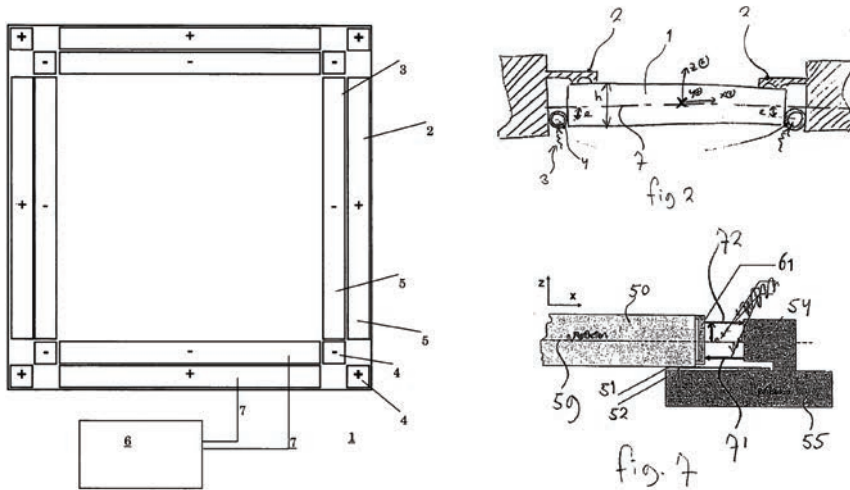


Figure 1.10: Two identified methods of direct reticle curvature manipulation. The left drawing shows the use of controlled pressure zones (+, -) along the reticle edge in order to manipulate the reticle curvature [86]. The right drawings show specific embodiments of reticle curvature manipulation by the application of bending moments to the reticle [53].

1.6.1 Direct reticle curvature manipulation

The literature study has identified two ways of direct reticle curvature manipulation. The first was patented in 2005 and consists of using multiple controlled pressure zones to bend a substrate such as a wafer or reticle [86]. The left picture in Figure 1.10 shows an embodiment of the specific invention.

The second manner of curvature actuation was patented in 2008 [53]. The invention consists of applying bending moments to the reticle with a separate bending mechanism. The patent specifically mentions that the mechanism is used to reduce reticle gravity and heating induced bending after the reticle has been clamped on the reticle stage. Embodiments of the patent are provided in the right drawings of Figure 1.10.

The above summary highlights that direct reticle curvature manipulation has been patented in 2008. Ways to achieve the desired correction potential have been provided on a conceptual level in the patents. The presented ideas were considered as possible curvature correction concepts in the remainder of this thesis.

1.6.2 Indirect reticle curvature manipulation

A method to indirectly control the curvature of the reticle has been reported in [13, 37, 133]. Publicly available information on the concept became available after the starting date of this thesis. It consists of introducing a bending moment into the reticle stage short stroke with the short stroke actuators. The bending moment propagates into the reticle via the non-kinematic reticle mount and results in the desired reticle curvature [13]. The described concept has been patented by Nikon in 2011 [98]. Figure 1.11 shows an em-

The first objective is achieved by identifying the impact of ideal photomask bending on the lithography system performance. This requires knowledge of achievable focus improvement by the manipulator as well as the high-level lithography system specifications and boundary conditions. Furthermore, idealized models of the photomask bending and the lithography system are developed to investigate the effects of photomask bending on the lithography system performance.

The second objective is pursued by the application of a mechatronic system design approach. The approach facilitates the identification of the design specifications and synthesis of a functional manipulator design. It uses knowledge from multiple disciplines such as mechanics, thermal, control, electronics and software. Furthermore, experimental techniques are applied for the validation of the manipulation concept.

Note that this thesis focusses on manipulation of the photomask curvature in lithography systems. Research into the design of advanced metrology techniques for the calibration and real-time feedback of the photomask curvature in the lithography system is conducted in another project [103].

1.8 Outline of thesis

This thesis is structured according to Figure 1.12. The first part provides the motivation of the research. Part two explains the reticle bending concept and the mechatronic design of the curvature manipulator. The third part covers the experimental validation of the manipulator. The thesis is closed by conclusions and recommendations in part four.

Chapter 2 starts the investigation into reticle bending by providing a simplified beam model representation of the concept. The model is used to demonstrate the higher level effects of reticle bending on the lithography process. The achievable focus improvement by a field curvature correction in lithography systems is thereafter analysed. Furthermore, system specifications and boundary conditions are derived for a field curvature correction functionality in a lithography system.

Chapter 3 provides the conceptual analysis of an ideal field curvature manipulator. An analytical and finite element model of the photomask under pure bending is introduced. These models are used to quantify the reticle bending effects. These effects are compared to the high level system specifications of Chapter 2. It is shown that additional corrections are needed by the lithography system in order to satisfy those high level system requirements.

The design of the photomask curvature manipulator is explained in Chapter 4. It first gives an overview of the derived design specifications for the curvature manipulator. The conceptual design choices are thereafter summarized. The chapter ends with an explanation of the detailed mechanical and electrical design of the manipulator. It is shown that the design satisfies the majority of the initial design specifications.

A performance analysis of the detailed manipulator design is provided in Chapter 5. The chapter first introduces the detailed numerical model of the manipulator design. This model is thereafter analysed for its mechanical and control performance. The chapter ends with a thermal evaluation of the manipulator concept. All analyses will demonstrate the feasibility of the manipulation concept.

The experimental validation of the manipulator is explained in Chapter 6. It provides

results for a full-scale functional model of the reticle and curvature manipulator. It is shown that the manipulator is able to realize a photomask curvature but that some improvements are still necessary for the integration into a lithography system. The thesis ends with Chapter 7. It provides conclusions and recommendations for future work in order to successfully implement a curvature manipulator in an immersion lithography system.

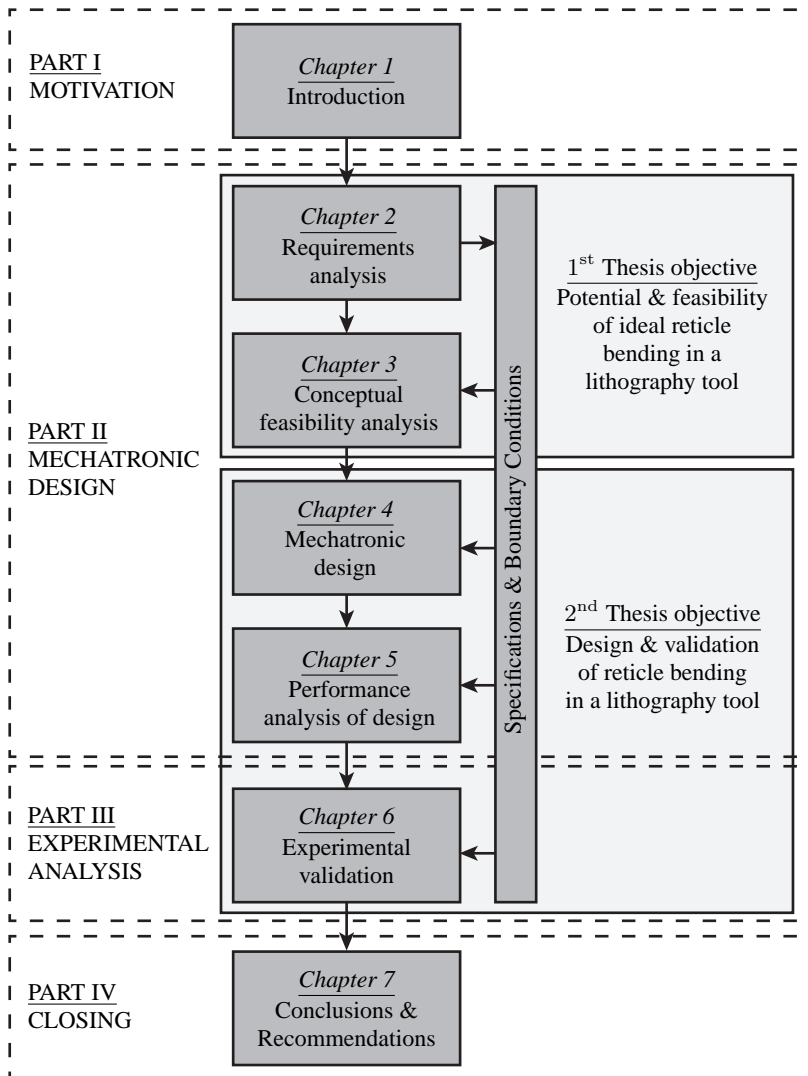


Figure 1.12: Flowchart showing the outline of this thesis.

Chapter 2

Curvature manipulator requirements analysis

This chapter identifies the specifications for a curvature manipulator in lithography machines. The effects of photomask bending on the lithography process are first investigated with the help of a simplified photomask curvature manipulator model. The focus improvement potential of a field curvature manipulator is thereafter studied. The boundary conditions and specifications of the manipulator are finally defined. These are used in Chapters 3 and 4 for the conceptual analysis and mechanical design of a curvature manipulator.

2.1 Introduction

It is essential for an engineer to have an understanding of the functionality, benefit and specifications of the system that they are designing. The objective of this chapter is to provide an explanation on the benefit and the derived specifications for the photomask curvature manipulator. Section 2.2 provides an elementary explanation of the reticle bending concept and its physical effects in the lithography tool. Section 2.3 quantifies the benefit of a curvature manipulator in the lithography tool by analysing its potential to correct lens heating and wafer unflatness induced defocus. The system boundary conditions and specifications are thereafter defined in respectively Section 2.4 and 2.5. The chapter ends with a summary and conclusions in Section 2.6. The results of this chapter are used during the conceptual analysis and the mechatronic design of the manipulator in Chapter 3 and 4.

2.2 Field curvature correction by reticle bending

Reticle bending was introduced in Chapter 1 as a method to achieve a field curvature correction at wafer level in the lithography machine. The concept is schematically shown in the left picture of Figure 2.1. This section provides an elementary explanation of reticle bending. The objective is to show that the desired curvature correction at wafer level can be achieved by the application of bending moments to the reticle. The parasitic effects that are introduced by the bending moment application are also explained.

Section 2.2.1 introduces simplified physical relations between the applied bending moment and the resulting reticle bending effects. The relation between the reticle and wafer curvature in the lithography system is thereafter derived in Section 2.2.2.

2.2.1 Simplified model of reticle bending

The first-order-effects of a bending moment application to the edges of the reticle can be identified by modelling the reticle as a bending beam. This representation is the most elementary model of the reticle when it undergoes bending because it only describes the bending behaviour along the x -dimension of the reticle. More detailed models of the reticle bending behaviour are introduced in Chapter 3. The one-dimensional approximation is considered to be valid for the moment because of the following reasons:

- The scanning nature of the exposure process in combination with the small slit size in y -direction as was shown in Figure 1.4 limits the impact of effects in the scan direction.
- The dominant bending behaviour will be experienced in the x -direction. This is attributed to the fact that the location of bending moment application is limited to the reticle's x -edge as is shown in Figure 2.1 because of reticle boundary conditions. A further explanation is provided in Section 2.4.

Figure 2.1 shows the schematic representation of the reticle as a bending beam. It corresponds to the *pure bending case* because of a constant bending moment along the axis of the beam and the absence of shear forces which results in a constant beam curvature κ along its x -axis. The curvature is equal to [43]:

$$\kappa = -\frac{M}{EI} \quad (2.1)$$

where $M(x)$ is the applied bending moment, E is the elasticity modulus of the reticle material and I is the area of inertia of the reticle. The latter two are fixed quantities for each photomask as will become clear in Section 2.4.1. They define the bending stiffness $1/(EI)$ of the beam. Equation (2.1) shows that the reticle curvature is proportional to the applied bending moment.

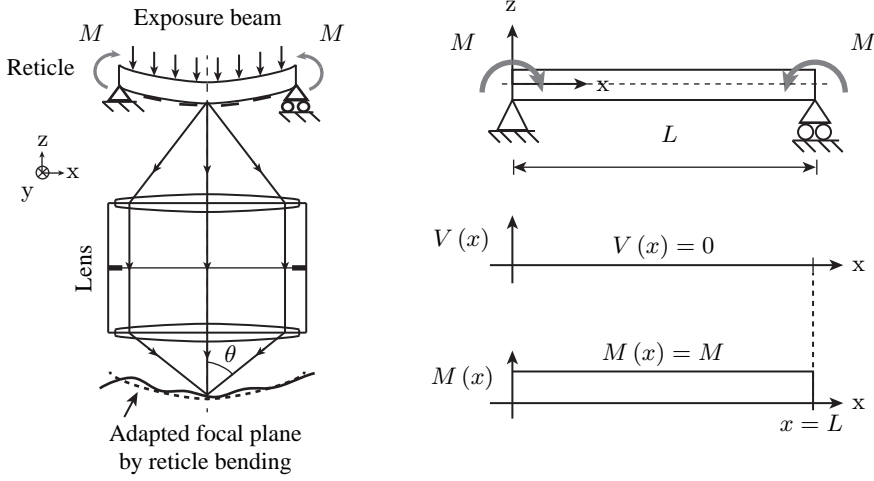


Figure 2.1: A simplified model of reticle bending. The left drawing provides a schematic of the lithography imaging system where bending moments M are applied to the edges of the reticle. This results in a curved aerial image at wafer level. The right drawings provides a mechanical equivalent where the reticle is modelled as a bending beam. The internal shear force $V(x)$ and bending moment diagrams $M(x)$ for a beam under pure bending are also provided.

The curvature of the beam is defined as the double derivative of the beam deflection w with respect to the beam axis x , i.e. [43]:

$$w = \int \int \frac{d^2w}{dx^2} dx dx \Rightarrow w = \frac{1}{2} \kappa x^2 \quad (2.2)$$

where the integration constants have been neglected for simplicity. This simplified expression for the out-of-plane beam deflection is used in Section 2.2.2 to derive the relation between the reticle and wafer curvature.

The applied bending moment does not only result in a curvature but also in stresses and strains in the photomask. The strain ε_x in the reticle is defined by [43]:

$$\varepsilon_x = -\kappa z \quad (2.3)$$

where z is the out-of-plane distance with respect to the neutral bending axis of the reticle as is shown in Figure 2.1. The neutral axis is located in the centre of the reticle in the absence of in-plane normal forces through the beam. The stress σ_x in the reticle is equal to [43]:

$$\sigma_x = -E\kappa z \quad (2.4)$$

Equations (2.3) and (2.4) highlight the presence of stresses and strains in the photomask after the application of the bending moment. These stresses and strains are proportional

to the applied bending moment and also vary linearly across the thickness of the reticle and can affect the system's imaging performance in the following way:

- The largest bending strain occurs at the bottom surface of the photomask which corresponds to the location of the photomask pattern as will be shown in Section 2.4.1. The pattern therefore undergoes an elongation or shortening during photomask bending which can translate into overlay errors when left uncorrected. An overlay specification must therefore be derived for the bending manipulator. This is done in Section 2.5.2.
- The lithography processes for the critical IC layers use a polarized laser beam for the exposure process [60]. Photomask stresses lead to stress-birefringence which changes the polarization state of the laser beam and subsequently deteriorates the system's imaging performance. The stress-birefringence specification is further explained in Section 2.5.1.3.

2.2.2 Relation between wafer and reticle curvature

The previous section provided simplified expressions for the reticle's physical behaviour when it undergoes bending. This section uses the results of that section to demonstrate that the reticle curvature translates into an aerial image at wafer level with the same curvature. The lateral and longitudinal magnification values of state-of-the-art lithography lenses are used for the proof.

Figure 2.2 shows a simplified representation of the lens that is used in lithography systems [79]. It corresponds to a finite conjugate model of an afocal imaging system. The afocal system consists of two serially placed focal systems where the back focal plane f_1 of the first coincides with the front focal plane f_2 of the latter. The amount of light that travels through the lens is defined by the aperture stop which is placed at the location of the coinciding focal planes.

The configuration in Figure 2.2 is known as a *double telecentric* lens. It has the specific characteristic that any shift of the image or object planes does not affect the magnification M of the image. This is advantageous for the lithography process because an out-of-plane translation of the reticle or wafer with respect to the lens will not result in pattern distortions [79, 83]. Figure 2.2 provides a schematic explanation of this principle. It shows that the image size does not change for varying object distance Δz_o . The only change is the position of the image on the optical axis by Δz_i which corresponds to a defocus if the wafer is not shifted by the same distance. The position of the wafer at the image side must therefore follow the image in order to avoid defocus [79].

The above described effect can be captured into simplified imaging relationships for a paraxial approximation of the lens. The imaging relationships for a rotationally symmetric double-telecentric lens are described by [85]:

$$x_o = \frac{x_i}{M}, \quad y_o = \frac{y_i}{M}, \quad z_o = \frac{z_i}{M^2} \quad (2.5)$$

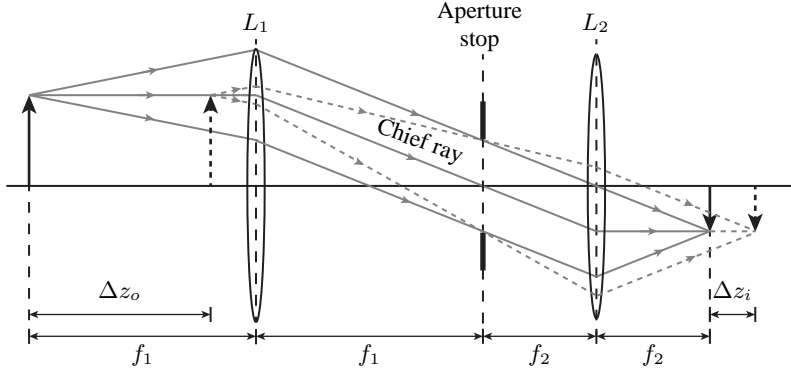


Figure 2.2: The simplified representation of the afocal optical configuration in lithography systems [79].

where x_o, y_o, z_o and x_i, y_i, z_i are respectively the object and image dimensions in a Cartesian coordinate system. These dimensions relate to respectively the reticle and aerial image at wafer level when the lithographic lens is considered. The magnification of that lens is equal to $1/4$ [59].

Equation (2.5) will now be used to determine the relation between the curvature at wafer and reticle level. The derivation is only provided for the x - and z -direction because rotational symmetry of the lens. Furthermore, the derivation assumes that a curved aerial image is obtained at wafer level by the photomask curvature. In that case, the out-of-plane deflection of the reticle w_r and the aerial image at wafer level w_w across the exposure area is defined by:

$$\kappa_r = \frac{2w_r}{x_r^2}, \quad \kappa_w = \frac{2w_w}{x_w^2} \quad (2.6)$$

where x_r and x_w are the across slit position and κ_r and κ_w the field curvatures at respectively reticle and wafer level. From Equation (2.5) it is known that the across slit position and the out-of-plane deflection at reticle and wafer stage are related by respectively the lateral and longitudinal magnification, i.e.:

$$x_r = \frac{x_w}{M}, \quad w_r = \frac{w_w}{M^2}. \quad (2.7)$$

Substitution of Equation (2.6) into (2.7) results in the relation between the reticle and wafer curvature

$$\kappa_r = \frac{2w_w}{x_w^2} \frac{M^2}{M^2} = \kappa_w. \quad (2.8)$$

which shows that the image curvature at wafer level is equal to the reticle curvature for the paraxial approximation. Section 3.6 will show that the acquired result also holds for the

immersion lithography lens when the paraxial approximation cannot be used. The unity relation between the reticle and image curvature will therefore be used in the remainder of this thesis.

2.3 Focus improvement analysis

Chapter 1 introduced lens heating and wafer non-flatness as defocus contributors in state-of-the-art lithography systems. The chapter also indicated that their contribution can be reduced by a field curvature correction in the lithography system. The previous section demonstrated that the desired curvature correction can be obtained by reticle bending. This section provides details of the analyses that were performed to identify the potential focus improvement by a field curvature correction at wafer level. Section 2.3.1 presents the analysis of the induced defocus by lens heating. Section 2.3.2 provides the results for the wafer topology analysis. The results also provide estimates of required curvature ranges. These values are used as input for the manipulator design specifications in Section 2.5.

2.3.1 Lens heating

Section 1.4.1 introduced lens heating as an increasingly prominent defocus contribution. It especially occurs during High Volume Manufacturing (HVM) of memory structures such as Flash and DRAM where dense line and space patterns are projected onto the photoresist. The optical errors that are induced by lens heating differ for each device. Each case required different lens settings for the aberration correction [69].

The effect of localized lens heating for memory structures is explained by Figure 2.4. The manufacturing process of those structures employs photomasks with horizontal (H) or vertical (V) oriented lines and spaces as is shown in the top-left drawing of Figure 2.4. The manufacturing of these devices uses off-axis illumination in order to enhance resolution [71]. This illumination setting projects an exposure beam with two different angles of incidence on the reticle which is illustrated by the top-right drawing of Figure 2.4. The 0th and 1st diffraction orders of the beams that are needed to form an image at wafer level overlap. This leads to a concentration of the exposure beam intensity on two small spots in the lens pupil as is shown in the bottom-left picture of Figure 2.4. The energy concentrations result in local heating of lens elements which causes them to expand. The expanding lenses change the optical path of the rays and cause an in-plane and out-of-plane shift of the image as is schematically illustrated by the bottom-right picture of Figure 2.4. These resulting defocus is different for V- or H-lines when the lens has been heated by the dipole-X illuminator settings. This is because the diffracted orders go through orthogonal paths of the lens. It is shown below that the resulting defocus for the described application is a combination of field curvature and astigmatism [71, 111]. These effects are difficult to independently correct with current lens manipulators and has triggered the investigation into an independent field curvature manipulator.

The correction potential of a field curvature manipulator on the induced defocus by lens heating was analysed using lens heating simulations [7]. The simulations are able to de-

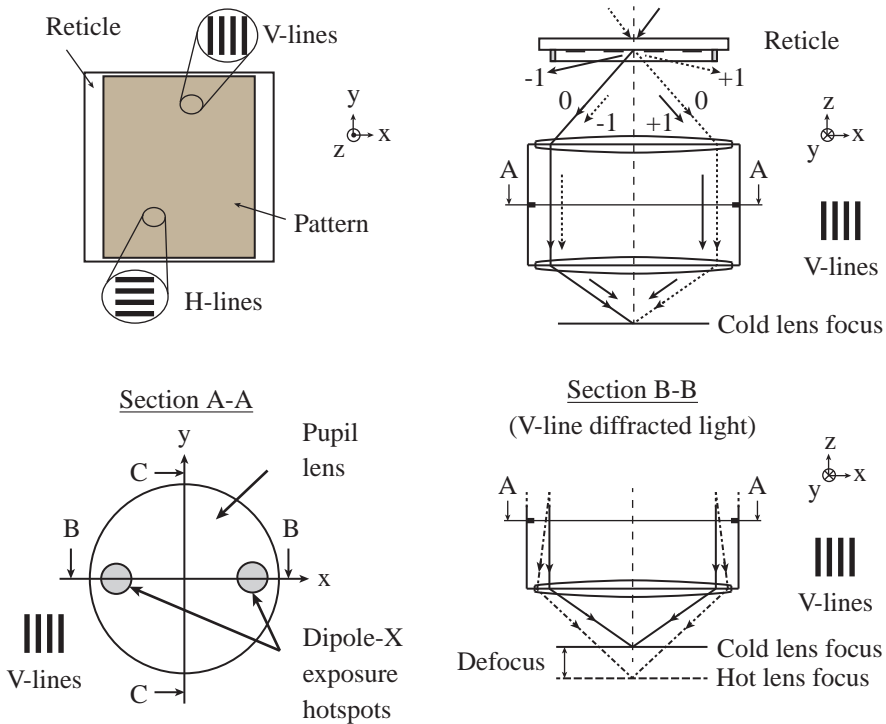


Figure 2.3: A schematic explanation of the induced defocus by lens heating. The top-left drawing shows a top-view of the reticle with the vertical (V) and horizontal (H) oriented lines. The top-right drawing represents the imaging configuration when off-axis dipole-X illumination is used. The bottom-left figure shows the lens pupil-plane with the local hotspots that are caused by the illuminator settings and the pattern orientation. The bottom-right drawing illustrates the induced defocus due to the localized lens heating.

termine the in-plane image shift and defocus as a function of lithography machine properties. These include items such as the source power, illuminator settings, photomask pattern and lens properties.

Figure 2.4 provides the results of the lens heating simulation for a 42 [nm] Flash memory structure at 230 WPH throughput in a state-of-the-art immersion lithography system. An off-axis dipole-X illuminator setting was used for the simulation. Both graphs show the defocus across the width of the slit in x -direction for horizontal and vertically oriented lines. The left graph shows the defocus for a conventional lithography lens whilst the right graph gives the result for the same lens with an additional field curvature correction. The following conclusions are drawn from the graphs:

- The lens heating simulation results for the conventional lithography lens show a defocus range of ± 10 [nm]. The defocus has a curved shape across the slit for both the horizontal and vertically oriented lines which are approximately equal but of opposite sign. This confirms the above statement that lens heating induces an astigmatic curvature.

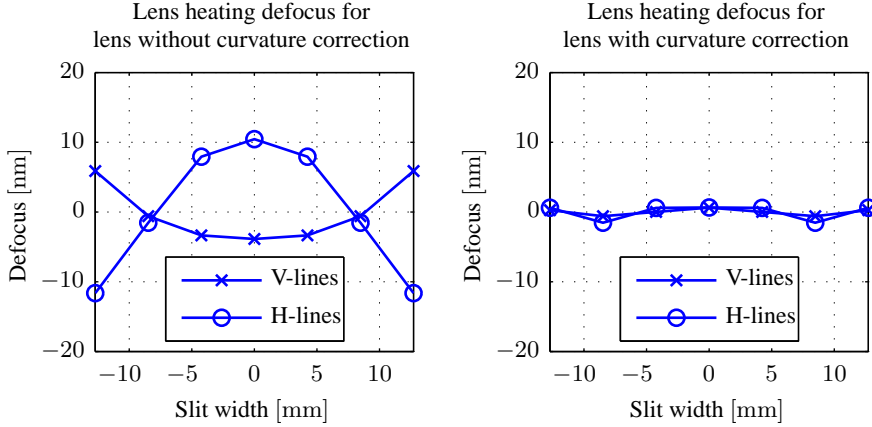


Figure 2.4: Simulation results for lens heating defocus [7]. The left graph shows the defocus for horizontal (H) and vertical (V) lines across the slit width for the current lithography lens. The right graph shows the defocus for the current lens with an additional curvature correction.

- An additional curvature manipulator in the lithographic lens is able to eliminate the astigmatic curvature and reduce the defocus from ± 10 [nm] to ± 1 [nm].
- The magnitude of the required curvature correction κ to correct for lens heating is equal to:

$$w(x) = \frac{1}{2}\kappa x^2 \Rightarrow \kappa \approx 0.4 \times 10^{-3} [1/m] \quad (2.9)$$

where w is the defocus by lens heating and x the position across the slit width.

Note that the thermal behaviour of the lithographic lens is low frequent with respect to the repetitive nature of the exposure process. The curvature defocus contribution by lens heating can therefore be considered as a quasi-static focus error.

2.3.2 Wafer topology

Another focus budget contributor that can be reduced by a field curvature correction in the lithography system is wafer unflatness. The contribution of wafer unflatness to the focus budget was introduced in Section 1.4.2. This section first provides an explanation of the levelling strategy in the lithography scanner. The impact of a field curvature correction on residual wafer non-flatness and the identified wafer curvature amplitudes are presented thereafter.

Figure 2.5 provides a flowchart of the levelling strategy in an immersion lithography system [14, 101]. The first step of the strategy consists of measuring the wafer topology $h(x, y)$ with the level sensor that is shown in Figure 1.3.

The second step consists of calculating the optimal wafer stage setpoints in order to minimize defocus during the exposure process. The defocus can be minimized by the

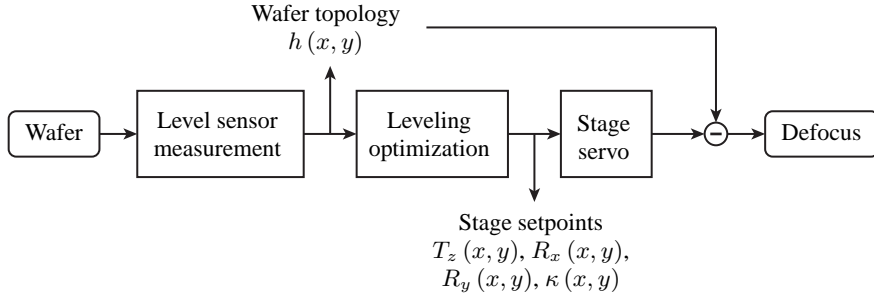


Figure 2.5: Flowchart of the levelling procedure [14] in a lithography system. The current strategy uses wafer stage translations $T_z(x, y)$ and rotations $R_x(x, y)$, $R_y(x, y)$ to reduce the defocus by wafer non-flatness. A further reduction of this error can be achieved by the addition of a field curvature correction $\kappa(x, y)$.

adaptation of the wafer stage translation $T_z(x, y)$ as well as the wafer stage rotations $R_x(x, y)$ and $R_y(x, y)$. The optimal wafer stage setpoints are obtained by minimizing the focus error between the wafer topology and flat lens focal plane at the exposure area. The final step of the levelling strategy consists of providing the wafer stage setpoints to the stage controller during the exposure process. The out-of-plane stage servo performance and the wafer unflatness eventually define the wafer defocus.

The above described levelling procedure was used to determine the impact on wafer defocus by an additional field curvature correction $\kappa(x, y)$ in the lithography system [124]. The analysis used wafer topology data that was measured in state-of-the-art lithography machines. An ideal stage positioning performance was also assumed for the analysis. The residual defocus was calculated for both the conventional levelling strategy that employs wafer stage translation and rotations as well as the levelling strategy with an additional curvature correction.

Figure 2.6 provides an example of the achieved focus improvement by an additional curvature correction. The top-left graph shows the initial chucked wafer topology that was measured by the level sensor. The top-right graph provides an estimate for the average defocus MA_z when the conventional levelling strategy is used. Two phenomena are visible from this plot. First, it has larger values of defocus at the wafer edge. Second, the negative defocus at the centre and the positive defocus at the edge of each field indicates a curved defocus across the field width.

The focus improvement by an additional curvature correction is represented by the bottom graphs of Figure 2.6. The bottom-left graph shows the calculated average defocus after levelling with an additional curvature correction. It indicates that the curved defocus trend across the field width is removed. This is confirmed by the bottom-right graph in Figure 2.6. The plot shows the focus difference between the conventional levelling and field curvature levelling strategy results. This indicates that the majority of the MA focus improvement falls within a band of ± 10 [nm] for this particular case.

The above results have shown that a field curvature correction is able to reduce the defocus contribution by wafer non-flatness. This led to an investigation of the required curvature range in order to facilitate a focus improvement. The results of the investiga-

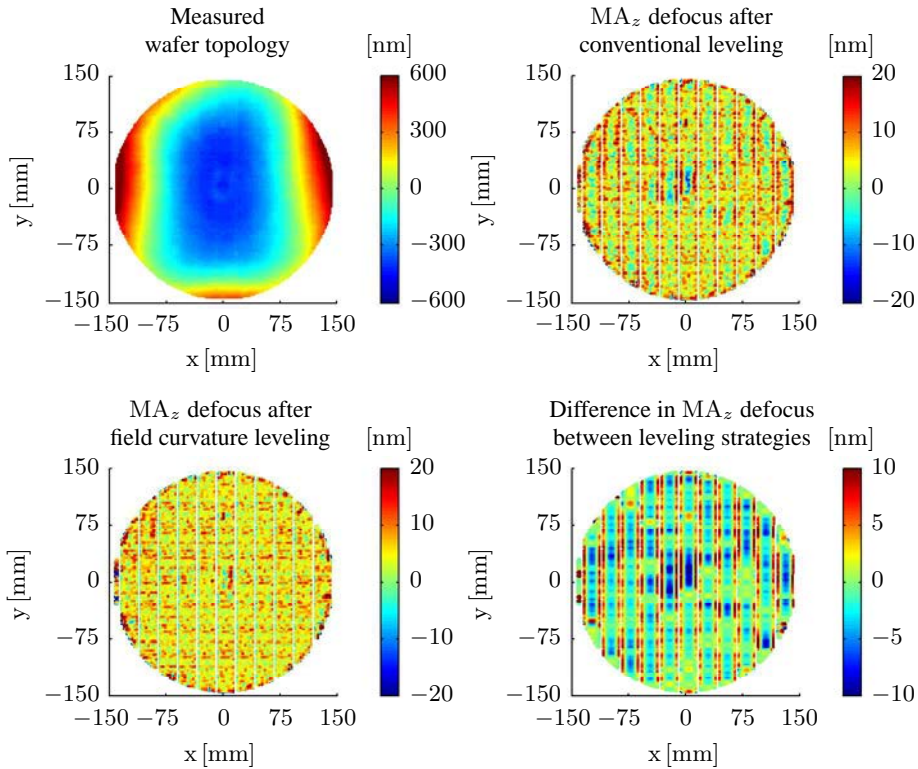


Figure 2.6: An example showing the reduction in wafer unflatness defocus by an additional field curvature correction in the lithography tool. The top-left surface plot shows the initial wafer unflatness after chucking. The top-right plot provides the average defocus after applying the conventional scanner levelling algorithm. The bottom-left graph shows the average defocus after applying the scanner levelling algorithm with an additional field curvature correction. The bottom-right graph provides the difference in defocus between the two levelling strategies which clearly shows the removed curvature contribution.

tion are presented below.

The first step of the investigation consisted of identifying the wafer curvature distribution. A set of 67 wafers with different types of critical IC layers was used for the analysis. The left graph of Figure 2.7 provides a cumulative frequency diagram of the curvature distribution. The diagram is obtained by taking the cumulative curvatures from the minimum to maximum curvature value and dividing by the number of curvatures within the total range. The graph shows that the majority of the curvature values fall within a range of $\pm 0.8 \times 10^{-3}$ [1/m].

The identified curvature range can act as an ultimate design specification for the curvature manipulator. It is questionable however if this full range is really necessary because a limited range may already provide a sufficient focus improvement. The focus improvement across the whole wafer set was therefore quantified for three types of levelling strategies. These consisted of the conventional levelling strategy without curvature correction κ_0 ,

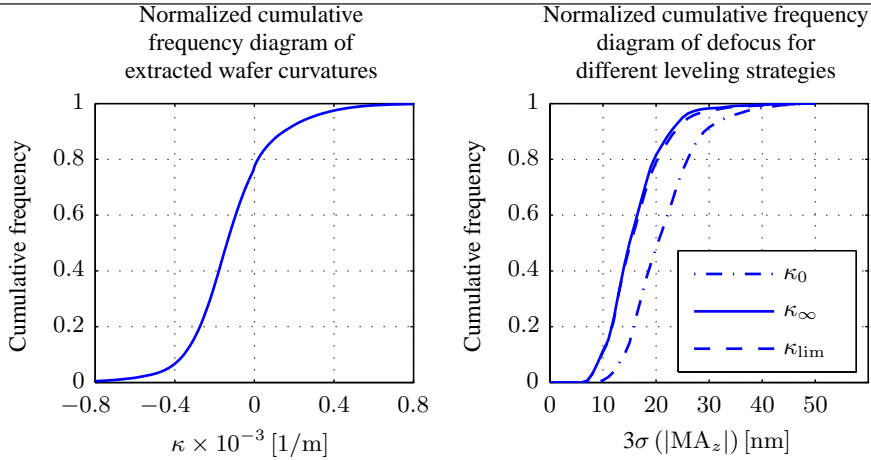


Figure 2.7: Results of the levelling investigation for the measured wafer set. The left graph shows the cumulative frequency diagram of the identified curvatures from the wafer topology data. The right graph provides a cumulative frequency diagram of the average defocus on the wafer for different levelling strategies. The conventional strategy corresponds to κ_0 whilst the κ_∞ corresponds to the curvature levelling strategy without limitations on curvature. The line for κ_{lim} provides the results for a curvature levelling strategy with an absolute curvature limitation of $\max(|\kappa|) = 0.4 \times 10^{-3}$ [1/m].

the levelling strategy with a curvature correction of infinite range κ_∞ and the levelling strategy with a constrained curvature correction range κ_{lim} of $|\kappa| < 0.4 \times 10^{-3}$ [1/m]. The focus improvement was quantified for each levelling strategy by considering the standard deviation σ of the MA_z residual defocus for each field. The right graph in Figure 2.7 shows the cumulative frequency diagram of wafer fields that fall within a certain 3σ ($|MA_z|$) range for the three levelling strategies. The graph highlights the following:

- The curvature correction with infinite range has approximately 30% more fields between 7 and 40 [nm] in comparison to the conventional levelling strategy. The result confirms the earlier conclusion that defocus by wafer non-flatness can be reduced by a field curvature correction in the machine.
- There is only a marginal difference between the results of the infinite and constrained curvature levelling strategies. The difference becomes larger when tighter curvature constraints are defined. The result indicates that the full range of wafer curvature is not required for the desired focus improvement.

The above analysis has demonstrated that the variation of the MA defocus across the fields are reduced with a field curvature correction. Furthermore, it showed that a curvature limit of $\max(|\kappa|) = 0.4 \times 10^{-3}$ [1/m] provides a similar focus improvement as for the unlimited curvature range. This knowledge will be used in Section 2.5.1.1 when the curvature actuation range is specified for the manipulator.

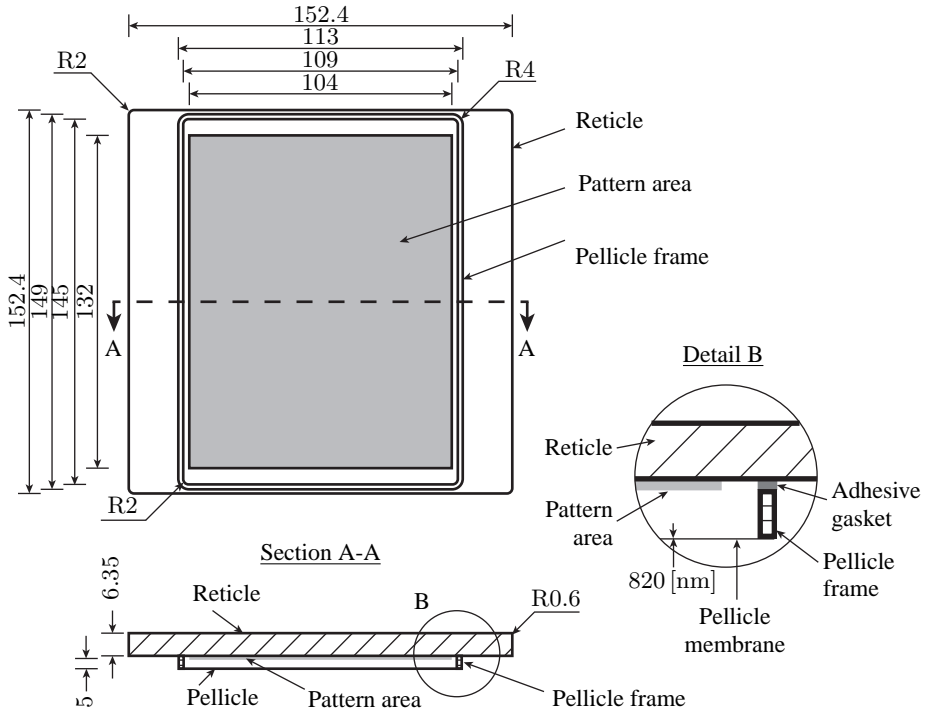


Figure 2.8: The geometry of the photomask with pellicle.

2.4 Boundary conditions

Sections 2.2 and 2.3 have demonstrated that reticle bending can result in a focus improvement in the lithography system. It is therefore desired to identify the feasibility of a manipulator that can realize this effect. The feasibility study requires input on the manipulator system specifications and its boundary conditions when used in the lithography tool.

This section gives a summary of the identified boundary conditions for the photomask curvature manipulator. These are largely driven by the photomask dimensions and the clamping configuration in the current lithography system. Section 2.4.1 provides an overview of the photomask geometry and material properties. The reticle stage architecture and reticle constraints in the reticle stage are thereafter introduced in Section 2.4.2. An allowed volume claim for the curvature manipulator is derived from that discussion.

2.4.1 Reticle properties

The properties of the photomasks that are used in the semiconductor industry are defined in a SEMI standard [96]. The geometry of the photomask that is most commonly used in immersion lithography systems is provided in Figure 2.8. It consists of a square Fused

Silica or ULE plate with a nominal size of $152.4 \times 152.4 \times 6.35$ [mm]. These materials are chosen because of their low coefficient of thermal expansion (CTE) and transparency for DUV [65]. Other material properties are provided in Table 2.1.

An area of 104 [mm] by 132 [mm] photomask's bottom surface is reserved for pattern placement. The pattern is made from a 100 [nm] thick Chrome layer where material has been removed at specific locations. The exposure beam is diffracted at these locations but blocked at the Chrome covered areas.

Pellicles are normally added to the photomask in a production environment. These consist of a transparent pellicle membrane, pellicle frame and adhesive gasket. The pellicle has the function of isolating the pattern area from the scanner environment. This has two main advantages [28]. First, dust particles will collect onto the pellicle membrane instead of the pattern area. Because the pellicle membrane is out-of-focus, these particles do not print during the exposure process. Second, the risk of removing a dirty pellicle and replacing it with a clean one has a lower risk than cleaning the pattern area. The standard dimensions of the pellicle and its material properties are provided in respectively Figure 2.8 and Table 2.1.

The reticle geometry has a number of impacts on the curvature manipulator design. These are the following:

- Reticles have length and thickness tolerances of respectively 0.4 [mm] and 0.1 [mm], see [96]. The tolerances affect the manipulator design specifications and subsequently manipulator design as will be shown in Section 4.2.
- The photomask area is dominated by the reticle pattern and the attached pellicle as is clearly shown in Figure 2.8. No objects are allowed to obscure the pattern area or interface to the pellicle because it impacts the lithographic process. This limits the interface locations of the manipulator to the reticle to the photomask edges and the areas next to the pellicle. Section 2.4.2 will show that the latter areas are also used for the reticle clamping configuration in the current reticle stage.

2.4.2 Reticle clamping configuration

The curvature manipulator design should not impact the reticle acceleration and positioning accuracy during the lithography exposure process. The curvature manipulator boundary conditions are therefore also dependent on the reticle clamping configuration in the reticle stage.

Figure 1.3 provided an impression of the lithography system. It also contained a representation of the reticle stage architecture and clamped reticle. The specific reticle clamping configuration that is used in the stage is schematically shown in the left drawing of Figure 2.9. Vacuum membranes at the reticle's bottom surface are used as clamping mechanism. The bottom surface was chosen because of reticle dimensional tolerances, the necessity to be able to exchange reticles in a lithography tool and the fact that the pattern is located on the bottom surface. The clamping area is restricted to the regions outside the pattern and pellicle area because of the transmissive nature of the lithography tool.

The clamping configuration constrains the reticle in the following manner. The reticle's out-of-plane degrees-of-freedom are fixed by three support pins on the reticle stage.

Part	Material property	Symbol	Value	Unit	Ref.
Reticle (Fused Silica)	Density	ρ	2200	[kg/m ³]	[1]
	Elasticity modulus	E	72.6	[GPa]	[136]
	Poisson ratio	ν	0.16	[-]	[23]
	CTE	α	0.55	$\times 10^{-6}$ [1/K]	[23]
	Thermal conductivity	k	1.38	[W/m/K]	[1]
	Stress optic coefficient	R	51	[nm/cm/MPa]	[93]
Adhesive gasket (SEBS)	Elasticity modulus	E_g	0.157	[MPa]	[24]
	Thickness	t_g	250	[μ m]	[24]
	Poisson ratio	ν_g	0.25	[-]	[24]
Pellicle frame (Aluminium)	Elasticity modulus	E_f	72.0	[GPa]	[24, 28]
	Thickness	t_f	5	[mm]	[24, 28]
	Poisson ratio	ν_f	0.33	[-]	[24, 28]
Pellicle membrane (Fluoropolymer)	Elasticity modulus	E_m	1.2	[MPa]	[23]
	Thickness	t_m	824 – 834	[nm]	[28]
	Poisson ratio	ν_m	0.30	[-]	[23]

Table 2.1: Material properties of the reticle, adhesive gasket, pellicle frame and pellicle membrane.

These are known as *z-supports*. The reticle's in-plane degrees-of-freedom are constrained by two opposing vacuum membranes. These are attached to the chuck along one end and have a vacuum cup that interfaces to the reticle's bottom surface at the other end [28, 30]. The membranes are compliant in the out-of-plane direction and will conform to the reticle's natural gravity deflection when it is placed on the three *z*-supports. This deformation is normally referred to as *gravity sag*. The reticle's in-plane mechanical coupling to the reticle stage is defined by the in-plane stiffness of the membranes and the available friction force between the vacuum area and reticle.

It is evident that friction forces are key in retaining the position of the reticle on the chuck during the reticle stage movements. This is especially the case because the reticle stage position is measured and fed to the reticle positioning feedback loop instead of the reticle position. A translation of the reticle in the reticle stage will result in an erroneous measurement of the reticle position which translates into an overlay error when left uncorrected. Furthermore, local sliding between the reticle and vacuum clamp can also induce overlay errors because of local shear stress variations between the reticle and the clamp. These shear stresses propagate into the reticle and lead to pattern deformations. A further explanation of the local slip effects is provided in Section 4.2.4.

A Coulomb friction model was made to identify the slip limits between the reticle and the vacuum clamps [117]. The model assumes rigid body behaviour of the reticle and membranes as well as a uniform contact pressure at their interface. The minimum required friction coefficient to ensure no slip between the reticle and the membranes was derived using Newton's second law. It resulted in the following expression:

$$\mu \geq \frac{m\ddot{y}}{p_r A_m} \quad (2.10)$$

where μ is the friction coefficient, m is the mass of the reticle, \ddot{y} is the stage acceleration, p_r is the vacuum pressure and A_m is the mounting area over which the pressure differ-

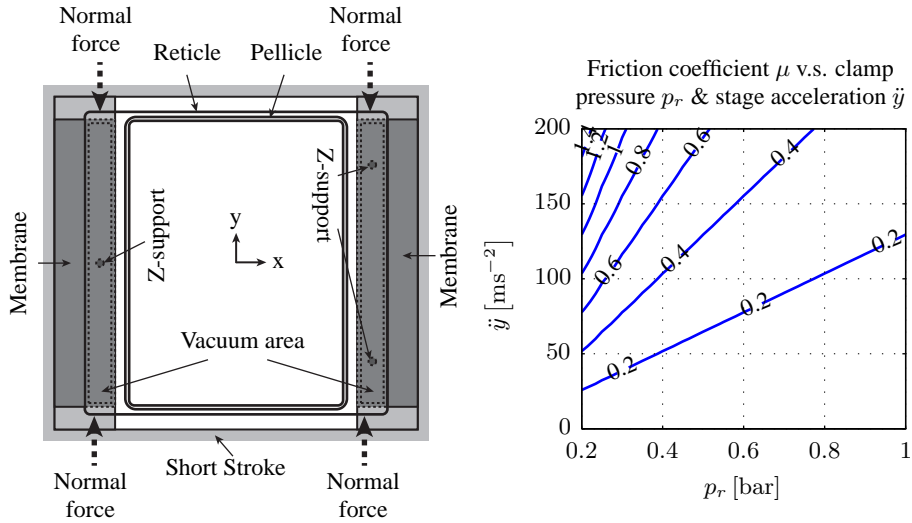


Figure 2.9: The reticle clamping configuration in the reticle stage. The left drawing provides a schematic top view of the mounting configuration in the short stroke. The reticle is clamped in plane by two vacuum membranes and constrained out-of-plane by three z-supports. The dotted arrows that are indicated with normal forces correspond to an alternative way of reticle clamping. The left graph shows an estimate of the required friction coefficients as a function of clamping pressure and stage acceleration for a two clamping areas of 7×150 [mm].

ence acts. The right graph in Figure 2.9 shows a contour plot of the required friction coefficient in order to avoid slip between the reticle and the vacuum membrane when a vacuum area of 7×150 [mm] is assumed. Lithography scanners are able to realize vacuum pressures of $0.6 - 0.8$ [bar] and the reticle stage operates with 150 [m/s^2] accelerations [21]. Friction coefficients between $0.3 - 0.5$ are required in order to guarantee no relative rigid body motion between the reticle and clamp whilst higher values are probably needed to eliminate the local slip effects. Although there is no publicly available data on the achievable friction forces, it is expected that such high friction forces are difficult to achieve.

Several solutions have been identified in order to reduce the input of reticle slip on overlay. A specific strategy is explained in [12]. A fundamental way to eliminate it completely is to use normal forces on the reticle edges instead of friction forces on its bottom surface for the in-plane positioning of the reticle [4, 98]. This is illustrated by the large dotted arrows in the left drawing of Figure 2.9. The concept is currently under investigation in another STW funded research project [80, 103]. This thesis assumes the use of this novel configuration for the following reasons:

- Machine throughput is steadily increasing [15]. This requires higher reticle stage accelerations and therefore an increase in reticle slip risk with the conventional clamping configuration.
- The clamping membrane adds rotational stiffness to the reticle because of its large in-plane stiffness and offset with respect to the reticle's neutral bending axis. The

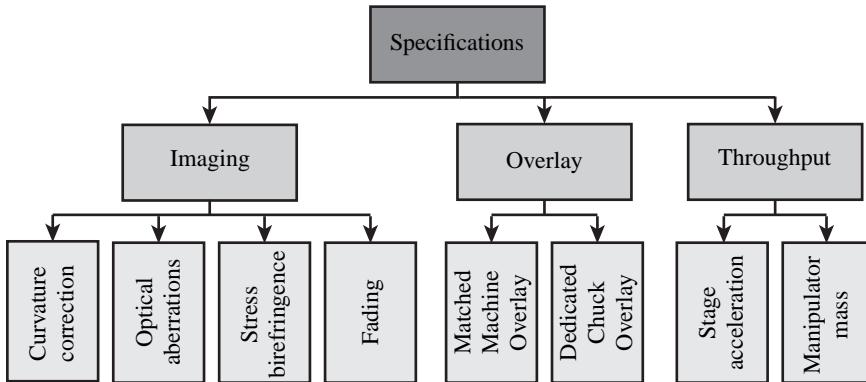


Figure 2.10: An overview of the system specifications for the photomask curvature manipulator and their relation to the lithographic performance parameters of Chapter 1.

added rotational stiffness results in lower achievable curvature amplitudes.

- The bottom surface of the reticle expands and contracts under ideal bending as was explained in Section 2.2. Friction forces between the clamp and the reticle need to ensure that the clamping membrane follows the reticle expansion and contraction. It results in slip between the reticle and clamp as well as in-plane distortion forces on the reticle. The latter lead to additional pattern distortions.

The above assumption of a novel clamping architecture makes it possible to use the volume of the current clamping configuration for the curvature manipulator. This corresponds to a volume claim with a length of $l = 160$ [mm], width of $w = 35$ [mm] and height of $h = 11$ [mm].

2.5 Specifications

System specifications are the other required input for the feasibility investigation of the curvature manipulator. They are derived in this section and categorized according to the three photolithographic performance parameters of Chapter 1.

An overview of the contributors to each category is shown in Figure 2.10. Table 2.2 provides a summary of the defined manipulator system specifications. Further clarification of these values are provided below. Section 2.5.1 introduces the specifications that are related to imaging. The reserved overlay budget for the curvature manipulator is provided in Section 2.5.2. Section 2.5.3 explains the allowable impact of the manipulator in terms of machine throughput.

2.5.1 Imaging

The specifications that are related to the machine imaging performance are presented first. The imaging performance is influenced by the machine's depth-of-focus, optical

Manipulator specification			Parameter	Value	Unit	Section
Imaging	Curvature correction (Focus)	Range	κ	$\pm 0.4 \times 10^{-3}$	[1/m]	2.5.1.1
		Velocity	$d\kappa/dt$	± 0.2	[1/(ms)]	
		Acceleration	$d^2\kappa/dt^2$	± 42	[1/(ms ²)]	
		Jerk	$d^3\kappa/dt^3$	$\pm 44 \times 10^3$	[1/(ms ³)]	
	Aberrations	Spherical	$\sigma_{w,s}$	< 4	[m λ]	2.5.1.2
		Coma	$\sigma_{w,c}$	< 4	[m λ]	
	Polarization	Birefringence	Δn_{12}	1	[nm/cm]	2.5.1.3
	Fading (in-plane)	Image vibrations	$\sigma_{x,y}$	0.5	[nm]	2.5.1.4
asymmetric mag.		σ_{asym}	2	[nm]		
Overlay	Dedicated chuck overlay ¹		DCO	0.45	[nm]	2.5.2.2
	Matched machine overlay		MMO	0.6	[nm]	2.5.2.3
Throughput	Reticle stage velocity		v	3.6	[m/s]	2.5.3.2
	Reticle stage acceleration		a	150	[m/s ²]	
	Manipulator mass		m	0.3	[kg]	2.5.3.3

¹ The overlay value corresponds to the total budget for reticle clamping and heating. A further budget division is provided in Section 2.5.2.2.

Table 2.2: A summary of the system specifications for the photomask curvature manipulator.

aberrations, the polarization state of the exposure beam and fading. Section 2.5.1.1 introduces the curvature specifications that have been defined for the desired focus improvement. The limits for allowable optical aberrations during the imaging process are thereafter provided in Section 2.5.1.2. The allowable effect of stress-birefringence on exposure beam polarization is defined in Section 2.5.1.3. Tolerated fading contributions are finally explained in Section 2.5.1.4.

2.5.1.1 Curvature setpoints

The curvature setpoint specifications have been defined with the results from the focus improvement analysis of Section 2.3. The analysis showed that both lens heating and wafer non-flatness require a curvature correction range of approximately $\kappa = \pm 0.4 \times 10^{-3}$ [1/m]. The manipulator requirement should be able to correct for the sum of the contributions. A range specification of $\kappa = \pm 0.4 \times 10^{-3}$ [1/m] was nevertheless defined for the curvature manipulator because this was identified relatively early on in the design process.

The specifications for the dynamic curvature adaptation is dependent on the curvature correction strategy, the stage motion profile and the wafer topology data. The following assumptions were made for the derivation. First, contribution of lens heating was neglected in the derivation because of its low frequency content with respect to the wafer curvature profile under scanning conditions. Furthermore, third order setpoint trajectories of the wafer and reticle stage were assumed because these are implemented in current lithography machines [68]. Third, it is assumed that a uniform curvature is introduced in the reticle and that this is continuously adapted for each slit position during the scan. Section 3.2 will explain that this configuration is preferred because of the ease of implementation and minimization of overlay errors.

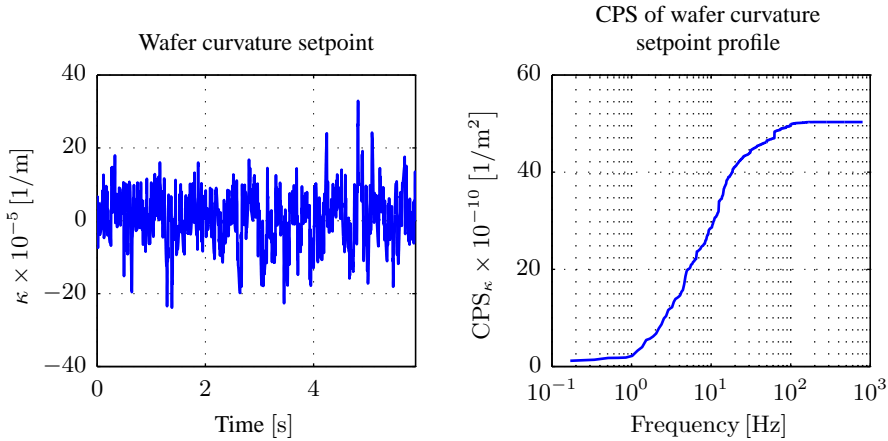


Figure 2.11: Example of a wafer curvature profile. The left graph shows the curvature setpoint profile with respect to time. The right graph shows its Cumulative Power Spectrum (CPS).

The specifications for the dynamic curvature adaptation were derived from the analysed 67 wafers of Section 2.3.2. Curvature setpoint profiles for the full meander scans across the wafers were constructed by the addition of third order point-to-point profiles between each field. These point-to-point profiles were designed by setting the turnaround time equal to the scan time and the scan speed to 0.8 [m/s]. Numerical differentiation resulted in the curvature velocity ($d\kappa/dt$), acceleration ($d^2\kappa/dt^2$) and jerk ($d^3\kappa/dt^3$) specifications of Table 2.2.

The frequency content of the curvature setpoint profiles was also determined. It provides input on what curvature frequencies the manipulator should be able to track. Figure 2.11 provides a Cumulative Power Spectrum (CPS) of one specific wafer curvature profile. It shows that the majority of the frequency content falls below 100 [Hz]. This trend was also visible in the other curvature setpoint profiles from the remaining wafermaps.

2.5.1.2 Optical aberrations

The geometric image formation in a lithography system can deviate from the ideal case. These errors are known as *optical aberrations* and are caused by lens design, the lens construction and by its use. Examples of the latter two are lens thickness variation and lens heating [71].

Reticle curvature manipulation could potentially induce additional optical aberrations. It is therefore necessary to identify the allowable aberrations that still guarantee sufficient imaging quality. The optical aberrations are normally defined in terms of RMS wavefront error σ_w in the pupil plane for lithographic applications [46]. A power series expansion of Zernike polynomials is frequently used to decompose the wavefront error into specific aberration groups such as astigmatism, coma and spherical aberrations. The definition of the RMS wavefront error and the Zernike terms are provided in Appendix A.

The allowable wavefront error differs for each specific imaging process. Rules-of-thumb have nevertheless been identified for pattern sizes down to the 45 [nm] node when low- k_1

lithographic imaging processes and high numerical apertures are used [44]. Coma and spherical aberrations were identified as the critical optical aberrations for these processes. The RMS wavefront error for both aberrations types, i.e. ($\sigma_{w,c}$ and $\sigma_{w,s}$), must be below 4 [m λ]. These values will be used in this thesis because aberration specifications for pattern sizes below 45 [nm] were not found in literature.

2.5.1.3 Stress birefringence

The vector nature of the exposure beam and its polarization influence the achieved image contrast in imaging systems at large Numerical Apertures [60, 71]. Section 2.2.1 introduced that photomask stress-birefringence will have an impact on the beam polarization state. This section provides an explanation of the phenomena and defines a stress-birefringence specification.

Light can be considered as an electromagnetic wave. The polarization state of the wave corresponds to the directional variation of its electric field in time or space [47]. The impact of polarization on image contrast can be explained by Figure 2.13. It provides a schematic drawing of the interference of two monochromatic polarized electromagnetic waves \mathbf{E}_1 and \mathbf{E}_2 that propagate to the wafer surface at an angle of incidence θ . The polarization state of each beam is expressed in terms of a Transverse Magnetic (TM) and Transverse Electric (TE) component. The former component coincides with the plane A that is spanned by the two beams whilst the latter correspond to the contribution that is perpendicular to the plane.

It is evident from Figure 2.13 that constructive interference occurs for the TE components and that the interference is independent on the angle of incidence θ . This is not the case for the TM interference where the intensity becomes smaller for larger angles of incidence. This is exactly the reason why for high-NA lithography TE polarization is desired in order to maximize the image intensity after interference in order to get the highest image contrast [60, 107].

The polarization state of the exposure beam in the lithography system is shaped by the illuminator. Birefringence in the reticle and lens contribute to the eventual polarization state at wafer level however [60]. This optical phenomenon corresponds to the variation of the refractive index of optical materials between two perpendicular directions [47]. The magnitude can be dependent on the stress-state in certain optical materials. This effect is known as *stress-birefringence* and is also present in the Fused Silica bulk material of a reticle. The stresses in the reticle by the applied bending moments can potentially increase the birefringence.

Investigations have been performed on the allowable stress-birefringence in photomasks for the manufacturing of 45 [nm] nodes and beyond [22, 41, 121]. These recommended to use reticles with birefringence levels below 5 [nm/cm]. The contribution of reticle chucking, pellicle mounting and reticle gravity sag is currently below 1 [nm/cm]. The allowed birefringence penalty by reticle bending has therefore been defined at 1 [nm/cm].

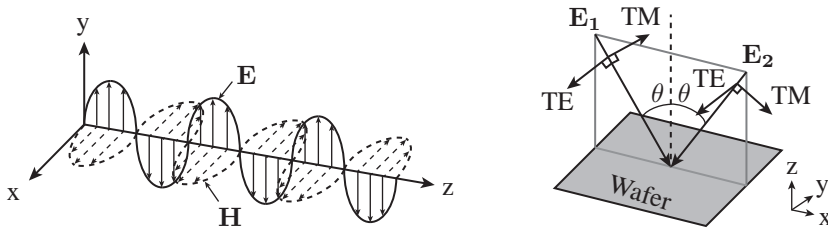


Figure 2.13: The interference of two polarized electrical fields E_1 and E_2 at wafer level.

2.5.1.4 Fading

Pattern fidelity is influenced by the achieved image quality or contrast during the exposure process. Image positioning errors during the exposure process can cause loss of image contrast as well as overlay. The loss of image contrast is also known as image blurring or *fading* [17, 63, 65].

Fading can occur in the in-plane (x, y) and out-of-plane (z) direction of the wafer. Sources of the image blur can be classified into three categories [63]. These are image vibrations, scan set-up errors and lens errors. Specific examples for each are stage vibrations, asymmetric scan field magnification and variations of the lens distortion along the scan direction of the exposure slit. Chapter 3 will show that errors like an asymmetric magnification are also introduced by reticle curvature manipulation. It is therefore necessary to define the allowable fading contribution by this novel functionality.

An in-plane fading budget for the manufacturing of 45 [nm] node was found in literature [63]. The budget had 2 and 5 [nm] contributions for image vibrations and asymmetric magnification. Contributions by the curvature manipulator were defined for these sub-budgets. It resulted in values of 0.5 [nm] for in-plane image vibrations and 2 [nm] by asymmetric magnification. Contributors to vertical fading budgets were analysed in [17] but no overall fading budget was found. A specification for the allowable vertical fading penalty by photomask bending was therefore not defined.

It was mentioned above that vibrations contribute to the fading budget. An additional manipulator specification was therefore defined in terms of its impact on reticle resonance frequencies for which the reticle resonance frequencies in the current reticle stage were taken as reference. The first in-plane resonance frequency of the manipulator should be above 2 [kHz] because this is also the case of the current reticle stage. Furthermore, the out-of-plane eigenmodes and eigenfrequencies of the reticle with manipulator must correspond to the shapes and values of a kinematically constrained reticle on the z -supports. The derived design specifications and achieved resonances are provided in Chapters 4 and 3.

2.5.2 Overlay

The second machine performance parameter that was introduced in Chapter 1 was overlay. It corresponded to the alignment error of a layer in the Integrated Circuit with respect to a previously printed layer. This section defines the allowable contribution of the field

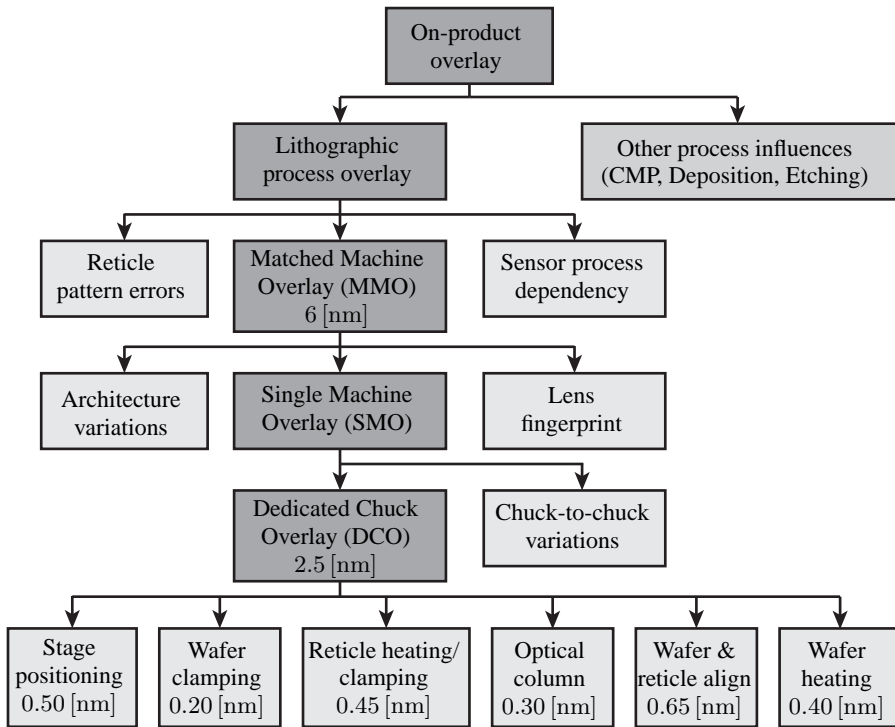


Figure 2.14: A simplified summary of on-product overlay contributors.

curvature correction to the machine overlay budget. Section 2.5.2.1 provides an introduction to the overlay budget. The manipulator's contribution to two types of machine overlay budgets is thereafter defined in Sections 2.5.2.2 and 2.5.2.3.

2.5.2.1 Introduction to the overlay budget

The overlay budget of state-of-the-art lithography machines is considered in order to identify the overlay contribution by the reticle bender. Figure 2.14 provides a schematic drawing of the overlay contributors on a realized product. The product overlay is largely defined by the lithographic process. Its contribution is defined by the overlay performance of the lithography tool and other contributors such as reticle pattern placement errors and the sensitivity of lithography tool metrology systems on materials that have been deposited onto wafers.

The specific overlay contribution of the lithography tool that has to be considered depends on the tool combination that is used to expose subsequent IC layers. The *Matched Machine Overlay (MMO)* budget should be used when two different lithography systems are utilized for each lithography step. Any variation of the machine tool architecture such as the lens or stage design can have a contribution to that budget [128]. The MMO performance of the latest generation lithography systems is in the order of 6 [nm], see [21, 50, 133].

The *Single Machine Overlay (SMO)* or *Dedicated Chuck Overlay (DCO)* must be considered when the same lithography tool or chuck are used for the exposure process¹. Both budgets are significantly smaller than the MMO budget because of the absence of the architecture variations and lens fingerprints. The DCO budget is the smallest because chuck-to-chuck variations are eliminated. This is highlighted by the 2.5 [nm] DCO budget for an immersion lithography system that was reported in [21]. Its DCO budget build-up is summarized in Figure 2.14.

2.5.2.2 Curvature manipulator DCO contributions

Inspection of the DCO overlay budget in Figure 2.14 indicates that the curvature manipulator will have a dominant contribution to the reticle clamping/heating budget and limited effect on the other budgets. A more detailed budget breakdown of the reticle clamping/heating budget was therefore made.

Table 2.3 provides the breakdown of the reticle clamping budget with the identified contributions of the curvature manipulator. It was made with the assumption that that all budget contributions had a normal distribution as well as the same weighting. In that case, the total overlay budget is equal to the root sum square of each distribution [63]:

$$o = \sqrt{\sum_{n=1}^N o_n^2} = \sqrt{N \cdot o_n^2} \quad (2.11)$$

where o_n is the value of the n^{th} overlay contribution and N signifies the total number of contributors.

The budget breakdown in Table 2.3 shows three main budget contributors. These are reticle heating, reticle clamping and bending induced distortions. The latter was included because of the induced pattern strains by bending as was explained in Section 2.2.1. Further details of the overlay contributions by the manipulator have been derived. These include an additional reticle heating contribution by the curvature manipulator, parasitic reticle clamping effects of the manipulator such as slip and the curvature control accuracy by the manipulator. The budget also contains a specification in terms of calibration accuracy. Such a calibration is probably needed because of reticle thickness variations or sensor drift.

It is common practice during the design of any lithography tool to define an *overlay design rule*. It corresponds to a threshold value below which overlay contributions are neglected. The overlay design rule that has been defined in this thesis is equal to 50 [pm] which assumes eighty uncorrelated contributions to the reticle clamping budget of 0.45 [nm].

¹Note that the SMO budget is the DCO budget when a single chuck is present in the lithography tool.

Overlay budget contributor	Value	Unit
Reticle heating/clamping distortions	0.45	[nm]
Reticle heating distortions	0.26	[nm]
Exposure beam heat load	0.15	[nm]
Actuator heat load	0.15	[nm]
In-plane actuation	0.09	[nm]
Out-of-plane actuation	0.09	[nm]
Curvature manipulation	0.09	[nm]
Thermal conditioning variations	0.15	[nm]
Reticle clamping distortions	0.26	[nm]
Reticle loading	0.15	[nm]
Reticle slip	0.15	[nm]
Reticle bending parasitics	0.15	[nm]
Reticle bending distortions	0.26	[nm]
Curvature control accuracy	0.18	[nm]
Actuator	0.10	[nm]
Sensor	0.10	[nm]
Servo	0.10	[nm]
Curvature calibration	0.18	[nm]

Table 2.3: Proposed overlay budget for the reticle heating/clamping distortion term in Figure 2.14 which includes the contribution of the curvature manipulator. Note that all entries correspond to values at wafer level.

2.5.2.3 Curvature manipulator MMO contributions

Section 2.4.2 already mentioned that the integration of a reticle bender into the reticle stage requires a novel reticle clamping configuration. The changed clamping configuration impacts the reticle clamping fingerprint and will therefore contribute to the MMO budget. The allowed change of the clamping fingerprint was defined by considering the 6 [nm] MMO budget and assuming a $N = 100$ uncorrelated contributions. This results in $\sigma_n = 0.6$ [nm] with Equation (2.11). The effect of the manipulator stiffness and added mass to the reticle clamping fingerprint is investigated further in Chapters 4 and 3.

Note that the variation of the stiffness and the mass of the manipulators also contributes to the MMO. These variations are not considered in this thesis because only one prototype is going to be built.

2.5.3 Throughput

The final machine performance parameter that was introduced in Chapter 1 was machine throughput. Throughput is defined as the amount of exposed *wafers-per-hour* (*WPH*). This section identifies the throughput related requirements for the curvature manipulator. Section 2.5.3.1 first introduces the throughput budget for state-of-the-art lithography systems. Section 2.5.3.2 thereafter defines the expected reticle stage accelerations that the manipulator must be able to withstand. A specification for overall manipulator mass is finally derived in Section 2.5.3.3.

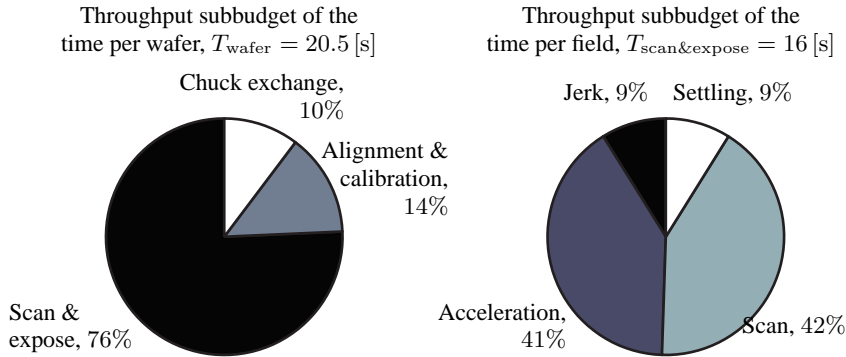


Figure 2.15: The throughput budget breakdowns. The left chart shows the timing budget per wafer with its different contributions. The right chart provides the timing budget with the relevant contributions for the scan-and-expose sequences for a single wafer. The different contributions were estimated from information out of [21] and a simplified third-order motion profile for the scan-and-exposure sequence.

2.5.3.1 Introduction to the throughput budget

The productivity of a lithography tool is dependent on a number of parameters. The left chart of Figure 2.15 shows the high-level breakdown of the throughput budget for a state-of-the-art lithography system that runs at 175 WPH [21]. The chart shows three budget contributors, namely wafer exchange, alignment & calibration and scan & expose where the latter is clearly the largest. It indicates that a throughput improvement can be achieved by a reduction of the scan-and-expose time.

An example of the scan-and-expose timing budget is provided in the right chart of Figure 2.15. It was determined for the following assumptions. First, a third-order motion profile was assumed for the stage meander scan of Figure 1.4 [20, 68]. Second, the stage motion in x -direction was not considered to be throughput limiting. Finally, some milliseconds of settling time are reserved per exposed field in order to suppress the stage errors before the exposure process. The scan & expose budget build-up shows that the acceleration and scan phase are the dominant contributors.

The potential throughput improvement by an increase of stage scan speed and acceleration can be demonstrated by Figure 2.16. The graphs relate to the case of Figure 2.15 where the settling time, the time for chuck exchange as well as alignment and calibration were kept constant. The laser power was also not assumed to be limiting. Note that the acceleration and velocity values relate to those of the reticle stage. The top-left graph shows the throughput values as a function of scan speed. The 150 $[\text{m/s}^2]$ acceleration corresponds to that of the current reticle stage [21]. The graph clearly shows the existence of an optimal scan speed that maximises throughput. This machine setting relates to the most cost effective production of ICs. The top-right graph of Figure 2.16 shows the optimal scan speed as a function of stage acceleration. The corresponding throughput values with respect to both parameters are provided in the bottom two graphs of Figure 2.16. They confirm that the machine throughput is improved for an increase in scan speed and acceleration. Note that the rate of throughput improvement gradually reduces

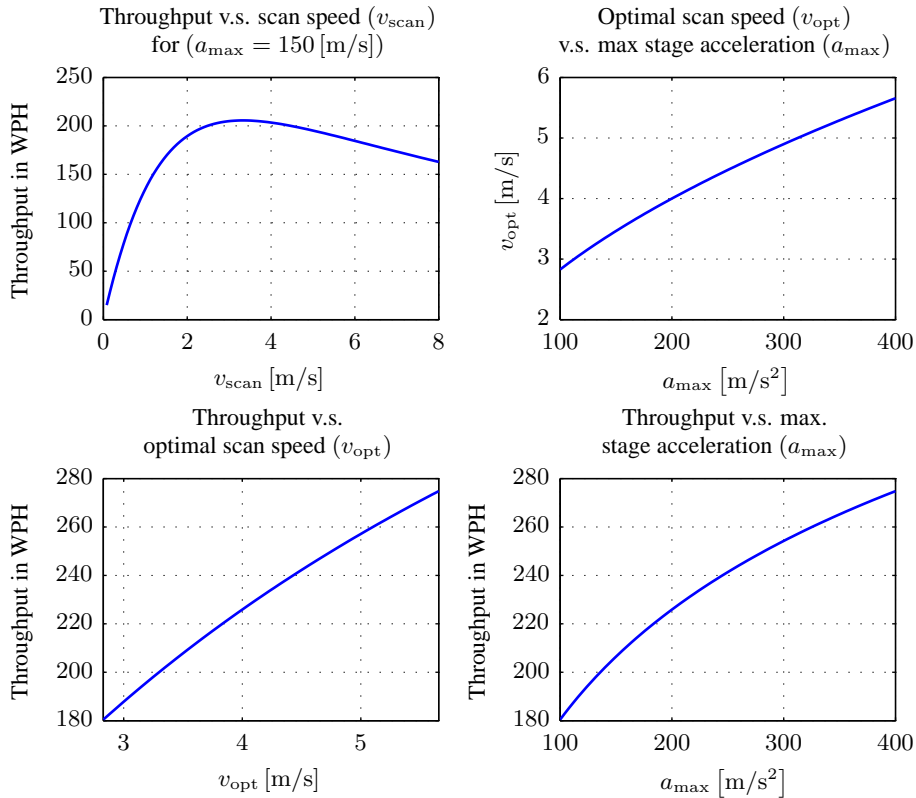


Figure 2.16: The dependency of machine throughput on reticle stage scan velocity and maximum acceleration. The top left plot shows the relation between throughput and scan velocity v_{scan} for a fixed maximum acceleration a_{max} . An optimum scan speed v_{opt} exists where the throughput is maximized. The top right graph shows the optimal scan speed as a function of maximum stage acceleration. The bottom left and right graphs respectively show the maximum throughput values as a function of optimal scan speed and stage accelerations.

because other budget contributors like chuck exchange will become more dominant.

The above discussion demonstrated the possible gain by an increase of stage velocity and acceleration. The scan velocity in the immersion lithography systems is currently limited to wafer stage and reticle stage scan speeds of 0.8 [m/s] and 3.6 [m/s]. Higher wafer stage scan speeds result in bubble formation in the immersion liquid which causes printed defects [15, 21, 76]. Throughput improvements are therefore sought by a reduction of other items like alignment & calibration [15].

2.5.3.2 Reticle stage velocity and acceleration

The stage velocity and acceleration in future lithography systems impact the curvature manipulator specifications. The curvature setpoint velocity, acceleration and jerk is dependent on the reticle stage scan speed. The curvature manipulator must also be able to withstand the continuous acceleration and deceleration of the reticle stage. The current

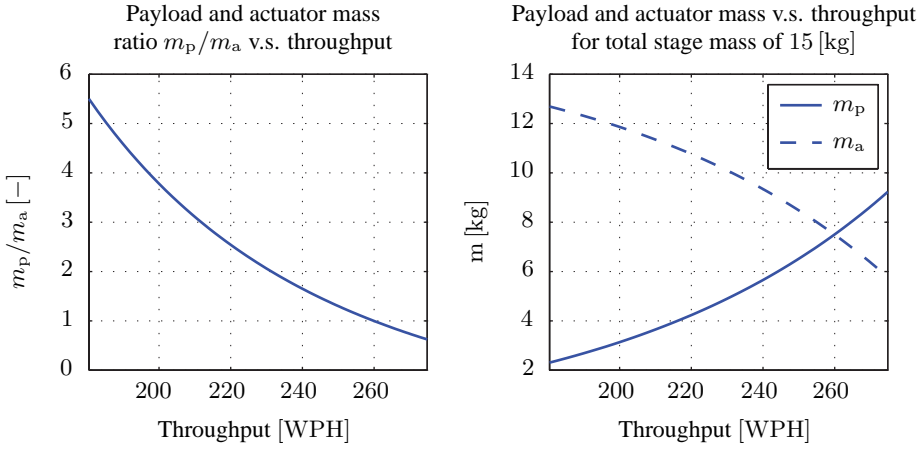


Figure 2.17: The relation between the stage mass and throughput. The left graph shows the payload and actuator mass ratio as a function of throughput. The right graph provides the values for the payload and actuator mass as a function of throughput for a total stage mass of 15 [kg].

reticle stage velocity and accelerations of 3.6 [m/s] and 150 [m/s²] were used as reticle stage specifications in this thesis.

2.5.3.3 Manipulator mass

The manipulator mass specification was determined by considering the impact of a reticle stage mass increase on machine throughput. Section 1.2.1 explained that Lorentz actuators are used to accelerate the reticle in one direction. The stage mass is the sum of the actuator's moving mass m_a and that of the payload m_p . The required actuator force F_{act} to accelerate the stage is equal to:

$$(m_p + m_a) \ddot{y}_p = F_{act} \quad (2.12)$$

where \ddot{y}_p corresponds to the stage acceleration. The ratio between payload and actuator mass is therefore equal to:

$$\frac{m_p}{m_a} = \frac{F_{act}}{m_a} \frac{1}{\ddot{y}_p} - 1 \quad (2.13)$$

where F_{act}/m_a represents the *effective actuator force* or *specific peak force*. This value is equal to 650 [N/kg] for well designed Lorentz actuators [79].

The effect of payload and actuator mass on machine throughput is shown in Figure 2.17. The results were determined with Equation (2.13) and the throughput model of Section 2.5.3.1. The left graph in Figure 2.17 shows the ratio between payload and motor mass as a function of throughput. The corresponding payload and actuator masses for a 15 [kg]

reticle stage are provided in the right plot. The left graph illustrates that throughput is less sensitive to a payload mass increase for lower throughput values when a fixed actuator mass is assumed.

A manipulator mass specification of 0.3 [kg] was defined after considering its effect on throughput². Figure 2.16 provided a throughput estimate of 205 WPH for a reticle stage acceleration specification of 150 [m/s²] without curvature manipulator. This corresponds to a payload/actuator mass ratio of approximately 3.4 and a payload and actuator mass of respectively 11.6 and 3.4 [kg] in Figure 2.17. The added manipulator mass changes the payload/actuator mass ratio from 3.4 to 3.5. This boils down to a throughput reduction of approximately one wafer per hour which is considered allowable for the additional curvature correction functionality.

2.6 Summary & Conclusions

The objective of this chapter was to determine the focus improvement potential of a photomask curvature manipulator and define its system specifications. It started with an explanation of the reticle bending effect at wafer level. The simplified bending beam representation of the reticle in Figure 2.1 and the optical model of the lithographic system in Figure 2.2 was used for this purpose. The following was demonstrated:

- The reticle acquires a curvature κ for an applied bending moment M at its edges.
- Reticle bending introduces bending stresses σ in the fused silica material and strain ε of the pattern area. These potentially have detrimental effects on imaging and overlay because they introduce stress-birefringence and pattern distortions.
- A reticle curvature gives a curved aerial image at the wafer of the same amplitude.

The benefit of the curvature manipulator was demonstrated by investigating the focus improvement potential of a field curvature correction in the lithography system. This was done for two prominent defocus contributors, namely lens heating and wafer non-flatness. The results are summarized in Table 2.4. It was shown that a field curvature correction of $\pm 0.4 \times 10^{-3}$ [1/m] reduces the focus error of each contributor by approximately 10 [nm]. A time varying curvature correction is needed in order to correct wafer non-flatness defocus during the exposure process.

The curvature manipulator has to achieve the desired focus improvement whilst minimizing other detrimental effects by bending on the overall lithography performance. Manipulator boundary conditions and system specifications were identified from literature. The reticle and pellicle dimensions limit the location of bending moment application to the reticle edge. A different reticle clamping configuration is assumed in this thesis because the current configuration will lead to reticle slip. Furthermore, it adds bending stiffness to the reticle. Manipulator system specifications were derived for the three lithography performance parameters (overlay, imaging and throughput). These are summarized in Table 2.2.

²The 0.3 [kg] mass estimate was obtained by assuming that the manipulator volume claim of Section 2.4.2 is filled with aluminium. Aluminium was chosen because it is used for the final manipulator design.

	Defocus contribution		Unit
	Lens heating	Wafer unflatness	
Field curvature	$\pm 0.4 \times 10^{-3}$	$\pm 0.4 \times 10^{-3}$	[1/m]
Focus correction	10	10	[nm]
Correction frequency	Static	Dynamic	[nm]

Table 2.4: The expected focus improvement by a static or dynamic field curvature correction in the lithography tool.

The results of the requirements analysis in this chapter lead to the following conclusions:

- Reticle bending gives the desired field curvature correction at wafer level in the lithography system.
- A curvature correction can correct both lens heating and wafer non-flatness induced defocus by 10 [nm].
- Further analysis is needed in order to identify the feasibility of reticle bending with respect to the specifications in Table 2.2.

The conceptual investigation of the reticle bending feasibility is provided in Chapter 3.

Chapter 3

Conceptual analysis of photomask curvature manipulation

The conceptual feasibility of the photomask curvature manipulator is proven in this chapter. Mechanical and optical models are used for this purpose. The chapter explains the identifies the curvature manipulation strategy that is able to achieve the desired field curvature correction whilst satisfying the system specifications of Chapter 2.

3.1 Introduction

Chapter 1 defined two thesis objectives. The first objective consisted of investigating the feasibility of a field curvature correction in an immersion lithography system assuming an ideal adaptation of the photomask curvature. This chapter will demonstrate this feasibility using opto-mechanical models of a reticle that undergoes pure bending. The impact of parasitic forces and stiffnesses of a bending manipulator are neglected in this chapter. The modelling results are compared to the boundary conditions and system specifications of Chapter 2.

The feasibility of the reticle bending concept will be explained in the following order. Section 3.2 explains the preferred bending strategies. Section 3.3 introduces the analytical and numerical mechanical models that are used to investigate the feasibility of reticle bending. The modelling results provide insights into the achieved reticle deflections, pattern distortions and stress levels. Their impact on the lithography process is studied in the sections thereafter. Section 3.4 analyses the effect of bending induced pattern distortions

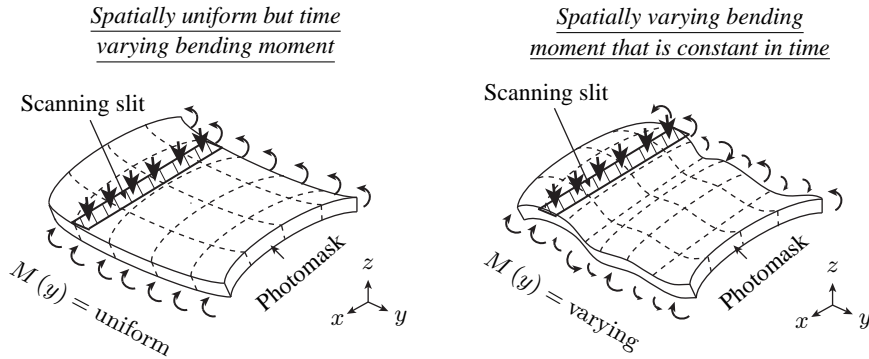


Figure 3.1: Possible reticle bending strategies to achieve a time varying curvature κ at wafer level. The left drawing shows the configuration with a spatially uniform but time varying bending moment along the photomask edge. The right drawing shows the strategy whereby a spatially varying bending moment is applied along the photomask edge.

on the lithography process. Sections 3.5 and 3.6 respectively study the induced stress-birefringence and optical aberrations by ideal photomask bending. The chapter ends with a summary and conclusions in Section 3.7.

3.2 Reticle bending strategies

Chapter 2 showed the potential focus improvement by a time varying curvature correction during the exposure process. The chapter also showed that this correction can be achieved by the adaptation of the reticle curvature during the exposure process. This section provides an overview of the different reticle bending strategies that are able to achieve the time varying curvature correction at wafer level. It also identifies the preferred strategy for further investigation in this thesis.

The two reticle bending strategies that were identified are shown in Figure 3.1. The left drawing shows the case where a spatially uniform bending moment is applied along the photomask edge. Adaptation of this uniform bending moment during the exposure process results in a time varying curvature correction across the slit at wafer level because of the limited slit dimension in y -direction.

An alternative strategy to achieve the time varying curvature is to apply spatially varying bending moments to the photomask such that it acquires a spatially varying curvature in the scan direction. This is shown in the right drawing of Figure 3.1. The spatially varying curvature translates to a time varying curvature correction at wafer level by the scanning process.

This thesis investigates the application of a time varying uniform bending moment to the photomask as is shown in the left drawing of Figure 3.1. Both strategies can in achieve the same amount of focus improvement in the system. The strategy was chosen for the following reasons:

- Section 3.3 will show that the application of a uniform bending moment results

in a constant magnification of the photomask pattern for each slit position. It is shown in Section 3.4 that the pattern magnification error can be corrected by the lithographic system and that the final overlay and fading penalties are within specification. The higher order pattern distortion that are induced for the right strategy in Figure 3.1 are not fully correctable by the lithography system.

- The higher order static deformation of the photomask is more difficult to achieve. This has two main causes. First, the photomask boundary conditions constrain the location of force or bending moment application. Second, the varying bending moments along the photomask edge must not only overcome the bending stiffness but also the shear stiffness of the photomask. It is therefore expected that larger bending moments are needed in order to achieve the higher order deformations.

It should be noted that the application of a time varying uniform bending moment to the reticle can generally be considered as a larger challenge in terms of system dynamics. Chapter 5 investigates the bending strategy in terms of its dynamic feasibility.

3.3 Mechanical modelling of photomask bending

The conceptual feasibility of reticle bending is dependent on the achieved photomask deflection as well as the induced pattern distortions and stress levels. The geometry of the photomask makes it necessary to consider the bending effects in both x - and y -direction instead of the elementary beam model that was introduced in Section 2.2.1. More detailed mechanical models were therefore developed in order to quantify these effects for the preferred reticle bending strategy of Section 3.2.

This section introduces the analytical and numerical model

3.3.1 Analytical modelling

An analytical mechanical model of the photomask was developed in order to provide physical insights into its bending behaviour. The pellicle was neglected because of the difficulty to describe it analytically. The simplification also made it possible to describe the reticle by the Kirchhoff plate model. This model considered as a two dimensional version of the Euler-Bernoulli beam model because it uses the same assumptions to describe the plate bending behaviour in x - and y -direction [42, 126].

Appendix B provides a detailed explanation of the Kirchhoff plate model relations and its validity to describe the behaviour of the photomask in pure bending. The appendix also derives specific relations for the reticle's bending behaviour when it is kinematically constrained on the three z -supports¹ and uniform bending moments are applied at its x -edges. This configuration corresponds to the preferred bending strategy of Section 3.2 that is shown in Figure 3.1. In that case, the out-of-plane photomask deflection w is

¹The z -supports were introduced in Section 2.4.2 as three discrete locations where the reticle is supported out-of-plane, see Figure 2.9.

described by:

$$w = \frac{1}{2}\kappa_x (x^2 - \nu y^2) + 0.0012\kappa_x x - 0.0023\kappa_x \quad (3.1)$$

where κ_x is the curvature of the photomask in the x -direction, ν is the Poisson ratio of Fused Silica as provided in Table 2.1 whilst x and y are locations in the Cartesian Coordinate system (x, y, z) which has its origin in the photomask centre. The curvature κ_x in Equation (3.1) is defined by:

$$\kappa_x = -\frac{M}{D(1-\nu^2)}, \quad \text{with} \quad D = \frac{ELt^3}{12(1-\nu^2)} \quad (3.2)$$

where D is the flexural rigidity of the plate, E is the elasticity modulus of Fused Silica whilst L and t respectively correspond to the length and thickness of the reticle. Appendix B also shows that the photomask will acquire a smaller opposite curvature in the y -direction which is defined by $\kappa_y = -\nu\kappa_x$. This effect is known as the *anticlastic curvature*.

Section 2.2.1 already mentioned that the applied bending moment will result in strains at the photomask bottom surface. These translate into pattern deformations because the pattern is printed on the reticle's bottom surface. Appendix B shows that the expressions for the reticle pattern deformations are obtained by multiplying the photomask local angle by its thickness. Relations for the local photomask angles θ_x and θ_y are obtained by taking the partial derivative of (3.1) with respect to x and y , i.e.:

$$\theta_x = \frac{\partial w}{\partial y} = -\nu y \kappa_x \quad (3.3)$$

$$\theta_y = \frac{\partial w}{\partial x} = (x + 0.0012) \kappa_x. \quad (3.4)$$

This leads to the following expressions for the photomask pattern deformations:

$$u = -\frac{1}{2}t \frac{\partial w}{\partial x} = -\frac{1}{2}t (x + 0.0012) \kappa_x \quad (3.5)$$

$$v = -\frac{1}{2}t \frac{\partial w}{\partial y} = -\frac{1}{2}t \nu y \kappa_x \quad (3.6)$$

where u and v are respectively the pattern deformation in x - and y -direction.

The above derived expressions for the photomask deflection, local angle and pattern deformation provide a number of insights into the photomask bending behaviour and its effect on the lithography process. These insights are the following:

- Equation (3.2) shows that a constant bending moment at the photomask x -edge results in a constant curvature across the slit. Furthermore, a uniform curvature

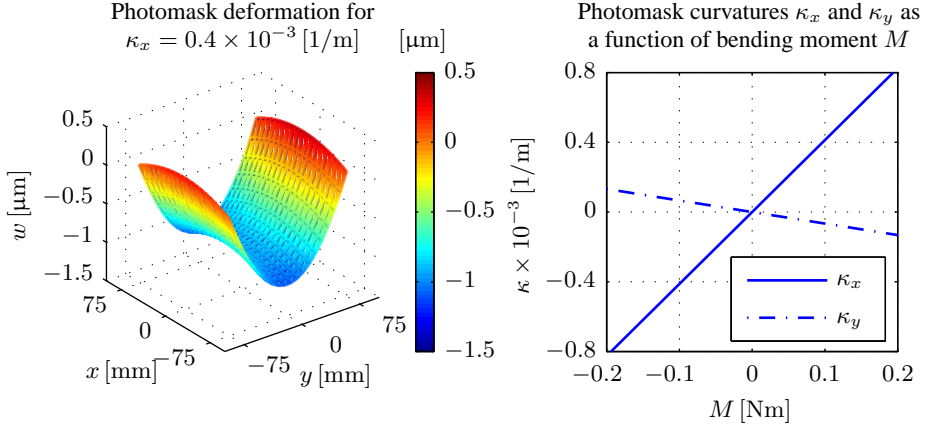


Figure 3.2: The photomask deflection and curvature when it undergoes pure bending. The left graph shows the reticle deflection for a curvature of $\kappa_x = 0.4 \times 10^{-3} [m^{-1}]$. The right graph shows the photomask curvature as a function of applied bending moment M .

κ_x is acquired along the full length of the reticle. This can be verified by taking the second partial derivative of the photomask deflection w in Equation (3.1) with respect to x .

- The application of a bending moment at the x -edge also invokes a smaller opposing curvature in the orthogonal direction. This corresponds to the *anticlastic curvature* and is visible in the out-of-plane deflection that is provided in the left plot of Figure 3.2.
- The right graph of Figure 3.2 shows the achieved photomask curvature as a function of bending moment which has been determined with Equation (3.2). It shows that a bending moment of approximately 0.1 [Nm] is needed to achieve the curvature specification of $\kappa_x = 0.4 \times 10^{-3} [1/m]$ in Table 2.2.
- The photomask curvature in around the x -axis and the scanning motion of the reticle can introduce a defocus if the stage is kept at the same z -position. This defocus can be counteracted by adapting the out-of-plane position as a function of slit position and photomask curvature.
- The reticle must be kept in the optimal focal plane of the lens at reticle level during the exposure process. The photomask anticlastic curvature shape by bending in combination with the rectangular exposure slit that scans across the reticle in y -direction can result in a defocus. The defocus effects are related to the terms in Equation (3.1) and (3.3) that are related to y . The reticle stage has to counteract these defocus by adapting its out-of-plane position and angle as a function of slit position.
- Equation (3.4) shows two contributions to the photomask local angle θ_y . The former corresponds to the contribution by the photomask elastic deformation whilst the second terms corresponds to an additional parasitic tilt. The parasitic tilt is

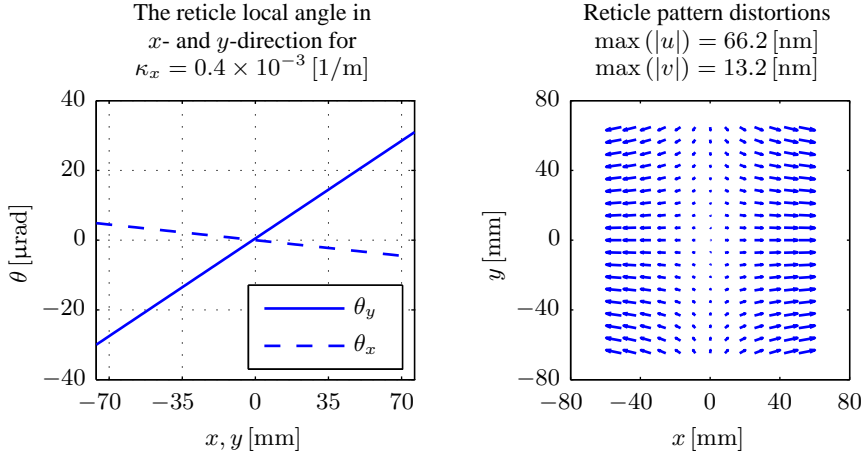


Figure 3.3: The photomask local angle and pattern distortions when it undergoes pure bending. The left graph shows the local angle around the x - and y -axis across the width and length of the reticle. The right vector plot provides the reticle pattern deformations with its maximum distortion values in x - and y -direction. Both graphs are related to the deformation at reticle level for a curvature of $\kappa_x = 0.4 \times 10^{-3} [1/m]$.

caused by the non-symmetry of the z -support locations across the y -axis in combination with the induced anticlastic curvature shape of the photomask. The contribution of the parasitic tilt is a factor 1000 smaller than the tilt by the elastic deformation and is therefore neglected.

- Figure 3.3 shows the reticle's local angles and pattern distortions for the curvature specification of $\kappa_x = 0.4 \times 10^{-3} [1/m]$. They have been estimated with Equations (3.5) to (3.6). The pattern distortions were evaluated for the a qualification grid or *Qgrid* which is defined by an array of thirteen-by-nineteen overlay markers across the pattern area of qualification reticles [28]. The right graph shows that the pattern is stretched with different and opposite amplitudes in the x - and y -direction. The maximum absolute pattern deformations in these directions are respectively 66.2 and 13.2 [nm] at reticle level which correspond to image distortions of 16.5 and 3.3 [nm] at wafer level. These pattern distortions can lead to overlay errors when left uncorrected. They currently exceed the overlay specifications in Table 2.2 by approximately two orders. Section 3.4 will show that the lithography system is able to correct the majority of these pattern distortions by a feedforward adaptation of the lithographic lens and stage during the exposure process.
- The photomask pattern distortions by bending correspond to an asymmetric pattern magnification. An asymmetric magnification can be corrected by the lithography system at the cost of fading [63]. The fading penalty in y -direction σ_y is estimated at:

$$\sigma_y = W\alpha \approx 1.9 [nm] \quad (3.7)$$

where $\alpha \approx 0.529 \times 10^{-6} [-]$ is the asymmetric magnification error and $W \approx$

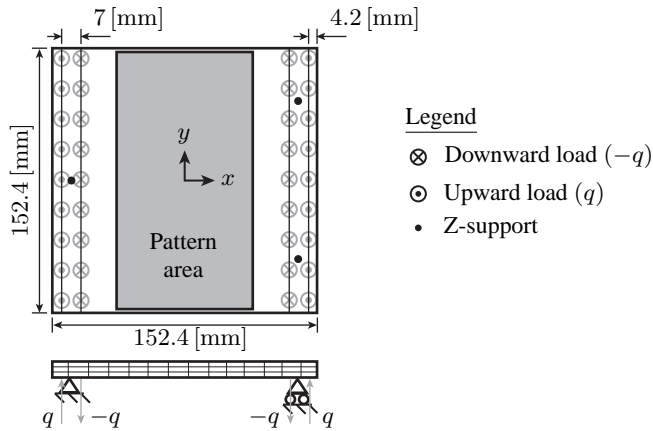


Figure 3.4: Schematic of photomask FE model undergoing pure bending by distributed loads q .

3.6 [mm] the slit width. This is just within the 2 [nm] fading specification of Section 2.5.1.4.

- The feedforward accuracy of the pattern distortion corrections contribute to the overlay error due to reticle bending. This overlay error is the largest at the edge of the pattern area in x -direction. A requirement for the curvature setting accuracy was determined with Equation (3.5) and the 0.1 [nm] overlay requirement that was defined in Table 2.3. This gave the following result:

$$\kappa_x = \frac{2}{t(x + 0.0012)} \frac{u}{M} \approx 2.4 \times 10^{-6} [1/m]. \quad (3.8)$$

where M is the magnification factor of the lens. The bending moment accuracy was determined at $M \approx 0.6 \times 10^{-3}$ [Nm] with Equation (3.2).

3.3.2 Numerical modelling

The analytical model in the previous section provided the first insights into the reticle bending effects on the lithography process. This section introduces the Finite Element (FE) model of the photomask that is used to investigate the effects of the pellicle and the curvature manipulator on the bending performance. Section 3.3.2.1 presents the FE model results for photomask bending without a pellicle and compares them to the analytical model results of Section 3.3.1. The effect of the pellicle on the photomask bending is thereafter treated in section 3.3.2.2.

3.3.2.1 Photomask without pellicle

The first FE model that was developed consisted of a kinematically constrained photomask without pellicle. The model was developed as reference in order to identify

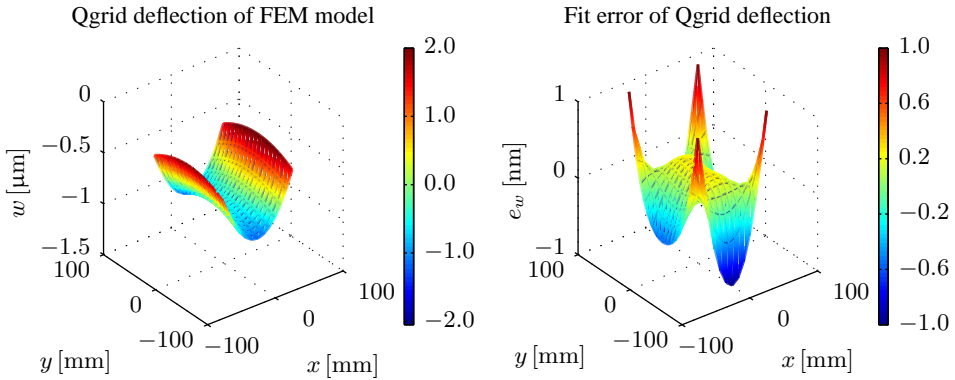


Figure 3.5: Comparison of the out-of-plane reticle deflection between the analytical and numerical photomask model without pellicle. The left graph shows the out-of-plane photomask deflection of the numerical model for a curvature of 0.4×10^{-3} [1/m]. The right graph shows the deflection difference between the numerical and analytical model results of Figure 3.2.

the difference in bending performance between the numerical and analytical photomask model. The reticle was modelled as a three dimensional solid instead of a two dimensional plate. This approach was chosen because it allows the addition of the pellicle and the curvature manipulator in future analysis. The geometry and material properties of Section 2.4.1 were used as model inputs.

The static deformation of the photomask was determined for an applied bending moment of 0.094 [Nm]. This resulted in a photomask curvature of 0.4×10^{-3} [1/m] across the pattern area which was also derived for the analytical model in Section 3.3.1. The bending moment was introduced by two equal but opposite distributed loads q in z -direction along the length of the reticle. This is schematically shown in Figure 3.4. The pitch between the distributed loads was chosen at 7 [mm] because it corresponds to the value that is used for the final design of the curvature manipulator. Tetrahedral and triangular mesh elements with quadratic shape functions were used to generate the photomask mesh. The mesh consisted of a minimum of three element layers across the plate thickness. Furthermore, it was refined until the difference in static deformation and stresses between each mesh refinement had converged.

The out-of-plane deflection and pattern distortions results of the numerically modelled photomask without pellicle are provided in the left plots of respectively Figure 3.5 and 3.6. The right graphs in those figures show the difference between the numerical and the analytical model of Section 3.3.1. The values of the pattern distortions are provided at wafer level. The correlation of the analytical and numerical model was further investigated by fitting the general solution to the Kirchhoff plate model, see Equation (B.22), through the out-of-plane pattern deflection of the numerical model. The identified coefficients are provided in Table 3.1. Inspection of the out-of-plane and in-plane deflection differences between the numerical and analytical model as well as the identified fit coefficients provided the following insights:

- The out-of-plane deflection shows the same anticlastic shape that was observed for

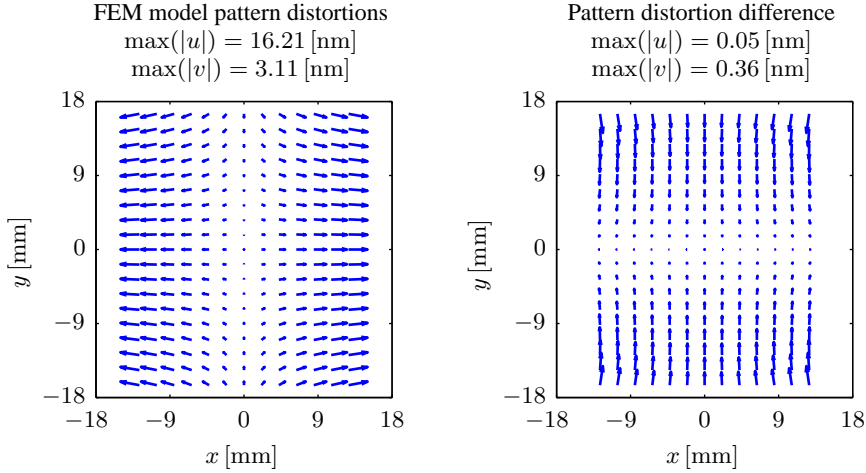


Figure 3.6: The in-plane pattern distortions of the qualification grid for a photomask curvature of $\kappa_x = 0.4 \times 10^{-3} [1/m]$. The left plot provides the result for the photomask FEM model using 3D solids. The right plot shows the difference between the analytical model and FEM model.

the analytical model. Furthermore, the difference between the out-of-plane deflection of the analytical model and the numerical model is limited to $\pm 1 [nm]$ across the pattern area. This difference has two causes. First, the analytical model is limited to plane stress whilst the numerical model considers stresses in three dimensions. Second, the analytical model assumed a pure bending moment introduction whilst the bending moment in the numerical model is generated by distributed loads along the photomask edges. The difference is nevertheless neglected because it translates to a sub-nanometre difference at wafer level.

- Comparison of the fit coefficients between the analytical model and the numerical model without pellicle in Table 3.1 show that the values agree to within 10%. The differences in y -curvature (C_2) and parasitic y -tilt (C_3) are the largest. They are attributed to the above described differences between the analytical and numerical model. Note that both models have the parasitic tilt around the y -axis that is caused by the z -support locations and the anticlastic curvature shape as was described in Section 3.3.1.
- Analysis of the in-plane pattern distortions in Figure 3.6 shows that the initial photomask pattern distortions of the numerical model are dominated by a x - and y -magnification. This was also the case for the analytical model. The pattern distortion difference between the analytical and numerical model that is provided in the right plot of Figure 3.6 shows a magnification difference in y -direction. This is attributed to the discrepancy in the y -curvature as is clear from Table 3.1. Section 3.4 will show that the lithographic system is able to correct this magnification.

The comparison between the numerical and analytical photomask bending model prove that their results are similar. It is expected that the three-dimensional solid model gives a

Coefficient	Model			Unit
	Analytical	Numerical without pellicle	Numerical with pellicle	
C_1	0.400×10^{-3}	0.399×10^{-3}	0.397×10^{-3}	[1/m]
C_2	-0.064×10^{-3}	-0.058×10^{-3}	-0.056×10^{-3}	[1/m]
C_3	0.490×10^{-6}	0.436×10^{-6}	0.427×10^{-6}	[rad]
C_4	0	5.017×10^{-16}	-1.282×10^{-9}	[rad]
C_5	-0.905×10^{-9}	-0.907×10^{-9}	-0.904×10^{-9}	[m]

Table 3.1: Identified coefficients to show the difference in photomask deflection between the analytical and numerical models. The values were obtained by fitting the general solution to the Kirchhoff plate model, i.e. $w = \frac{1}{2}(C_1x^2 + C_2y^2) + C_3x + C_4y + C_5$, through the pattern deflection of the photomask for the different models.

better representation of the photomask bending behaviour because it does not limit itself to the plane stress configuration which is the case for the Kirchhoff plate model. The numerical model of the photomask will therefore be used in the remainder of this thesis.

3.3.2.2 Photomask with pellicle

The effect of the pellicle on the reticle bending behaviour was investigated with FE. The adhesive gasket and the pellicle frame that were introduced in Section 2.4.1 were added to the photomask FE model of Section 3.3.2.1. The pellicle membrane was neglected because of its smaller thickness and elasticity modulus with respect to the pellicle components. The analysis was performed with the same boundary conditions, bending moment configuration and mesh settings as the photomask FE model of the Section 3.3.2.1.

The simulation results of the photomask with pellicle model were compared to the analytical and numerical model without pellicle. Table 3.1 shows the identified coefficients after fitting the general solution to the Kirchhoff plate model through the out-of-plane deflection data. Figure 3.7 shows the out-of-plane and in-plane deformation difference with respect to the numerical model without pellicle for the same curvature. The results highlight the following:

- The curvature difference between the model with and without pellicle is equal to 2×10^{-6} [1/m] for the same applied bending moment. It is caused by the added bending stiffness of the pellicle assembly. In order to obtain the desired curvature across the slit, the bending moment must be increased by approximately 0.5%. The limited added bending stiffness of the pellicle is attributed to the low elasticity modulus of the pellicle gasket.
- The difference in out-of-plane pattern distortions between the numerical model with and without pellicle is limited to ± 2 [nm] at reticle level. This translates to a sub-nanometre error at wafer level which is considered negligible.
- The in-plane pattern distortion difference between the reticle with and without pellicle is close 50 [pm] at wafer level. It approaches the overlay design rule that

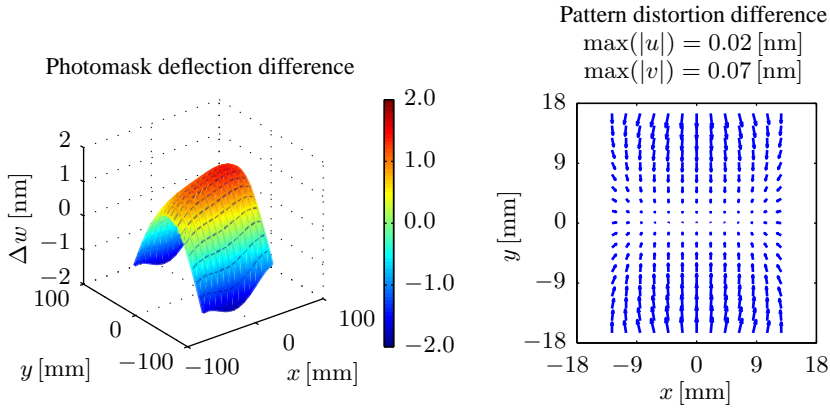


Figure 3.7: Difference in bending behaviour for a photomask with and without pellicle for a curvature of $\kappa_x = 0.4 \times 10^{-3}$ [1/m]. The left plot shows the difference in the out-of-plane deflection of the reticle. The right plot provides the difference of the in-plane pattern distortions.

was defined in Section 2.5.2.2. The dominant contributor is a y -magnification error which can be corrected by the lithography system.

The above analysis has shown that there is a negligible difference between the bending behaviour of the reticle with and without pellicle. For this reason, the pellicle will not be taken into account in future analysis or measurements. The geometry of the pellicle is considered during the design of the curvature manipulator however because it is still a relevant boundary condition.

3.4 Pattern distortion estimation

Section 3.3 has demonstrated that reticle bending induces pattern distortions. The distortions are in the order of 16 [nm] for a reticle curvature of 0.4×10^{-3} [1/m]. The magnitude is approximately two orders of magnitude larger than the budgeted pattern distortions in Table 2.3. Reticle bending can be considered infeasible if these pattern distortions are left uncorrected.

The pattern distortions can be corrected in two ways. The first consists of applying additional in-plane forces on the reticle edges such that the photomask neutral axis is shifted to the photomask's bottom surface [43]. Section 3.5 will show that this configuration is not preferred because of its stress-birefringence penalty. The second alternative is to use the correction potential of the lithographic system to correct for in-plane pattern distortions. These corrections are achieved by adapting stage positions and active lenses in the optical column during the exposure process [71, 94, 133]. The downside of the corrections is that they can come at the cost of fading [63].

Figure 3.8 shows the proposed method to counteract reticle bending induced pattern distortions with the lithography system [115]. The strategy uses a curvature setpoint that is generated from wafer topology and lens heating curvature data before the start of the exposure process. The controller of the scanner estimates the pattern distortions by reti-

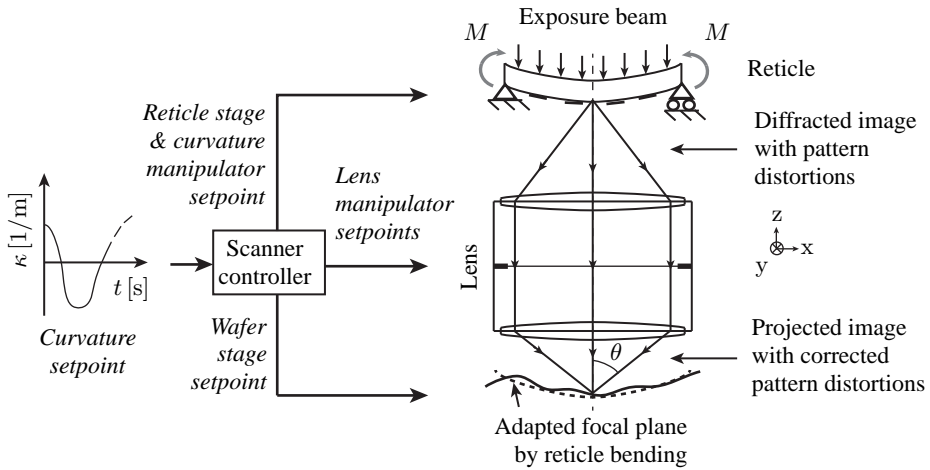


Figure 3.8: The feedforward correction strategy to counteract reticle bending induced pattern distortions as patented in [115]. The scanner controller determines the required feedforward actions for the lens and stages from the a priori curvature setpoint. These corrections are then executed by the stages and lens during the exposure process.

cle bending and derives the required corrective actions by the lens and stages. They are translated into feedforward control signals which are sent to the curvature manipulator, lens and stages during the exposure process. It results in a curved aerial image with corrected pattern distortions at wafer level.

The correction potential of this strategy was estimated with a mathematical system model of a state-of-the-art immersion lithography system. This model describes the dependencies of the lithographic image quality (overlay, focus, aberrations) in the exposure area as a function of lens and stage manipulator settings. The required manipulator settings for the pattern distortion correction are determined with a least squares optimization procedure. The settings are then used to determine the image quality after correction such as the residual pattern distortions and fading penalty. More details on the optimization procedure are provided in Appendix A.

The results of the pattern distortion correction analysis are provided in Figures 3.9 and 3.10. The left and right graph of Figure 3.9 respectively provide the pattern distortions before and after corrections of the lithography system. The induced fading penalty in the x - and y -direction are shown in the left and right graph of Figure 3.10. The results demonstrate the following:

- Figure 3.9 shows that the pattern distortions after correction are below the 50 [pm] overlay design rule that was defined in Section 2.5.2.2. The residual pattern distortions for ideal bending and machine corrections satisfy the design rule by approximately a factor of 3.
- Figure 3.10 shows a maximum fading penalty of 6 [pm] and 1.6 [nm] in respectively the x - and y -direction. This demonstrates that the fading penalty in x -

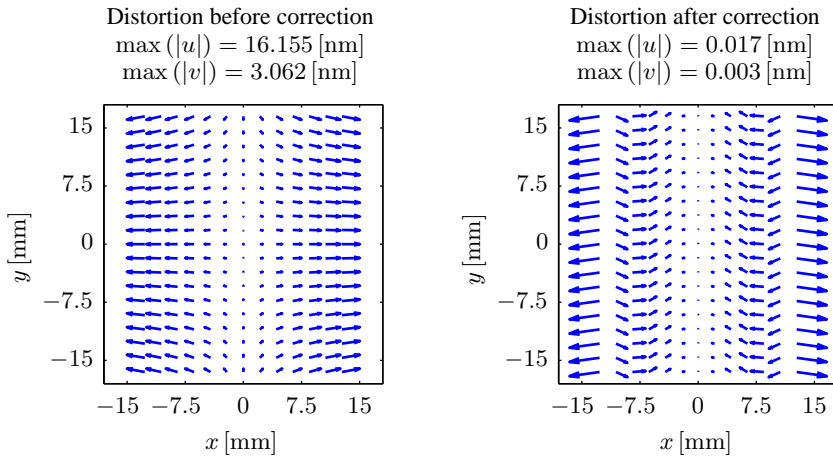


Figure 3.9: Difference in photomask pattern distortion at wafer level before and after feedforward corrections of the lithography system for a curvature of $0.4 \times 10^{-3} \text{ [1/m]}$.

direction is negligible. The calculated fading penalty in y -direction is approximately equal to the value that was estimated in Section 3.3.1. It satisfies the 2 [nm] fading penalty specification of Section 2.5.1.4 by a factor of 1.25.

- Fading is the limiting factor if curvatures above $0.4 \times 10^{-3} \text{ [1/m]}$ need to be realized. This is demonstrated by the above identified margins on pattern distortion and the fading penalty.
- The required lens manipulator ranges for the pattern distortion correction were also analysed. All values were within the manipulator range budgets which indicates that the correction can be achieved with the current lithography system.

The analysis results have shown that the pattern distortions and the fading penalty after correction stay within the defined system specifications of Section 2.5. The results prove the feasibility of reticle bending under the condition that lens and stage corrections are used to counteract the induced pattern distortions. Note that no parasitic effects of the manipulator were included in this analysis. The effect of the manipulator on the bending performance is analysed in Chapter 5.

3.5 Induced stress birefringence

Photomask bending not only results in pattern distortions but also induces bending stresses. Section 2.5.1.3 explained that photomask stresses can lead to stress-birefringence which changes the polarization state of the exposure beam and subsequently image contrast loss. This section provides estimates of the photomask stress-birefringence when it undergoes pure bending. The acquired values are compared to the birefringence specification of Section 2.5.1.3.

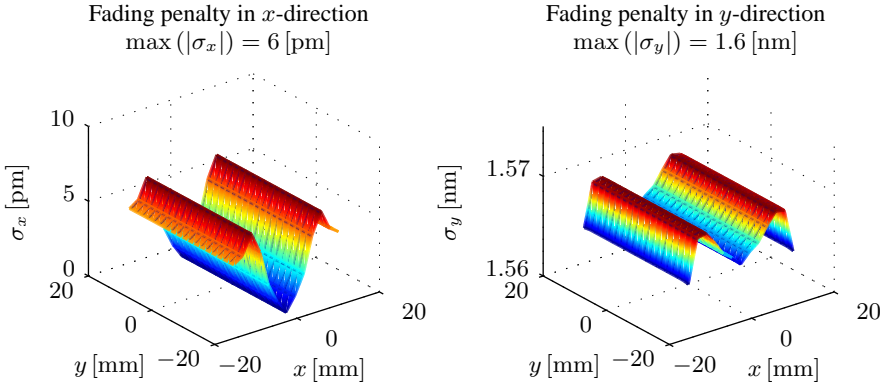


Figure 3.10: The induced fading penalty after correcting the pattern distortions in Figure 3.9. The left and right graph respectively show the fading penalty in x - and y -direction for a curvature of $0.4 \times 10^{-3} \text{ [1/m]}$.

The photomask stress-birefringence due to bending was determined with the approach of [22]. The analysis was based on the following assumptions:

- The exposure beam consists of parallel rays which propagate in z -direction.
- The photomask has plane stress in its xy -plane when it undergoes pure bending.

The stress-birefringence in the photomask is calculated with the steps that are shown in Figure 3.11. The first step in the calculation procedure is to determine the normal (σ_x, σ_y) and shear (τ_{xy}) stresses in the bent photomask as is shown in the top-left drawing of Figure 3.11. The stress values are obtained from either the analytical or FE model. The second step in the calculation procedure is to translate the normal and shear stresses into principal stresses (σ_1, σ_2) and principal directions (n_1, n_2). This translation is needed because the birefringence of isotropic material is dependent on the principal stress difference [134]. The principal stresses and principal angle θ are defined by [43]:

$$\sigma_{1,2} = \frac{\sigma_x + \sigma_y}{2} + \frac{\sigma_x - \sigma_y}{2} \cos(2\theta) + \tau_{xy} \sin(2\theta), \quad \sigma_1 \geq \sigma_2 \quad (3.9)$$

$$\theta = \frac{1}{2} \tan^{-1} \left(\frac{2\tau_{xy}}{\sigma_x - \sigma_y} \right) + \frac{1}{2} k\pi, \quad k = 0, 1. \quad (3.10)$$

Note that the largest principal stress defines the first principal stress σ_1 . The angle θ defines the orientation of the first principal direction n_1 with respect to the x -axis. The third step of the analysis procedure comprises of calculating the stress-birefringence at locations (x, y) for discrete photomask cross sections. The magnitude (Δn_{12}) of the local birefringence is equal to [22]:

$$\Delta n_{12} = R(\sigma_1 - \sigma_2). \quad (3.11)$$

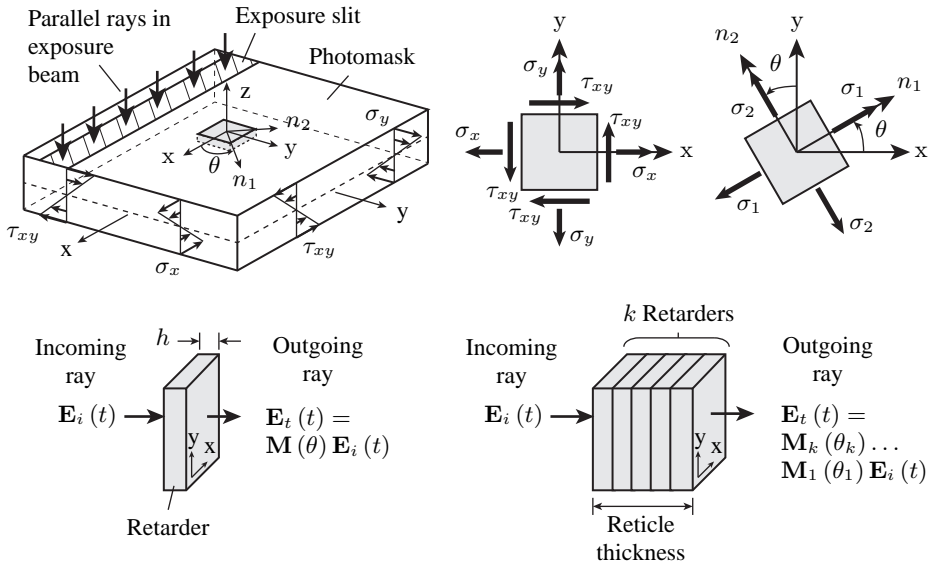


Figure 3.11: A schematic representation of the photomask stress birefringence analysis. The top left picture show the photomask being exposed whilst undergoing bending. The middle and right top drawing represent the plane stress configuration of part of the photomask in the Cartesian coordinate frame and the plane stress situation described in principal stresses and directions. The bottom left drawing shows the effect of a retarder on the polarisation state of the light. The bottom right drawing represents the reticle as a discrete number of retarders.

with R the stress-optic coefficient of the material, see Table 2.1. The value quantifies the difference in index of refraction between the two principal directions n_1 and n_2 which are respectively known as the *fast* and *slow axis*. The fast axis corresponds to the direction the largest propagation speed of the electromagnetic wave [47].

The final step in the analysis procedure is to determine the total birefringence magnitude and direction at each x, y -location across the photomask thickness. These are calculated by considering the photomask as a series of arbitrary oriented optical retarders at every x, y -position along its thickness. Each retarder has the ability to change the polarization state of the incident beam. The retardation can mathematically be described with Jones Calculus [47]:

$$\begin{bmatrix} E_{t_x}(t) \\ E_{t_y}(t) \end{bmatrix} = \mathbf{M} \begin{bmatrix} E_{i_x}(t) \\ E_{i_y}(t) \end{bmatrix} \quad (3.12)$$

where $E_{t_x}(t), E_{t_y}(t)$ and $E_{i_x}(t), E_{i_y}(t)$ respectively represent the instantaneous scalar components of the transmitted $\mathbf{E}_t(t)$ and incident $\mathbf{E}_i(t)$ polarized wave in the x, y -directions. The Jones matrix \mathbf{M} provides a mathematical description of the retarder. A retarder that has its fast axis rotated by an angle θ with respect to the x -axis can be

described by:

$$\mathbf{M}(\theta) = \mathbf{R}(\theta) \mathbf{M} \mathbf{R}(-\theta) \quad (3.13)$$

$$= \begin{bmatrix} \cos \theta & -\sin \theta \\ \sin \theta & \cos \theta \end{bmatrix} \begin{bmatrix} e^{i\frac{\delta}{2}} & 0 \\ 0 & e^{-i\frac{\delta}{2}} \end{bmatrix} \begin{bmatrix} \cos \theta & \sin \theta \\ -\sin \theta & \cos \theta \end{bmatrix} \quad (3.14)$$

where $\delta = 2\pi h \Delta n_{12} / \lambda$ is equal to the retardation, h the thickness of the retarder in [m] and λ the wavelength of the propagating wave in [m]. The total effect of k serially placed retarders is equal to the product of their Jones matrices, i.e.:

$$\mathbf{E}_t(t) = \mathbf{M}_k(\theta_k) \mathbf{M}_{k-1}(\theta_{k-1}) \dots \mathbf{M}_2(\theta_2) \mathbf{M}_1(\theta_1) \mathbf{E}_i(t) \quad (3.15)$$

The nett stress-birefringence Δn_{12} and orientation θ of the fast axis for the series of retarders can be obtained by calculating the eigenvalues and eigenvectors of the cumulative Jones matrix in Equation (3.15). The eigenvector that corresponds to the eigenvalue with positive imaginary part defines the fast axis orientation θ with respect to the original x -axis. The total stress-birefringence amplitude can be derived from the eigenvalue using $\Delta n_{12} = \delta / (2\pi h)$ where h corresponds to the summed thickness of the retarders. It is equal to the reticle thickness for the photomask bending case.

The photomask stress-birefringence for the ideal bending case was determined for both the analytical and numerical model. The analytical model was analysed as reference case because of its pure plane stress behaviour. Its net birefringence was equal to 0 [nm/cm] for a curvature of 0.4×10^{-3} [1/m]. This result is also expected after considering the photomask stress state of Figure 3.12. The top-left, top-right and bottom-left graph respectively show the normal and shear stresses, principal stresses and principal angle across the photomask thickness under pure bending. Equation (3.11) and the principal stress values demonstrate that the birefringence magnitude Δn_{12} is always positive across the photomask thickness. The 90 [deg] change of the principal angle at the centre of the photomask indicates that the top and bottom half respectively have their fast axis in the x - and y -direction. The retardation in the upper half of the reticle cancels the effect of the bottom half leading to a zero net birefringence across the photomask thickness.

The photomask stress-birefringence was also determined for the numerical model that had a curvature of 0.4×10^{-3} [1/m]. The results are provided in the bottom-right graph of Figure 3.12. The maximum stress-birefringence was determined at 0.07 [nm/cm] which satisfies the 1 [nm/cm] stress-birefringence specification of Section 2.5.1.3. The plot also shows that the largest stress-birefringence occurs at the corners of the pattern area. This relates to the phenomena that was seen in Figure 3.5. It is attributed to the difference in bending moment introduction between the analytical and numerical model as explained in Section 3.3.2.1.

The analysis results have shown that the stress-birefringence specifications are satisfied for the case of pure bending. This is not the case for the proposed configuration in Section 3.4 where additional in-plane forces are applied to the reticle edges in order to correct for pattern distortions. The induced stress-birefringence by those forces is estimated at $\Delta n_{12} = 4.7$ [nm/cm] which exceeds the specifications by more than a factor of

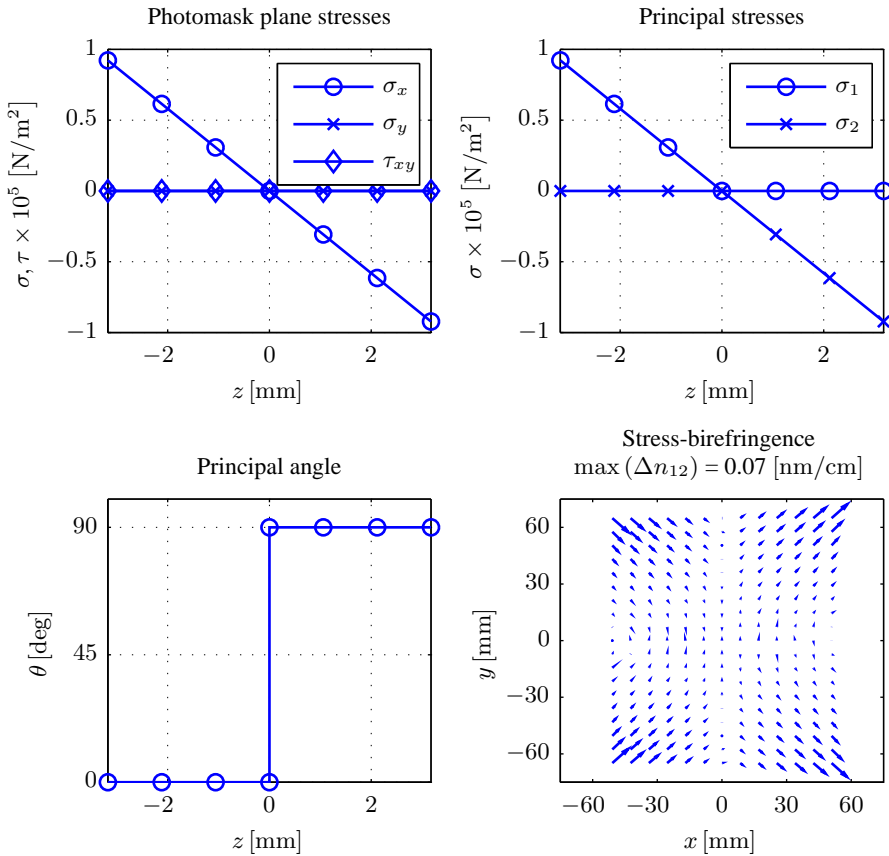


Figure 3.12: Results of the stress-birefringence analysis. The top-left graph shows the normal and shear stresses across the photomask thickness for the analytical plate model of Section 3.3.1. The top-right graph and bottom-left graph provide the corresponding principal stresses and angle for that same model. The bottom-right graph shows the net stress-birefringence in the pattern area of the numerical photomask model of Section 3.3.2.1.

4. The use of additional in-plane forces for pattern distortion correction is therefore not considered further in this thesis.

3.6 Generated optical aberrations

The previous part of this thesis has demonstrated that ideal reticle bending results in a field curvature correction at wafer level with negligible stress-birefringence and pattern distortions. Figure 2.1 showed that the field curvature correction can be considered as the reduction of defocus between the aerial image and the wafer surface for each position in the slit. It is unknown if the focus correction induces other optical aberrations. This section provides estimates of the introduced optical aberrations by the reticle bending correction. The values are compared to the specification of Section 2.5.1.2.

The induced optical aberrations by a focus correction were determined for the simplified geometrical optical model of Figure 3.13 [61]. The model assumes an ideal lens and shows the original focus error between a field point P on the curved wafer surface and the corresponding field point Z in the aerial image. An expression for the wavefront error due to defocus is obtained by considering the optical path difference (OPD) between rays of an ideal spherical wave that travel from the lens to points P and Z . The OPD between these points and position E in the lens is equal to [47]:

$$\text{OPD} = \int_E^Z n ds - \int_E^P n ds = n(\tilde{r} + dr) - nr \quad (3.16)$$

$$\approx ndr = ndz\sqrt{1 - \sin^2\theta} \quad (3.17)$$

where $\theta \approx \theta_p$ and $n = 1.44$ is the index of refraction of the water between the wafer and the lens [19]. The simplification from Equation (3.16) to (3.17) is allowed because the water film thickness dz between the wafer and lens is several millimetres thick whilst the defocus error f is in the order of tens of nanometres [76].

Equation (3.17) shows that the OPD is dependent on the ray's angle of incidence θ and the defocus error. It is desirable to have the expression as a function Numerical Aperture (NA) for the remainder of the analysis. The expression can be obtained from the relation between the lens pupil diameter and the NA. The pupil radius can be expressed as [45]:

$$\text{NA} \approx n \frac{d}{2f} \Rightarrow \frac{d}{2} \approx \frac{f\text{NA}}{n}. \quad (3.18)$$

A relation between the NA and the angle of incidence θ can then be obtained by defining a normalized pupil radius ρ and rewriting it as:

$$\rho = \frac{2a}{d} = \frac{nr \sin\theta}{f\text{NA}} \Rightarrow \sin\theta \approx \frac{\rho\text{NA}}{n}, \quad \text{for } dz \ll f. \quad (3.19)$$

The expression for the defocus induced wavefront error as a function of NA and normalized pupil radius ρ is finally obtained by substitution of Equation (3.19) into (3.17):

$$\text{OPD} \approx ndz\sqrt{1 - \left(\frac{\rho\text{NA}}{n}\right)^2}. \quad (3.20)$$

The right graph in Figure 3.13 shows the normalized wavefront error (OPD/dz) in the normalized pupil plane. It has a circular symmetric profile with its maximum in the centre of the pupil. This profile is also expected when considering Equation (3.20).

The next step in the analysis is to determine the contributing aberrations to the defocus

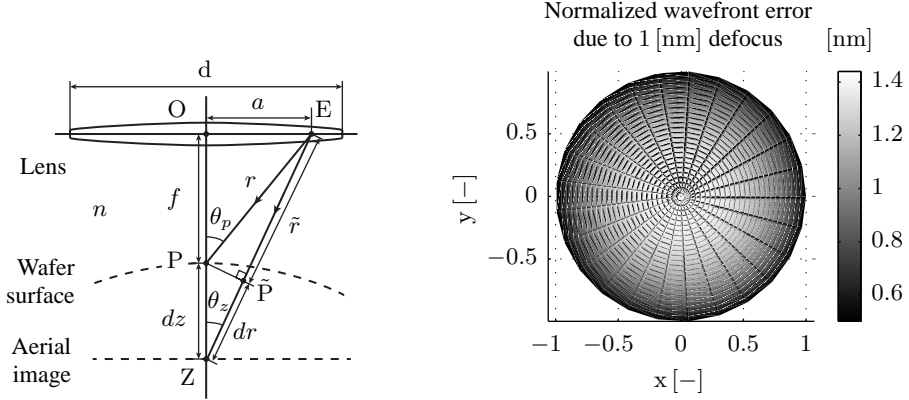


Figure 3.13: Model of the induced optical aberrations by reticle bending. The left drawing shows the geometrical optical model that was used to determine the wavefront error by defocus. The right graph shows the normalized wavefront error due to 1 [nm] defocus in normalized pupil coordinates.

induced wavefront error of Equation (3.20). They can be obtained by first expressing the wavefront error as a series expansion of orthogonal Zernike polynomials $Z_i(\rho, \phi)$, i.e.:

$$ndz \sqrt{1 - \left(\frac{\rho NA}{n}\right)^2} = \sum_{i=1}^{\infty} A_i Z_i(\rho, \phi) \quad (3.21)$$

where A_i is the amplitude of the i^{th} Zernike polynomial. A general expression for the coefficients A_i is thereafter obtained by projecting the wavefront error of Equation (3.21) onto each Zernike polynomial whilst making use of the orthogonality between each Zernike. This gives:

$$A_i = \frac{\int_0^{2\pi} \int_0^1 ndz \sqrt{1 - \left(\frac{\rho NA}{n}\right)^2} Z_i(\rho, \phi) \rho d\rho d\phi}{\int_0^{2\pi} \int_0^1 Z_i(\rho, \phi) Z_i(\rho, \phi) \rho d\rho d\phi} \quad (3.22)$$

because

$$\int_0^{2\pi} \int_0^1 Z_i(\rho, \phi) Z_j(\rho, \phi) \rho d\rho d\phi = 0, \quad i \neq j. \quad (3.23)$$

Equation (3.22) was used to estimate the induced optical aberrations for a $dz = 20$ [nm] offset between the wafer and the aerial image. This value was chosen because it is approximately equal to the lens heating and wafer curvature focus error. Furthermore, the

Case	Optical aberration amplitudes						Unit
	A_4	A_9	A_{16}	A_{25}	A_{36}	A_{37}	
Initial aberrations by a wafer field point focus error of 20 [nm]	9.0	1.4	0.4	0.1	0.1	0.0	[nm]
Residual aberration after a reticle field point z -translation of 306 [nm] by reticle bending	0.0	1.3	0.4	0.1	0.1	0.0	[nm]

Table 3.2: An overview of the induced optical aberrations by a 20 [nm] offset between the aerial image and wafer as is shown in Figure 3.13. It also provides the residual aberrations after adaptation of the reticle curvature.

index of refraction of water ($n = 1.44$) and Numerical Aperture of the immersion lithography lens ($NA = 1.35$) were used for the calculation.

The estimated aberrations for the focus error at wafer level are provided in Table 3.2. It highlights that only a defocus term (A_4) and higher order spherical aberrations (A_9, \dots) are introduced by a 20 [nm] offset between the aerial image and wafer surface. Furthermore, the defocus contribution is the dominant aberration. This is exactly the focus error that is going to be corrected by the reticle curvature manipulation.

The field curvature correction by reticle bending relates to a local z -translation of a reticle field point with respect to the lens focal plane. This translation is similar to the above described focus error at wafer level. It is therefore possible to estimate the required z -translation at reticle level in order to eliminate the (A_4) defocus at wafer level with:

$$\Delta z = A_4^w \frac{dz}{A_4^r} \quad (3.24)$$

where A_4^w is the value of the defocus at wafer level in [nm] as provided in Table 3.2 and dz/A_4^r is the defocus sensitivity with respect to the z -translation of the reticle. The latter coefficient can be obtained from Equation (3.22) for the index of refraction and Numerical Aperture at reticle level. These are respectively equal to $n = 1$ and $NA^r = NA^w/M$ where M is the magnification factor of the lens [71].

Table 3.2 provides the residual aberrations after correcting the 20 [nm] focus error at wafer level with a local reticle z -translation of 306 [nm]. The latter value was determined with Equation (3.24). Adding the aberrations of the corrective action to the aberrations of the focus error highlights the following:

- The ratio between the initial 20 [nm] wafer focus error and the reticle z -translation of 306 [nm] is equal to $1/15.3$. This factor represents the longitudinal magnification of the lens and is approximately equal to the simplified longitudinal magnification of $1/16$ that was used in Section 2.2.2 to find the relation between the reticle and wafer curvature.
- Reticle bending reduces the optical aberrations that result from an initial 20 [nm] wafer focus error. This is especially the case for the defocus but also for the first spherical aberration A_9 . Effects on higher order aberrations are negligible.

The above results demonstrate that reticle bending does not induce additional optical aberrations during the lithography process. The optical aberration specifications of Section 2.5.1.2 are therefore satisfied for ideal bending conditions.

3.7 Summary & Conclusions

The first objective of this thesis is to investigate the potential and conceptual feasibility of a field curvature correction in an immersion lithography system, assuming an ideal adaptation of the reticle curvature. This chapter investigated the conceptual feasibility with mechanical models of the photomask when it undergoes ideal bending. The derived overlay and imaging specifications of Chapter 2 were used for the investigation. The analysis results are summarized in Table 6.3.

Two reticle bending strategies that are able to realize a time varying curvature correction during the exposure process were introduced at the start of this chapter. The first strategy consisted of applying a uniform but time varying bending moment to the reticle edge. The second strategy involved the application of a time constant but spatially varying bending moment to the reticle edge. Both are represented in Figure 3.1. The former strategy is preferred because a uniform bending moment is easier to apply. Furthermore, it results in a uniform curvature and pattern distortions which can be corrected by the lithography system.

The reticle bending effects were investigated by mechanical modelling. An analytical Kirchhoff plate model of the reticle without pellicle gave the following insights:

- A 0.1 [Nm] bending moment results in a reticle curvature of $\kappa_x = 0.4 \times 10^{-3}$ [1/m].
- The applied bending moment also induces an opposite but six times smaller parasitic reticle curvature in the scan direction. This reticle deflection must be followed by the reticle stage in order to avoid a focus offset.
- Reticle bending induces an asymmetric pattern magnification. The deformations are 16.5 and 3.3 [nm] in x - and y -direction at wafer level for a curvature of $\kappa_x = 0.4 \times 10^{-3}$ [1/m]. They exceed the overlay specifications in Chapter 2 by two orders of magnitude and therefore need to be corrected by the lithography system.
- The required curvature setting accuracy is driven by the minimum allowed pattern distortion penalty. A curvature error of 2.4×10^{-6} [1/m] is taken because it gives a pattern distortion of 0.1 [nm] at wafer level.

Finite element models of the photomask with and without pellicle were also developed. They had negligible difference in bending behaviour with respect to the analytical model. The effect of the pellicle is limited because the pellicle frame and reticle are mechanically decoupled by the low elasticity modulus of the applied adhesive.

The feasibility of the reticle bending concept depends on the potential of the lithographic system to correct the induced pattern distortions. Analysis showed that the pattern distortions are below 50 [pm] after adaptation of stage positions and lens elements in the

Criteria		Specification	Ideal reticle bending	Unit	Satisfies specification?
Imaging	Curvature	0.4×10^{-3}	0.4×10^{-3}	[1/m]	Yes
	Aberrations	4	0	[m λ]	Yes ¹
	Birefringence	1	0.07	[nm/cm]	Yes
	Fading	2	1.6	[nm]	Yes
Overlay (DCO)	Design rule	0.05	0.017	[nm]	Yes ²

¹ Without considering aberration impact of lens adaptations for overlay correction.

² Can only be achieved with additional machine overlay corrections.

Table 3.3: Comparison of the curvature manipulator specifications of Chapter 2 and the analysis results of ideal photomask bending that were obtained in this chapter. The results demonstrate that ideal bending satisfies the curvature manipulator specifications.

lithography system. The correction does come at the cost of a 1.6 [nm] fading penalty. Both the pattern distortions and the fading penalty are within the defined specifications of Chapter 2.

The induced stress-birefringence by reticle bending was also investigated with the mechanical models. It was shown that there is no birefringence for the ideal bending case because of the symmetric stress-conditions across the reticle thickness. The analysis also showed that the application of additional in-plane forces to correct for pattern distortions is undesired because it leads to a stress-birefringence of $\Delta n_{12} = 4.7$ [nm/cm]. This exceeds the specification of Chapter 2 by approximately a factor of 4.

An optical model was used to identify the reticle bending effects on optical aberrations. It demonstrated that a defocus at wafer level introduces spherical aberrations. Correcting the defocus by reticle bending also results in a reduction of the first spherical aberrations (Z_9) whilst the higher order spherical aberrations are unaffected.

The following conclusions are drawn from the conceptual analysis results in this chapter:

- The pellicle can be neglected in the remainder of this thesis because it has negligible effects on bending deformation and pattern distortions.
- Reticle bending is only feasible if the induced pattern distortions are corrected by the lithography system.
- There are no stress-birefringence and optical aberrations penalties for the case of ideal reticle bending.
- In-plane forces on the reticle must be avoided because they lead to stress-birefringence.

The above proves that reticle curvature manipulation is conceptually feasible when it is used in combination with available overlay correction mechanisms in the lithography tool. The first thesis objective is therefore satisfied. The next objective is to design and validate a reticle curvature manipulator that satisfies the high-level lithography specifications and boundary conditions. This is done in Chapters 4 to 6.

Chapter 4

Design of the curvature manipulator

This chapter covers the design of the photomask curvature manipulator. The explanation is provided using the system specifications and conceptual analysis results of respectively Chapters 2 and 3. It provides the design specifications, the conceptual design choices and the detailed design of the curvature manipulator. A detailed investigation of the manipulator performance is provided in Chapter 5.

4.1 Introduction

The first objective of this thesis was satisfied with the results of Chapters 2 and 3. The chapters proved the focus improvement potential and feasibility of a field curvature correction in an immersion lithography system by adaptation of the photomask curvature. The feasibility was demonstrated without considering a specific manipulator design however.

This chapter tackles part of the second thesis objective. It introduces the preferred manipulator design that is able to apply the bending moment to the photomask whilst satisfying the design specifications. Section 4.2 introduces the design specifications of the curvature manipulator. The conceptual choices and detailed design are thereafter discussed in Sections 4.3 and 4.4. The chapter ends with a summary and conclusions in Section 4.5.

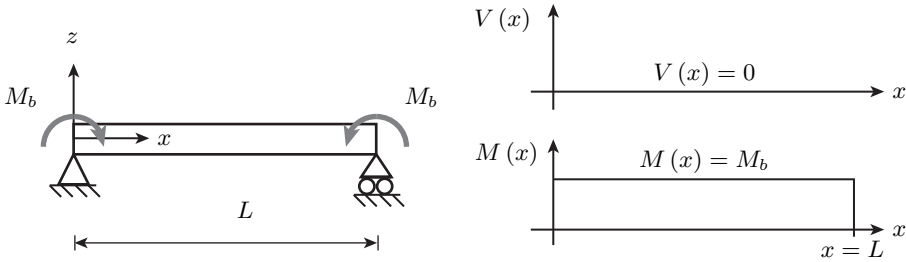


Figure 4.1: A simplified two-dimensional representation of the reticle bending configuration. The left drawing shows a beam where two equal but opposite bending moments M_b that are applied to its edges in order to generate an internal bending moment. The right diagrams show the distribution of the shear force $V(x)$ and the internal bending moment $M(x)$ across the photomask width.

4.2 Design specifications

The results of the conceptual reticle bending analysis in Chapter 3 were obtained with the assumption of an ideal curvature manipulator. That specific case can be approximated by the simplified representation of Figure 4.1 where two equal but opposite moments are applied to a beam without any additional shear forces. The ideal configuration will not occur in reality however. This section identifies allowable parasitic effects and derives manipulator design specifications. The specifications are summarized in Table 4.1. The table also provides the section numbers in which the specifications are derived. These sections are provided below.

4.2.1 Parasitic loads

Levels for the allowable parasitic forces and moments need to be identified because they lead to pattern distortions and possibly overlay. First-order estimates for the parasitic forces were obtained by considering the simplified two-dimensional representations of the photomask in the reticle stage as shown in Figure 4.2. The left figure shows the photomask in the xz -plane where two equal but opposite in-plane forces act on the edges of the simply supported photomask. The right figure shows the photomask in the yz -plane assuming a single z -support in the centre and two equal out-of-plane forces on the photomask ends. Both models can be simplified because of symmetry.

Relations for the allowed parasitic forces are obtained using the formula for respectively a bar in compression and a beam undergoing bending. The formula for the allowed in-plane parasitic force F_x in the left drawing of Figure 4.2 is equal to [43]:

$$u = \frac{F_x (1/2L)}{EA} = \frac{F_x}{2Et} \implies F_x = 2Etu \quad (4.1)$$

where u is the in-plane deformation of the reticle, t is the reticle thickness, L is the reticle length whilst E and A are respectively the elasticity modulus and the cross-section of the photomask. An estimate of the pattern distortions by the out-of-plane parasitic force F_z

Design specification		Parameter	Value	Unit	Reference
Curvature		κ_x	0.4×10^{-3}	[1/m]	Section 2.5.1.1
Bending moment		M_b	0.1	[Nm]	Section 3.3.1
Parasitic loads	In-plane force	F_x	180	[mN]	Section 4.2.1
	Out-of-plane force	F_z	5	[mN]	
	Moment	M_θ	0.2	[Nmm]	
Stroke	In-plane ¹	u_{tot}	0.55	[mm]	Section 4.2.2
			98	[nm]	
	Out-of-plane	w_{tot}	0.9	[μ m]	
	Rotational	θ_{tot}	41.5	[μ rad]	
Parasitic stiffness	In-plane ¹	k_x	335	[N/m]	Section 4.2.3
			4.7×10^5	[N/m]	
	Out-of-plane	k_z	5.7×10^3	[N/m]	
	Rotational	k_θ	4.7	[Nm/rad]	
Mass	In-plane ²	m_y	$39.4/n$	[g]	Section 4.2.4
	Out-of-plane	m_z	15	[g]	
Mechanical resonance	In-plane	$f_{x,y}$	> 2000	[Hz]	Section 4.2.5
	Out-of-plane	f_z	> 430	[Hz]	
Volume	Length	l	160	[mm]	Section 4.2.6
	Width	w	35	[mm]	
	Height	h	11	[mm]	
Power dissipation		P_{diss}	4	[mW]	Section 4.2.7

¹ The top value corresponds to the manipulator interface at the edge of the reticle whilst the bottom value corresponds to the interface at the photomask bottom surface.

² The allowed in-plane mass is dependent on the number of photomask-manipulator interfaces n .

Table 4.1: A summary of the design specifications for the photomask manipulator.

is obtained by multiplying half the reticle thickness by the photomask's local angle [43]:

$$u = \frac{1}{2}t\theta_x = \frac{1}{2}t \frac{F_z (1/2L)^2}{2EI} = \frac{18F_z}{Et} \implies F_z = \frac{Et}{18}u. \quad (4.2)$$

The first-order estimates of Equations (4.1) and (4.2) show that the pattern distortion sensitivity to out-of-plane parasitic forces is approximately a factor thirty-six larger than to in-plane forces. This contradicts the conception that out-of-plane parasitic forces have a larger sensitivity to focus and in-plane forces to overlay. The impact of out-of-plane forces on pattern distortions is attributed to the offset of the chrome pattern to the neutral bending axis and the smaller out-of-plane than in-plane stiffness of the photomask.

Values for the allowed parasitic force levels were obtained by substituting the reticle physical properties and the allowable pattern distortion into Equations (4.1) and (4.2). The 50 [pm] design rule for the maximum allowable in-plane pattern distortions at wafer level was also used for the estimation. This results in the $F_x \approx 180$ [mN] and $F_z \approx 5$ [mN] that are provided in Table 4.1.

The value for the parasitic bending moment was determined using the relation of the photomask between the bending moment and the in-plane pattern distortion. The allowable bending moment M_θ is obtained by multiplying half the reticle thickness by the

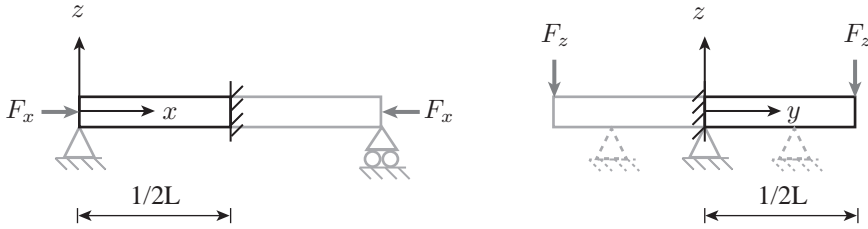


Figure 4.2: Simplified models that were used to get an estimate of the allowable force errors for the in-plane (F_x) and out-of-plane (F_z) actuation configuration.

photomask's local angle [43]:

$$u = \frac{1}{2}t\theta_x = \frac{1}{2}t \frac{M_\theta (1/2L)}{EI} = \frac{3M_\theta}{Et^2} \implies M = \frac{Et^2}{3}u. \quad (4.3)$$

Substituting the values of the photomask properties and the design rule for the in-plane pattern distortions at wafer level into Equation (4.3) gives $M_\theta = 0.2$ [Nmm].

Note that the above estimates of the parasitic forces and moments are obtained from simplified photomask representations which assumes a uniform parasitic force across the depth of the model. Furthermore, simplified out-of-plane reticle constraints are assumed. It is therefore expected that the exact values for the parasitic forces and bending moments will differ. The values do provide an order of magnitude for the allowable parasitics and will therefore be used for the conceptual design of the bending mechanism.

4.2.2 Manipulation range

In order to derive values for the allowed parasitic stiffness it is necessary to consider the required range in which the manipulator must be able to apply the bending moment. Figure 4.3 provides three possible configurations for the bending moment introduction. The left concept uses in-plane friction forces W at a pitch d to generate the bending moment. The middle and right respectively use in-plane and out-of-plane normal forces N for the bending moment generation. The location of force application in those cases is either at the photomask edge or bottom surface.

The required manipulator range is dependent on the location of force application, the required stroke for bending and position tolerances of the reticle in the chuck. The derived manipulator range for the different cases are described below.

Required stroke for bending

The required stroke for bending is dependent on the location where the manipulator will introduce the bending moment to the photomask. Estimates of the required actuator strokes were obtained by considering the analytical reticle bending model of Chapter 3 and identifying the photomask deflection along its edge. Equations (3.1) and (3.1) provided the following relations for the reticle's in-plane u, v and out-of-plane w defor-

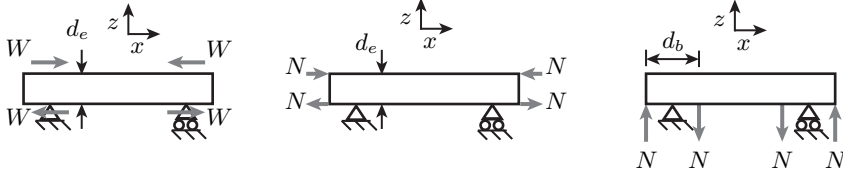


Figure 4.3: Possible configurations to generate an internal bending moment in the photomask. The left concept uses in-plane friction forces W at a pitch d to generate the bending moment. The middle and right respectively use in-plane normal forces N on the photomask edge and out-of-plane normal forces on its bottom surface for the bending moment generation.

mations:

$$u = -\frac{1}{2}t \frac{\partial w}{\partial x} = -\frac{1}{2}t(x + 0.0012)\kappa_x \quad (4.4)$$

$$v = -\frac{1}{2}t \frac{\partial w}{\partial y} = -\frac{1}{2}t\nu y \kappa_x \quad (4.5)$$

$$w = \frac{1}{2}\kappa_x(x^2 - \nu y^2) + 0.0012\kappa_x x - 0.0023\kappa_x. \quad (4.6)$$

The largest in-plane deformation of the reticle due to bending is present at its corners whilst its largest out-of-plane deflection was identified using Figure 3.2. This resulted in maximum deformation values of $\max |u| \approx 98$ [nm], $\max |v| \approx 16.5$ [nm] and $\max |w| \approx 0.2$ [μm] for a curvature of $\kappa_x = 0.4 \times 10^{-3}$ [$1/\text{m}$].

The manipulator must also follow the photomask angular deformation. The largest angular deflections are present at the photomask edges. The values can be estimated with Equations (3.3) and (3.4) of Chapter 3. It results in local angles of $\max |\theta_x| \approx 5$ [μrad] and $\max |\theta_y| \approx 30.5$ [μrad] for a curvature of $\kappa_x = 0.4 \times 10^{-3}$ [$1/\text{m}$].

Photomask position tolerance in chuck

The second contribution to the actuator range is the reticle position tolerance in the chuck. Figure 4.4 provides a schematic drawing of the in-plane and out-of-plane tolerances. Estimates for these tolerances are obtained by assuming an ideal placement of the bending mechanism in the reticle chuck.

The in-plane position error of the reticle with respect to the bending mechanism can be described by:

$$\Delta x_{\text{tol}} = \Delta x_r + \frac{1}{2}\Delta\theta_z L + \frac{1}{2}\Delta L + \frac{1}{2}\Delta S \quad (4.7)$$

where Δx_r and $\Delta\theta_z$ are the reticle rigid body placement errors in the reticle stage, ΔL is the reticle length tolerance and ΔS corresponds to the error caused by the reticle squareness. The first two terms are neglected because of the lack of publicly available information on the loading placement accuracy of the reticle in the chuck. The other two quantities are obtained from the photomask SEMI specification [96], where $\Delta L = 0.7$ [mm] and $\Delta S = 0.3$ [mm]. This gives a position tolerance of $\Delta x_{\text{tol}} = 0.55$ [mm].

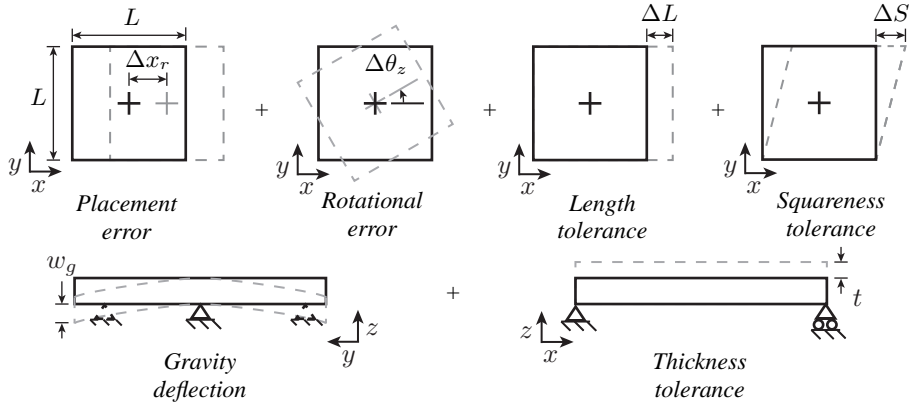


Figure 4.4: The position and dimensional tolerances of the reticle in the stage. The top drawings shows its in-plane tolerances whilst the bottom figures represent its out-of-plane tolerances.

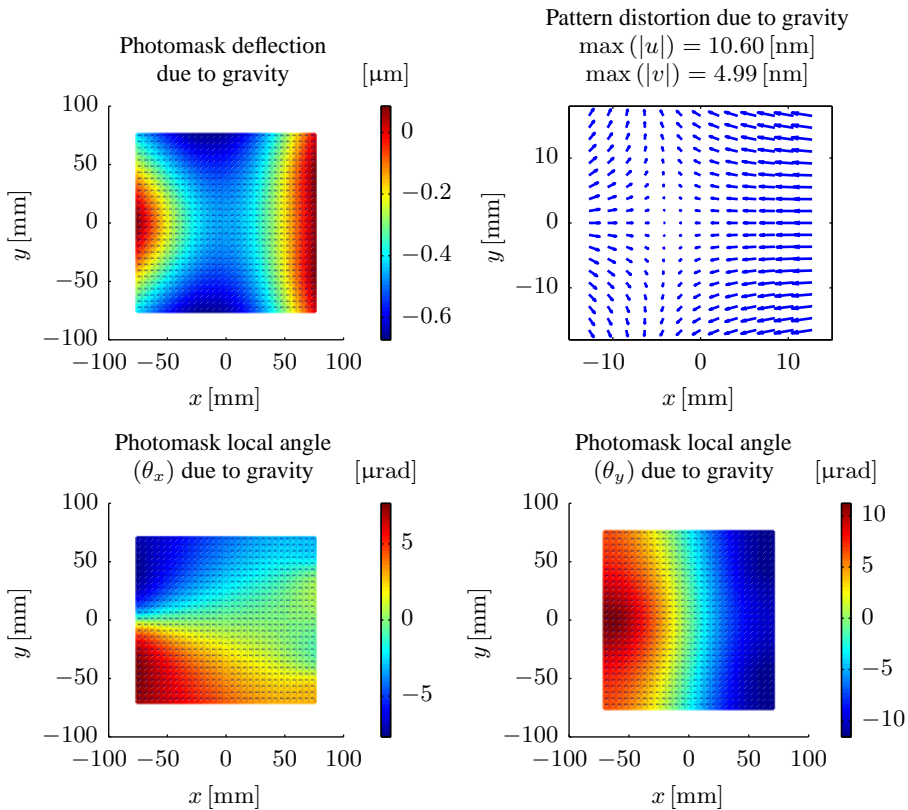


Figure 4.6: The influence of gravity on the photomask deformation in the chuck. The top-left and top-right plots show the out-of-plane photomask deflection and its pattern distortion that is induced by gravity. The bottom-left and bottom-right graphs show the corresponding photomask local angles.

		Bending deformation	Position tolerance	Total	Unit
In-plane	Δx	98.0×10^{-6}	0.55	0.55	[mm]
	Δy	16.5×10^{-6}	0.55	0.55	[mm]
Out-of-plane	Δz	0.2	0.7	0.9	[μm]
Rotational	$\Delta\theta_x$	5.0	7.0	13.0	[μrad]
	$\Delta\theta_y$	30.5	11.0	41.5	[μrad]

Table 4.2: An overview of manipulator range requirements for different directions. The final range depends on the configuration of the bending moment application.

For simplicity it is assumed that the length and squareness tolerances are the same in the x - and y -direction.

The out-of-plane position tolerance of the photomask in the chuck has two contributions. The first is the photomask deflection due to the gravity Δw_g and the second is the reticle thickness tolerance Δt . The out-of-plane position tolerance Δz_{tol} is therefore equal to:

$$\Delta z_{\text{tol}} = \Delta w_g + \Delta t. \quad (4.8)$$

Section 2.5.2.3 introduced the desire to match the gravitational deflection of the photomask in order to minimize Matched Machine Overlay (MMO). An estimate of the gravitational sag of the photomask in the chuck is provided in Figure 4.6 which shows that $|\Delta w_g| \approx 0.7 [\mu\text{m}]$ along its edge. The thickness tolerance of the photomask can be as large as $0.1 [\text{mm}]$. The latter is neglected in the overall tolerance budget for two reasons. First, the introduction of a bending moment at the top side of the reticle like the left most configuration in Figure 4.3 complicates the reticle loading strategy in the chuck. Second, it results in more stringent specifications on allowed out-of-plane stiffness of the bending manipulator. A further explanation of the reasons is provided in Section 4.3.

The rotational tolerances of the photomask around the x - and y -axis are also considered. The main contributor is the photomask's local angle due to the gravity deflection. The manipulator must be compliant enough to adapt to its natural deflection on the z -supports. Any parasitic rotational stiffness will result in bending moments on the photomask and subsequently a different reticle gravity sag. This contributes to the MMO budget. Figure 4.6 provides the values of the photomask local angle due to gravity. These are equal to $\Delta\theta_{x,\text{tol}} = 7 [\mu\text{rad}]$ and $\Delta\theta_{y,\text{tol}} = 11 [\mu\text{rad}]$ along the photomask edge.

Table 4.2 provides a summary of the required manipulation range for different degrees-of-freedom. The values show that the in-plane range is approximately three orders larger than the out-of-plane tolerances of the photomask when the reticle thickness is neglected. The identified ranges and allowable parasitic loads in Section 4.2.1 lead to design specifications for the manipulator parasitic stiffness. These are provided in Section 4.2.3.

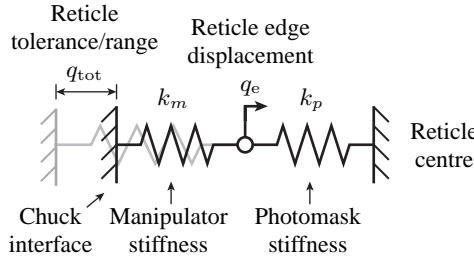


Figure 4.7: The serial stiffness model that was used to estimate the allowable manipulator stiffness for both the in-plane and out-of-plane actuation concepts. The manipulator and reticle stiffness are respectively represented by k_m and k_p whilst q_{tot} and q_e are respectively the reticle tolerance and the reticle edge displacement for $q = x, z, \theta$.

4.2.3 Parasitic stiffnesses

The manipulator stiffness across its stroke must be limited because it induces parasitic forces and moments that act on the photomask. This section provides estimates of the allowable parasitic stiffnesses using input from Section 4.2.1 and 4.2.2.

The parasitic stiffnesses were determined with the generalized lumped stiffness model of the manipulator and photomask as shown in Figure 4.7. It assumes that the position of the chuck and the reticle centre are fixed and that the reticle tolerance q_{tot} must be consumed by the serial stiffness of the photomask k_p and the manipulator k_m . Expressions for the parasitic force or moment F_q on the photomask and the allowed manipulator stiffness k_m are equal to:

$$F_q = \frac{k_m k_p}{k_m + k_p} q_{tot} \quad (4.9)$$

$$k_m = k_p \frac{q_e}{q_{tot} - q_e} \quad (4.10)$$

where q_e is the allowed rotation or displacement of the reticle edge for the degrees-of-freedom $q = x, y, \theta$.

Table 4.3 provides estimates of the allowable parasitic manipulator stiffnesses that were determined with Equation (4.10), the manipulator ranges in Table 4.2 and the photomask stiffness values. The allowed reticle edge displacements in the different directions were derived using the 50 [pm] design rule at wafer level and Equations (4.1) to (4.3). The results in Table 4.3 highlight the following:

- The allowed parasitic stiffness is approximately one order smaller for the configurations in Figure 4.3 when the bending moment is realized with out-of-plane instead of in-plane forces. The difference is smaller than that of the manipulator ranges of Section 4.2.2. The lower value is attributed to the higher in-plane stiffness of the photomask in comparison to its out-of-plane stiffness.
- The in-plane parasitic stiffness specification can be relaxed when the manipulator does not interface with the photomask edge. In that case, only the photomask

Degree of freedom	Displacements			Stiffness			
	Range (q_{tot})	Edge (q_e)	Unit	Photomask (k_p)		Actuator (k_m)	Unit
	Value	Value		Relation	Value	Value	
x^1	5.5×10^5	0.2	[nm]	$2EA/L$	9.2×10^8	335	[N/m]
	98	0.2	[nm]	$8EA/L / \dots$ ($4LI + t^2LA$)	2.3×10^8	4.7×10^5	[N/m]
z	900	3.2	[nm]	$24EI/L^3$	1.6×10^6	5.7×10^3	[N/m]
θ	41.5	0.06	[μ rad]	$2EI/L$	3.1×10^3	4.7	[Nm/rad]

¹ Two values are provided for the in-plane parasitic stiffness. The top value corresponds to a parasitic in-plane force that acts along the neutral line of the photomask. The bottom value corresponds to a parasitic in-plane force that acts at the bottom or top surface of the photomask. In the latter case, the in-plane tolerance of the photomask can be neglected which relaxes the required in-plane manipulator range.

Table 4.3: First order estimates of the allowable parasitic stiffnesses of the manipulator.

deformations need to be considered as manipulation range and the allowable in-plane parasitic stiffness increases by three orders of magnitude.

4.2.4 Added mass

Manipulator mass also introduces parasitic forces on the reticle which can lead to overlay errors. These parasitic forces are present in two directions. The first is gravity which always acts on the reticle in the out-of-plane direction. Added mass changes the reticle gravity sag and therefore results in different pattern distortions. The changed distortion contributes to MMO. The second parasitic force is the in-plane inertia load of the added mass which is exerted onto the reticle during the acceleration phase. This is a potential contributor to the DCO. Specifications for both effects are derived below.

Effect of added manipulator mass on MMO

The effect of added manipulator mass in the out-of-plane direction were determined using the photomask FE model of Section 3.3.2. Figure 4.8 shows a schematic drawing of the simulation that was used to estimate the effect. An added mass of $m = 15$ [g] was simulated by applying a negative pressure $p = 100$ [N/m²] across an area $A = lw = 1500$ [mm²] at the bottom of the photomask. The resulting in-plane pattern distortions are provided in the left plot of Figure 4.8. It shows pattern distortions of approximately 0.4 [nm] at wafer level which consumes approximately 50% of the specified 0.7 [nm] MMO budget in Section 2.5.2.3. The 15 [g] is used as design specification for the amount of added mass to the reticle in the remainder of this thesis.

Effect of added manipulator mass on DCO

The manipulator mass also has a contribution to in-plane parasitic forces. This is explained using Figure 4.9 which provides a simplified representation of the manipulator, photomask and reticle stage in the scan direction y . The manipulator mass m_y is attached to the reticle by a preload force N . The preload force is needed in order to be able to introduce a positive and negative bending moment by the configurations of Figure 4.3. It

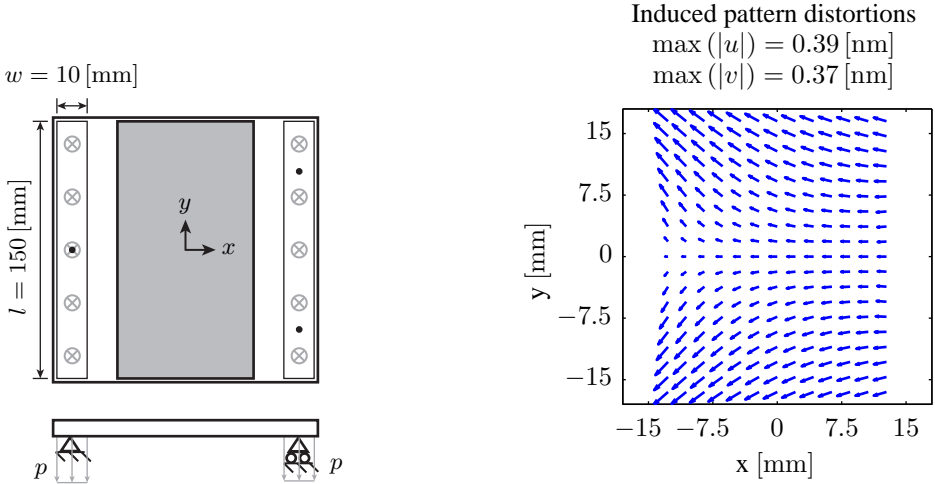


Figure 4.8: Simulations that were performed to identify the induced in-plane pattern distortions by added manipulator mass to the photomask. The left drawing provides a schematic representation how a uniform pressure p was used to simulate a manipulator mass of 15 [g] in the photomask FE model of Figure 3.4. The right plot shows the in-plane pattern distortions.

results in the presence of a friction force W which acts between the reticle and the interface mass in the x - and y -direction. The manipulator mass is also attached to the reticle stage by the manipulator stiffness k_m . It is assumed that the photomask is accelerated by the normal force configuration in Section 2.4.2 which ensures that the reticle follows the reticle stage motion.

The cyclical nature of the exposure sequence induces a repetitive inertia force F on the manipulator mass in y -direction. A relative position change between the manipulator mass and the reticle occurs when the inertia load F_y exceeds the available friction force W [62]. A graph of the interface position versus the inertia load is provided in Figure 4.9. It contains a position uncertainty s_v between the manipulator interface and reticle when the inertia load is zero. This corresponds to the situation of constant stage scan velocity during the exposure process. The position uncertainty of the manipulator mass multiplied by the manipulator stiffness results in a parasitic force that acts on the photomask.

The above illustrates that it is desired to keep the inertia load on the manipulator mass at the photomask interface below the available friction force. The manipulator mass that can be attached to the photomask before the occurrence of slip is equal to:

$$m_y = \frac{W}{\ddot{y}} = \frac{\mu p A}{\ddot{y}} = 39.4 \text{ [g]} \quad (4.11)$$

for a friction coefficient of $\mu = 0.1$ [-], clamping pressure of $p = 0.75 \times 10^5$ [N/m²], reticle stage acceleration of $\ddot{y} = 200$ [m/s²] and clamping area of 7 [mm] by 150 [mm]. Note that the derived value provides an estimate for the case when a single manipulator is used to apply the bending moment and when the photomask and the manipulator behave

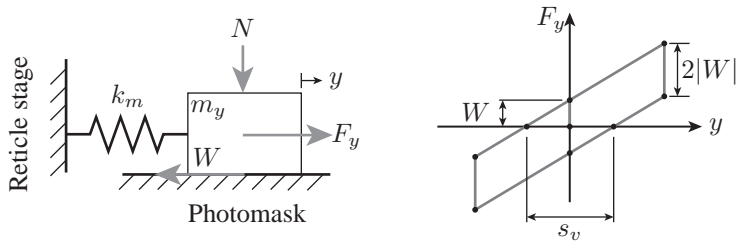


Figure 4.9: A simplified representation of the frictional interface between the manipulator mass m_y and the photomask in scan direction. It also shows the hysteretic behaviour in the interface for a cyclical inertial force F that is larger than the available friction force W [62].

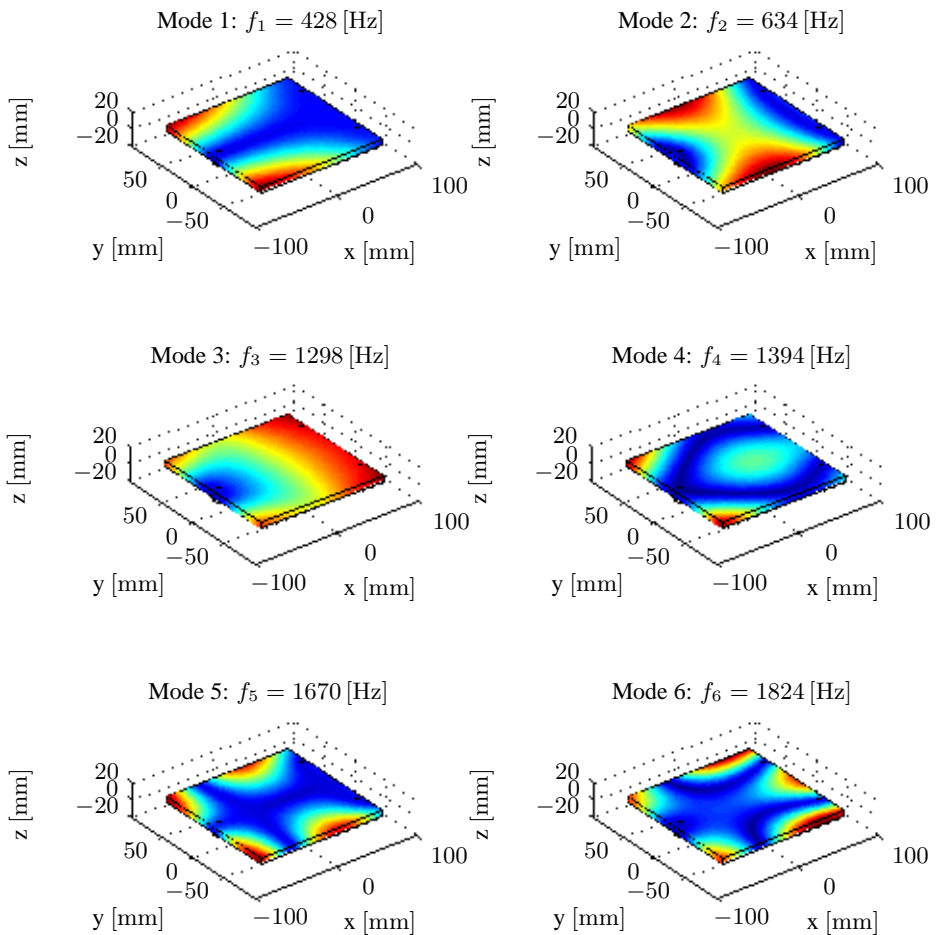


Figure 4.10: The first six eigenmodes of a kinematically supported reticle on three z -supports.

like a rigid body. The value must be divided by the number of interface locations n when more than one interface is used, i.e. $m_y = 39.4/n$.

4.2.5 Mechanical resonance frequencies

Section 2.5.1.4 mentioned that stage vibrations contribute to fading. Specifications for mechanical resonance frequencies were also defined in that section. The first in-plane mechanical resonance frequency of the manipulator should be above 2 [kHz] whilst the out-of-plane mechanical resonances of the photomask and manipulator assembly must correspond to the resonances of a kinematically mounted reticle.

Figure 4.10 shows the first six modes of a kinematically mounted reticle on three z-supports. The first out-of-plane eigenfrequency is approximately 430 [Hz]. This value is used as a first design specification for the first out-of-plane mechanical resonance of the photomask with manipulator. A more detailed analysis of the impact of the manipulator on the reticle eigenfrequencies is provided in Section 5.3.1.

4.2.6 Volume claim

The manipulator must be designed within the available chuck volume. The manipulator volume claim that was specified in Section 2.4.2 had a length $l = 160$ [mm], width $w = 35$ [mm] and height $h = 11$ [mm].

4.2.7 Power dissipation

Power dissipation of the manipulator near the reticle leads to a thermal expansion of the photomask and subsequently an overlay error when left uncorrected. The allowable power dissipation by the manipulator must therefore be specified.

The value was derived using the simplified thermal model of Figure 4.11. It shows an incoming manipulator heat load \dot{Q}_i at the reticle edge and an outgoing heat load \dot{Q}_o across the reticle surface. The latter is driven by convection to the surrounding air of temperature $T_a = 295$ [K]. The convection is generated by the scanning motion of the stage which is considered to be constant along the reticle's x -direction. The thermal model is limited to the x -direction because of the uniform bending moment application in y -direction. Only half of the reticle is considered because of symmetry. Finally, radiation was neglected because the transfer mechanism is inferior to the convective heat loss.

The temperature profile in the photomask is derived by considering the energy conservation principle on the piece of photomask that is shown in the right drawing of Figure 4.11. Heat enters the element at x by conduction and leaves the element at $x + \Delta x$ by conduction and convection. This is mathematically equal to:

$$qA_r|_x - qA_r|_{x+\Delta x} - 2h_cL\Delta x(T - T_a) = \rho Vc \frac{dT}{dt} \quad (4.12)$$

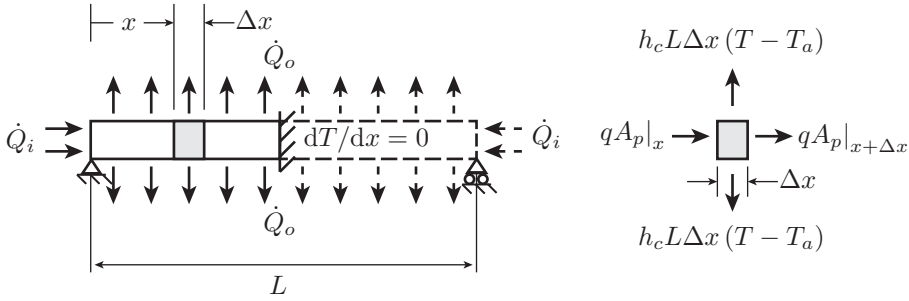


Figure 4.11: Simplified thermo-mechanical model of a photomask. The left figure shows the photomask with the ingoing actuator heat load \dot{Q}_i and convective heat loss \dot{Q}_o . The right figure shows the energy balance on an element of the photomask.

where ρ , V , T are respectively the photomask material density in $[\text{kg}/\text{m}^3]$, volume in $[\text{m}^3]$ and temperature in $[\text{K}]$, c is the specific heat in $[\text{J}/(\text{m}^3\text{K})]$, q is the heat flux in $[\text{W}/\text{m}^2]$, A_r is the photomask cross-section perpendicular to the heat flow direction in $[\text{m}^2]$, L is the photomask length in $[\text{m}]$, and h_c is the convective heat transfer coefficient in $[\text{W}/\text{m}^2\text{K}]$. Using Fourier's conductivity law $q = -k dT/dx$ and the assumption of steady state conditions allows the simplification of Equation (4.12) into:

$$kA_r \frac{d^2T}{dx^2} - 2h_c L (T - T_a) = 0. \quad (4.13)$$

where k is the material's conductivity coefficient [73].

An expression for the temperature profile along the reticle is obtained by solving Equation (4.13) for the reticle's boundary conditions at its edge and centre. These are:

$$\left. \frac{dT}{dx} \right|_{x=0} = -\frac{\dot{Q}_i}{kA_r}, \quad \left. \frac{dT}{dx} \right|_{x=\frac{1}{2}L} = 0. \quad (4.14)$$

The former boundary condition is obtained by using the relation between the heat flow and the heat flux $\dot{Q} = qA$ in addition to Fourier's conductivity law. The latter holds because of model symmetry. Solving the differential equation (4.14) for the boundary conditions results in the following relation for the photomask temperature profile [16]:

$$T - T_a = \frac{\dot{Q}_i}{A_r \beta k} \frac{\cosh \beta (\frac{1}{2}L - x)}{\sinh \frac{1}{2}\beta L}, \quad \text{with } \beta^2 = \frac{2h_c L}{kA_r}. \quad (4.15)$$

The convection coefficient needs to be determined in order to evaluate the reticle's temperature profile. The convection can be modelled as a forced flow across an isothermal surface during the stage scanning motion. Its value depends on the type of flow regime.

The Reynolds number of the flow was therefore determined. It is equal to [73]:

$$\text{Re}_y = \frac{\rho v y}{\mu} \implies \text{Re}_L \approx 3.6 \times 10^4 < 5 \times 10^4 [-] \quad (4.16)$$

for an air density of $\rho = 1.288 \text{ [kg/m}^3\text{]}$, stage scan speed of $v = 0.8 \text{ [m/s]}$, reticle length of $y = L = 152.4 \text{ [mm]}$ and dynamic viscosity of air $\mu = 1.736 \times 10^{-5} \text{ [kg/(ms)]}$. The flow is laminar because it stays below the threshold value of $\text{Re}_y \approx 5 \times 10^4$.

The average convection coefficient \bar{h}_c was determined from the local convection coefficient h_c using:

$$\bar{h}_c = \frac{1}{L} \int_0^L h_c dy = 0.664 \frac{k}{L} \text{Re}_L^{\frac{1}{2}} \text{Pr}^{\frac{1}{3}} \approx 18.5 \text{ [W/(m}^2\text{K)]}. \quad (4.17)$$

In Equation (4.17), the reticle length is equal to $L = 152.4 \text{ [mm]}$ whilst the Prandtl number and conductivity of air are equal to $\text{Pr} = 0.69 [-]$ and $k = 0.0252 \text{ [W/(mK)]}$. Equation (4.17) used an expression for the local convection coefficient h_c in a laminar forced flow across an isothermal surface. The expression was obtained from the empirical relation of its local Nusselt number $\text{Nu}_{y,\text{lam}}$ [73]:

$$\text{Nu}_{y,\text{lam}} = \frac{h_c y}{k} \approx 0.332 \text{Re}_y^{\frac{1}{2}} \text{Pr}^{\frac{1}{3}} \quad (4.18)$$

where y is the characteristic length.

The thermal expansion of the photomask can be obtained from the derived reticle temperature profile and convection coefficient. The one-dimensional thermal expansion for the piece of photomask material between x and $x + \Delta x$ in Figure 4.11 is equal to [43]:

$$\Delta u = \alpha \Delta T \Delta x \quad (4.19)$$

where Δu is the elongation of the element with respect to its initial state, α is the coefficient of thermal expansion and ΔT is the temperature difference between the steady state temperature and the initial temperature. The expression for the photomask thermal expansion is therefore equal to:

$$u = \int \alpha (T - T_a) dx = -\frac{\alpha \dot{Q}_i}{2\bar{h}_c L} \frac{\sinh \beta \left(\frac{1}{2}L - x\right)}{\sinh \frac{1}{2}\beta L} \quad (4.20)$$

when it is assumed that the centre of the photomask is fixed.

An expression for the allowed thermal load \dot{Q}_i by the manipulator is obtained by solving Equation (4.20) for $x = 0$. This gives an allowed thermal load of:

$$\dot{Q}_i = -\frac{2\bar{h}_c L}{\alpha} u \approx 4 \text{ [mW]}. \quad (4.21)$$

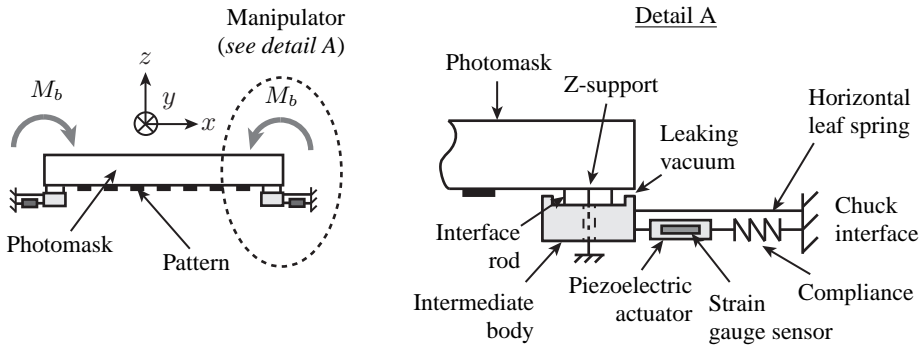


Figure 4.12: A simplified two dimensional representation of the photomask curvature manipulator concept. The left drawing shows the photomask with the two bending manipulators on either side. The right drawing provides a more detailed view of the manipulation mechanism.

The dissipation value of Equation (4.21) was obtained for a reticle thermal expansion coefficient of $\alpha = 0.51 \times 10^{-6}$ [1/K] and $u = 4 \cdot 0.09$ [nm], where 0.09 [nm] corresponds to the overlay penalty by the manipulator thermal load in Table 2.3.

4.3 Conceptual design

A conceptual manipulator design was distilled from the design specifications of Section 4.2. This section introduces the preferred manipulator concept and clarifies the design choices that were made after considering the specifications.

Figure 4.12 shows a two-dimensional representation of the chosen manipulator concept. It consists of a piezoelectrically driven mechanism which interfaces with the bottom surface of the photomask. The interface is realized by an intermediate body with two vertical interface rods that are preloaded to the photomask by a leaky vacuum cup. The interface rods are included to mechanically decouple the intermediate body from the photomask in horizontal x -, y -, R_z -directions. They provide a stiff coupling between the reticle and manipulator in the vertical z - and rotational θ_y -directions however. The latter allows the transfer of a bending moment from the intermediate body to the reticle.

A local force loop is created between the chuck and intermediate body by the piezoelectric actuator, serial compliance and horizontal leaf spring. An expansion of the piezoelectric actuator propagates into the serial compliance. This generates an active force in the path of the piezoelectric actuator and a reactive force through the parallel placed horizontal leaf spring. The active and reactive force in combination with the pitch between the piezoelectric actuator and horizontal leaf spring results in a bending moment on the intermediate body. This moment is transferred to the photomask via the interface rods.

The piezoelectric actuator is equipped with a strain gauge which measures the piezoelectric actuator elongation. The latter information is used to close a local feedback loop across the actuator and strain gauge sensor. It enables an indirect control of the photomask curvature and counteracts actuation non-linearities such as hysteresis and creep. The following sections provide a more detailed explanation on the preferred manipula-

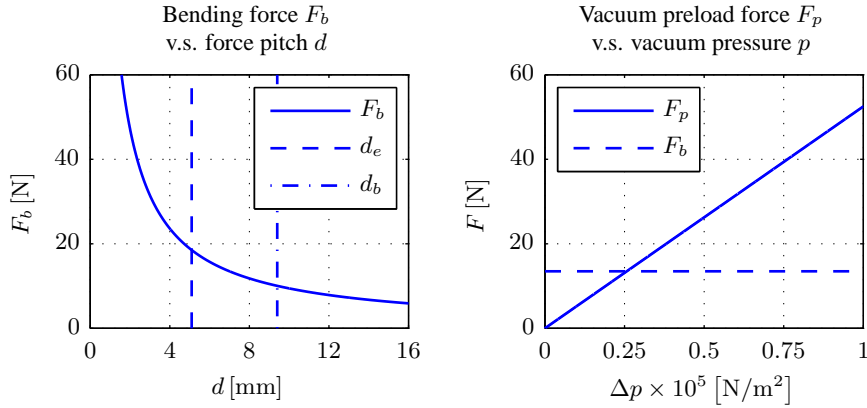


Figure 4.13: The required bending force F_b and vacuum preload F_p at the photomask-manipulator interface for a curvature of $\kappa = 0.4 \times 10^{-3}$ [1/m]. The left graph shows the actuation force as a function of the force pitch d_e and d_b for the concepts in Figure 4.3. The right graph shows the preload force for a vacuum pressure and area of Δp and $A = 1050$ [mm²] for the concept in Figure 4.14. The dotted line corresponds to the bending force requirement for $d_b = 7$ [mm].

tion concept. Section 4.3.1 clarifies the mechanism design choices. An explanation of the chosen metrology and control architecture are thereafter explained in Sections 4.3.2 and 4.3.3.

4.3.1 Actuation mechanism

The manipulator design in Figure 4.12 uses an actuation mechanism for the application of a bending moment to the reticle. This section provides the justification for the chosen actuation mechanism. Section 4.3.1.1 motivates the manipulator interface to the reticle. The mechanism and actuator design choices are explained in Sections 4.3.1.2 and 4.3.1.3.

4.3.1.1 Photomask-manipulator interface

The design of the interface between the photomask and the manipulator consisted of two parts. The first consideration that was made was the location of bending moment introduction into the reticle. The second involved the design of the interface between the manipulator and the photomask. Both are explained below.

Figure 4.3 provided three configurations for the introduction of a bending moment into the reticle. They employ a pair of in-plane or out-of-plane friction forces W or normal forces N to generate the moment. The right configuration was chosen for the following reasons:

- The achievable bending moments for the normal force N and friction force W configuration are respectively equal to $M = dN$ and $M = dW = d\mu N$ when

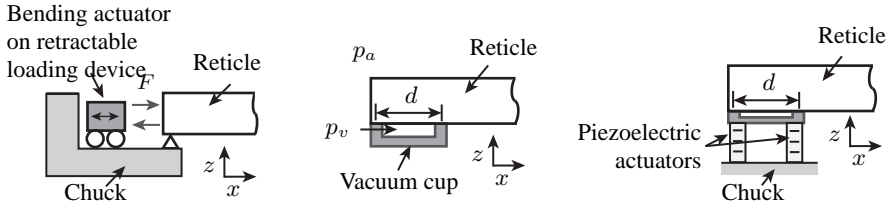


Figure 4.14: Considered concepts during the manipulator design. The left drawing shows a way to reduce the impact of the reticle size tolerances on the design specifications by mounting the manipulator on a miniature positioning system. The middle drawing shows an interface that is preloaded onto the reticle using vacuum. The right drawing shows an example of a direct drive concept where two piezoelectric actuators are used to deform the reticle.

the friction coefficient is $\mu < 1$. Normal forces are preferred over friction forces because larger bending moments can be achieved for the same pitch d .

- The pitch d_e for in-plane actuation is limited to 5.1 [mm] by the reticle thickness and its chamfered edge whilst the pitch d_b at the bottom surface is limited to 9.4 [mm] because of the available clamping area [96]. The required normal forces for the generation of the bending moment are therefore a factor 2 lower than the out-of-plane actuation case as is shown by the left graph of Figure 4.13.
- Section 4.2 showed that the use of out-of-plane forces at the photomask bottom surface relaxes the manipulator requirements in terms of required stroke and allowable parasitic stiffness. The impact of the reticle dimensional tolerances on these specifications can be reduced by the approach mechanism in the left drawing of Figure 4.14. This is not considered because of the added complexity.

Introducing the bending moments by vertical normal forces does imply that the out-of-plane parasitic forces must stay below 5 [mN]. This is approximately a factor 2700 lower than the required bending forces for an actuation pitch of $d = 7$ [mm].

The introduction of the bending moment requires the application of push-pull forces on the reticle. Pulling forces can only be applied through an interface that is fixed or preloaded onto the reticle. A vacuum preloaded interface with mechanical contact as depicted by the middle drawing in Figure 4.14 was selected as preferred concept for the following reasons:

- The achievable preload force F_p with the interface is approximately three times larger than the required bending force F_b . This is highlighted by the right graph in Figure 4.13 which shows the vacuum preload force $F_p = A\Delta p/2$ at the clamp edge as a function of the vacuum pressure Δp for a clamping area of 150×7 [mm]. Mechanical contact will not be lost because achievable vacuum pressures in lithography systems are around -0.75 [barg].
- Reticle in-plane and out-of-plane size tolerances do not have to be accounted for when the contact area is limited to the photomask bottom surface. It also minimizes the impact on the reticle exchange procedure in the lithography machine.

Actuator	Property						Ref.
	Force [N]	Stroke [μm]	Mass ¹ [g]	Dissipation [mW]	Dimensions [mm]	Stiffness [N/m]	
Lorentz	10	1000	25	21×10^3	$21 \times 21 \times 7$	800	[127]
Reluctance	10	1000	25	900	$47 \times 4 \times 4$	-1.5×10^4	[127]
Piezoelectric ²	210 (0)	0 (18)	< 4	< 1	$18 \times 3 \times 2$	1.2×10^7	[88]
Specification	10	0.9	15	4	$160 \times 35 \times 11$	6×10^3	Tab. 4.1

¹ The mass corresponds to the actuator moving mass instead of its total mass.

² The achievable force and stroke of a piezoelectric actuator relate to an applied voltage of 120 [V] and depend on the stiffness that surrounds the piezoelectric actuator. Furthermore, its dissipation depends on the excitation frequency [88].

Table 4.4: A comparison of identified actuator properties from literature and the manipulator specifications of Table 4.1 for a direct drive manipulator concept.

4.3.1.2 Moment generation mechanism

The desired reticle curvature is obtained by the application of a bending moment to the manipulator-photomask interface. The bending moment can be generated by a direct drive configuration or a mechanism. A patent has been applied for both configurations [114]. The former are normally preferred in precision engineering applications because they translate the actuator power into a desired motion without any reduction. This increases the drive stiffness and avoids possible backlash.

The feasibility of a direct drive concept was investigated by considering widely used actuator types in the field of precision engineering. Their characteristics were identified from literature and compared to the manipulator specifications of Section 4.2. The results of the comparison is provided in Table 4.4. A direct drive configuration was considered infeasible for the following reasons:

- The power dissipation of Lorentz and reluctance actuators are respectively four and two orders of magnitude larger than the 4 [mW] specification of Section 4.2.7.
- The piezoelectric actuator stiffness in the direct-drive concept of Figure 4.14 exceeds the manipulator stiffness specification by five orders of magnitude.

The non-feasibility of a direct drive concept made it necessary to generate the bending moment by a mechanism that is vacuum preloaded interface to the reticle. The following considerations were made for the mechanism design:

- The mechanism requires a stiff connection to the chuck in x -, y - and θ_z -direction. This minimizes the inertial load of the mechanism on the reticle during acceleration. It also facilitates an in-plane mechanical resonance of the mechanism above the 2 [kHz] specification of Table 4.1.
- The vacuum preloaded interface must be rigidly coupled to the photomask in the θ_y degree-of-freedom in order to be able to transfer the bending moment.

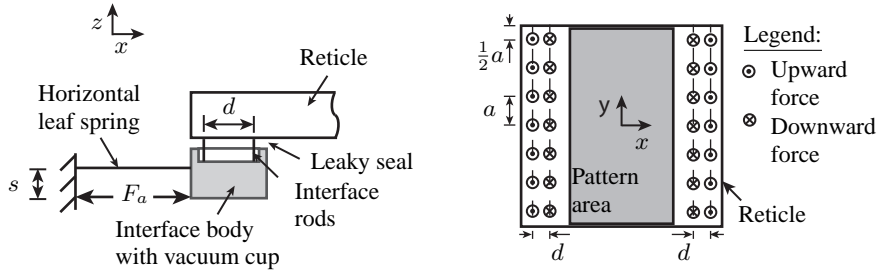


Figure 4.15: The identified moment generation mechanism. The left drawing shows a side view of the mechanism which translates the actuator force F_a into a bending moment on the reticle. The right drawing shows a top view of the photomask with the discrete push-pull force locations of the interface rods which are placed at a pitch a .

- The interface must be decoupled from the chuck in z -, θ_x - and θ_y -direction to allow the natural deflection of the reticle by gravity. The interface must be rigidly coupled to the reticle in those degrees-of-freedom in order to follow the reticle deformation and satisfy the mechanical resonance specifications in Table 4.1.

The left drawing in Figure 4.15 provides the preferred mechanism that was identified using [62]. The horizontal leaf spring between the intermediate body and chuck ensures a rigid in-plane coupling of the interface to the chuck. The interface rods and leaky vacuum cup were included for the following two reasons:

- It has a lower amount of in-plane added mass and therefore inertial load on the reticle than the clamping concept in the right drawing of Figure 4.14.
- It provides a rigid out-of-plane and compliant in-plane coupling between the intermediate body and the reticle. It also facilitates the tuning of the stiffnesses to the specifications of Table 4.4.

The mechanism of Figure 4.15 is able to generate a bending moment on the reticle by the application of an in-plane actuator force F_a between the intermediate body and the chuck. The applied actuator force results in an opposing reaction force through the horizontal leaf spring at a distance s . This generates a bending moment on the intermediate body which is transferred to the reticle by the discrete interface rods. The selected mechanism makes optimal use of the available design volume.

The presence of interface rods in the manipulator concept implies that the bending moment is introduced by discrete push-pull force pairs along the reticle edge. This is schematically shown in the right picture of Figure 4.15. The concept assumes that all force pairs contribute evenly to the overall bending moment which means that each pair has to apply $M_b = 13.5$ [Nmm]. It also assumes that one mechanism is used to generate each force pair.

The bending moment introduction of Figure 4.15 differs from the continuous bending moment application that was analysed in Chapter 3. Its pattern distortion levels were therefore analysed for varying number of interface rods. The results are provided in

Appendix C. Seven pairs of interface rods were finally chosen because it satisfies the 50 [pm] pattern distortion design rule of Section 2.5.2 after lens correction.

The deterministic bending behaviour of the curvature manipulator depends on the presence of slip in the mechanical contact between the reticle and the interface rods. The available friction force W per interface rod was estimated at:

$$W = \mu (F_p - F_b) / 7 \approx 0.37 \text{ [N]} \quad (4.22)$$

where $\mu = 0.1$ is the assumed friction coefficient whilst F_b and F_p correspond to the identified bending force and preload force in Figure 4.13 for a vacuum pressure of $p_v = -0.75$ [barg]. The friction force is a factor two larger than the allowed parasitic force $F_x = 0.18$ [N] in Table 4.1. No slip is therefore expected if the interface rods account for the photomask deformation by bending.

4.3.1.3 Actuator selection

The final manipulation concept in Figure 4.12 includes a piezoelectric actuator with serial compliance for the generation of the actuator force F_a . A piezoelectric actuator is favoured over a Lorentz or Reluctance actuator because of its power dissipation¹, volume and mass satisfy the high level manipulator specifications as is clear from Table 4.4.

The achievable force levels and stroke of the piezoelectric actuator depends on the stiffness of its surroundings [89]. Piezoelectric actuators are able to generate a maximum force when its ends are fully constrained. Inversely, they can realize a maximum displacement but no force when one end is left unconstrained. These two extreme operating conditions were also provided in Table 4.4. It highlights that force generation is linked to a reduction in achievable displacement and that both a displacement and force can be achieved by the addition of the serial compliance.

Investigations were performed on the achievable force levels and elongations for a piezoelectric actuator as a function of serial compliance. The results are provided in Figure 4.16. The preferred configuration employs a P-882.50 piezoelectric actuator by Physik Instrumente with the specifications of Table 4.4 and a serial compliance with stiffness $k_s = 2 \times 10^6$ [N/m]. They are placed at a distance $s = 2.15$ [mm] from the horizontal leaf spring which implies that each actuator must generate a force of $F_a = 6.3$ [N]. The piezoelectric actuator is operated at a 60 [V] offset in its 0 – 120 [V] range in order to apply both a positive and negative bending moment. The configuration has the following characteristics:

- It provides a force of $F_a = 15.42$ [N] and elongation of $\Delta L_p = 7.71$ [μm] for an applied voltage of $U = 60$ [V]. The required 6.3 [N] actuator force for bending is therefore satisfied by a factor of 2.4.
- Each mechanism has a rotational stiffness around the y -axis of $k_\theta = 7.92$ [Nm/rad] and subsequently a total stiffness of $k_\theta = 55.4$ [Nm/rad] for seven actuators along

¹The piezoelectric actuator can be approximated by an ideal capacitance. In that case, it has no power dissipation.

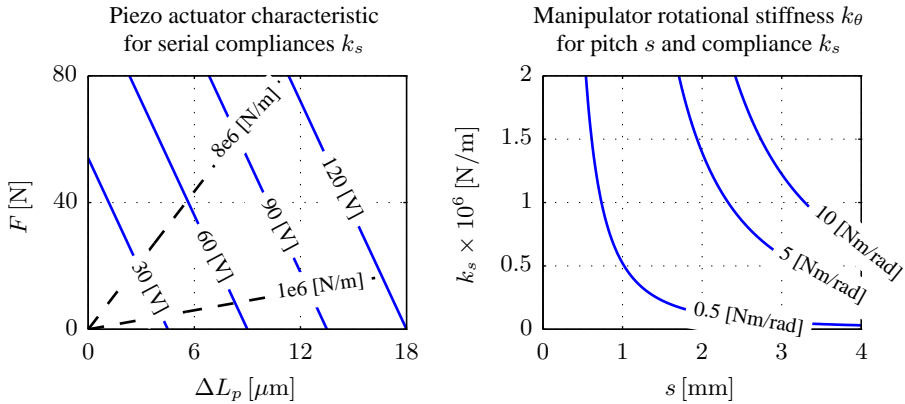


Figure 4.16: The identified characteristic for the P-882.50 piezoelectric actuator with serial compliance. The left graph shows the achievable force F and elongation ΔL_p as a function of serial compliance k_s and applied voltage. The right graph shows the rotational stiffness k_θ for the single bending mechanism in Figure 4.15 as a function of the serial compliance k_s and pitch s .

the reticle's edge. This exceeds the design specification in Table 4.1 by one order of magnitude. The stiffness cannot be reduced by a smaller pitch s or serial stiffness k_s because of design constraints and achievable actuator force. Section 5.3.5 will show that the added manipulator stiffness is still within the MMO specifications and can therefore be allowed.

It is widely known that piezoelectric actuators have hysteresis and drift when operated in open loop. The hysteresis can be as large as 15% of the full stroke when voltage amplifiers are used or 1% for charge amplifiers [40, 89]. This corresponds to a curvature error of 0.15×10^{-3} [1/m] for the preferred actuator configuration when it is assumed that it can achieve a maximum curvature of 1×10^{-3} [1/m] for an elongation of $\Delta L_p = 7.71$ [μm] using voltage amplification. The value exceeds the 2.4×10^{-6} [1/m] curvature error specification of Section 3.3.1 by a factor of 62. The allowable curvature error is exceeded by a factor 4 when charge amplifiers are considered.

The estimate of the curvature error by hysteresis demonstrates that the non-linearity must be counteracted by feedback control. This is covered in Sections 4.3.2 and 4.3.3 when the conceptual choices for metrology and control are presented.

4.3.2 Metrology

The curvature tracking performance of the manipulator is influenced by system disturbances and physical behaviour of the manipulator. This is specifically the case for piezoelectric actuator hysteresis that was introduced in Section 4.3.1.3. The curvature tracking performance of the manipulator can be improved by implementing feedback control so that the system non-linearities and disturbances can be counteracted. The following measurement information is desired in that case:

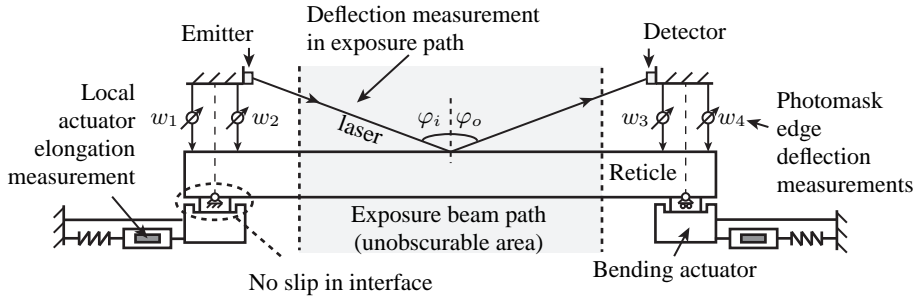


Figure 4.17: Possible metrology configurations for the reticle bending configuration. The actuator elongation measurement can be used to counteract the piezoelectric actuator non-linearities or as an estimate of the reticle curvature when there is no slip in the photomask-manipulator interface. The photomask out-of-plane deflection measurements can be used to determine the reticle curvature.

- *Piezoelectric actuator elongation* ΔL_p - This information is desired so that feedback loops can be closed across each piezoelectric actuator. The feedback loop is used to counteract the actuator non-linearities such as hysteresis and drift.
- *Photomask curvature* κ_x - The manipulator's objective is to track a curvature setpoint. The implementation of a curvature feedback loop is therefore favourable. The photomask curvature can directly be derived from measured photomask deflection or potentially be estimated from measured actuator elongation.

Figure 4.17 provides a schematic drawing of possible metrology configurations to derive the above information. A patent has been filed for several curvature sensing configurations [129]. For the final curvature manipulator design it was chosen to measure only the local piezoelectric actuator elongations and not to measure the photomask curvature for the following reasons:

- Off-the-shelf curvature sensors are unavailable. Derivation of the photomask curvature from the reticle's out-of-plane deflection using optical or capacitive sensors were not pursued because of volume constraints and sensor resolution limitations.
- The development of a custom-made curvature sensor was not pursued in this thesis because it is part of another work package in [103].
- Section 4.3.3 will show that a quasi-static relation exists between the piezoelectric actuator elongation and the reticle curvature for setpoint frequencies up to 100 [Hz]. This is because the reticle eigenfrequencies are above 428 [Hz]. Note that this only holds when there is no slip in the photomask-manipulator interface and when the manipulator eigenfrequencies are above the reticle eigenfrequencies.
- The piezoelectric actuator non-linearities are considered as the main limitation to the curvature setting accuracy. These non-linearities can be counteracted by controlling the actuator elongation with a feedback control [29].

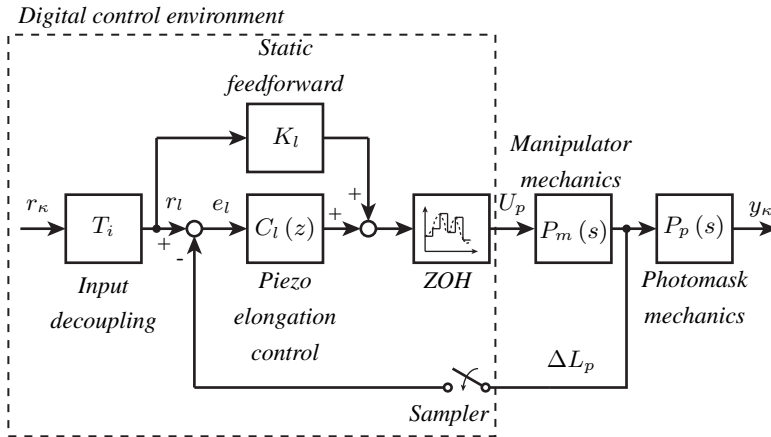


Figure 4.18: The proposed control architecture for the curvature manipulator concept. The input decoupling vector translates the curvature setpoint to the piezoelectric actuator elongation set-points. Local SISO feedback controllers are implemented across each collocated piezoelectric actuator and strain gauge sensor. A static feedforward path is included to boost tracking behaviour.

Strain gauge sensors on the piezoelectric actuators as schematically shown in Figure 4.17 were chosen as the preferred metrology system for the piezoelectric actuator elongation measurement. These sensors were chosen because of their negligible mass and size. The sensors are also able to measure both the static and dynamic elongations of the piezoelectric actuators.

The measurement performance (noise, resolution, etc.) of the strain gauge sensor depends on the electrical architecture of the strain gauge readout configuration. Section 4.4.3 provides details of the electrical design. It also shows that the power dissipation of the strain gauge sensors is fifty times larger than the 4 [mW] specification of Section 4.2.7. A detailed thermal analysis in Section 5.5.3 shows that the effect of the strain gauge power dissipation is still within limits because it is not located directly at the reticle's edge.

4.3.3 Control

Figure 4.18 shows the selected control architecture for the curvature manipulator. The choice was made after considering the metrology concept of Section 4.3.2. The strategy has an input decoupling vector T_i that scales the curvature setpoint to the piezoelectric actuator elongation setpoints r_l . Feedback control C_l is implemented across the piezoelectric actuators and strain gauge sensors to counteract the piezoelectric actuator non-linearities and disturbances. The strategy also has a feedforward path with static gain K_l in order to boost the tracking behaviour of the system.

The complexity of the feedback control architecture in Figure 4.18 depends on the amount of cross-coupling between the piezoelectric actuators and strain gauge sensors. The cross-coupling defines the necessity of MIMO feedback control across all actuators and sensors or local SISO feedback loops across each collocated actuator and sensor pair.

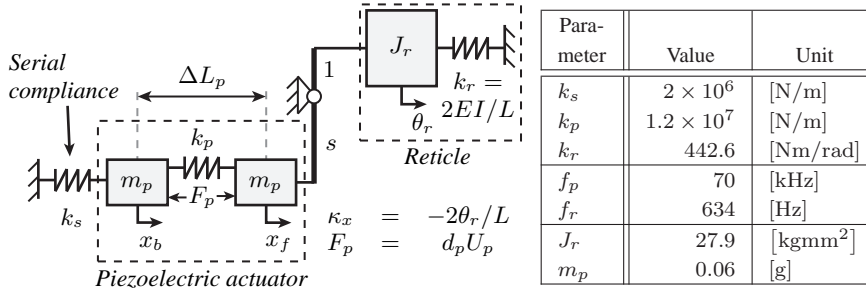


Table 4.5: The lumped mass-stiffness model of the manipulator concept in Figure 4.12 and 4.15. The piezoelectric actuator mass m_p and reticle inertia J_r were derived from the known eigenfrequencies (f_p, f_r) and stiffnesses (k_p, k_r) of respectively the actuator and reticle.

The ratio of piezoelectric actuator elongations between a single active actuator and thirteen idle actuators provides an estimate of the manipulator cross-coupling. The manipulator concept in Section 4.3.1.3 is able to generate a bending moment of $M_b = 33.2$ [Nmm] for a piezoelectric actuator elongation of $\Delta L_p = 7.7$ [μm]. Each idle manipulator counteracts a bending moment of $M_c = M_b/13$. The total elongation ΔL_c of the serial stiffness and piezoelectric actuator of an idle actuator is equal to:

$$\Delta L_c = M_c s / k_\theta = 0.7 \text{ } [\mu\text{m}] \quad (4.23)$$

where $k_\theta = 7.92$ [Nm/rad] corresponds to the manipulator rotational stiffness. The idle piezoelectric actuators elongate one-seventh of that length because the serial stiffness k_s is a factor six smaller than the piezoelectric actuators stiffness k_p . The elongation ratio of the active and idle actuators is therefore equal to $\Delta L_p / (7\Delta L_c) = 78$. The frequency response between the non-located actuators and sensors are expected to be 37 dB lower than that of collocated pairs for frequencies below 100 [Hz]. It indicates that local SISO feedback loops across each collocated actuators and sensors are possible.

A lumped mass-stiffness model of a single manipulator and reticle was generated in order to estimate the system dynamics and control performance of the local SISO feedback loop across the piezoelectric actuator. The model is provided in Figure 4.5. It assumes a rigid connection, i.e. no slip, between the manipulator and reticle. The piezoelectric actuator mass was determined from its eigenfrequency and stiffness [88]. The reticle inertia was identified in the same manner using one-seventh of the reticle bending stiffness and the reticle eigenfrequencies in Figure 4.10. The second reticle eigenfrequency was used for the derivation because it corresponds to the first mode shape with a rotation of the reticle edge around the y -axis. A modal damping of 0.3% was added to the model. Figure 4.19 shows the open-loop frequency responses of the manipulator from an applied actuator voltage U_p to the actuator elongation ΔL_p and reticle curvature κ_x . The results were generated for a sample frequency of 4 [kHz] and provide the following insights:

- There is a static relation between the actuator elongation and the reticle curvature until approximately 250 [Hz]. This is attributed to the constant gain of both frequency responses in Figure 4.19 up to that frequency.

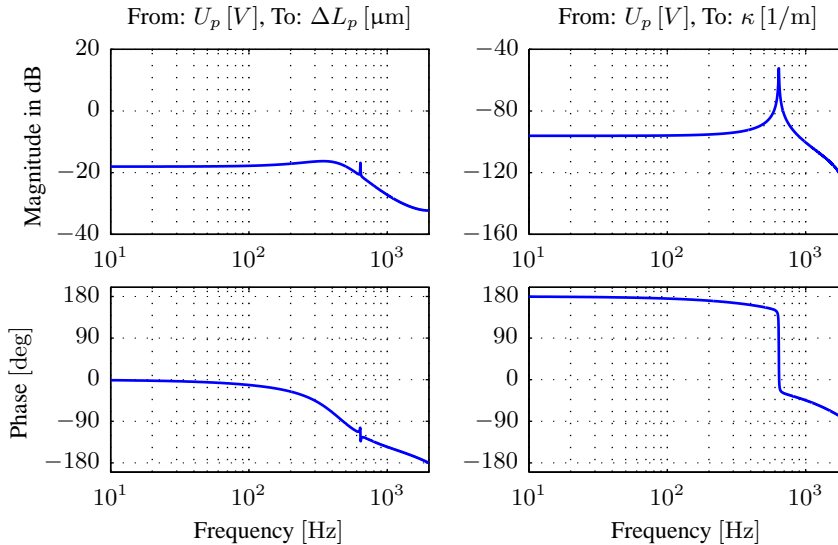


Figure 4.19: Estimated frequency responses of the manipulator model in Figure 4.5. The left and right Bode plots respectively show the frequency responses between an applied voltage U_p across the piezoelectric actuator and the piezoelectric actuator elongation ΔL_p and reticle curvature κ_x .

- The piezoelectric actuator resonance is not visible in the FRF between the applied voltage and the piezoelectric actuator elongation because it is two orders higher than the sample frequency.
- The piezoelectric actuator elongation signal is dominated by the actuator stiffness. Reticle dynamics are largely unobservable because the actuator has a six times larger stiffness than the serial compliance. The parasitic reticle motions will therefore propagate into the serial compliance instead of the piezoelectric actuator.

The achievable bandwidth and disturbance suppression of the control strategy in Figure 4.18 was also estimated using the model of Figure 4.5. A PI^2D -controller was used to close the loop between the piezoelectric actuator elongation error e_l and the actuator command voltage U_p . The 0-dB crossing of the loop gain $L(j\omega)$ and subsequently bandwidth of the controlled system was equal to 210 [Hz]. The Nyquist plot of the loop gain is provided in the left graph of Figure 4.20. It falls outside the 6 dB robustness circle that is normally used to ensure controller stability for plant variations by a mass production process.

The right graph in Figure 4.20 shows the sensitivity S and complementary sensitivity T for the feedback loop across the piezoelectric actuator and strain gauge. The sensitivity corresponds to the ratio between the actuator elongation error e_l and its setpoint r_l and provides an estimate of the disturbance suppression by the feedback controller [79]. The complementary sensitivity provides a measure for the tracking performance of the controlled system and is defined by the ratio between the elongation setpoint r_l and realized elongation ΔL_p [79]. The results show that the curvature error is suppressed by the controller for frequencies below a 100 Hz].

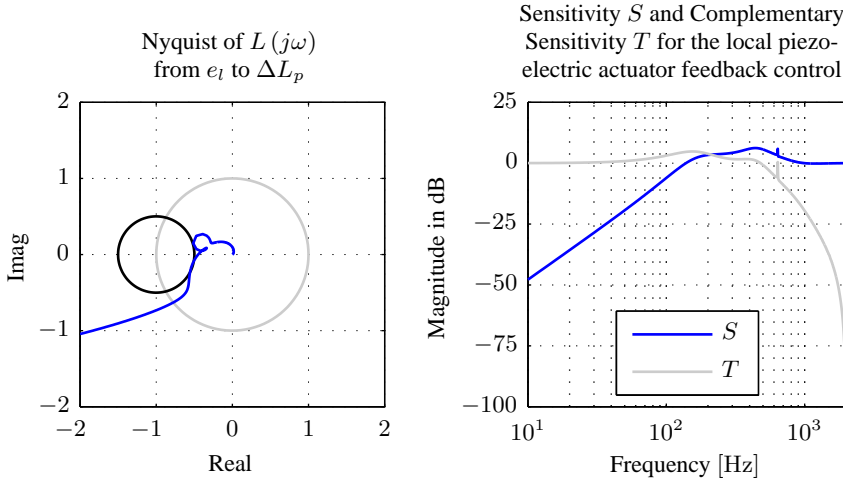


Figure 4.20: Performance estimate of the curvature manipulator in Figure 4.5 and the control strategy in Figure 4.18. The left graph provides the Nyquist diagram for the loop gain L between e_l and l_p which demonstrates the controller stability. The right graph shows the sensitivity and complementary sensitivity for the controlled piezoelectric actuator elongation.

The achieved 210 [Hz] controller bandwidth was compared to a bandwidth requirement. The requirement was estimated using the identified curvature error by the piezoelectric actuator hysteresis of Section 4.3.1.3. It was assumed that this error occurs for a reference signal of 16 [Hz]^2 and that it has to be suppressed by a factor 100. The tuned feedback controller satisfies this requirement because the sensitivity function has a value of -40dB at that frequency.

The above analysis provided first insights into the control performance of the curvature manipulator. The control performance of the final design is investigated in Chapter 5.

4.4 Final design

The final design of the curvature manipulator is shown in Figure 4.21. It evolved from the conceptual design choices of Section 4.3 and shows two curvature manipulator arrays that are located at the reticle's edges. Each array consists of seven actuation mechanisms of Figure 4.12 that are attached to the same vacuum preload cup. Interface rods in the vacuum cup ensure a 10 [\mu m] distance between the reticle and intermediate body as well as an in-plane mechanical decoupling between them.

This section provides an explanation of the final manipulator design. Section 4.4.1 provides details of the manipulator kinematics. The mechanical and electrical design of the manipulator is explained in Section 4.4.2 and 4.4.3. Details of each component design can be found in [118].

²The frequency estimate was obtained after assuming a (half) sinusoidal curvature setpoint that goes from its maximum to minimum value during a 30 [ms] scan time. Figure 2.7 shows that the majority of the spectral content of the curvature setpoints is also present around this frequency.

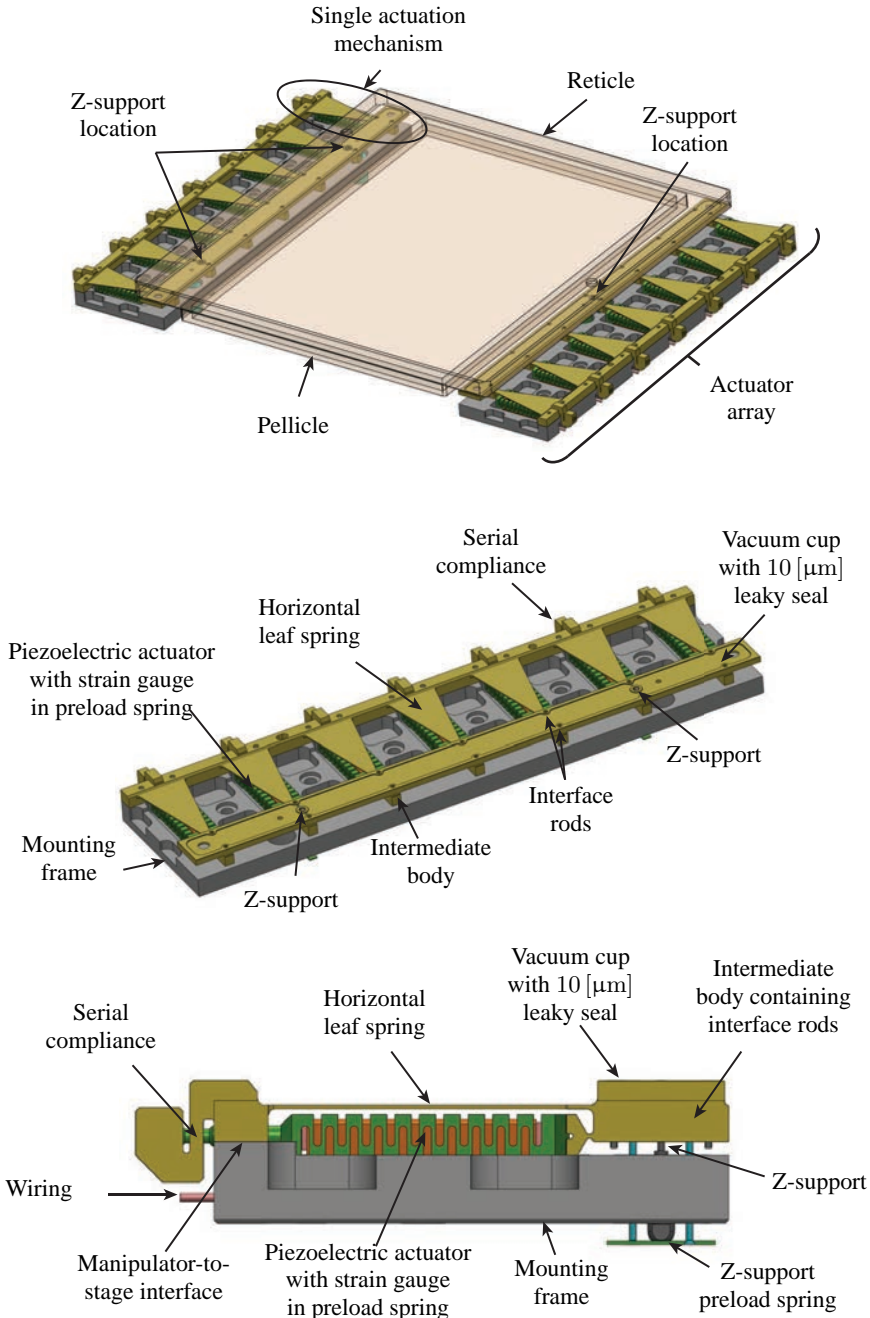


Figure 4.21: The detailed design of the curvature manipulator. The top, middle and bottom picture respectively show a 3D view of the manipulator arrays with respect to the photomask, a 3D view of a single array containing seven actuation mechanisms and a side view of the manipulator array.

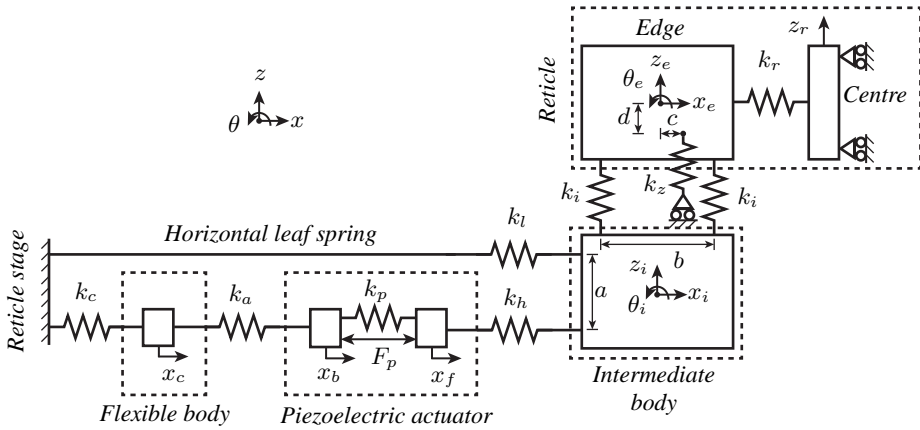


Figure 4.22: The lumped stiffness model of the photomask curvature manipulator that was used to optimize its mechanical design. Note that the stiffnesses are drawn as springs but represented as beams or bars in the kinematic model.

4.4.1 Kinematic analysis

A two-dimensional lumped stiffness model of the manipulator was developed in order to provide insights into its kinematic behaviour for varying component stiffnesses. Figure 4.22 provides a drawing of the model. It shows the different manipulator components which are interconnected by stiffnesses. The stiffnesses are represented as beams or bars in the kinematic model and have contributions in x -, z - and θ -direction. One-seventh of the reticle bending stiffness was used because the model corresponds to that of a single actuator.

Table 4.6 provides an overview of the manipulator performance for the component stiffnesses of the final manipulator design in Figure 4.21. The results are provided for a manipulator with and without z -support constraints in order to determine the influence of the z -support on the manipulator bending behaviour. They are obtained after applying the maximum 60 [V] across the actuator. The results highlight the following:

- Both cases result in a reticle curvature of $\kappa_x = 0.7 \times 10^{-3}$ [1/m]. The curvature specification is therefore satisfied by a factor 1.6.
- The piezoelectric actuator force and elongation are respectively 4 [N] smaller and 0.15 [μm] larger than the estimated values in Section 4.3.1.3. The difference is attributed to the use of a more simplified lumped stiffness model in Section 4.3.1.3.
- The reticle edge obtains a parasitic z -displacement of 4.5 [μm] when there is no z -support. The z -support constrains the out-of-plane deflection of the reticle edge. The behaviour is also reflected by the location of the rotational pole³ for both cases.
- A vertical force goes through the z -support in order to constrain the reticle edge.

³The rotational pole corresponds to the location where a body has no x or z -displacement.

Parameter		Value		Unit
		Case 1 With z-support	Case 2 Without z-support	
Curvature	κ_x	66.8×10^{-5}	66.9×10^{-5}	[μm]
Photomask deflections	x_e	9	31	[pm]
	z_e	1.4	4535	[nm]
	θ_e	50.95	51.05	[μrad]
	z_r	1.94	6.48	[μm]
Piezo characteristics	F_a	11.468	11.466	[N]
	ΔL_p	7.849	7.849	[μm]
Force through z-support	F_{zx}	-2.847	0	[mN]
	F_{zz}	-3.61	0	[mN]
Force through interface rod	F_{ix}	2.017	2.011	[mN]
	F_{iz}	3.2225 / - 3.2189	3.2262 / - 3.2262	[N]
Reticle edge pole location	p_x	-2.83×10^{-5}	-0.089	[mm]
	p_z	1.77×10^{-7}	5.98×10^{-7}	[mm]
Manipulator stiffness	k_x	28560	28560	[N/m]
	k_z	795.8	795.8	[N/m]
	k_θ	6.6	6.6	[Nm/rad]

Table 4.6: Results for the kinematic analysis of the final curvature manipulator design for the case with and without z-support constraints.

This highlights that a pure bending moment is not applied by the mechanism. Analysis in Section 5.3.3 will show that these parasitics effects are within specifications.

- The vertical force through the interface rods are limited to $F_{iz} \approx \pm 3$ [N]. It is expected that the interface rods stay in contact with the reticle because the value is smaller than the available 5.625 [N] vacuum preload per interface rod.
- The parasitic x -force through each interface rod is limited to $F_{ix} = 2$ [mN]. No slip is expected between the reticle and interface rods because the parasitic force is smaller than the identified 0.37 [N] friction force in Section 4.3.1.2.
- Seven manipulators introduce a total parasitic x -force of 28 [mN]. It satisfies the design specification in Table 4.1 by a factor six. The value ensures that the in-plane displacement x_e of the reticle edge is smaller than the 50 [pm] design rule.
- The total stiffness of the seven manipulators is equal to $k_x \approx 2 \times 10^5$ [N/m], $k_z \approx 5.6 \times 10^3$ [N/m] and $k_\theta \approx 46.2$ [Nm/rad]. The x - and z -stiffnesses satisfy the design specification in Table 4.1. The rotational stiffness k_θ is approximately a factor ten too large. Section 5.3.5 will show that the added rotational stiffness of the manipulator is still within the MMO specifications however.

The results of the kinematic analysis have demonstrated that the manipulator is able to achieve the majority of design specifications in Table 4.1. The analysis also showed that the photomask will have a parasitic out-of-plane motion without the presence of a z-support. Z-supports cannot be integrated into each of the seven actuators along the

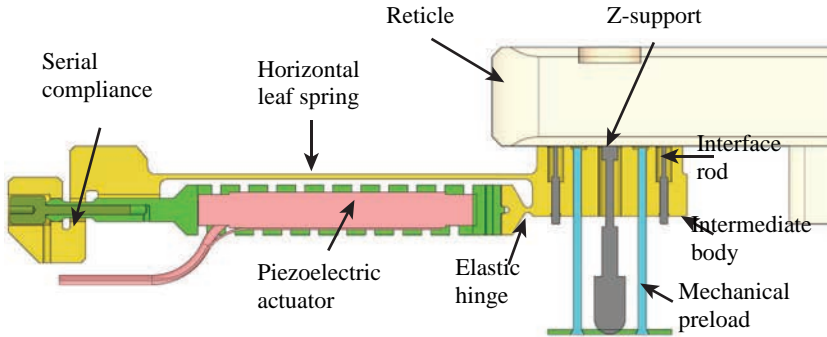


Figure 4.23: A cross section of the curvature manipulator mechanism and its components.

photomask edge because it would disturb the photomask gravity sag. A mechanical model of the manipulator with the reticle and z-supports is therefore developed in Chapter 5 to estimate the final bending performance.

4.4.2 Mechanical design

The mechanical design of the manipulator is provided in Figure 4.23. The design is able to preload itself to the reticle and generate the desired bending moment. Its components are shortly described below. More details of the component design considerations are given in [118].

Vacuum cup

The final manipulator design consists of a single vacuum cup for all seven discrete manipulators. A single cup was selected in order to maximize the vacuum surface area and therefore the achievable preload force in the interface rods. The leaky seal gap between the reticle and the vacuum cup was chosen at $10\ [\mu\text{m}]$ because of the $1\ [\mu\text{m}]$ reticle flatness specification and manufacturability reasons.

A measurement setup was built in order to identify the achievable vacuum preload by the leaky seal [118]. Its results showed that a vacuum pressure of $-0.7\ [\text{barg}]$ could be achieved for the $10\ [\mu\text{m}]$ gap. The pressure ensures contact between the reticle and manipulator as is clear from Figure 4.13.

The vacuum cup deformation by the applied vacuum preload was analysed with the mechanical model in [118]. It showed that the vacuum cup acquires a maximum out-of-plane deflection of $0.4\ [\mu\text{m}]$ for a vacuum pressure of $-0.7\ [\text{barg}]$ which confirms that there is no contact between the reticle and vacuum cup.

Mechanism

The intermediate body, horizontal leaf spring, elastic hinge and serial compliance were integrated into a single monolithic structure. The structure is made from aluminium because of its lower mass and ease of machining. Milling and Electro Discharge Machining (EDM) processes are used to manufacture the component. An explanation of the

leaf spring, elastic hinge and serial compliance design choices is left to [118].

Interface rods

The interface rods are bending beams with a diameter of 0.2 [mm] and free length of 2 [mm]. They are attached to the intermediate body with glue. The top of the rod has a radius of 3.2 [mm] in order to ensure a rolling contact between the reticle and rod.

The axial stiffness of the rod was designed for a maximum deformation of 5 [μm] for the applied bending moment such that mechanical contact with the reticle and vacuum clamp is avoided. Its tangential stiffness and added mass were designed in order to satisfy the k_x and m_y specifications of Table 4.1.

The interface rods must be able to transfer a force of 8.85 [N] without buckling. Analysis showed that this will not occur because the buckling load of the interface rod was estimated at 23.5 [N].

Preloading the interface rod on the reticle results in Hertz contact stresses. These stresses were analysed in order to determine the probability of photomask cracking and eventual failure. It assumed a ball-on-flat contact configuration. The maximum Hertz contact pressure was determined at 538 [MPa] for a force of 8.85 [N]. It exceeds the 350 [MPa] compressive strength of fused silica for long duration loading [123]. The applied force is lower than the 193 [N] critical force for the initiation of cone cracks as defined by Auerbach's law however [123]. It is recommended to investigate this further for future applications because of the failure uncertainty.

Z-support

The z-supports are integrated into the bending manipulator at the three locations in Figure 2.8. The z-supports have a radial and axial stiffness of respectively $k_x = 1.76 \times 10^4$ [N/m] and $k_z = 2.5 \times 10^6$ [N/m]. One end is attached to the short stroke whilst the other protrudes through holes in the vacuum clamp and intermediate body before making contact with the reticle, see Figure 4.23. The configuration provides an in-plane decoupling between the mechanism and z-support. A preloading mechanism is placed between the z-support and intermediate body in order to ensure that the z-support and reticle stay in contact during bending.

Piezoelectric actuator

The piezoelectric actuator is preloaded by a mechanical preload spring. The spring is included because piezoelectric material is not able to withstand tensional loads [89]. It was designed to give a minimum preload force of 60 [N].

The two ends of the mechanical preload spring are designed to interface with the elastic hinge and serial compliance. The piezoelectric actuator and preload spring are integrated into the monolithic mechanism structure using Araldite glue.

4.4.3 Electrical design

The electrical design of the curvature manipulator must be able to drive the piezoelectric actuators, acquire the strain gauge signal and apply the feedback control. Its main build-

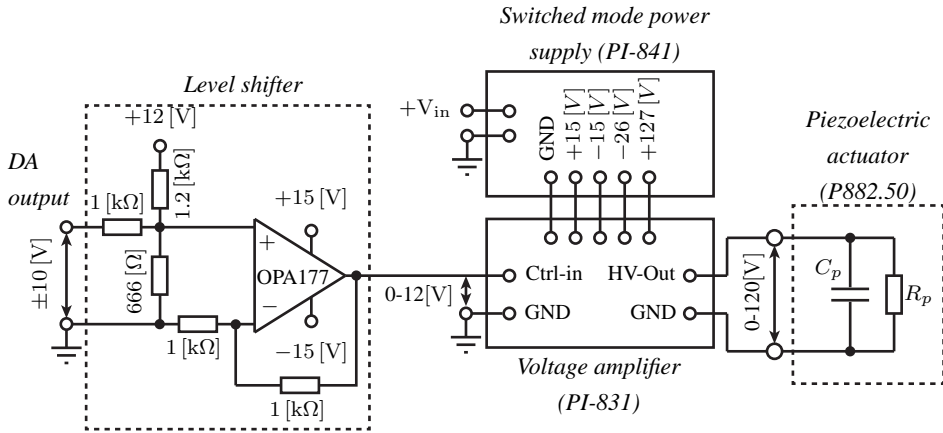


Figure 4.24: The electrical configuration used to drive a piezoelectric actuator.

ing blocks which are explained below. Section 5.4.5 provides a more detailed analysis of the electrical disturbances and their effect on the manipulator performance.

Digital controller

xPC target was chosen as digital control environment because of its flexible MATLAB/SIMULINK programming language and ability to acquire, process and send out large amounts of data. The 16-bits UEI PD2-AO-32/16 analog output card was selected because the corresponding curvature resolution is a factor 400 larger than the error specification of Section 3.3.1 [113]. The control environment has to run at 4 [kHz] in order to limit the amount of phase lag up to the desired bandwidth of 200 [Hz].

Piezoelectric actuator amplifier

Figure 4.24 shows a diagram of the piezoelectric actuator drive electronics. The level shifter transforms the analog output voltage of the digital controller to the required amplifier input value. A PI-831 voltage amplifier that is powered by a PI-841 switched mode power supply amplifies the voltage and applies it across the piezoelectric actuator [90]. A voltage instead of charge amplifier was selected because of cost reasons. Each piezoelectric actuator is driven by its own amplifier to allow individual actuation.

Strain gauge sensor electronics

Figure 4.25 shows the electrical configuration of the strain gauge sensor electronics. The Wheatstone bridge converts the impedance variation of the strain gauge into a measurable voltage. It is fed by a voltage supply U_p of ± 5 [V] and includes two capacitances of 100 [nF] in order to reduce high frequency noise in the bridge supply voltage.

The Wheatstone bridge has a quarter bridge configuration⁴ with three fixed resistances (R_1, R_2, R_3) of 700 [Ω] and one strain gauge on the piezoelectric actuator (R_4) with a

⁴A quarter bridge was implemented because of the availability of a single strain gauge on each piezoelectric actuator. The configuration has disadvantages with respect to a full bridge because it is sensitivity to temperature changes, bending strains and has non-linearity [11].

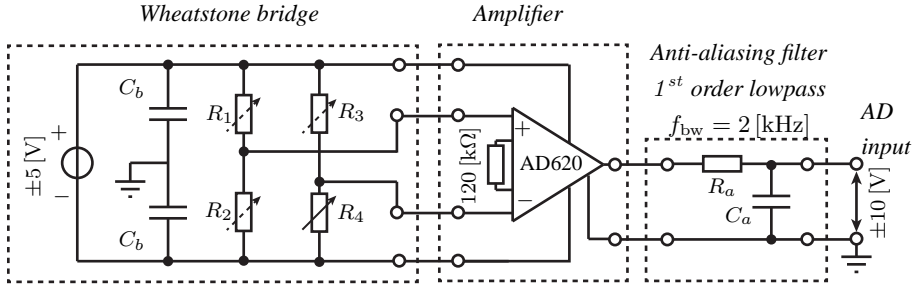


Figure 4.25: The electrical configuration used to read out the strain gauge sensor on each piezo-electric actuator.

resistance of $701\ [\Omega]$. Its sensitivity S_b is equal to [79, 97]:

$$S_b \approx \frac{U_p}{4R_1} \approx 3.6 \times 10^{-3} \text{ [V}/\Omega\text{]}. \quad (4.24)$$

The strain gauges had a maximum resistance variation of $1.8\ [\Omega]$ for a full piezo expansion of $18\ [\mu\text{m}]$. The AD620 differential instrumentation amplifier with a gain of $413\ \text{[V/V]}$ was included in order to amplify bridge signal from $6.4\ \text{[mV]}$ to $2.6\ \text{[V]}$ for the full actuator expansion. This is well within the $\pm 10\ \text{[V]}$ range of the AD input. The constant voltage across the strain gauge results in a power dissipation near the reticle. The power dissipation of each strain gauge is equal to:

$$P_d \approx \frac{U_p^2}{4R_1} \approx 36\ \text{[mW]} \quad (4.25)$$

or $250\ \text{[mW]}$ for seven piezoelectric actuators. This is a factor 50 larger than the $4.4\ \text{[mW]}$ specification in Table 4.1. Section 5.5.3 will show that the effect of the strain gauge power dissipation in the mechanism is too large. It is recommended to use a lower voltage U_p which will come at the cost of a lower bridge sensitivity and lower signal-to-noise ratio. Input noise levels of the differential instrumentation amplifier can become limiting in that case.

Signal conditioning

The strain gauge measurement signals are passed through a first-order low-pass analog filter in order to overcome aliasing of higher frequency signals. The filter specifically removes a $100\ \text{[kHz]}$ electrical disturbance of the switched mode power supply that couples into the strain gauge. The filtered analog signal is then converted into a digital signal by the 16-bits NI-PCI6224 data acquisition card [82].

4.5 Summary & Conclusions

This chapter provided an explanation of the curvature manipulator design by covering the design specifications, the conceptual design choices and the detailed design.

The manipulator design specifications are provided in Table 4.1. They were derived from the system specifications of Chapter 2 in combination with simplified mechanical and thermal models of the photomask. The following insights were obtained:

- The manipulator stroke and stiffness requirements are three orders of magnitude less stringent when the bending moment is introduced from the reticle's bottom surface instead of its edge. This is attributed to the reticle dimensional tolerances.
- The manipulator mass and heat load on the reticle must be kept below 15 [g] and 4 [mW] in order to satisfy overlay specifications.

The design specifications were taken as input for the conceptual manipulator design of Figure 4.3. It consists of a piezoelectrically driven mechanism that is vacuum preloaded onto the bottom surface of the photomask. This interface location was chosen because of less stringent manipulator design specifications and larger achievable bending moments. The mechanism has in-plane decoupling with the photomask in order to allow the photomask bending without slip.

A mechanism was preferred over a direct drive concept in order to satisfy the manipulator stiffness specifications. A minimum of seven mechanisms are needed along the reticle length in order to achieve the desired bending moment whilst keeping the non-correctable pattern distortions below 50 [pm]. The piezoelectric actuator was chosen because it satisfies the power dissipation, volume and mass requirements. A compliance is placed in series with the actuator in order to minimize the manipulator's rotational stiffness.

The manipulator control architecture is provided in Figure 4.18. It consists of local feedback loops across each piezoelectric actuator in order to suppress its non-linearities. Strain gauges measure the actuator elongations which are used as feedback signal. The sensors were chosen because of their size and mass. An outer curvature feedback loop was not included because a suitable metrology concept could not be identified. It is recommended to develop a curvature measurement concept in order to implement a curvature feedback loop in future designs.

A simplified control analysis showed that the manipulator axes are decoupled which allows the application of local SISO controllers. It also showed that a 210 [Hz] bandwidth is needed in order to suppress the actuator hysteresis. The model demonstrated that reticle dynamics are unobservable in the strain gauge measurement signal and that the piezoelectric actuator elongation and reticle curvature have a static relation up to 250 [Hz]. It indicates that the actuators can manipulate the reticle curvature up to 100 [Hz] but that higher order curvature disturbances cannot be counteracted by the local actuator feedback.

The detailed design of the manipulator is provided in Figure 4.21. The kinematics of the design was analysed using a lumped stiffness model. It showed that the manipulator is able to achieve the required reticle curvature by a factor of 1.6 but that the z-supports are needed in order to constrain the reticle out-of-plane deflection. It also demonstrated the

unlikeliness of slip between the reticle and the interface rods.

The explanation of the mechanical and electrical design proved that the design satisfies the majority of the design specifications. There is uncertainty about the allowable contact stresses in the reticle however. It is recommended to investigate the occurrence of micro-cracks in the reticle by the Hertz contact stresses. Furthermore, the strain gauge power dissipation exceeds the 4 [mW] specification. It is recommended to change the strain gauge readout electronics in order to satisfy this specification.

Chapter 5

Performance estimation of the manipulator design

This chapter provides performance estimates of the final curvature manipulator design of Chapter 5. These estimates are obtained by numerical modelling of the manipulator concept. The static bending performance is investigated in terms of curvature, overlay and stress-birefringence. Its dynamic curvature tracking performance is also quantified using control models of the manipulator. The chapter ends with a thermal performance estimate of the manipulator.

5.1 Introduction

Chapter 4 provided an explanation of the photomask curvature manipulator design considerations and the chosen manipulation concept. This chapter investigates the performance of the manipulator design and compares it to the system performance specifications of Chapter 2 and the ideal bending results in Chapter 3.

The performance of the manipulator is investigated in a number of steps. Section 5.2 introduces the mechanical and control model of the final manipulator design. The system's mechanical performance is thereafter investigated in Section 5.3. It provides reticle curvature, overlay and stress-birefringence results for the manipulator and compares it to the ideal reticle bending results of Chapter 3. Section 5.4 discusses the control performance of the manipulator. The achievable controller bandwidths, tracking performance and disturbance errors are presented. Section 5.5 provides a thermal analysis in order to identify the reticle thermal expansion by the manipulator design. The chapter ends with a summary and conclusions in Section 5.6.

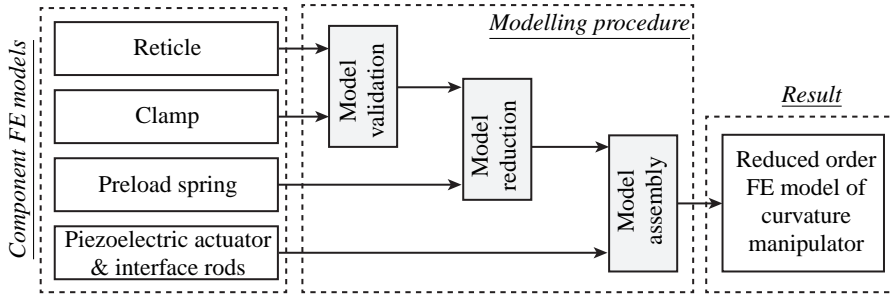


Figure 5.1: The steps that were used to obtain the FE model of the curvature manipulator.

5.2 Models of the manipulator

The performance analysis of the manipulator was investigated using numerical models of the reticle and bending actuator. A mechanical and control model was generated for the investigation. They are explained in respectively Sections 5.2.1 and 5.2.2.

5.2.1 Mechanical model

A mechanical model of the curvature manipulator was developed for two purposes. First, it is used in Section 5.3 to identify the effect of the manipulator on the achievable reticle deflection, overlay and stress-birefringence. Second, it is part of the manipulator control model that is used in Section 5.4 for the control performance analysis.

The mechanical model of the curvature manipulator and photomask was acquired with a method called Dynamic Substructuring [27]. This method can synthesize a mechanical model of a large complex system by assembling component FE models. It is preferred because it reduces the model size whilst still providing an accurate description of the system dynamics [42]. The reduced order model has an advantage that it can be used for the control investigation in Section 5.4.

The generation of the curvature manipulator mechanical model with reticle is explained in [124]. A short summary of the methodology is explained below with the help of Figure 5.1. The first step of the process consisted of generating Finite Element models of the different components. The reticle and vacuum clamp models were thereafter validated using Experimental Modal Analysis [31]. Validation measurements were limited to these components because they are considered as the largest part of the total assembly. Furthermore, the other components were difficult to validate because of their size. The experimental analysis showed that the eigenfrequencies of the modelled and measured reticle matched to within 5% whilst the modes had a Modal Assurance Criterion (MAC) of ($\text{MAC} > 0.9$) up to 2.5 [kHz] [124]. The latter value demonstrates that the eigenmodes of the measured and modelled system correlate. Similar values were obtained for the vacuum clamp up to 2.5 [kHz]. The identified modal damping values were below 1% for both components. The FE models of the reticle and clamp were therefore considered to be validated.

The final steps of the model synthesis consisted of reducing the model size of the reticle,

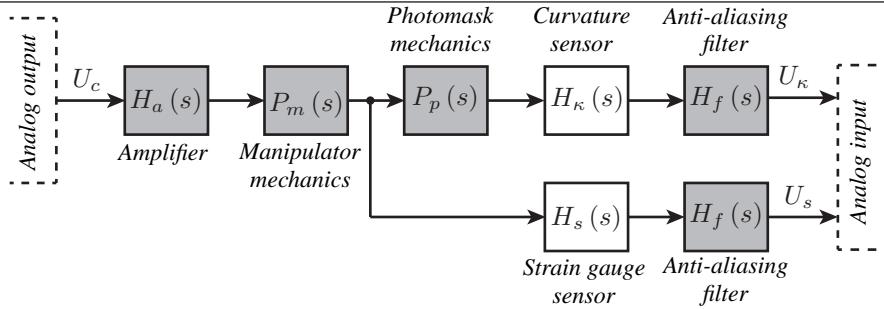


Figure 5.2: A flowchart showing the subsystems in the manipulator model for the control analysis. The grey blocks correspond to subsystems that have dynamic contributions. The voltage U_o corresponds to the output signal from the digital control environment. The voltages U_s and U_κ relate to the measurement signals from the strain gauge and curvature sensor.

vacuum clamps and preload springs. Different model reduction techniques were investigated for this step [124]. The Craig Bampton reduction technique with ten interface fixed modes was finally selected because it provides a better description of the higher order component dynamics and an acceptable model size. The component models were finally assembled using the Dynamic Substructuring technique.

5.2.2 Control oriented model

A system model of the reticle with curvature manipulator was developed for the control analysis in Section 5.4. The model consists of the components that are present between the analog output and analog input of the digital control environment. An overview of those subsystems is provided in Figure 5.2. The curvature sensor subsystem was included in the model in order to investigate the manipulator control performance for an additional curvature feedback loop. This is discussed further in Section 5.4.3.

The components in the control oriented model were described in the following manner:

- *Piezoelectric voltage amplifier, $H_a(s)$* - The voltage amplifier was modelled as a second-order low-pass filter with a cut-off frequency of 5.5 [kHz]. The characteristic was derived from identification measurements of the amplifier with attached piezoelectric actuator [3]. The electrical impedance of the actuator is therefore accounted for in the model.
- *Manipulator and photomask, $P_m(s)$ and $P_p(s)$* - The model of Section 5.2.1 was used to describe the mechanical behaviour of the piezoelectric actuator, manipulator and photomask. It was described in a modal state-space representation such that it can be used for further control analysis [39]. A modal damping of 0.3% was added to the model. This provides a worst case scenario because modal damping values of 0.8% were identified for the experimental modal analysis of the photomask [124].

The piezoelectric actuator hysteresis and drift were not included in the manipulator model because it makes it possible to describe the system as a Linear-Time-

Invariant (LTI) system. The local feedback control across the piezoelectric actuator should be able to account for the hysteresis and drift of the piezoelectric actuator.

- *Strain gauge sensor, $H_s(s)$* - The strain gauge sensor and its electronics were described by a unit gain. This description was chosen because the strain gauge is rigidly connected to the piezoelectric actuator. Furthermore, the readout electronics consist of several resistances and a differential amplifier with a bandwidth of 50 [kHz]. The latter is a factor 25 larger than the Nyquist frequency for a 4 [kHz] sample frequency. The dynamic contribution of the strain gauge and readout electronics is therefore neglected.
- *Curvature sensor, $H_\kappa(s)$* - A curvature measurement path was included in order to identify the manipulator performance under curvature feedback control. The reticle curvature is identified by fitting the anticlastic curvature model of Section 3.3.1 onto the reticle out-of-plane deflection using the least squares algorithm. This is mathematically equal to:

$$\mathbf{c} = (\mathbf{X}^T \mathbf{X})^{-1} \mathbf{X}^T \mathbf{w}, \quad (5.1)$$

where \mathbf{w} is the photomask deflection, \mathbf{c} the identified coefficients and \mathbf{X} the fitting matrix. The latter two are defined by:

$$\mathbf{c} = \begin{bmatrix} T_z \\ \alpha_y \\ \alpha_x \\ \kappa_y \\ \kappa_x \end{bmatrix}, \quad \mathbf{X} = \begin{bmatrix} 1 & x_1 & y_1 & \frac{1}{2}x_1^2 & -\frac{1}{2}\nu y_1^2 \\ \vdots & \vdots & \vdots & \vdots & \vdots \\ 1 & x_n & y_m & \frac{1}{2}x_n^2 & -\frac{1}{2}\nu y_m^2 \end{bmatrix} \quad (5.2)$$

where T_z is the z-translation of the photomask, α_i and κ_i are respectively the photomask rotations and curvatures in the direction $i = x, y$ whilst x_n and y_m are the $n \times m$ measurement locations of the photomask deflection. Note that the measurement of the out-of-plane reticle deflection is assumed ideal. The effect of curvature sensor noise on the bending performance is analysed in Section 5.4.5.

- *Anti-aliasing filter, $H_a(s)$* - The anti-aliasing filter was modelled as a first-order low-pass filter with a cut-off frequency at 2 [kHz]. The filter was added to the curvature and strain gauge sensor paths.

The above described subsystems resulted in an overall state-space model of the curvature manipulator. The model dynamics and the manipulator control performance are evaluated in Section 5.4.

5.3 Mechanical performance

The mechanical performance of the curvature manipulator is investigated using the manipulator model of Section 5.2. The results are compared to the system performance

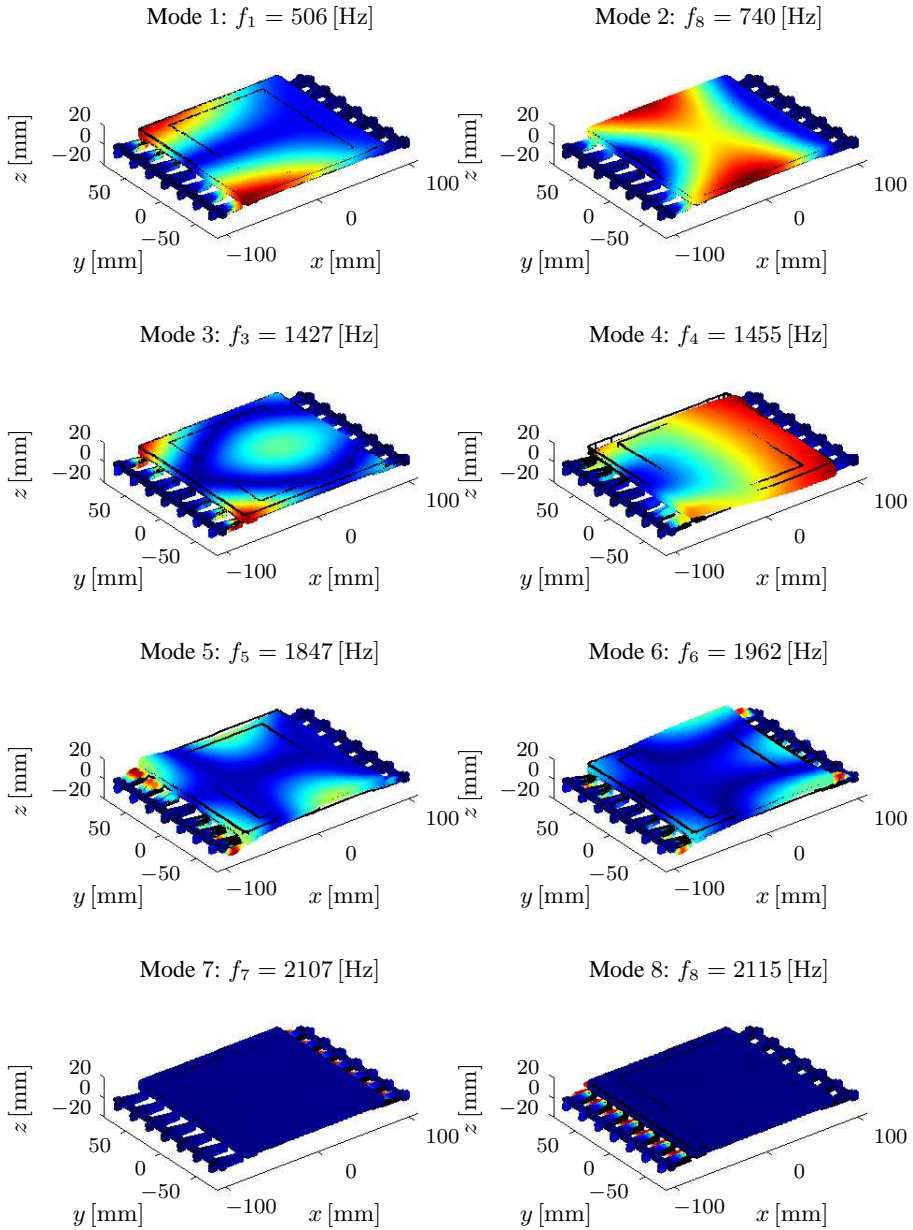


Figure 5.3: The first eight eigenmodes of the photomask with attached bending manipulator. The colours correspond to the absolute value of the out-of-plane modal deflection.

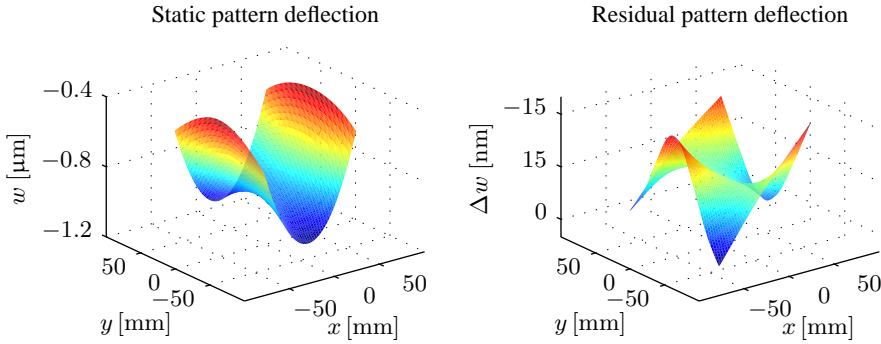


Figure 5.4: Modelled bending performance of the manipulator for a curvature of $\kappa_x = -0.4 \times 10^{-3}$ [1/m]. The left plot shows the deflection of the pattern area. The right graph provides the deflection difference with respect to the ideal bending case in Section 3.3.1.

specification of Chapter 2 and the ideal photomask bending case in Chapter 3. Section 5.3.1 introduces the identified eigenfrequencies and eigenmodes of the manipulator configuration. The achieved reticle deflection and pattern distortions are covered in Section 5.3.3 and 5.3.3. Sections 5.3.4 and 5.3.5 respectively present the reticle stress-birefringence and clamping fingerprint that is introduced by the bending manipulator.

5.3.1 System eigenfrequencies

Figure 5.3 shows the first eight eigenfrequencies and eigenmodes that were derived from the numerical model of the curvature manipulator. The results are compared to resonance frequency specifications in Table 4.1 and the eigenmodes and eigenfrequencies of the kinematically constrained photomask without a bending manipulator of Section 4.2.5. The comparison highlights the following:

- The 1st eigenmode shows the first out-of-plane mechanical resonance. Its eigenfrequency lies above the 430 [Hz] specification of Table 4.1.
- The general shape of the first six out-of-plane photomask eigenfrequencies have not significantly changed.
- The value of the first eigenfrequencies have increased indicating that the manipulator adds stiffness to the photomask. It is expected that the added stiffness improves the out-of-plane positioning of the reticle because it translates to smaller reticle deformations for the same disturbance. Larger clamping distortions are expected by the higher stiffness however.
- The 3rd and 4th eigenfrequency and mode have switched order by the addition of the manipulator.

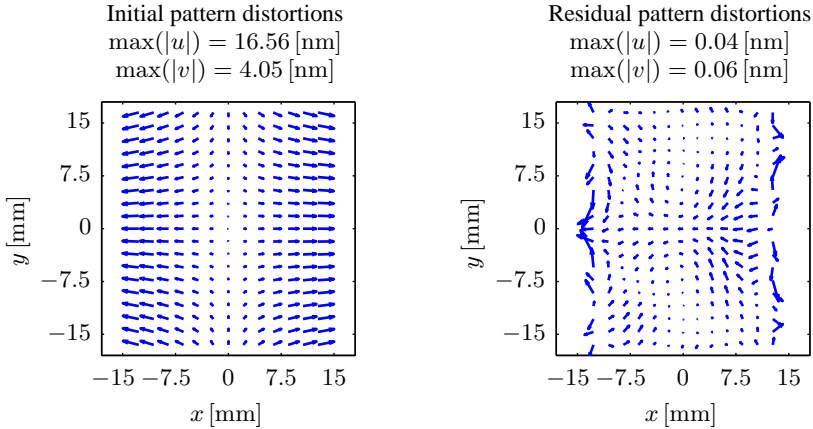


Figure 5.5: The pattern distortions for a static photomask curvature by the manipulator. The left figure shows the raw pattern distortions for a curvature of $\kappa_x = -0.4 \times 10^{-3} [1/m]$. The right figure shows residual pattern distortions after lithography machine corrections.

- The 7th and 8th eigenmode show the first in-plane resonance of the manipulator. The corresponding eigenfrequencies lie above the 2 [kHz] eigenfrequency specification.

The eigenfrequency analysis has shown that the manipulator satisfies the eigenfrequency specification. It is therefore expected that the manipulator dynamics has no detrimental effects on the lithography process.

5.3.2 Photomask deflection

The curvature manipulation performance by the bending manipulator was determined with the reduced order FE model of Section 5.2.1. Figure 5.4 shows the achieved out-of-plane deflection of the reticle after the application of $U_p = 44.8 [V]$ across all piezoelectric actuators. It shows the expected anticlastic deformation of the reticle surface. The left graph shows the achieved deflection of the pattern area by the manipulator. The right figure shows the residual pattern deflection after fitting the ideal anticlastic curvature shape of Section 3.3.1 through the photomask deflection data. The results highlighted the following:

- A voltage application of $U_p = 44.8 [V]$ results in a reticle curvature of $\kappa_x = -0.4 \times 10^{-3} [1/m]$. The manipulator satisfies the curvature specification by a factor of 1.4 because 60 [V] can be applied across the actuators.
- The reticle has a higher order out-of-plane deflection. This is attributed to the added stiffness and parasitic motion of the manipulator. The error is approximately 21 [nm] at reticle level or 1.3 [nm] at wafer level. This is approximately one-tenth of the expected focus improvement.

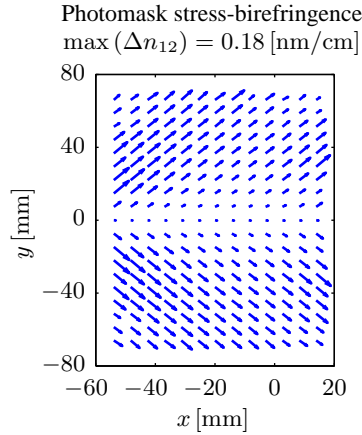


Figure 5.6: The induced photomask stress-birefringence by the manipulator for $\kappa_x = -0.4 \times 10^{-3} \text{ [1/m]}$. The arrows represent the birefringence amplitude and direction at each location.

The reticle deflection results highlight that the manipulator is able to achieve the desired reticle deflection shape. It is recommended to further optimize the design in order to relieve the parasitic higher order deformation.

5.3.3 Reticle pattern distortions

The corresponding pattern distortions for the reticle deformation in Figure 5.4 is given in Figure 5.5. The left figure shows the initial pattern distortions. The right figure provides the residual pattern distortions after application of the lithographic system corrections of Section 3.4. The results show the following:

- The pattern distortions correspond to an asymmetric magnification like the ideal bending case in Section 3.4. The manipulator induced distortions are slightly larger.
- The pattern distortion values after correction are close to the $50 \text{ [}\mu\text{m]}$ design rule and within 0.1 [nm] overlay budget limit as specified in Section 2.5.2.
- The residual pattern distortions clearly show the contribution of the z-support constraints and discrete bending moment introduction. These are difficult to counteract by the lithography system.

The above results highlight that the manipulator design satisfies the pattern distortion specifications.

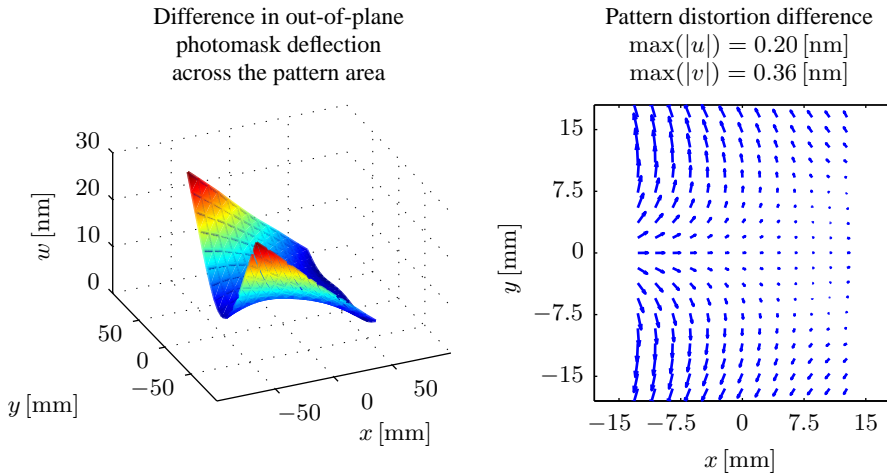


Figure 5.7: The influence of the manipulator on the reticle's gravity deformation. The left and right figure respectively show the out-of-plane and in-plane pattern deformation difference with respect to the kinematically constrained photomask of Figure 4.6.

5.3.4 Photomask stress-birefringence

The mechanical model of the reticle with bending manipulator was used to determine the introduced stress-birefringence by the manipulator. The results were obtained using the procedure in Section 3.5. Figure 5.6 provides the vector plot of the stress-birefringence for a reticle curvature of $\kappa_x = -0.4 \times 10^{-3}$ [1/m]. The maximum value was equal to 0.18 [nm/cm] which satisfies the 1 [nm/cm] birefringence specification of Chapter 2 by more than a factor of five. The induced stress-birefringence on the imaging process can therefore be neglected.

5.3.5 Reticle gravity deflection

Section 4.2 highlighted that the manipulator must facilitate the natural deformation of the photomask on its three z-supports in order to limit the Matched Machine Overlay (MMO) penalty. The change in reticle gravity deflection by the added manipulator mass and stiffness was estimated with the mechanical model of Section 5.2.1.

The difference in out-of-plane and in-plane pattern deformation between the kinematically supported reticle of Section 4.2.2 and the mechanical model of the reticle with manipulator is provided in Figure 5.7. The result shows the following:

- The manipulator changes the out-of-plane deflection due to gravity by a maximum of 30 [nm] at reticle and 1.9 [nm] at wafer level. This is approximately one-seventh of the pursued focus improvement. The difference is attributed to the out-of-plane stiffness of the manipulator. The effect is most predominant at the left side which corresponds to the edge with the single z-support.

- The maximum value of the in-plane pattern distortion is lower than the 0.6 [nm] MMO budget that was defined in Section 2.5.2.3.

The result shows that the manipulator's effect on the gravity deformation is acceptable.

5.4 Control performance

The control performance of the manipulator was evaluated using the model of Section 5.2.2. The performance is quantified for two strategies. The first consists of applying local feedback across each collocated piezoelectric actuator and strain gauge sensor as was proposed in Section 4.3.3. The second strategy consists of the first with an additional curvature feedback loop. It was investigated in order to identify the tracking improvement when directly controlling the desired control variable.

The explanation of the control performance is given in the following manner. Section 5.4.1 presents the manipulator dynamics. The feedback controller tuning of the two control strategies is provided in Sections 5.4.2 and 5.4.3. The curvature tracking performance of both strategies is compared in Section 5.4.4. The contribution of disturbances on the curvature error is quantified in Section 5.4.5.

5.4.1 System dynamics

Insights into the dynamics of the curvature manipulator with photomask was obtained by the analysis of the control oriented model of Section 5.2.2. The model was discretised using the Zero-Order-Hold (ZOH) method and a sample frequency of $f_s = 4$ [kHz]. Time delays were assumed to be absent in the system.

Figure 5.8 provides the Bode plots of the system from the applied piezoelectric actuator voltage to the measured strain gauge elongation. The left and right plots respectively show the collocated and non-collocated transfer functions. Visual inspection of the frequency responses gave the following insights:

- The frequency response of the collocated actuator and sensor shows a zero slope for the frequencies below 1 [kHz]. This behaviour was also seen for the conceptual design in Section 4.3.3. Reticle resonance frequencies are not visible in the FRF.
- The phase of the collocated FRF drops to -180 [deg] at the Nyquist frequency. This phase lag is caused by the plant discretization and is bandwidth limiting.
- The magnitude difference between the collocated and non-collocated FRFs is 50dB or more. The difference is attributed to the mechanical decoupling of the actuators in the manipulator design as was explained in Section 4.3.3. The final decoupling is larger than the estimated 37 dB of the conceptual design in that section.

The FRFs in Figure 5.8 indicate little interaction between the different axes. Their interaction was quantified with the Relative Gain Array (RGA) [72, 100]. It is defined

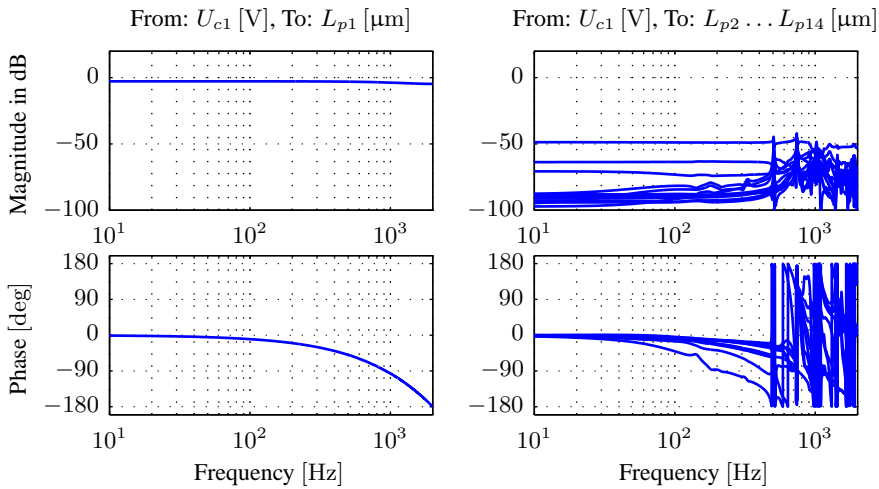


Figure 5.8: Dynamic behaviour of the curvature manipulator system. The left Bode plot shows the collocated frequency response from the first piezoelectric actuator U_{c1} to the first strain gauge L_{p1} . The right Bode plot shows the non-collocated frequency responses from the actuator to the other strain gauges.

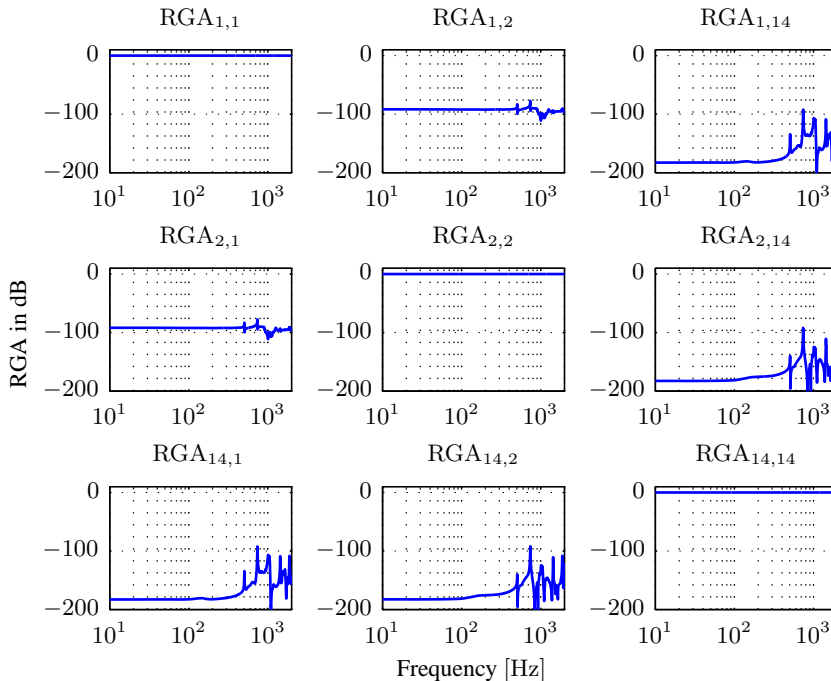


Figure 5.9: RGA of the plant between the 1st, 2nd and 14th piezoelectric actuator to strain gauge axes of the curvature manipulator. Note that the RGA is unitless.

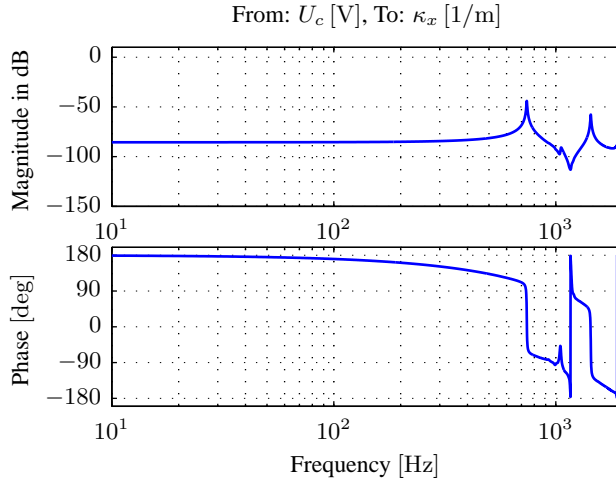


Figure 5.10: Frequency response of the plant without applied feedback for the same voltage U_c across all piezoelectric actuators to the photomask curvature κ_x .

as:

$$\text{RGA}(P(\omega)) = P(\omega) \times (P(\omega)^{-1})^T \quad (5.3)$$

where the \times sign represents the element-by-element multiplication of the plant FRFs $P(\omega)$. The axes are perfectly decoupled when the RGA is equal to the identity matrix for all frequencies ω .

Figure 5.9 provides the relevant RGA results for the FRFs between the first, second and fourteenth piezoelectric actuator voltages and strain gauge elongations. The remaining RGA contributions were omitted because they showed the same trend. The RGA results demonstrate the following:

- The RGA approaches the identity matrix for all frequencies. The contributions on the off-diagonals stay below -90dB .
- The interaction between the 1st and 14th axes is lower than the first and second. This is attributed to the larger distance between the axes.

The RGA results confirm that the piezoelectric actuator to strain gauge axes are decoupled. Local feedback control can therefore be applied across each collocated piezoelectric actuator and strain gauge sensor. This strategy is known as decentralized control [100] and allows the use of SISO control tuning techniques. MIMO controller tuning is therefore not considered in this thesis.

The frequency response of the manipulator between the applied voltages across all piezoelectric actuators and the reticle curvature was also investigated with the model of Section 5.2.2. Its Bode plot is provided in Figure 5.10 which gave the following insights:

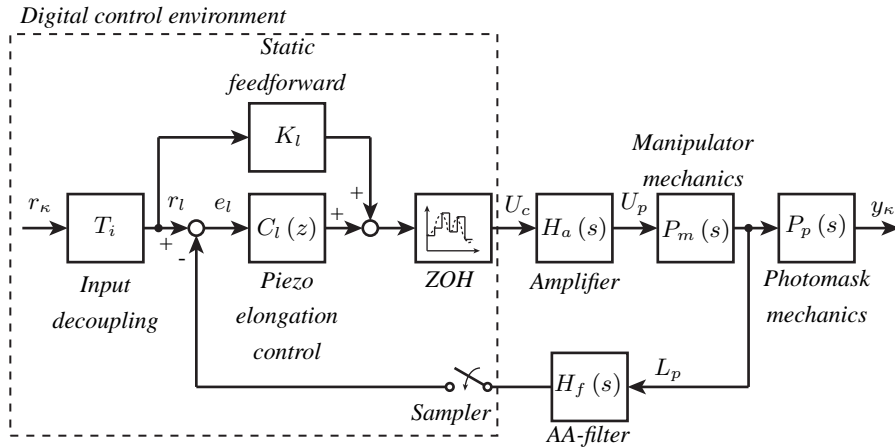


Figure 5.11: The primary control strategy that is proposed for the photomask manipulator. It consists of a decentralized controller $C_l(z)$ across each collocated piezoelectric actuator and strain gauge sensor. The strategy also contains a feedforward path consisting of a static gain K_l .

- There is a static relation between the applied voltage and the reticle curvature up to 200 [Hz].
- The first resonance peak in the FRF corresponds to the second mechanical eigenfrequency of the assembly as is clear from Figure 5.3. It was explained in Section 4.3.3 that this is also expected because the first eigenmode represents a tilt motion of the reticle on the z-supports whilst the second can be considered as a bending mode of the reticle on its z-supports.
- The negative sign in the relation of the applied voltage (bending moment) and achieved curvature in Equation (3.2) relates to the 180 [deg] phase at 10 [Hz].

The above presented results provided insights into the dynamics of the curvature manipulator. The information is used for the controller tuning in Sections 5.4.2 and 5.4.3.

5.4.2 Piezoelectric actuator elongation feedback control

The first control strategy that was analysed with the curvature manipulator model is the decentralized control across the piezoelectric actuators and strain gauge sensors. The strategy was introduced in Section 4.3.3 and is shown in Figure 5.11. It also has a feedforward path in order to improve tracking behaviour which consisted of static gains on the diagonal of the feedforward block K_l instead of a MIMO feedforward for simplicity. The input decoupling vector T_i scales the curvature setpoint r_κ to the piezoelectric actuator elongation setpoints r_l .

The FRFs between the collocated piezoelectric actuator and strain gauge sensors are shown in the left Bode plot of Figure 5.12. The FRFs have little variation. A single robustly stable controller was therefore applied to all fourteen feedback loops.

The robustly stable controller was tuned with manual loop-shaping techniques [35]. A

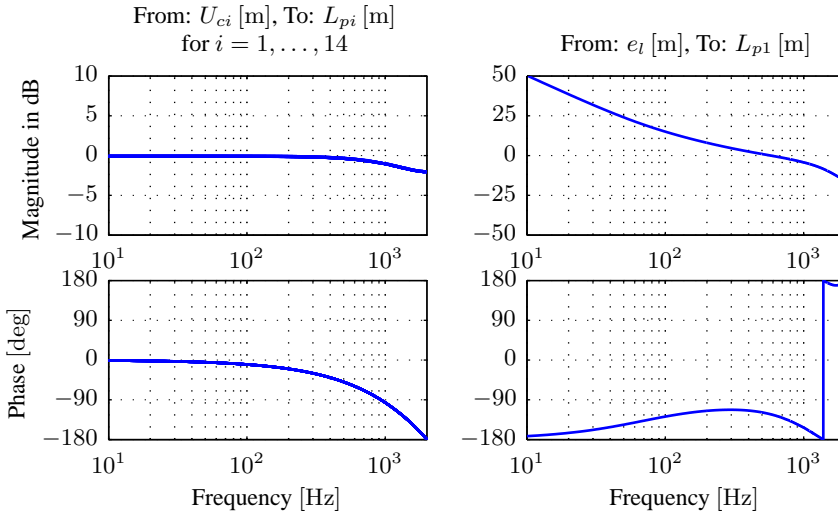


Figure 5.12: Decentralized controller tuning results for the control strategy in Figure 5.11. The left Bode plot provides the FRFs of the fourteen collocated piezoelectric actuators and sensors. The right Bode plot shows the open-loop frequency response of a single piezoelectric actuator control loop after neglecting the interaction with the other axes.

PI²D-controller was chosen for a larger disturbance suppression at the lower frequencies as was explained in Section 4.3.3. The right Bode plot in Figure 5.12 shows the open loop frequency response for one of the piezo elongation control loops where the interaction with the other plant dynamics has been neglected. The plot highlights that the unity-gain cross-over frequency or controller bandwidth lies at 580 [Hz]. This is approximately a factor 2.7 higher than the achieved 210 [Hz] bandwidth for the simplified manipulator model in Section 4.3.3. The bandwidth limitation is caused by the phase lag due to sampling. It is recommended to increase the sampling frequency in future systems.

Although Section 5.4.1 showed that there is hardly any interaction between the axes, it is necessary to consider the stability of the controlled MIMO plant when the fourteen SISO loops are closed. The stability is investigated using the Nyquist diagram of the eigenvalues or *characteristic loci* of the MIMO open loop FRF matrix $L(j\omega)$. The *Generalized Nyquist Criterion* holds for these eigenvalues [70?]. Figure 5.13 provides the result of the analysis. The left graph shows the Nyquist plots of the fourteen separate diagonal loop gains $\text{diag}(L(j\omega))$ whilst the right graph provides the Nyquist plot of the characteristic loci $\lambda(L(j\omega))$. The results provide the following insights:

- The characteristic loci of the controlled MIMO system do not enter the circle with radius 0.5. It indicates that the controller is robustly stable to 6 dB plant variations. Section 4.3.3 explained that this margin is normally used for industrial applications.
- The Nyquist diagram of each loop resembles that of the characteristic loci. It confirms that the axes are decoupled and that SISO control can be used.

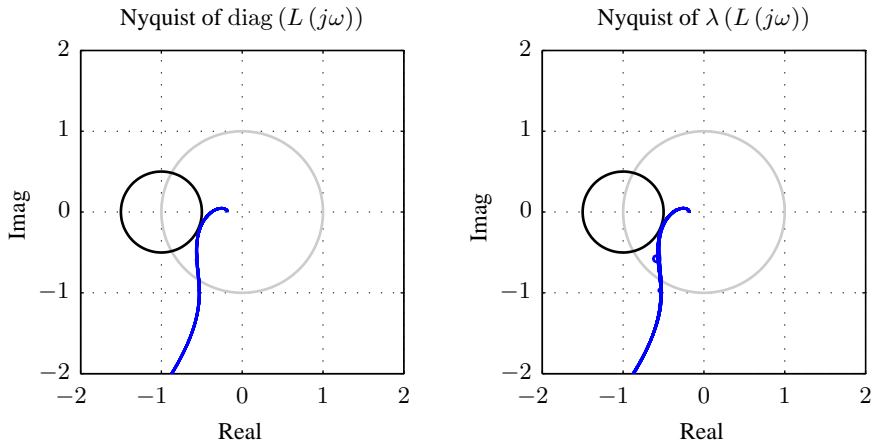


Figure 5.13: Nyquist diagrams of the fourteen diagonal loop gains $\text{diag}(L(j\omega))$ on the left and that of the characteristic loci $\lambda(L(j\omega))$ on the right. The graphs highlight that the open loop plant is robustly stable because the Nyquist plots do not encircle the -1 point nor enter the circle with radius 0.5. Furthermore, the similarity between the two graphs indicate that the plant is fully decoupled.

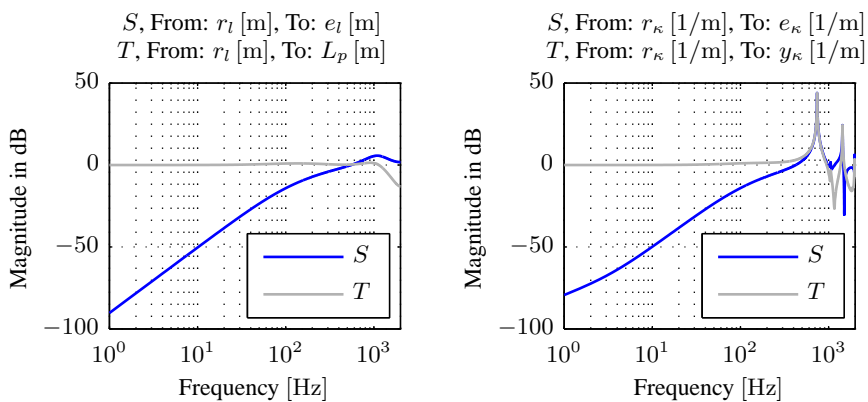


Figure 5.14: The sensitivity S and complementary sensitivity T of the decentralized control strategy in Figure 5.11.

The disturbance rejection and tracking performance of the closed loop system of Figure 5.11 is described by the sensitivities S and complementary sensitivities T in Figure 5.14. The left graph shows the two quantities for one of the inner closed loops across the piezoelectric actuator. The right graph shows their values in terms of curvature control. The graphs provide the following insights:

- The sensitivity function of the inner closed loop across the actuator has a disturbance suppression of 42 dB at 16 [Hz]. This is larger than the factor 100 that was identified for the suppression of piezoelectric actuator in Section 4.3.3.
- The peak of the sensitivity for the inner closed loop stays below the 6 dB robustness margin for industrially manufactured systems that was introduced in 4.3.3.
- The sensitivity in the left and right graphs show similar disturbance suppression performance below 500 [Hz].
- The curvature sensitivity and complementary sensitivity have a 44 dB peak at 740 [Hz] which relates to the second eigenfrequency of the reticle with manipulator. Large curvature tracking errors can be expected at that frequency.

The difference in sensitivity and complementary sensitivity at the piezoelectric actuator and reticle curvature level indicates that the feedback control strategy in Figure 5.11 is not able to control the reticle curvature for frequencies above 500 [Hz]. This is investigated further in Sections 5.4.4 and 5.4.5.

5.4.3 Curvature feedback control

The investigation of the local piezoelectric actuator feedback control in Section 5.4.2 highlighted that the second reticle eigenfrequency has an influence on the curvature control performance. The control strategy of Figure 5.15 with an additional curvature feedback loop was therefore analysed. A feedforward path with unity gain was added to boost the curvature tracking performance.

The curvature feedback controller tuning was performed using manual loop-shaping. A PI²D-controller was again used to achieve higher disturbance suppression at lower frequencies. A low-pass filter was added to suppress the modes above the first resonance. Figure 5.16 provides the results of the controller tuning process. The left Bode plot shows the FRF of the plant for which the curvature feedback controller was tuned. The right Bode plot shows the loop gain for the tuned curvature controller. It has a unity-gain cross-over frequency or controller bandwidth of 130 [Hz].

The corresponding Nyquist plot of the open-loop is provided in 5.17. It demonstrates that the tuned controller is robustly stable to 6 dB plant variations. It also shows that the controller was tuned in order to damp the mechanical resonance at 740 [Hz]. This mechanical resonance and the system phase lag limit the achievable bandwidth.

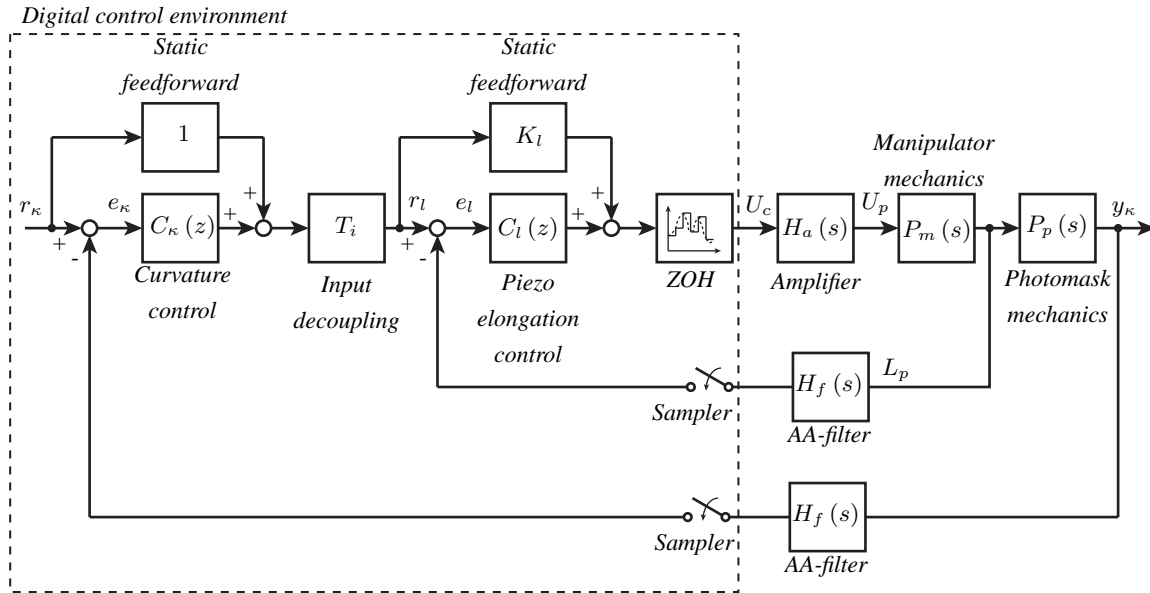


Figure 5.15: The second control strategy that is proposed for the photomask manipulator. It consists of augmenting the strategy in Figure 5.11 with an outer feedback loop across the curvature. The strategy also has a feedforward path consisting of a static gain K_k .

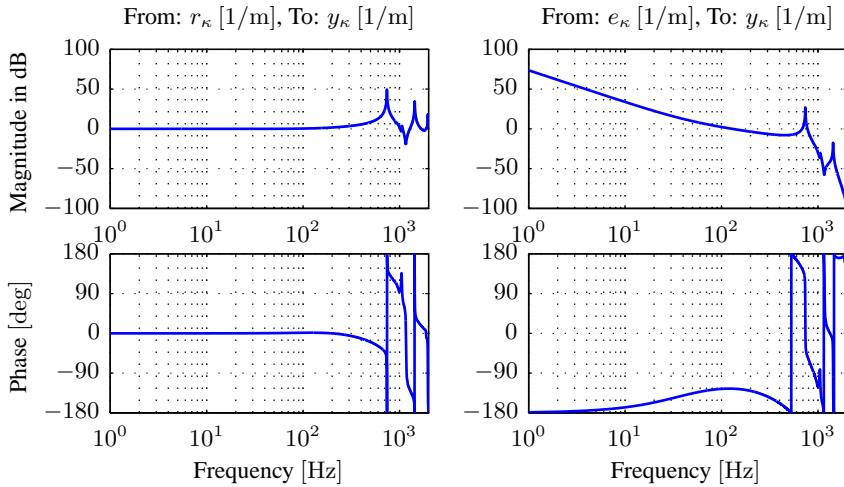


Figure 5.16: Controller tuning results for the strategy in Figure 5.15. The left Bode plot provides the system's FRF from r_κ to y_κ without the application of curvature feedback. The right Bode plot shows the open-loop frequency response of the curvature feedback control loop.

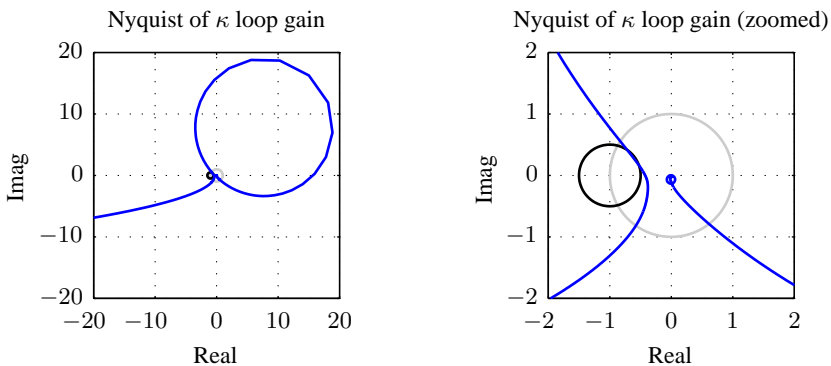


Figure 5.17: The Nyquist plot of the curvature loop gain. The right graph provides a more detailed view of the Nyquist plot around the $(-1, 0)$ point.

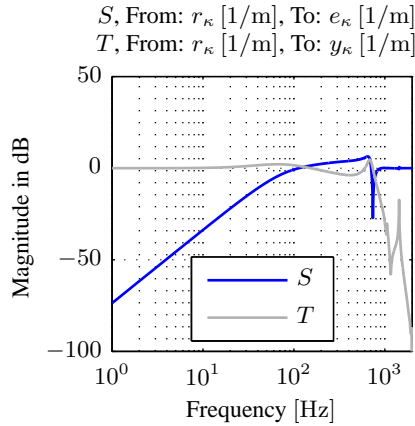


Figure 5.18: The sensitivity S and complementary sensitivity T of the curvature control strategy in Figure 5.15.

The disturbance rejection and tracking performance of the curvature control configuration in Figure 5.15 are described by the sensitivities S and complementary sensitivities T of Figure 5.18. Their values were compared to the results for the decentralized piezo-electric actuator control in the left graph of Figure 5.14. This provided the following insights:

- The outer curvature feedback loop is able to reject curvature disturbances up to approximately 100 [Hz].
- The peak in the sensitivity and complementary sensitivity at the mechanical resonance frequency of 740 [Hz] is removed by the addition of the outer curvature feedback loop.

The above highlights that the addition of a curvature feedback loop is advantageous in terms of achievable curvature control performance. The difference in terms of curvature tracking performance and disturbance suppression between the control strategies of Figure 5.11 and 5.15 is further investigated in Sections 5.4.4 and 5.4.5.

5.4.4 Curvature tracking performance

The time domain curvature tracking performance of the manipulator was investigated for the control strategies of Sections 5.4.2 and 5.4.3. The top-left graph in Figure 5.19 shows the curvature setpoint profile that was used for the analysis which is equal to the one in Section 2.5.1.1. Note that the contribution of lens heating to the curvature setpoint is neglected in this analysis because of its quasi-static nature.

The curvature tracking performance of both configurations is quantified by looking at the tracking error $e_\kappa(t)$. The raw tracking error is split up into two performance measures that are commonly used in the lithography industry. These are the Moving Average

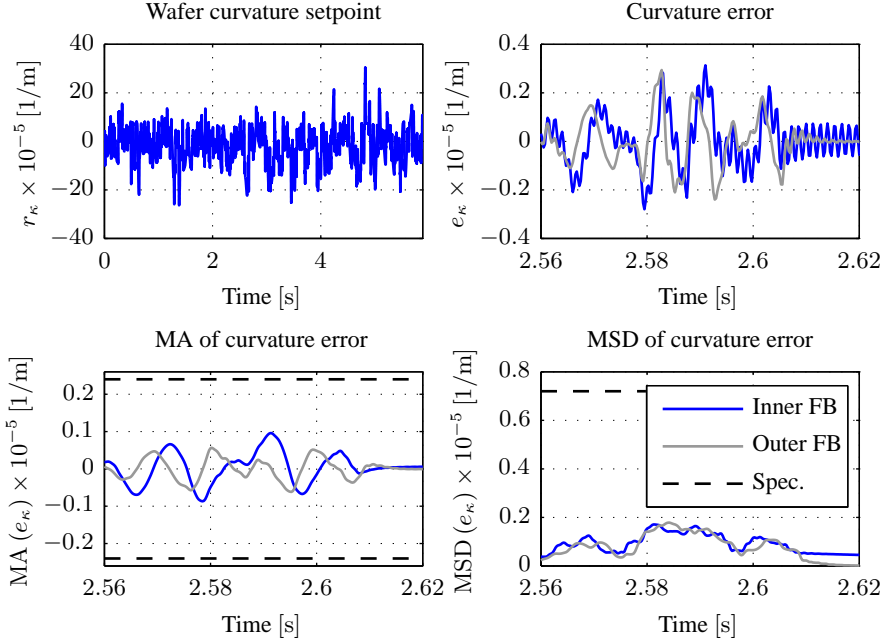


Figure 5.19: Results of the curvature tracking analysis. The top graphs respectively show the curvature setpoint and the raw curvature error as a function of time. The dark and grey solid lines respectively represent the results for the local piezo elongation feedback of Figure 5.11 and outer curvature feedback of Figure 5.15. The bottom two graphs respectively show the MA and MSD value of the curvature error. The dotted lines represent the allowable error for both quantities.

(MA) and Moving Standard Deviation (MSD) error. An MA error is related to defocus or overlay whilst MSD contributes to fading. They are respectively defined by [20]:

$$\text{MA}(e_{\kappa}(t)) = \frac{1}{T} \int_{-T/2}^{T/2} e_{\kappa}(t) dt \quad (5.4)$$

$$\text{MSD}(e_{\kappa}(t)) = \sqrt{\frac{1}{T} \int_{-T/2}^{T/2} [e(t) - \text{MA}(e_{\kappa}(t))]^2 dt} \quad (5.5)$$

where T is the total exposure time of a point on the reticle.

The curvature tracking errors are provided in the Figure 5.19. The top-right graph shows the tracking errors for the decentralized feedback control across the piezoelectric actuators (dark solid line) and the outer curvature control (grey solid line) as a function of time. The result shows that the error signal of the former strategy has higher frequency content than the latter which is attributed to the 740 [Hz] resonance frequency of the photomask. The result demonstrates that the curvature feedback controller does indeed counteract the 2nd mechanical resonance. This is not the case for the piezoelectric actuator controller

because it is unobservable by the strain gauge. It is recommended to investigate feedforward control strategies that can further reduce the tracking errors.

The bottom two graphs in Figure 5.19 provide the MA and MSD values of the curvature error for both control strategies. The MA error satisfies the curvature accuracy specification of Section 3.3.1 by a factor of 2.5. The MA error for the outer curvature feedback is slightly smaller than that for the decentralized feedback control across the piezoelectric actuators. The bottom right figure shows that the MSD curvature error satisfies the specification of Section 3.3.1 by a factor of 4. The outer feedback loop suppresses the MSD error even further from $t = 2.6$ [s] onwards. It confirms that the photomask resonance frequency is counteracted by this control strategy.

The MA and MSD results of the setpoint tracking analysis has shown that the curvature requirements are met by the manipulator system when no additional disturbances act on it. Section 5.4.5 investigates the effect of disturbances on the manipulator performance.

5.4.5 Effect of disturbances on curvature manipulation

The curvature control performance is influenced by disturbances that act on the manipulator system. This section investigates the curvature errors that are caused by disturbances for the control strategies of Section 5.4.2 and 5.4.3.

Figure 5.20 provides an overview of the identified disturbances and the locations where they are introduced into the system. They are expressed in terms of their Power Spectral Densities (PSDs) in order to use the Dynamic Error Budgeting methodology [51, 64]. The PSD of each disturbance is limited to a frequency range of 1 to 2000 [Hz]. They are defined below.

Digital-to-Analog Conversion noise (PSD_{DA}) - The DAC noise has two contributions. The first is caused by the quantization process during sampling. Its contribution can be approximated by white noise [51]:

$$\text{PSD}_{\text{DA,quant}} = \frac{Q_a^2}{12f_N}, \quad \text{with} \quad Q_a = \frac{R}{2^s} \quad (5.6)$$

where Q_a is the quantization interval, f_N is the Nyquist frequency, s are the number of bits and R is the range of the DA converter. Values of $f_N = 2$ [kHz], $R = 20$ [V] and $s = 16$ bits were used for the disturbance analysis.

The other contributor is the electronic noise of the DAC [113]. It has a noise specification of 2 Least-Significant-Bit (LSB) RMS between 0 and 10 [kHz]. The disturbance was modelled as white noise with a standard deviation of $\sigma = 6.1035 \times 10^{-4}$ [V].

Amplifier noise (PSD_{amp}) - The amplifier noise is equal to 5 [mV] peak-to-peak for frequencies below 10 [kHz] when it is used in combination with a switched mode power supply [90]. It was assumed that the peak-to-peak value corresponds to a 6σ value. The noise was therefore modelled as white noise with a standard deviation of $\sigma = 0.833$ [mV].

Strain gauge sensor (PSD_{sg}) - The strain gauge sensor noise is defined by the strain gauge sensor and its readout electronics. The strain gauge introduces thermal noise which

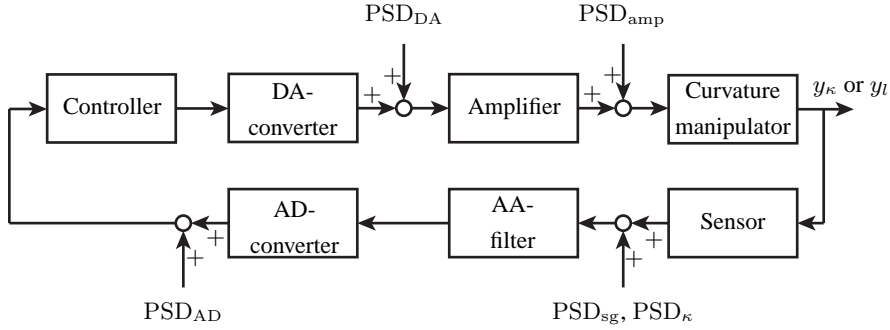


Figure 5.20: The disturbance sources (PSD) that act on the curvature manipulator system.

has a white spectral density. It is defined by [51]:

$$\text{PSD}_{\text{therm}} = 4kTR \quad (5.7)$$

where $k = 1.38 \times 10^{-23}$ [J/K] is the Boltzmann constant, T is the temperature of the strain gauge and R is the strain gauge resistance. It resulted in a noise with a standard deviation of $\sigma = 0.15$ [μV] for an assumed temperature of 293 [K] and nominal resistance of $R = 700$ [Ω].

The instrumental amplifier in the readout electronics also introduces noise. Its input noise is the dominant source [5]. It has a $1/f$ contribution up to 10 [Hz] and a constant PSD of 81 [nV^2/Hz] which results in noise with a standard deviation of $\sigma = 0.4$ [μV] between 1 and 2000 [Hz].

Note that both the strain gauge noise as the amplifier noise need to be multiplied by the instrumental amplifier gain.

Curvature sensor (PSD_{κ}) - The noise of the fictitious curvature sensor was defined by a white spectrum. Its standard deviation was taken as $\sigma = 1 \times 10^{-7}$ [1/m] between 1 and 2000 [Hz]. This is a factor 24 below the MA curvature error specification.

Analog-to-Digital Conversion noise (PSD_{AD}) - The contributors to the ADC noise are the quantization error and its electrical noise. The former is neglected because it is ten times smaller than the electrical noise [82]. The electronic noise of the AD was described by white noise with a standard deviation of $\sigma = 2.44 \times 10^{-6}$ [V].

Environmental disturbances - Environmental disturbances like floor vibrations were neglected in the analysis because the manipulator is mounted onto the reticle stage short stroke. This module is isolated from the environment in order to minimize the effects of environmental disturbances on the lithography process.

Figure 5.21 provides the results of the disturbance analysis for the feedback control strategies of Section 5.4.2 and 5.4.3 in terms of *Cumulative Power Spectra (CPS)* of the curvature error e_{κ} . The CPS sums up to the squared variance of the curvature error ($\sigma_{e_{\kappa}}^2$) and shows which contribution is dominant across its frequency range [51, 64]. The left graphs shows the initial, MA and MSD curvature error for the decentralized

control across the piezoelectric actuators. The right graphs provide the results for the curvature feedback controller. The MA and MSD values were obtained by passing the initial curvature error signal through the following MA and MSD-filters [25]:

$$H_{\text{MA}}(\omega) = \frac{1}{\sqrt{1 + \omega^2/\omega_c^2}} \quad (5.8)$$

$$H_{\text{MSD}}(\omega) = \frac{1/2\sqrt{2}}{\sqrt{1 + \omega_c^2/\omega^2}} \quad (5.9)$$

where $\omega_c = 2\pi/T = 914$ [rad/s] is the filter cross-over frequency for a scan time of $T = y_{\text{slit}}/v_{\text{scan}}$, slit length of $y_{\text{slit}} = 5.5$ [mm] and scan speed of $v_{\text{scan}} = 0.8$ [m/s]. The results of the disturbance analysis highlights the following:

- The curvature error for the inner and outer feedback loop are equal to $\sigma_{e_\kappa} = 2.2 \times 10^{-7}$ [1/m] and $\sigma_{e_\kappa} = 0.84 \times 10^{-7}$ [1/m]. The additional curvature feedback loop reduces the curvature error by a factor 2.6.
- The induced MA and MSD curvature error by the disturbances are lower than the 2.4×10^{-6} [1/m] MA and 7.2×10^{-6} [1/m] MSD curvature error specification for both control strategies.
- The strain gauge sensor and ADC noise are the largest contributors to the curvature error for the local actuator feedback configuration. This is attributed to the small signal-to-noise ratio (SNR) of the strain gauge measurement signal. The SNR is defined by the readout electronics design of Section 4.4.3.
- The outer curvature feedback loop reduces the contributions of the noise sources that enter in the local piezoelectric actuator feedback loop by a factor of 3. The reduction is caused by the damping of the 740 [Hz] photomask resonance by the outer curvature feedback loop.
- The MA error of the curvature feedback loop is larger than the error of the local piezoelectric actuator feedback. This is caused by the curvature sensor noise which couples into the curvature output via the complementary sensitivity of Figure 5.18. It is advised to use a curvature sensor with lower noise levels than the $\sigma = 1 \times 10^{-7}$ [1/m] even though the MA curvature error specification was met.
- The contribution of the 740 [Hz] mechanical resonance to the MA curvature error is limited because the cut-off frequency of the MA filter is equal to 145 [Hz].
- The comparison of the MSD curvature error shows that the outer feedback loop reduces the error contribution at the 740 [Hz] mechanical resonance.

The above analysis highlights that both configurations are able to satisfy the curvature error specifications. An additional outer curvature feedback loop is therefore not necessarily needed for the disturbance rejection. Note that the validity of the servo performance does depend on the validity of the assumptions in Section 5.2 and the achievable

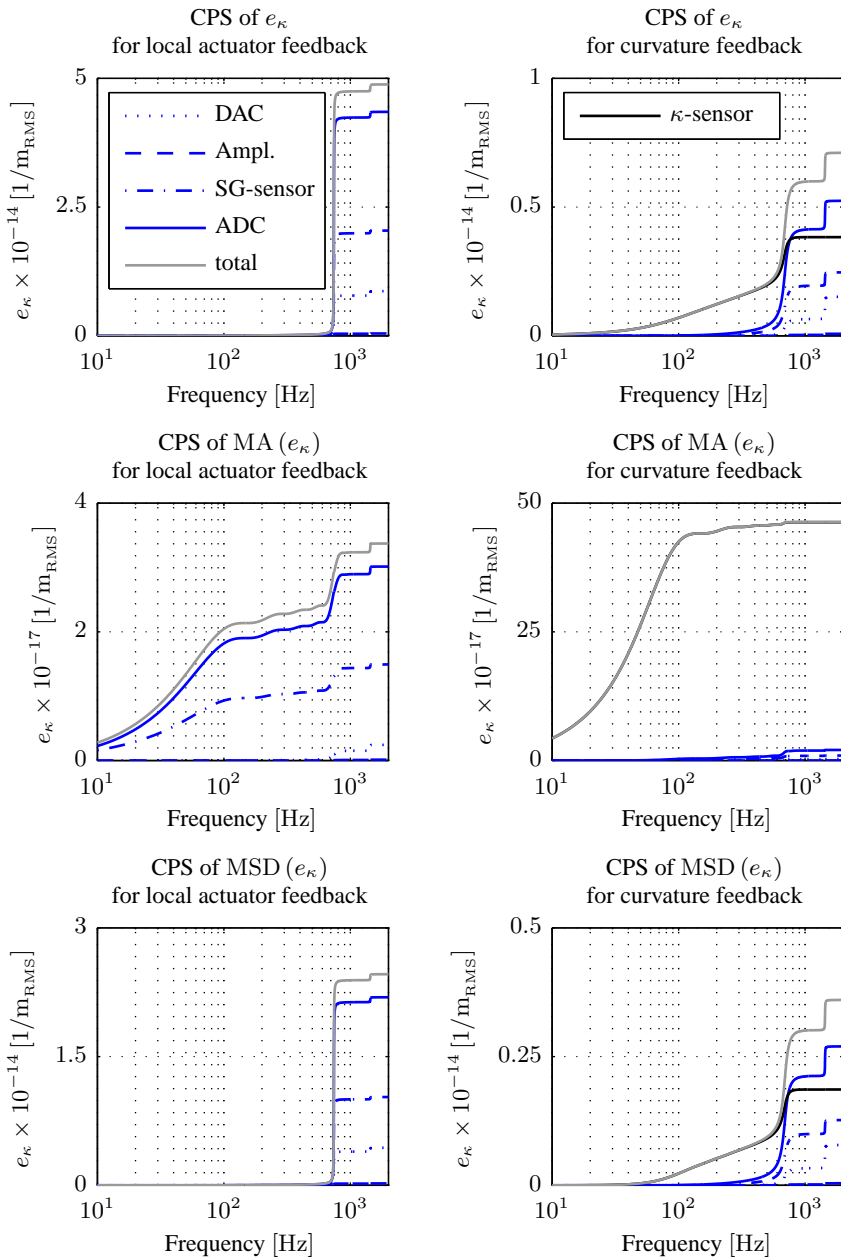


Figure 5.21: The results of the disturbance analysis for the system shown in Figure 5.20. The left graphs provide the results for the manipulator with local actuator feedback. The right graphs show the results for the additional curvature feedback.

controller bandwidth. Chapter 6 will provide a comparison between the controller modelling and measurement results.

5.5 Thermal performance

The thermal performance of the manipulator impacts the system's overlay. A budget of 90 [pm] was therefore allocated in Section 2.5.2 to the thermally induced overlay error. Section 4.2.7 showed that this corresponds to a heat load of 4 [mW] at the reticle edge. This section provides three analyses that evaluate the manipulator's thermal performance. Section 5.5.1 derives the power dissipation of the piezoelectric actuators. The thermal load by the leaky seal is determined in Section 5.5.2. The heat that is transferred from the strain gauge to the reticle is calculated in Section 5.5.3.

5.5.1 Piezoelectric actuator dissipation

The foregoing discussion mentioned that the piezoelectric actuator has negligible power dissipation when it is approximated by an ideal capacitance. This is not the case in reality. This section provides an estimate of the actuator's dissipation for the wafer curvature setpoint of Figure 5.19.

The power dissipation in the piezoelectric actuator was determined using the theory in [110]. It explains that heat generation in piezoelectric actuators is caused by the hysteretic relation between the electrical voltage U_p and electrical charge q . The hysteretic behaviour between the two quantities can be approximated by a phase delay δ' .

Appendix D shows that the addition of the phase lag in the linear piezoelectric actuator model makes it possible to describe the actuator by an equivalent electric circuit. This circuit consists of an ideal capacitor C' which is placed in parallel to a resistance R . The power loss in the circuit and hence the piezoelectric actuator for an applied sinusoidal voltage signal is described by:

$$P_{\text{loss}} = \frac{1}{2} \frac{U_n^2}{R} = \frac{1}{2} \omega_n C' \tan \delta' U_n^2 = \pi f_n C' \tan \delta' U_n^2 \quad (5.10)$$

where f_n is the excitation frequency, U_n the amplitude of the voltage signal and $\tan \delta'$ the loss coefficient. The latter has a constant value up to excitation frequencies of 2 [kHz], see [110].

An expression for the actuator power dissipation when it is excited by multiple excitation frequencies is obtained by taking the cumulative power dissipation [11]. This gives:

$$P_{\text{cum}} = \sum_{n=0}^N P_{\text{loss}} = \sum_{n=0}^N 2\pi f_n C' U_{\text{RMS}_n}^2 \tan \delta' \quad (5.11)$$

where $U_{\text{RMS}_n}^2 = U_n^2/2$ is the amplitude of the voltage power spectrum at frequency f_n . Figure 5.22 provides the cumulative power dissipation of one of the piezoelectric actuators in the curvature manipulator for the wafer curvature setpoint in Figure 5.19. It

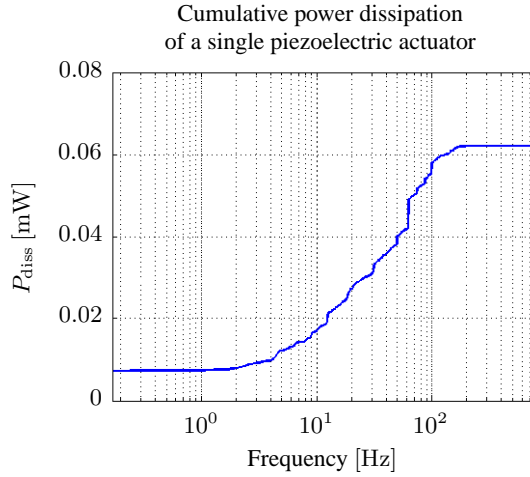


Figure 5.22: The cumulative power dissipation of one piezoelectric actuator in the curvature manipulator for the wafer setpoint profile in Figure 5.19.

was obtained using Equation (D.10) and the identified 1.13×10^5 [V/m] gain between the applied actuator voltage and the reticle curvature in Section 5.2. A loss tangent of $\tan \delta' = 0.02$ [-] and capacitance of $C' = 0.31$ [μ F] were used for the piezoelectric actuator properties [88]. Note that a static curvature correction is needed to account for lens heating induced defocus. The piezoelectric actuators have a negligible power dissipation for this setpoint because $f_n \approx 0$ [Hz].

The result in Figure 5.22 shows that the piezoelectric power dissipation for a single actuator is equal to $P_{cum} = 0.062$ [mW] which gives a total power dissipation of $P_{tot} = 0.43$ [mW] for seven piezoelectric actuators. It highlights that the power dissipation specification of 4 [mW] is satisfied by one order of magnitude.

5.5.2 Induced heat load by leaking vacuum clamp

The design of the manipulator includes a leaky seal between the photomask and the vacuum clamp. The pressure difference across the leaky seal results in a flow of air from the ambient surrounding to the vacuum chamber. This section estimates the thermal load of the air flow on the reticle. The calculation is performed in three steps [106]. First, the air temperature along the channel is determined. Second, the heat transfer between the air and the reticle and clamp is estimated using the calculated air temperature in the restriction. Third, the reticle temperature is determined using a steady state lumped thermal model of the actuator.

The thermal analysis is performed for the clamp geometry in Figure 5.23. It shows a two-dimensional cross section of the Fused Silica photomask and Aluminium clamp. The photomask and clamp are separated by a restriction with height $d_r = 10$ [μ m] and length $l_r = 1$ [mm] and a chamber with height $d_c = 200$ [μ m] and length $l_c = 3.5$ [mm] with respect to a symmetry axis. The width of the clamp is equal to the reticle length, i.e. $b = 152.4$ [mm]. The geometry of the restriction makes it possible to assume a two-

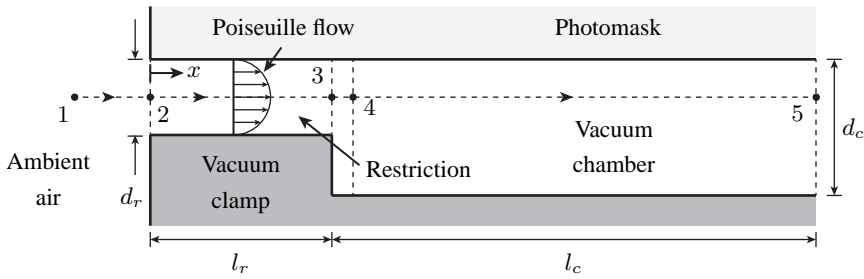


Figure 5.23: Geometry of the photomask and clamp interface. The interface has a depth b which is equal to the photomask length.

dimensional flow.

The pressure difference across the restriction drives the flow of air from the ambient surroundings into the vacuum chamber. The air will therefore follow a trajectory from 1 to 5. The ambient air has a pressure, density and temperature of respectively $p_1 = 1$ [bar], $\rho_1 = 1.24$ [kg/m³] and $T_1 = 293$ [K]. Section 4.4.2 explained that an absolute pressure of $p_5 = 0.3$ [bar] was measured in the vacuum cup. The pressure loss across the restriction is dominant. The air properties are therefore assumed equal to the ambient air properties at 1, i.e. $p_1 = p_2$, $T_1 = T_2$ and $\rho_1 = \rho_2$. A similar assumption for the pressure in the chamber gives $p_3 = p_4 = p_5$.

Air temperature along the restriction

The first step in the thermal analysis consists of estimating the temperature of the air along the x -direction of the restriction. The conservation of energy equation will be used to determine the air temperature in the direction of the flow. The calculation requires an estimate of the air velocity profile along the restriction. The estimate can be obtained by considering the Reynolds equation for a viscous flow between two stationary plates [117, 131, 132]:

$$\mu \frac{d^2 v(x, z)}{dz^2} = -\frac{dp(x)}{dx} \quad (5.12)$$

where x is the distance from the inlet of the restriction, z is the vertical direction across the height of the restriction, v is the flow velocity in x -direction, μ is the dynamic viscosity of the air and $dp(x)/dx$ is the pressure gradient along the length of the restriction. The Reynolds equation is a simplification of the Navier-Stokes momentum equation for fluid flow because the inertia and body force terms have been neglected. Furthermore, it assumes a thin film flow such that the pressure difference in z -direction is negligible. The thin film flow is also regarded as laminar ($Ma < 0.3$) and Newtonian. For the remainder of the analysis, it is also assumed that a Poiseuille flow profile has fully developed across the channel height and that the entry and exit effects are absent. The Poiseuille flow profile is schematically shown in Figure 5.23.

An expression of the velocity profile across the channel height is obtained by double

integration of Equation (5.12) with respect to the velocity profile. This gives:

$$v(x, z) = \frac{1}{\mu} \frac{dp(x)}{dx} \frac{z^2}{2} + C_1 z + C_2 \quad (5.13)$$

The air velocity is zero at the air-photomask and air-clamp interface. This translates into the following boundary conditions:

$$v(x, 0) = 0, \quad v(x, d_r) = 0. \quad (5.14)$$

Solving Equation (5.13) for the boundary conditions in (5.14) results in the following expression for the flow velocity:

$$v(x, z) = \frac{1}{2\mu} \frac{dp(x)}{dx} (z^2 - z d_r) \quad (5.15)$$

where d_r is the height of the restriction. An expression for the average velocity $\bar{v}(x)$ across the height of the restriction can then be obtained with:

$$\bar{v}(x) = \frac{1}{d_r} \int_0^{d_r} v(x, z) dz = -\frac{d_r^2}{12\mu} \frac{dp(x)}{dx}. \quad (5.16)$$

The next step is to derive the pressure variation along the length of the restriction. This is achieved by first rewriting Equation (5.16) as:

$$\frac{dp(x)}{dx} = -\frac{12\mu}{d_r^2} \bar{v}(x). \quad (5.17)$$

The conservation of mass defines that the mass flow \dot{m} along the restriction is constant. It is defined by:

$$\dot{m} = \rho(x) \bar{v}(x) A \quad (5.18)$$

where $A = d_r b$ is the surface area of a restriction's cross-section. Substituting the mass flow expression and the ideal gas law $\rho(x) = p(x) / (RT(x))$ into equation (5.17) gives:

$$\frac{dp(x)}{dx} = -\frac{12\mu}{d_r^2} \frac{\dot{m}}{A} \frac{RT(x)}{p(x)} \quad (5.19)$$

where R is the ideal gas constant.

The differential equation (5.19) cannot directly be solved for the pressure profile along

the restriction because the temperature $T(x)$ also depends on x . It is therefore proposed to first solve the equation for a constant temperature, i.e. $T(x) = T_2$ and later on verify what error is made by this approximation. Note that this only holds if the temperature variation ΔT across the restriction is small compared to the absolute temperature T , i.e. $\Delta T \ll T$.

The expression for the pressure in the channel is obtained by rearranging and integrating Equation (5.19) in the following way:

$$-\int_0^x p(x) dp = \int_0^x \frac{12\mu}{d_r^2} \frac{\dot{m}}{A} RT_2 dx \Rightarrow \frac{1}{2}p_2^2 - \frac{1}{2}p(x)^2 = \frac{12\mu}{d_r^2} \frac{\dot{m}}{A} RT_2 x \quad (5.20)$$

$$\Rightarrow \frac{p(x)}{p_2} = \sqrt{1 - \frac{24\mu}{d_r^2} \frac{\dot{m}}{A} \frac{RT_2}{p_2^2} x} \quad (5.21)$$

Substitution of $p(l_r) = p_3 = 0.3$ [bar] for $x = l_r$, $\mu = 18 \times 10^{-6}$ [Ns/m²] and the ideal gas relation $RT_2 = p_2/\rho_2$ into Equation (5.21) leads to the following estimate of the mass flow:

$$\dot{m} = \left(1 - \frac{p_3^2}{p_2^2}\right) \frac{d_r^2 A p_2 \rho_2}{24\mu l_r} \approx 40 \times 10^{-6} \text{ [kg/s]}. \quad (5.22)$$

The acquired mass flow value and the other known flow properties can then be used to rewrite Equation (5.21) into:

$$p(x) = p_2 \sqrt{1 - 914x}, \quad 0 \leq x \leq l_r \quad (5.23)$$

Similar formulae are obtained for the density and flow velocity when the ideal gas law $\rho(x) = p(x)/(RT(x))$, the mass flow $\bar{v}(x) = \dot{m}/(\rho(x)A)$ and Equation (5.23) are combined. This gives:

$$\rho(x) = \rho_2 \sqrt{1 - 914x} \quad (5.24)$$

$$\bar{v}(x) = \frac{\bar{v}_2}{\sqrt{1 - 914x}}. \quad (5.25)$$

The flow velocities at the start and end of the restriction are equal to $\bar{v}_2 = \dot{m}/(\rho_2 A) \approx 20$ [m/s] and $\bar{v}_3 \approx 68$ [m/s]. Both the Reynolds and the Mach number are evaluated at the end of the channel to see if the assumptions of a laminar and non-choking flow still hold. They are evaluated with the following formulae [132]:

$$\text{Re}_H = \frac{\rho \bar{v} D_H}{\mu} = \frac{\rho_3 \bar{v}_3 (2d_r)}{\mu} \approx 26 \quad (5.26)$$

$$\text{Ma}_3 = \frac{\bar{v}_3}{a} = \frac{68}{344} \approx 0.2 \quad (5.27)$$

where D_H is the hydraulic diameter of the channel and a is the speed of sound in air at $T = 293$ [K]. Note that the hydraulic diameter needs to be used because of the restriction's rectangular cross section. The derived Reynolds and Mach number for the isothermal flow confirm that the flow is laminar and non-choking flow because $Re_H < 2300$ and $Ma < 1$, see [132].

The next step in the analysis consists of estimating the change in the air temperature along the restriction for an adiabatic flow using the above derived flow velocity for an isothermal flow. The conservation of energy equation is used for this purpose. It is defined by:

$$h_2 + \frac{1}{2}v_2^2 = h(x) + \frac{1}{2}v(x)^2 \Rightarrow T(x) = T_2 + \frac{1}{2c_p} \left(v_2^2 - v(x)^2 \right) \quad (5.28)$$

where $h = c_p T$ is the enthalpy of the ideal gas and c_p is its specific heat. The temperature at the end of the restriction is estimated at $T_3 \approx 291$ [K] for the above derived flow velocities and $c_p = 1005$ [J/(kgK)].

The estimate of the 2 [K] temperature drop with the conservation of energy equation was obtained by using the derived pressure, density and velocity profile for the isothermal flow. The effect of the temperature drop on the initially calculated pressure profile along the restriction will now be considered. It is estimated by considering the following derivative of the ideal gas law:

$$p = \rho RT \Rightarrow dp = RTd\rho + \rho RdT \quad (5.29)$$

$$= RT_1(\rho_1 - \rho_3) + \rho_1 R(T_1 - T_2) \quad (5.30)$$

$$= 0.71 + 0.007 \text{ [bar]} \quad (5.31)$$

The second term in Equation (5.29) is approximately two orders lower than the former. It highlights that the effect of the temperature variation on the initial results are negligible and that the initially calculated temperature profile is probably a good first estimate.

Figure 5.24 provides a summary of the pressure, density, flow velocity and temperature distribution along the restriction. The graph of the temperature shows that the largest drop takes place at the end of the channel due to the expansion of the flow.

The results of the analytical model were verified using Computational Fluid Dynamics (CFD) software for the same channel geometry, initial conditions and adiabatic conditions [99]. The model had similar pressure, density, velocity and temperature profiles as shown in Figure 5.24. Furthermore, the temperature difference between the entry and exit of the restriction was equal to 1.6 [K] which is in the same order of magnitude as the 2 [K] of the analytical model. The results of the numerical model therefore verify the results of the analytical thermal model.

Heat exchange of the flow with its surroundings

The preceding part derived the air temperature profile for an adiabatic air flow through the restriction. In reality, the air temperature is somewhere in between the adiabatic and

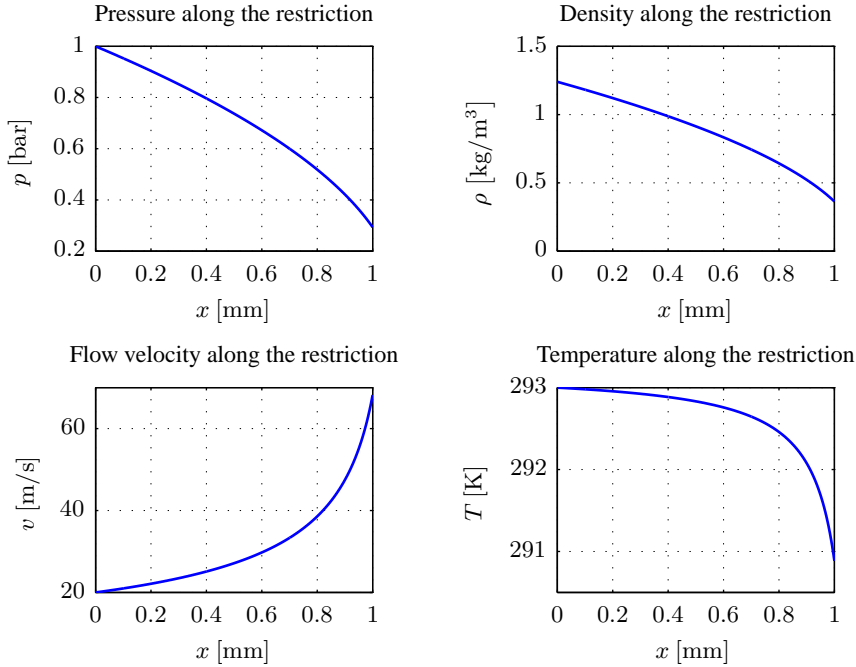


Figure 5.24: The pressure, density, velocity and the temperature of the air as a function of the position in the leaky seal. Note that the entry and exit effects are neglected in the analysis.

isothermal conditions because heat exchange will occur between the air and its surroundings when there is a temperature difference between them. The heat exchange will have an effect on the fluid flow. These effects should normally be quantified with a detailed model that couples the thermal conduction in the structure with the flow evolution along the channel. Such a model is outside the scope of this thesis however.

An alternative way to estimate the heat exchange between the reticle and its surroundings is to use the derived temperature profile of the above adiabatic analysis and quantify how much heat is needed in order to keep the air at its initial temperature (isothermal). The following part will estimate this heat transfer when it is assumed that the walls of the channel, i.e. the reticle and clamp, have a temperature of $T_w = 293$ [K]. Convection is the driving heat transfer mechanism between the air and the walls.

The first step is to derive an expression for the heat exchange between the gas and the walls with constant temperature for a restriction length dx . It is defined by [73]:

$$h_c P (T_w - T_g) = \dot{m} c_p \frac{dT_g}{dx} \quad (5.32)$$

where h_c is the convection coefficient in $[\text{W}/(\text{m}^2\text{K})]$, $P \approx 2b$ is the perimeter in [m] over which the convection takes place whilst T_w and T_g are the wall and gas temperature in [K].

An expression for the gas temperature change can be found by integrating Equation

(5.32) for a gas temperature $T_g(x)$ at location x and $T_g(x + \Delta x)$ at position $x + \Delta x$. This gives:

$$\int_{T_g(x)}^{T_g(x+\Delta x)} \frac{dT_g}{T_g - T_w} = - \int_x^{x+\Delta x} \frac{2bh_c}{\dot{m}c_p} dx \quad (5.33)$$

$$\ln \left(\frac{T_g(x + \Delta x) - T_w}{T_g(x) - T_w} \right) = - \frac{2bh_c}{\dot{m}c_p} \Delta x. \quad (5.34)$$

Equation (5.34) can be rewritten as [73, 125]:

$$E = \frac{T_g(x + \Delta x) - T_g(x)}{T_w - T_g(x)} = 1 - e^{-N_{tu}}, \quad N_{tu} = - \frac{2bh_c}{\dot{m}c_p} \Delta x \quad (5.35)$$

where E is the effectiveness of the heat exchange and N_{tu} is the Number of Transfer Units (NTU). The effectiveness can be considered as the actual heat transfer divided by the maximum heat transfer for an infinitely long channel. The NTU provides a measure of the heat transfer capability between the air and the walls.

Let's now consider the effectiveness of the heat transfer between the air flow and the walls. An estimate of the convection coefficient is first obtained with [73]:

$$h_c = \text{Nu} \frac{k}{d_r} \approx 2 \times 10^4 \text{ [W/(m}^2\text{K)]}, \quad (5.36)$$

where $\text{Nu} \approx 7.5 [-]$ is the Nusselt number of the air flow through the restriction and $k = 0.026 \text{ [W/(mK)]}$ is the conduction coefficient of the air. The convection coefficient is used to determine the NTU for one-tenth of the restriction length, i.e. $\Delta x = 0.1 \text{ [mm]}$. The NTU for that length is equal to:

$$N_{tu} = - \frac{2bh_c}{\dot{m}c_p} \Delta x \approx 15 [-] \quad (5.37)$$

which corresponds to a heat transfer efficiency of $E \approx 1 [-]$. The heat transfer efficiency value highlights that sufficient heat transfer takes place to keep the air temperature at the same temperature as the walls across relatively short lengths. This conclusion therefore also holds for the full restriction length l_r because the $N_{tu} = 80 [-]$.

The amount of heat that is transferred to the gas in order to compensate for the above estimated 2 [K] temperature drop is equal to:

$$\dot{Q}_{\text{air}} = \dot{m}c_p \Delta T \approx 80.4 \text{ [mW]}. \quad (5.38)$$

This exceeds the 4 [mW] specification of Section 4.2.7 by a factor of 20.

A CFD model was again made to verify the acquired analytical result [99]. The model

simulated the flow behaviour for the channel geometry, the initial conditions of the air and isothermal walls of $T_w = 293$ [K]. The analysis showed that the gas temperature was approximately equal to the wall temperature for the first half of the restriction. It had a temperature difference of 0.4 [K] at the end of the restriction however which is attributed to the steep temperature drop of the air near the end of the restriction. The calculated heat load from the wall to the air in the CFD model was equal to 56 [mW]. The above analytical approximation therefore provides a worst case estimate of the heat load by the air flow through the restriction.

The heat on the reticle by the air flow is not only limited to the area of the restriction. The ratio between the chamber and the restriction height of $d_c/d_r = 20$ results in a stagnation of the air when it flows into the vacuum chamber. Its velocity slows down to $v_4 \approx 68/20 = 3.4$ [m/s].

The temperature change by the stagnation just after the restriction can be determined using the conservation of energy as was done in Equation (5.28). It results in a temperature of $T_4 \approx 295$ [K] for $v_3 = 68$ [m/s] and $T_3 = 293$ [K]. The value highlights that the temperature change is equal but opposite to the adiabatic temperature drop in the restriction. The heat transfer efficiency E can again be used to determine if there is sufficient heat transfer between the air and its walls in order to keep the gas temperature at $T_w = 293$ [K]. The NTU and the heat transfer efficiency for the length of the vacuum chamber l_c is equal to:

$$\text{NTU} = 80 \frac{d_r}{l_r} \frac{l_c}{d_c} \approx 14 [-] \Rightarrow E \approx 1 [-]. \quad (5.39)$$

The heat transfer efficiency value again shows that the air temperature in the vacuum chamber return back to the wall temperature before it exits the clamp. This was confirmed by the CFD model [99]. Note that the heat that is transferred to the air in the vacuum chamber is equal but opposite to the value of Equation (5.38) because of the 2 [K] rise of the air temperature after the restriction.

Lumped thermal model of the manipulator

The above derivation showed that the local heat loads in the restriction and the vacuum cup exceed the 4.4 [mW] specification that was defined in Section 4.2.7. The lumped thermal model of Figure 5.25 was generated in order to quantify the effect of these heat loads on the reticle temperature distribution and its expansion. The figure shows the locations a to p within a single actuator unit and the thermal resistances (R_1 to R_{18}) between them. The latter were determined using the thermal resistance definition of a gas or a solid [73]:

$$R_{\text{solid}} = \frac{L}{kA}, \quad R_{\text{gas}} = \frac{1}{h_c A} \quad (5.40)$$

where h_c is the convection coefficient, k the conduction coefficient of the material whilst A and L are respectively the cross section and length of the solid through which the heat

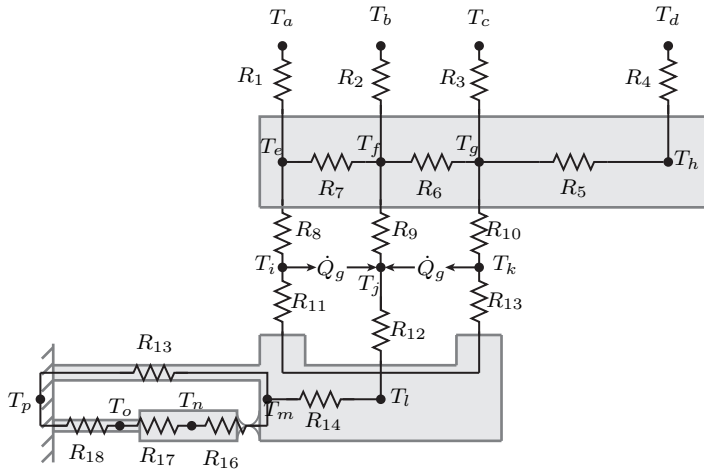


Figure 5.25: The lumped thermal model of the single bending actuator of Figure 4.23.

load travels.

The effect of the local cooling and heating of the gas due to its expansion was included by the addition of the heat flow $\dot{Q}_g = \dot{Q}_{\text{air}}/7$ in the restriction. The heat flow is extracted at the node in the restriction and inserted at the node of the vacuum area. This behaviour effectively simulates a local heat pump. The temperatures T_a to T_d correspond to the ambient air whilst T_p is that of the reticle chuck. They are assumed to have a constant temperature of 293 [K].

The steady state results of the thermal analysis are provided in Table 5.1. It shows that the temperatures of the photomask have changed in the order of milliKelvins. The values also demonstrates that the reticle cools down by the leaking vacuum clamp except at node j in the centre of the clamp. The calculated heat flux values also showed that the interaction between the air and the aluminium vacuum clamp is dominant. This is attributed to the factor 200 difference between the thermal conductivity of the aluminium and fused silica.

The thermal expansion of the reticle by the leaking vacuum clamp was finally estimated with Equation (4.19). It is equal to:

$$\Delta u = \alpha \Delta T_h \Delta x \approx -47 \text{ [pm]} \quad (5.41)$$

for a thermal expansion coefficient of $\alpha = 0.51 \times 10^{-6} \text{ [1/K]}$ and $\Delta x = 71.2 \text{ [mm]}$. The thermal expansion corresponds to a pattern distortion of approximately 10 [pm] at wafer level which satisfies the 90 [pm] specification of Chapter 2. It is nevertheless recommended to verify and to validate the thermal impact of the leaky vacuum clamp on the reticle with measurements.

Case	Temperature change at nodes in [mK]										
	ΔT_e	ΔT_f	ΔT_g	ΔT_h	ΔT_i	ΔT_j	ΔT_k	ΔT_l	ΔT_m	ΔT_n	ΔT_o
A	-14	37	-14	-2	-16	49	-16	-5	-5	-2	0
B	840	830	835	76	841	836	839	842	857	2503	108

Table 5.1: Calculated temperature change at the nodes of the thermal model in Figure 5.25 for different thermal loads. Case A: the temperature change that is induced by the air flow into the leaky vacuum clamp. Case B: the temperature change due to a strain gauge heat load of 36 [mW].

5.5.3 Strain gauge heat load

Section 4.4.3 showed that the power dissipation of the strain gauge on the piezoelectric actuator is equal to 36 [mW]. This exceeds the 4 [mW] power dissipation requirement by a factor of 9. The reticle thermal expansion by the strain gauge power dissipation was determined using the model in Figure 5.25 for an applied heat load of $Q = 36$ [mW] at location n . It resulted in the steady-state temperatures in Table 5.1. The thermal expansion of the reticle was estimated at 2.77 [nm] or 0.7 [nm] at wafer level. It exceeds the 0.09 [nm] elongation requirement by a factor 7.6.

The above shows that solutions need to be found to reduce the strain gauge heat load. One possibility is to lower the applied voltage across the Wheatstone bridge by a minimum of one order as was proposed in Section 4.4.3. The second possibility is to determine the thermal expansion of the reticle and identify its correctability with the lithography system just like the induced pattern distortions by bending. Finally, alternative sensor concepts for the measurement of the piezoelectric actuator elongation could be researched. It is recommended to investigate the above alternatives for future curvature manipulator concepts.

5.6 Summary & Conclusions

The objective of this chapter was to estimate the performance of the curvature manipulator. It was investigated using a reduced-order Finite Element model and control-oriented model of the manipulator design in Chapter 4. The results were compared to the system performance specifications and the ideal bending results of Chapters 2 and 3.

The chapter started with an explanation of the mechanical and control-oriented model of the curvature manipulator. The mechanical model was obtained by assembling reduced-order FE models of the manipulator components with the Dynamic Substructuring methodology [27]. The control-oriented model consisted of the reduced-order FE model of the manipulator with reticle, the piezoelectric actuator drive electronics and the strain gauge sensor electronics. Hysteresis and system delay were neglected in order to obtain an LTI system for the control analysis. A fictitious curvature sensor was included in the model in order to investigate the manipulator performance for a direct curvature feedback controller.

The mechanical performance of the manipulator was analysed first. It provided the following results:

- The first out-of-plane and in-plane resonance frequency of the reticle with manipulator are equal to 506 [Hz] and 2107 [Hz]. The eigenmodes of the reticle have not significantly changed by the addition of the manipulator.
- The manipulator satisfies the curvature specification of $\kappa_x = -0.4 \times 10^{-3}$ [1/m] with a factor 1.4. A higher-order deflection with an amplitude of 1.3 [nm] is also induced because of the parasitic stiffness and motion of the manipulator.
- The reticle pattern distortions by bending has the expected asymmetric magnification contribution with additional higher order errors by the manipulator. The residual distortions after correction are in the order of the 50 [pm] design rule.
- The manipulator induces a stress-birefringence of 0.18 [nm/cm] for a curvature of $\kappa_x = -0.4 \times 10^{-3}$ [1/m].
- The manipulator changes the reticle's induced in-plane distortions and out-of-plane deformation by gravity with 0.6 [nm] and 1.9 [nm] at wafer level.

The results of the mechanical analysis showed that the manipulator satisfies the specifications in terms of achievable curvature, pattern distortions, stress-birefringence. The Matched Machine Overlay and system eigenfrequency specifications are also satisfied. The control performance of the manipulator was investigated for two control strategies. The first consisted of a decentralized controller across each collocated piezoelectric actuator and strain gauge sensor. This controller could be applied because of the decoupling between the manipulator axes. The bandwidth was limited to 530 [Hz] by the 4 [kHz] sample frequency. The second strategy had the local feedback control across the actuators and an additional outer curvature feedback loop. The latter had a bandwidth of 130 [Hz]. The performance of both controllers was compared in terms of curvature tracking performance for a wafer curvature setpoint and the curvature error due to system disturbances. The analysis provided the following insights:

- The curvature tracking error for the first and second control strategy both satisfy the MA and MSD specifications. The MSD error is lower for the strategy with the curvature feedback loop because the 740 [Hz] resonance frequency of the reticle is damped. This is not the case for the local curvature feedback loop because the eigenfrequency is unobservable by the strain gauge.
- The MA and MSD curvature errors by identified system disturbances (sensor, amplifier, ADC and DAC noise) satisfy the MA and MSD curvature specifications. The strategy with the outer feedback loop has again a lower MSD error. Analysis showed that the curvature sensor noise should be below 1×10^{-7} [1/m]. The analysis confirmed that the disturbances for the inner loop strategy are not performance limiting.

The thermal performance of the manipulator was finally analysed. It provided the following results:

Criteria		Specification	Model of manipulator	Unit	Satisfies specification?
Imaging	Curvature	0.4×10^{-3}	0.4×10^{-3}	[1/m]	Yes
	Birefringence	1	0.18	[nm/cm]	Yes
	Fading	2	1.6	[nm]	Yes
Overlay	DCO	0.05	0.06	[nm]	Yes ¹
	MMO	0.60	0.36	[nm]	Yes

¹ Can only be achieved with additional machine overlay corrections.

Table 5.2: Comparison of the curvature manipulator specifications of Chapter 2 and the performance analysis results of the detailed curvature manipulator model in this chapter.

- The fourteen piezoelectric actuators have a power dissipation of 0.43 [mW] which satisfies the 4 [mW] dissipation specification by a factor of 10.
- The air flow into the leaky vacuum clamp results in a heat flow in the clamp and reticle. The induced thermal expansion is estimated at 47 [pm] at reticle level.
- The strain gauge power dissipation of 36 [mW] results in a reticle thermal expansion of 2.3 [nm] at reticle level.

The thermal analysis proved that the actuator and leaky seal satisfy the design specification. The introduced heat load by the strain gauge appears to be too large however. The following recommendations are given for future investigations:

- Include manipulator non-linearities in the model in order to investigate their effect on the manipulator performance. The non-linearities can include piezoelectric actuator hysteresis, drift and hysteresis in the reticle-manipulator contact. Examples of a model for the piezoelectric actuator hysteresis can be found in [57].
- Study the impact of higher sampling frequencies and system delay on the curvature manipulator performance.
- Investigate curvature sensor technologies such that direct curvature feedback can be applied. Furthermore, it is advised to use the disturbance analysis results to identify the curvature sensor requirements.
- Lower the drive voltage of the Wheatstone bridge in order to reduce the power dissipation by the strain gauge. Furthermore, it is recommended to investigate alternatives to the strain gauge sensor.

The following chapter continues the investigation into the curvature manipulator performance. It provides the experimental validation results for a realized manipulator setup.

Part II

Experimental Analysis of the Curvature Manipulator

Chapter 6

Experimental validation of the full actuator array

This chapter presents the experimental validation of the curvature manipulator of Chapter 4. The validation measurements are performed with a metrology system that measures the reticle deflection. The results are compared to the predicted bending performance in Chapter 5. It is shown that the modelled and measured deflection shapes are comparable but that further steps are needed in order to satisfy the bending manipulator specifications of Chapter 2.

6.1 Introduction

Chapter 1 defined two thesis objectives where the second objective was to design and validate a reticle curvature manipulator that satisfies high level lithography specification and boundary conditions. This chapter focusses on the validation of the designed manipulator in Chapter 4 by comparing its measured bending behaviour to the system design specifications of Chapter 2.

The validation measurements are covered in the following manner. Section 6.2 introduces the experimental setup that was used to perform the experimental validation of the curvature manipulator. This setup is known as the *Multi-Axis FUMO*. Section 6.3 presents the measurement results and the performance of the manipulator in terms of curvature. The chapter ends with a summary and conclusions in Section 6.4.

Note that a *Single-Axis* setup was also built for the validation of a single actuator unit. Its measurement results are provided in Appendix E.

6.2 Experimental setup

The experimental setup that was used to validate the curvature manipulator design of Chapter 4 is outlined in this section. Section 6.2.1 introduces the objectives of the measurement setup. The setup is thereafter explained in Section 6.2.2. The obtained insights during the realization of the measurement setup are provided in Section 6.2.3

6.2.1 Objectives

The validation measurements had two objectives. The first objective was to identify the static and dynamic bending performance of the curvature manipulator. Specific attention is given to the manipulator performance for the decentralized feedback control across the collocated piezoelectric actuators and strain gauge sensors. The second objective consisted of investigating calibration strategies for the manipulator in order to obtain the uniform bending moment with discrete bending actuators.

6.2.2 Setup description

The experimental setup that was used to validate the curvature manipulator design is provided in Figure 6.1. The top and bottom picture respectively show the curvature manipulator assembly and the external metrology setup that was used to measure the reticle deformation. The latter is an existing surface metrology setup which is placed on active vibration isolators with a cut-off frequency of 3 [Hz] in order to limit the transmission of ground vibrations into the setup.

It is desired to quantify both the out-of-plane and in-plane deformation of the reticle due to bending. Section 6.2.2.1 explains the measurement principle that was used to identify the out-of-plane reticle deformation by bending. The considerations for the pattern distortion measurements are thereafter provided in Section 6.2.2.2.

6.2.2.1 Reticle deflection measurements

Figure 6.2 gives a schematic view of the external metrology setup that was used to measure the reticle deflection. It shows the positioning stage that can be placed between the reference flat and the reticle at a desired x - and y -location. The distances to the chrome covered Zerodur[®] reference flat and the reticle surface are measured with off-the-shelf capacitive sensors in the stage.

Table 6.1 provides requirements for the reticle deflection measurements. The range and accuracy were identified with the beam deflection relation of Equation (2.2) for the curvature range and accuracy. Capacitive sensors were selected for the out-of-plane measurements because their 50 [μm] is large enough to capture the photomask deflection across the full curvature range. Furthermore, they have a resolution of 0.2 [nm] which should

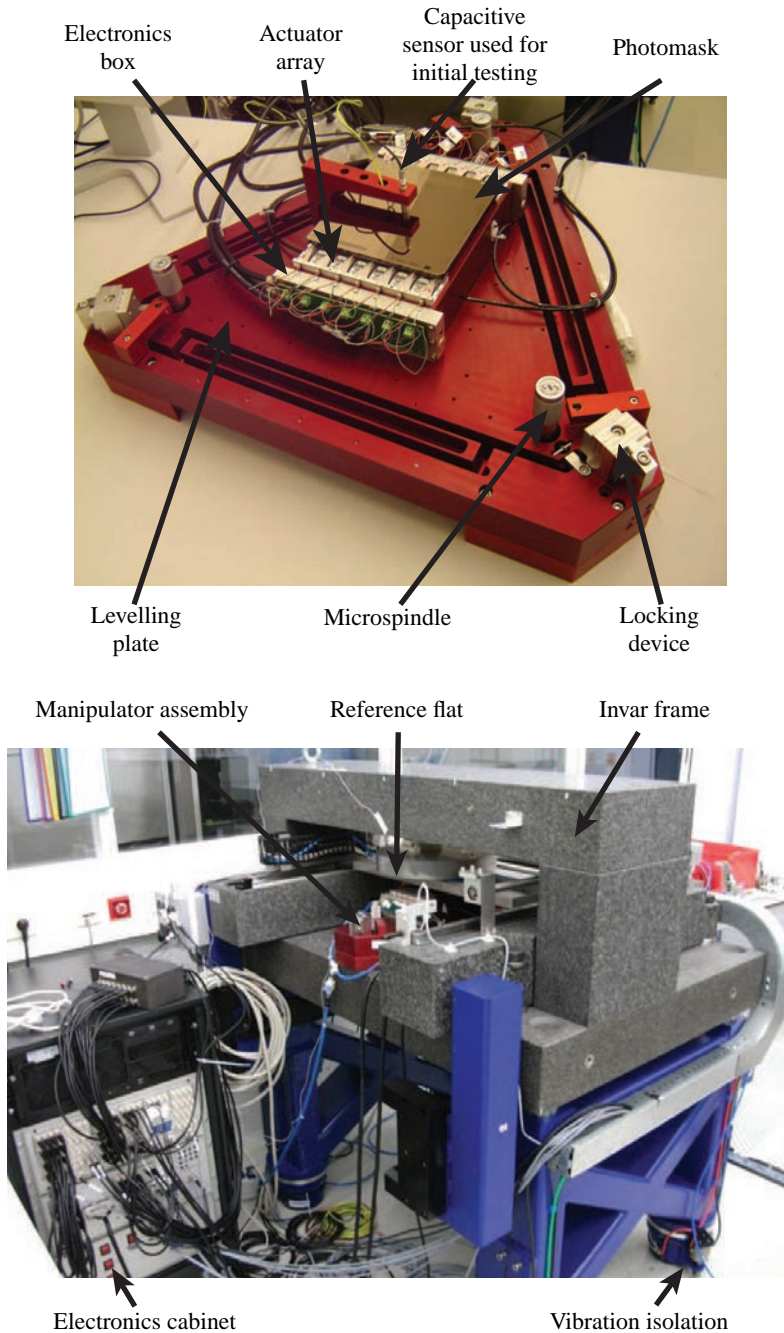


Figure 6.1: The measurement setup that was used for the experimental validation of the curvature manipulator. The top and bottom picture respectively show the realized curvature manipulator and the external metrology system.

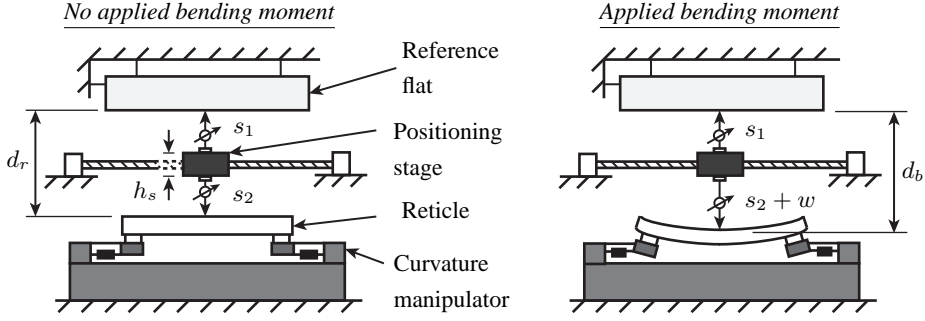


Figure 6.2: The differential measurement that is used to identify the reticle deflection by the curvature manipulator. It consists of subtracting the measured distance d_r between the reticle and the reference flat of an undeformed reticle (left picture) from the identified distance d_b of a bent reticle (right picture) in order to determine the reticle deformation w by bending.

make it possible to identify curvatures of:

$$\kappa_x = \frac{2w}{x^2} = \frac{2 \cdot 0.2 \times 10^{-9}}{(15 \times 10^{-3})^2} \approx 1.8 \times 10^{-6} \text{ [1/m]} \quad (6.1)$$

for a 15 [mm] pitch between measurement locations.

The reticle deformation w by bending is quantified by a differential measurement. It consists of subtracting the measured distance d_r between the reticle and the reference flat of an undeformed reticle from the identified distance d_b of a bent reticle. Both measurement configurations are drawn in Figure 6.2. The measurement is mathematically described by:

$$w(x, y) = d_b(x, y) - d_r(x, y) \quad (6.2)$$

where

$$d_b(x, y) = s_1(x, y) + s_2(x, y) + w(x, y) + h_s \quad (6.3)$$

$$d_r(x, y) = s_1(x, y) + s_2(x, y) + h_s \quad (6.4)$$

for a stage height h_s and measured distances $s_1(x, y)$ and $s_2(x, y)$ by the capacitive sensors for the configuration without applied bending moment. The applied differential measurement has the advantage over an absolute measurement because it reduces the contribution of systematic errors like stage dynamics, reticle flatness and gravity deflection. The inability to measure the latter quantity makes it impossible to determine the Matched-Machine-Overlay penalty however. The modelled MMO results of Section 5.3.5 are therefore not validated in this thesis.

The total reticle surface deflection is obtained by stitching measured reticle deflections at different x, y -locations. This approach has two advantages. First, it limits the time

Category	Requirement	Value	Unit	Ref.
Actuation	Maximum curvature	0.4×10^{-3}	[1/m]	Section 2.5.1
	Curvature accuracy	2.4×10^{-6}	[1/m]	Section 3.3.1
Metrology	Out-of-plane measurement range	± 1.16	[μm]	-
	Out-of-plane measurement accuracy	0.1	[nm]	-
	In-plane deformation range	97	[nm]	-
	In-plane deformation accuracy	0.58	[nm]	-
	Strain measurement range	1.27×10^{-6}	[-]	-
	Strain measurement accuracy	7.62×10^{-9}	[-]	-
	Mechanical eigenfrequency metrology system	> 500	[Hz]	-

Table 6.1: Overview of the derived measurement requirements for the Multi-Axis FUMO.

of a single differential measurement at each location to approximately 30 [s]. The short measurement time ensures thermal stability of the metrology setup. Second, the dynamic excitation of the setup is minimized because the measurement stage is kept at a stationary position during measurements. The stitching procedure does assume repeatability of the reticle manipulator. Section 6.3.3.1 will show that the reticle curvature manipulation has a standard deviation of $\max(\sigma(w)) = 5.6$ [nm]. It was unable to identify if the repeatability error is caused by the curvature manipulator or the metrology tool.

6.2.2.2 Pattern deformation measurements

It is desired to measure the in-plane pattern deformations by bending. Table 6.1 provides the measurement requirements in terms of strain and deformation. They were obtained with Equation (2.3) and the relation for the in-plane beam deformation [43]:

$$u = \frac{1}{2}t\kappa x \quad (6.5)$$

where u is the pattern deformation in [m], x is the location with respect to the reticle centre in [m] and $t = 6.35$ [mm] is the reticle thickness. The values in Table 6.1 should ideally be factor two smaller because the curvature accuracy specification of Section 3.3.1 corresponds to a distortion of 0.1 [nm] at wafer level instead of the 50 [pm] design rule.

Metrology concepts were pursued for the in-plane pattern deformation measurement of the reticle. It was finally chosen to omit this functionality in the setup because no commercially available sensor was found that could achieve the in-plane measurement requirements of Table 6.1. Instead, first-order estimates of the pattern distortions are obtained by deriving the reticle local angles from the measured out-of-plane deflection and then multiplying the angles by half the reticle thickness. This is explained in Section 6.3.4. The method is unable to predict the distortions by in-plane forces however.

It should be noted that novel sensor technologies have become commercially available after the validation measurements. One specific example are Fibre Bragg Gratings with a reported measurement resolution of 20 nano-strain [105]. It is recommended to inves-

tigate this further for future curvature manipulator experimental setups.

6.2.3 Realization

The realization of the Multi-Axis FUMO and initial testing provided a number of insights. This section gives an overview of the issues, acquired insights and explains their impact on the final manipulator performance.

Vacuum clamp manufacturing

Manufacturing of the monolithic leaf spring with integrated vacuum clamp demonstrated the manufacturing difficulty and fragility of the part. The former is caused by its three-dimensional shape, miniature details and compliancy. Multiple clamp prototypes fractured or did not satisfy the specifications because the part was difficult to constrain during the manufacturing process.

The flatness specification of the clamp has to be below 10 [μm] in order to ensure a nominal gap of 10 [μm] of the leaky seal. Milling and diamond turning process steps were used to be 5 [μm] off the 10 [μm] flatness requirement. This was considered acceptable because of the long lead time (approx. 3 months) and high cost (approx. € 10,000) of the clamps.

Piezoelectric actuator integration

The following issues were encountered when integrating the piezoelectric actuators with strain gauges in the manipulator assembly. First, the heat shrink around the actuator had to be removed in order to fit the actuator in the assembly. Kapton[®] foil was wrapped around the actuator in order to reduce the possibility of Electrostatic Discharge (ESD) between the piezoelectric actuator and other parts in the setup. Second, one of the soldering connections on the strain gauges broke during the assembly procedure. The setup was not disassembled to repair the strain gauge because of the large risk of other failures. One of the piezoelectric actuators could therefore not be operated in closed loop.

Achieved vacuum pressures in the clamp

The achievable bending moment on the reticle depends on the realized vacuum pressures in the clamp with the leaky seal. Special assembly tooling was developed to ensure that the top of the interface rods have a 10 [μm] offset with respect to the vacuum clamp top surface [118]. A pressure of -0.72 [barg] was measured in the vacuum clamps of the setup in Figure 6.1. This is 4% lower than the identified -0.75 [barg] in Section 4.4.2 which translates to a 4% drop in achievable bending moment.

Photomask z-supports

The z-supports and bending manipulator were mechanically decoupled in order to ensure a pure reticle pattern magnification error by bending. Section 4.4.1 demonstrated that the z-support stiffness in the z -direction is needed in order to avoid a parasitic z -translation of the reticle. The mechanical preloading mechanism in Figure 4.23 was therefore included

between the intermediate body and the z-support in order to constrain the reticle on the z-supports. The mechanism was omitted in the final setup however because it did not work properly.

The parasitic z-motion of the reticle indeed showed up in the first measurements with the experimental setup. This parasitic motion was visible in both directions which proved that the reticle was not supported in its neutral position. This is probably caused by the assembly tolerances and the 60 [V] bias voltage that is applied across the piezoelectric actuators in order to achieve the push-pull bending functionality. The following actions were taken in order to keep the reticle on the z-supports during measurements. First, mechanical contact between the reticle and the z-supports was realized by the application of a lower bias voltage to the piezoelectric actuators. This limited the actuator voltage range to only 16 [V]. Second, it was chosen to only realize downward deflections of the reticle centre in order to keep the reticle on the z-supports. The above highlights that the z-supports and bending manipulator must be integrated into one design and that the parasitic effects of the 60 [V] bias voltage must be minimized. It is recommended to investigate these items for future manipulator designs.

6.3 Measurements

The experimental validation of the curvature manipulator was performed with the introduced experimental setup of Section 6.2. This section provides a summary of the performed experiments. Section 6.3.1 presents the calibration measurements that were performed for the curvature manipulator. The feedback controller implementation is thereafter explained in Section 6.3.2. The static and dynamic curvature manipulation performance are finally provided in Section 6.3.3. The results are compared to the modelled results of Chapter 5.

6.3.1 Calibration

The first step in the experimental validation of the curvature manipulator consisted of calibration measurements. This step is necessary in order to relate the behaviour of the custom made actuators and sensors in terms of measurable quantities and to facilitate accurate reticle curvature control.

Figure 6.3 provides the selected control strategy for the curvature manipulator that was introduced in Chapter 5. It shows two grey blocks, namely the strain gauge sensor gains \mathbf{G}_{sg} to go from measured strain gauge voltages (\mathbf{U}_s) to actuator elongations (\mathbf{y}_l) and the input decoupling vector \mathbf{T}_i to go from photomask curvature (r_κ) to the piezoelectric actuator elongation setpoint (\mathbf{r}_l). Both gains were identified by calibration measurements. The calibration results are explained in respectively Section 6.3.1.1 and 6.3.1.2.

6.3.1.1 Calibration of strain gauge sensor gains

The strain gauge sensor gains need to be identified in order to ensure accurate control of the piezoelectric actuator elongation. Calibration measurements were therefore per-

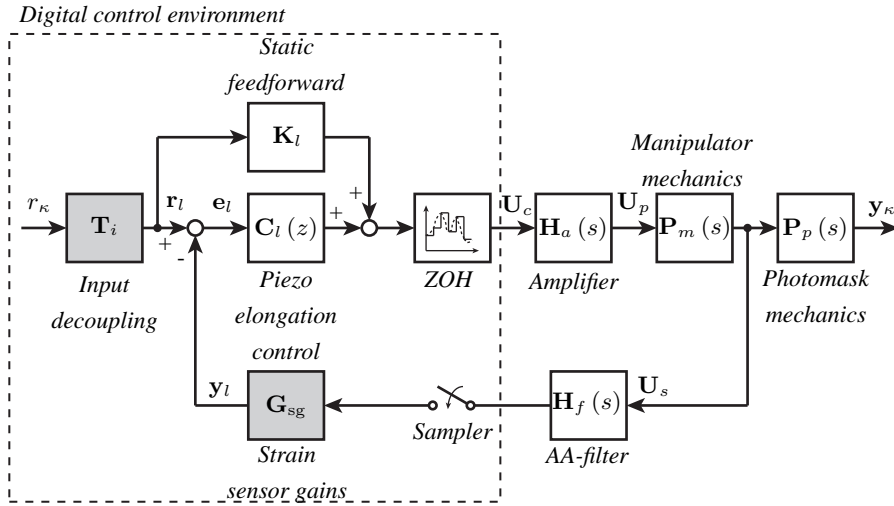


Figure 6.3: The control strategy for the curvature manipulator that was introduced in Figure 4.18. The grey blocks G_{sg} and T_i correspond to the strain gauge sensor gains to go from measured strain gauge voltages U_s to actuator elongations y_l and the input decoupling gains to go from curvature (r_κ) to actuator elongation (r_l) setpoints. Calibration measurements were performed to identify these gains.

formed in order to identify the relation between the measured strain gauge voltage and the actuator elongation for the fourteen strain gauge sensors. This section explains the calibration measurements and estimates the effects of the strain gauge sensor errors on the curvature manipulator performance.

The calibration measurements of the strain gauge gains were performed with the measurement setup of Figure 6.4. A separate measurement setup was used because it was easier to measure the actuator elongation with a reference measurement system. The setup has a removable top part to which one end of the piezoelectric actuator can be mounted. A reference target is fixed to its other end. The lid and piezoelectric actuator is then locked on a mounting frame. A calibrated capacitive sensor¹ with sub-nm noise level is placed in the mounting frame and measures the distance to the target.

The results of the calibration procedure for one of the piezoelectric actuators and strain gauge sensors is provided in Figure 6.5. The top-left graph shows the voltage setpoint U_c that was supplied to the piezoelectric actuator amplifier as a function of time. A triangular voltage signal was selected because it allows independent amplitude and velocity scaling of the setpoint.

The top-right graph of Figure 6.5 shows the measured elongation y_l of the piezoelectric actuator as a function of the applied triangular excitation signal. It confirms the hysteretic behaviour of the piezoelectric actuator. The hysteresis is approximately 13% of the piezoelectric actuator elongation amplitude of $15.8 [\mu\text{m}]$ and has to be counteracted by the feedback controller across the piezoelectric actuator. Measurements showed that the elongation of the piezoelectric actuator is only amplitude dependent.

The middle-left graph of Figure 6.5 shows the piezoelectric actuator elongation as a

¹Physik Instrumente capacitive sensor consisting of a probe (D-510.020) and signal conditioner (E-852.10).

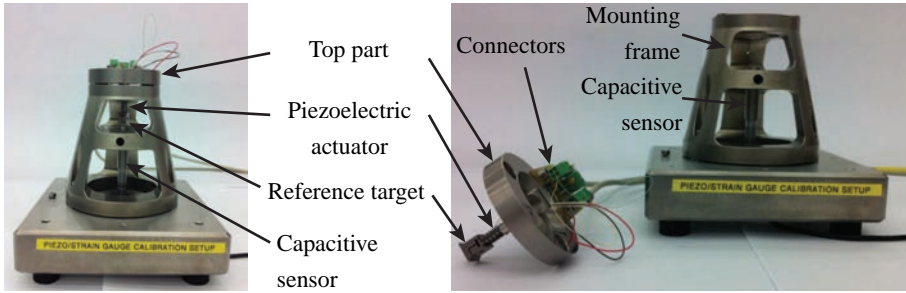


Figure 6.4: The realized piezoelectric curvature and strain gauge sensor calibration setup. The left picture shows the configuration of the setup when it is used during a calibration measurement. The right picture shows details of the mounted piezoelectric actuator on the removable lid.

function of the measured strain gauge voltage U_s . The strain gauge voltage offset by the unbalanced Wheatstone bridge has been removed from the result. The plot indicates that the strain gauge has a linear relation to the piezoelectric actuator elongation.

The static gain G_{sg} between the strain gauge voltage U_s and the piezoelectric actuator elongation y_l was determined by fitting a first order polynomial through the measured piezoelectric actuator elongation and strain gauge voltage ranges for repeated measurements. This is shown in the right-middle graph of Figure 6.5. The crosses (+) relate to the identified actuator elongation and strain gauge ranges whilst the line corresponds to the fitted polynomial with a least squares algorithm. The bottom-left graph of Figure 6.5 shows the fit error. It highlights that the error falls within a ± 10 [nm] range.

The calibration measurement was repeated for the other piezoelectric actuators with strain gauge sensors. The identified strain gauge gains G_{sg} for all sensors are provided in the bottom-right graph of Figure 6.5. It highlights that the variation of the strain gauge gains is limited to 0.2 [$\mu\text{m}/\text{V}$]. The fit errors of all strain gauge sensors were also compared. The maximum value was equal to ± 50 [nm] when a first order polynomial fit was used. Higher order polynomial fits (up to third order) were also investigated to reduce the fit error. This showed a suppression down to the ± 10 [nm] range.

The results of the strain gauge calibration measurements were used to predict the influence of the strain gauge sensor errors on the curvature manipulation performance. The calibration error can be considered as a sensor offset in the feedback path of the control strategy in Figure 6.3. This offset results in a piezoelectric actuator elongation offset because the sensor error is related to the actuator elongation via the complementary sensitivity [79]. The complementary sensitivity for the piezoelectric actuator control loop was estimated for the manipulator numerical model in Section 5.4.2. The left graph in Figure 5.14 showed that it had unity gain up to approximately 100 [Hz].

The prediction of the strain gauge errors on the curvature manipulation performance was obtained for the assumptions that all sensors have the same calibration error and all actuators the same gain. This resulted in the following insights:

- The strain gauge sensor error of 10 [nm] translates to the same piezoelectric actuator elongation error. This corresponds to a curvature error of -0.7×10^{-6} [$1/\text{m}$] when the -72.3 [$1/\text{m}^2$] gain between the piezoelectric actuator elongation and

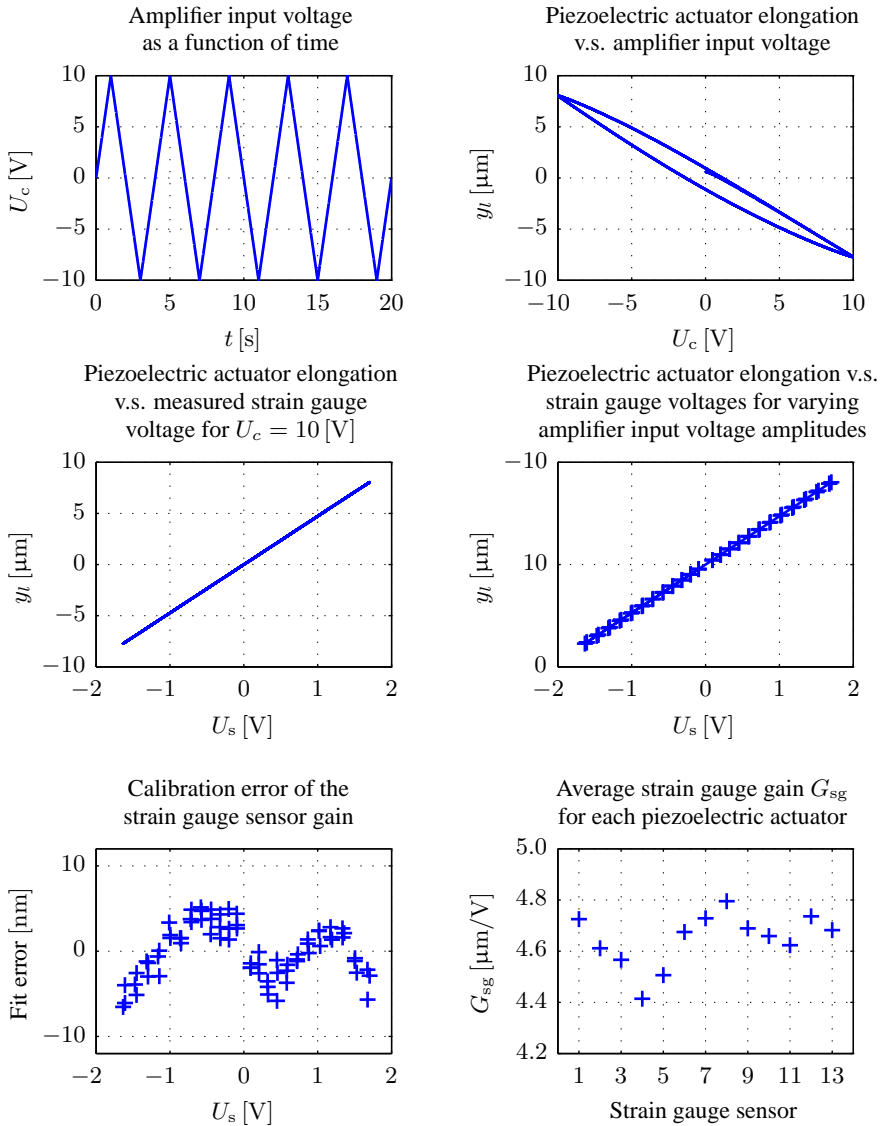


Figure 6.5: Results of the strain gauge gain calibration procedure that were acquired with the setup of Figure 6.4.

reticle curvature of the numerical curvature manipulator model is used. The error satisfies the 2.4×10^{-6} [1/m] curvature accuracy specification by a factor three. The error should ideally be lower because of the presence of other system errors.

- A gain variation of 5.5 [nm/V] will result in a piezoelectric actuator elongation error of 10 [nm] for a maximum strain gauge voltage of 1.8 [V]. This is more than a factor thirty smaller than the identified strain gauge gain variation between each

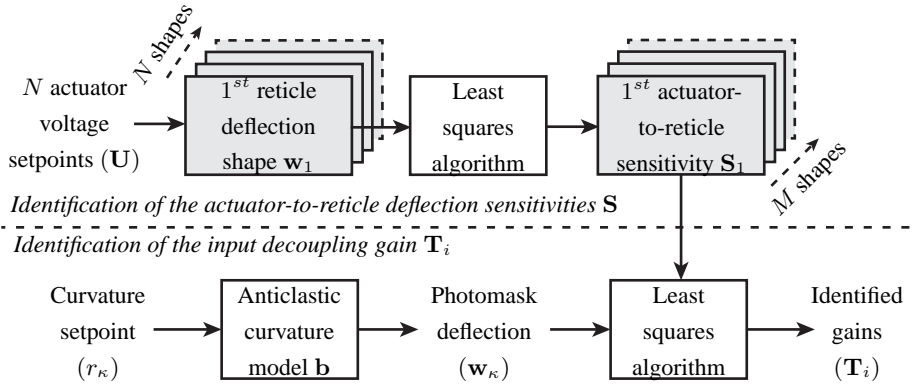


Figure 6.6: Flowchart of the calibration procedure that was used to identify the input decoupling gains \mathbf{T}_i for the control strategy of Figure 6.3.

strain gauge sensor in the setup. The result highlights the necessity to calibrate each strain gauge sensor independently.

- The measured strain gauge signal will have drift which will result in a piezoelectric actuator elongation and reticle curvature error. A specific source of the drift is heating of the sensor electronics. The allowable drift depends on the frequency of the strain gauge calibration in a final machine implementation. For an assumed calibration interval of 3 hours, the drift must be limited to 3.33 [nm/hour]. The effect of the strain gauge sensor drift is not considered further in this thesis.

The above discussion highlights that the piezoelectric actuator elongation measurement has stringent requirements which are barely met by the strain gauge sensor configuration. Another worry is the calibration of the strain gauge sensors before the actuators were assembled in the curvature manipulator assembly. The actuator mounting might result in additional stresses and strains in the piezoelectric actuator which can change the strain gauge sensor characteristics. The above identified gains are nevertheless used because no other calibration procedure was identified.

6.3.1.2 Calibration of input decoupling gains

The other calibration measurement that was performed consisted of identifying the input decoupling gains \mathbf{T}_i for the control strategy in Figure 6.3. These gains are used to translate the photomask curvature setpoint r_k to the required piezoelectric actuator elongation setpoint \mathbf{r}_1 for each of the fourteen piezoelectric actuators.

This section explains the calibration of the input decoupling gains in the following order. The calibration procedure is explained first. The requirements for the calibration procedure and the achieved calibration results are thereafter provided.

Calibration procedure

Figure 6.6 shows the calibration procedure that was pursued for the identification of the

input decoupling gains. The procedure consisted of the following steps:

- *Identification of the actuator-to-reticle deflection sensitivities \mathbf{S}* - The first step determines the sensitivities \mathbf{S} between the applied actuator voltage and the resulting reticle deflection. It consists of applying a set of independent voltage setpoints \mathbf{U} to the piezoelectric actuators and measuring the static deflection \mathbf{w} of the reticle for each voltage setpoint. The sensitivities are then determined by:

$$\mathbf{S}(\mathbf{x}, \mathbf{y}) \mathbf{U} = \mathbf{w}(\mathbf{x}, \mathbf{y}) \implies \mathbf{S}(\mathbf{x}, \mathbf{y}) = \mathbf{w}(\mathbf{x}, \mathbf{y}) \mathbf{U}^{-1} \quad (6.6)$$

for $\mathbf{S} = [\mathbf{S}_1 \cdots \mathbf{S}_M]$, $\mathbf{U} = [\mathbf{U}_1 \cdots \mathbf{U}_N]$, $\mathbf{w} = [\mathbf{w}_1 \cdots \mathbf{w}_N]$ and $N = M = 14$. Note that a pseudo inverse should be used for the case where $N > M$.

- *Identification of the input decoupling gain \mathbf{T}_i* - The second step consists of determining the contribution of each actuator to the ideal curvature deflection shape \mathbf{w}_κ for a curvature of $r_\kappa = 1$ [1/m]. The anticlastic curvature model of Section 3.3.1 is used because the induced pattern distortions by bending relate to a magnification error which are correctable by the lithography system. The expression for the input decoupling gain \mathbf{T}_i is obtained from:

$$\mathbf{S}(\mathbf{x}, \mathbf{y}) \mathbf{U}_p = \mathbf{w}_\kappa(\mathbf{x}, \mathbf{y}) = \mathbf{b}(\mathbf{x}, \mathbf{y}) r_\kappa \quad (6.7)$$

$$\implies \mathbf{U}_p = \underbrace{\left(\mathbf{S}(\mathbf{x}, \mathbf{y})^T \mathbf{S}(\mathbf{x}, \mathbf{y}) \right)^{-1} \mathbf{S}(\mathbf{x}, \mathbf{y})^T \mathbf{b}(\mathbf{x}, \mathbf{y}) r_\kappa}_{\mathbf{T}_i} \quad (6.8)$$

where \mathbf{b} represents the anticlastic curvature model that is evaluated at locations (\mathbf{x}, \mathbf{y}) , \mathbf{U}_p the applied voltages across the fourteen piezoelectric actuators and \mathbf{T}_i the vector containing the contribution of each actuator elongation deflection shape to the ideal reticle deflection. Note that the gain vector \mathbf{T}_i needs to be multiplied by the known ratio between the actuator elongation and the applied voltage in order to have the correct units for the control strategy of Figure 6.3.

It is important to underline that the above calibration procedure is based on a number of assumptions. First, the actuation by the curvature manipulator must be repeatable because a stitching procedure is used to measure the reticle deflection shapes. Second, the reticle and curvature manipulator must behave linearly across the applied bending moment range. Finally, the reticle must behave quasi-statically when undergoing bending. This assumption is necessary because the above calibration strategy uses static deflection shapes in order to identify the gains of the input decoupling vector \mathbf{T}_i . This is considered a valid assumption because the first resonance frequency of the reticle is at 506 [Hz] whilst wafer curvature setpoints have a relevant frequency content up to 100 [Hz].

Calibration accuracy requirements

The calibration accuracy requirements were investigated in two steps. An accuracy requirement for the input decoupling gain was first determined. This information was then

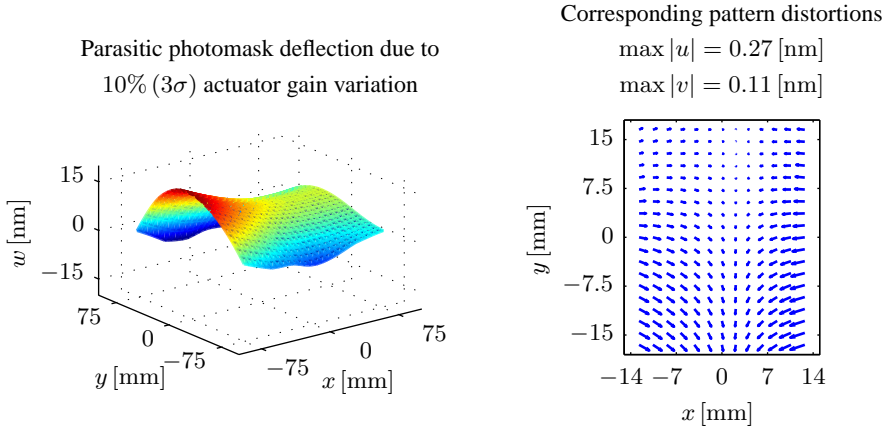


Figure 6.7: Out-of-plane (right) and in-plane (left) photomask deformation difference between an ideal curvature of $\kappa_x = 0.2 \times 10^{-3} \text{ [1/m]}$ and the result with an added 10% (3σ) random gain error. The random gain error had a normal distribution.

used to identify the accuracy requirement of the reticle deflection measurements. Both steps are explained below.

The required accuracy of the input decoupling gains was determined with the reticle FE model of Appendix C that has discrete locations of bending moment application. The requirement was obtained by adding a normally distributed actuator gain error of 10% (3σ) to the actuator gains that give a photomask curvature of $\kappa_x = 0.2 \times 10^{-3} \text{ [1/m]}$. The resulting reticle deflection and pattern distortion difference between the ideal case and the erroneous actuator gains are shown in the left and right graph of Figure 6.7. The following conclusions are drawn from the result:

- The peak-to-peak value of the out-of-plane photomask deflection is equal to 18 [nm] at reticle level and 1.13 [nm] at wafer level for a curvature of $\kappa_x = 0.2 \times 10^{-3} \text{ [1/m]}$. The same gain variation will result in a 2.25 [nm] focus error for the maximum curvature of $0.4 \times 10^{-3} \text{ [1/m]}$. This is approximately 6.7% of the 33.8 [nm] focus improvement that is obtained at wafer level by the curvature correction. An actuator gain variation of 4.4% (3σ) is allowed for an assumed parasitic focus error of 1 [nm] at wafer level.
- The maximum in-plane pattern distortion is equal to 0.27 [nm] at wafer level for a curvature of $\kappa_x = 0.2 \times 10^{-3} \text{ [1/m]}$. This corresponds to an error of 0.54 [nm] for the maximum curvature value of $\kappa_x = 0.4 \times 10^{-3} \text{ [1/m]}$. The required actuator gain error for the maximum curvature should therefore be lower than 0.93% (3σ) when the 50 [pm] design rule is used.

The analysis results confirm that the allowable gain errors are driven by the overlay requirements. It also indicates that the gain calibration is needed in order to achieve the curvature manipulator specifications.

The achievable accuracy of the input decoupling gains depends on the accuracy of the

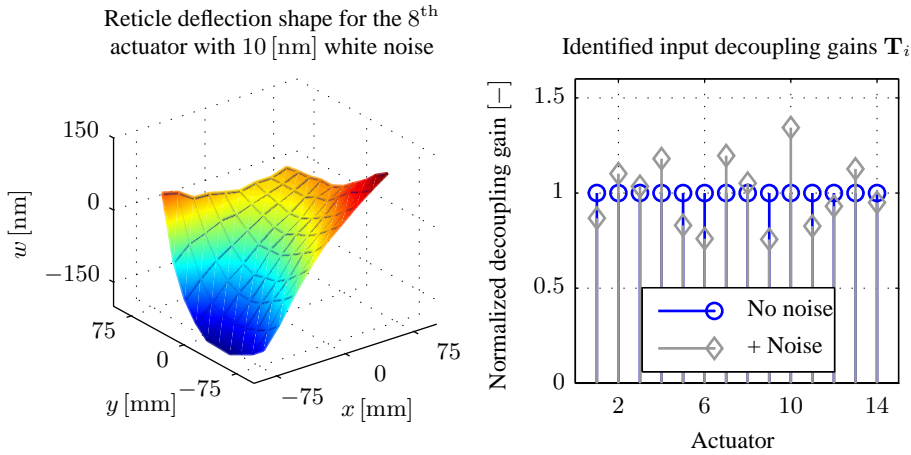


Figure 6.8: The effect of measurement noise on the identified input decoupling gains \mathbf{T}_i . The left graph shows the simulated reticle deflection for the 8th voltage setpoint of Equation (6.9) with 10 [nm] of added white noise. The right graph shows the effect of noise on the identified input decoupling gains \mathbf{T}_i for the shapes without and with the added white noise.

calibration measurements. An analysis was therefore performed to identify the allowable measurement uncertainty on the static actuator deflection shapes \mathbf{w} in order to satisfy the above derived actuator gain accuracy. Theoretical static deflection shapes were obtained from the reticle FE model. They were evaluated for a x, y -measurement grid of 9-by-10 points across the reticle surface and scaled such that their sum corresponded to a reticle curvature of $\kappa_x = 0.4 \times 10^{-3}$ [1/m]. White noise of 10 [nm] (3σ) was then added to the static deflection shape of each actuator. An example is provided in the left graph of Figure 6.8. The calibration steps of Equation (6.6) and (6.8) were thereafter applied. The acquired input decoupling gains by the noisy deflection shapes were compared to the identified gain error variation of 0.93% (3σ).

The left graph in Figure 6.8 shows the normalized input decoupling gains for the cases with and without noise to the reticle deflection shapes. The result shows that the maximum variation of the input decoupling gains is equal to 34% for a curvature of 0.4×10^{-3} [1/m]. This exceeds the input decoupling requirement by approximately a factor of 40. Analysis showed that the noise should be reduced to approximately 0.1 [nm] in order to satisfy the accuracy requirements. It is expected that the desired accuracy of the input decoupling gains will not be achieved with the measurement setup of Section 6.2 because the sensor resolution already exceeds this specification by a factor of 3.

Calibration results

The above analysis demonstrated the stringent measurement requirements for the input decoupling gain calibration. The strategy was nevertheless pursued with the measurement setup of Figure 6.1. The results of the calibration are provided below.

The first step of the calibration procedure consisted of identifying the actuator-to-reticle deflection sensitivities \mathbf{S} . These sensitivities were determined for the following voltage

setpoints across the piezoelectric actuators:

$$\mathbf{U} = \hat{U} \begin{bmatrix} \mathbf{J} & \mathbf{0} \\ \mathbf{0} & \mathbf{J} \end{bmatrix}, \quad \text{with } \mathbf{J} = \begin{bmatrix} 1 & 0 & 0 & 0 & 1 & 1 & 1 \\ 1 & 1 & 0 & 0 & 0 & 1 & 1 \\ 1 & 1 & 1 & 0 & 0 & 0 & 1 \\ 1 & 1 & 1 & 1 & 0 & 0 & 0 \\ 0 & 1 & 1 & 1 & 1 & 0 & 0 \\ 0 & 0 & 1 & 1 & 1 & 1 & 0 \\ 0 & 0 & 0 & 1 & 1 & 1 & 1 \end{bmatrix} \quad (6.9)$$

where \hat{U} is the amplitude of the voltage setpoint. These voltage setpoints were selected in order to maximize the signal-to-noise ratio of the measured reticle deflections \mathbf{w} which was necessary because part of the voltage range is used to constrain the reticle on the z-supports. Six measurement repetitions were used for each x, y -measurement location across the reticle in order to identify the repeatability of the measurement.

Figure 6.9 provides a summary of the calibration measurement results. The top-left and top-right graphs respectively show the 5th and 8th modelled photomask deflection shape for static actuator setpoints of Equation (6.9). The measured average deflection shapes for the same setpoints are provided in the middle two graphs. The bottom left and right graph show the measurement repeatability for the two shapes. The results led to the following insights:

- The global shape of the modelled and measured deflection shapes correspond. The measured deflection shapes have a jagged edge which can be attributed to the applied stitching procedure. The large outlier in the measurement data of the 8th shape is caused by the absence of Chrome on the reticle at that location.
- The measurement repeatability for both shapes is approximately 7.5 [nm] (1σ) and exceeds the 0.1 [nm] calibration measurement requirement by a factor of 75. No realistic gains were therefore obtained for the measurement results.

The calibration measurements demonstrate that the desired accuracy of the input decoupling gain \mathbf{T}_i cannot be obtained with the current measurement hardware. Probable causes of the error are the non-repeatability of the bending manipulator and that of the measurement setup. No attempt was made to investigate this further because of time limitations. Instead, it was chosen to use the same input decoupling gain for each actuator. The value was obtained by fitting the anticlastic curvature model through the static deflection shape of the photomask when all actuators received the same voltage setpoint.

6.3.2 Controller implementation

The second step in the experimental validation of the curvature manipulator was the implementation of the local feedback controllers \mathbf{C}_l in Figure 6.3 across the collocated piezoelectric actuators and strain gauge sensors. This section explains the steps that were taken to implement the feedback controllers. Section 6.3.2.1 presents the results of the system identification measurements. The feedback controller tuning is explained

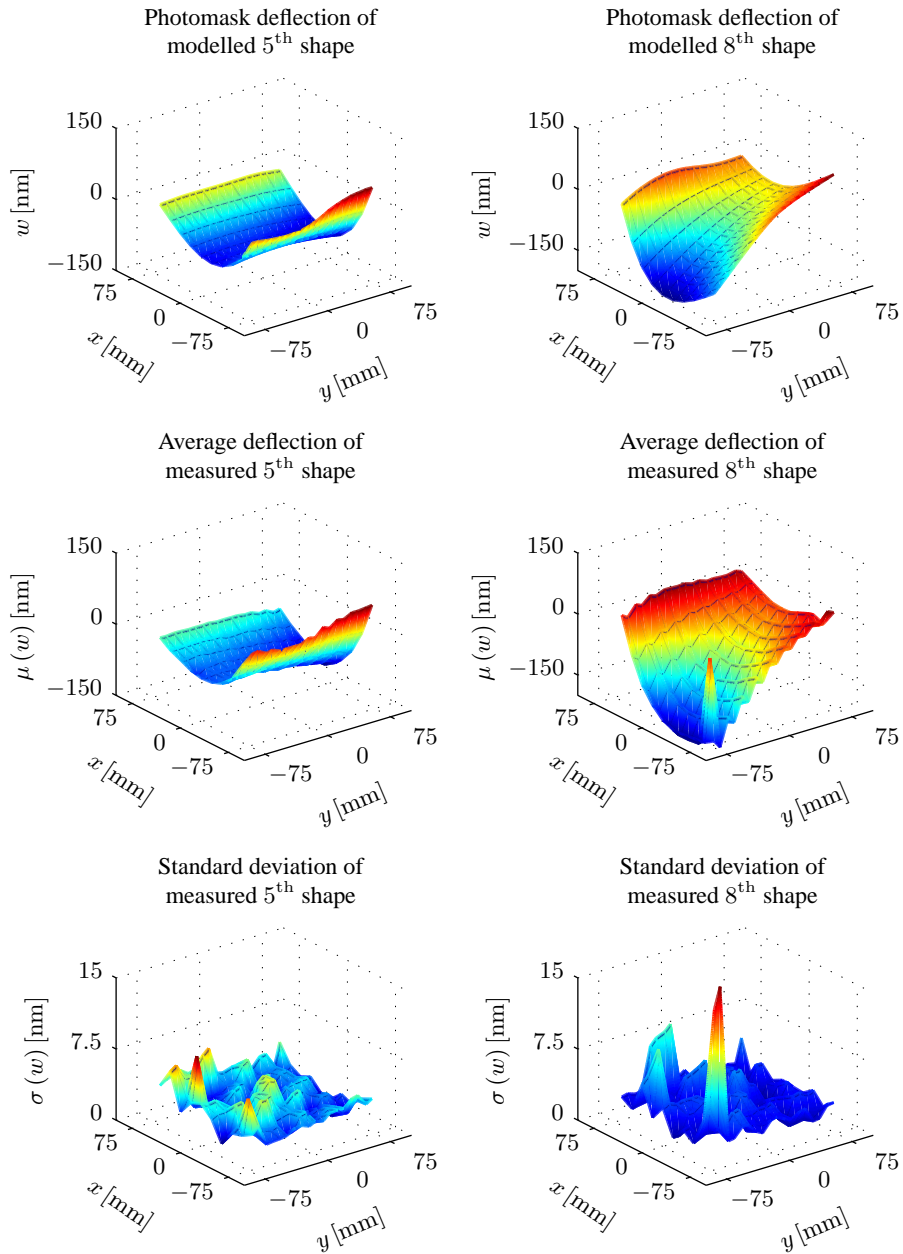


Figure 6.9: Comparison between the modelled and measured photomask deflections for 5th and 8th actuator setpoint of Equation (6.9). The top and middle graphs respectively show the modelled and average measured deflection shapes. The bottom plots show the measurement repeatability.

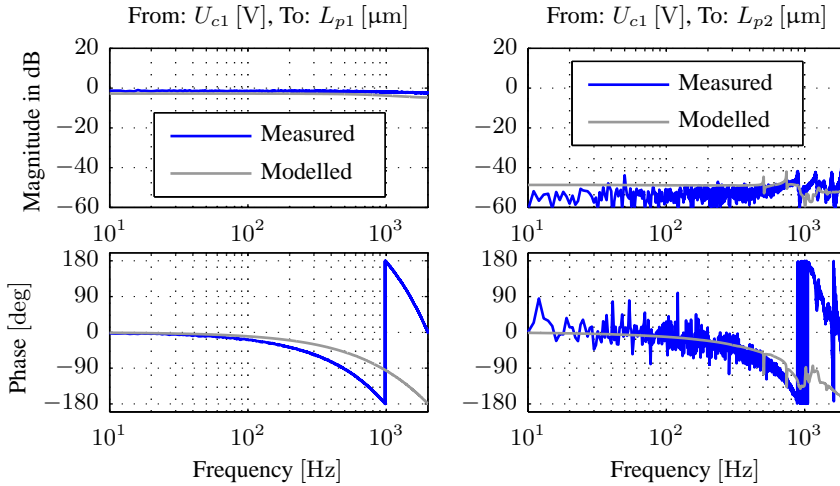


Figure 6.10: Modelled and measured FRFs from the applied voltage across the first piezoelectric actuator U_{c1} to the measured elongations L_{p1} and L_{p2} of the 1st and 1nd piezoelectric actuator by the attached strain gauges. The modelled results represent the FRFs in Figure 5.8.

in Section 6.3.2.2. System noise levels are quantified in Section 6.3.2.3. The results are compared to the control modelling of the curvature manipulator model in Section 5.4.

6.3.2.1 System identification

System identification measurements were performed on the curvature manipulator setup to determine the FRFs between the piezoelectric actuators and strain gauge sensors. The results were used for the following objectives. First, it allows the comparison of the modelled and measured curvature manipulator dynamics as well as the decoupling between the axes of the manipulator. Second, the measured FRFs are used to tune the decentralized feedback controller across the piezoelectric actuators and strain gauge sensors. This section focusses on the comparison of the modelled and measured manipulator dynamics and the decoupling between its axes.

The system identification was performed by sequentially applying a multi-sine excitation to each piezoelectric actuator. The strain gauge sensor signals were acquired during the excitation periods of 1 [s] with a sample frequency of 4 [kHz]. The identification could be performed in open loop because the system is already stable without a feedback controller. The FRFs were obtained by taking the average of a hundred measurement periods. This reduces the contribution of stochastic noise by a factor of $\sqrt{100}$ as stated by [91].

Figure 6.10 shows the modelled and measured FRFs from the applied voltage across the first piezoelectric actuator U_{c1} to the elongation L_{p1} and L_{p2} of the first and second actuator. Comparison of the measured and modelled results demonstrates the following:

- The measured and modelled FRF of the collocated actuator and sensor pair have

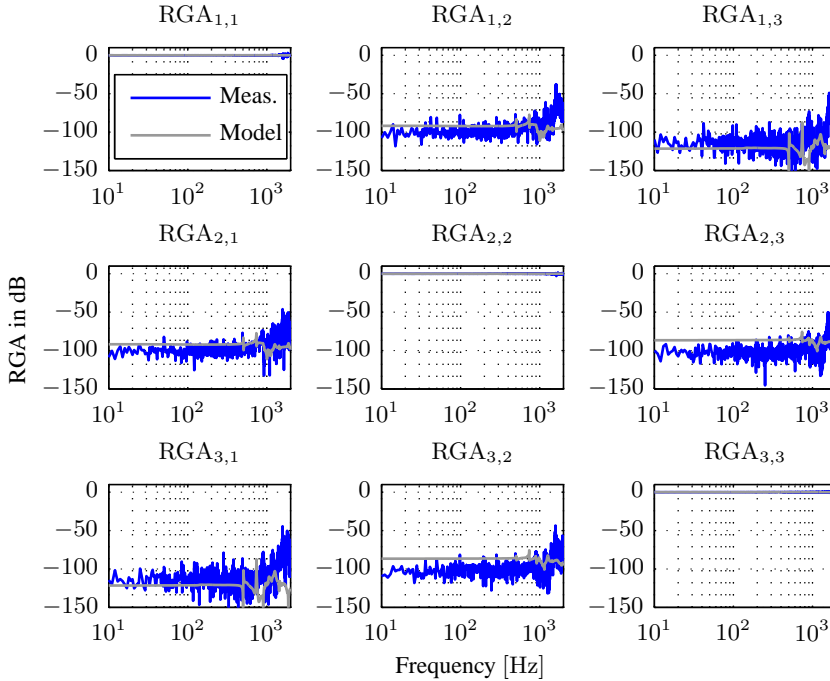


Figure 6.11: The Relative Gain Array (RGA) for the first three axes of the measured and modelled curvature manipulator FRFs. The modelled RGA results correspond to the values in Figure 5.8. The other RGAs are omitted because they have the same trend.

the same behaviour. Both FRFs have a zero slope for frequencies up to 1 [kHz]. Furthermore, the magnitude of the FRF agrees to within 1.4 dB. The phase of the measured FRF has a quicker roll-off. This is attributed to delay in the measurement system which was not taken into account in the model. The phase lag limits the achievable controller bandwidth.

- The measured and modelled FRF of the non-collocated actuator and sensor differ by approximately 7 dB. Resonance frequencies are also visible in the FRFs. They are different for the modelled and measured FRF however. The difference indicates changed reticle dynamics. The measured non-collocated FRF also has a quicker phase drop which is caused by the delay in the measurement system. The non-smooth nature of the non-collocated FRF is attributed to the poor signal-to-noise ratio of the strain gauge measurement signal. This is caused by the mechanical decoupling between the manipulator axes and limited voltage excitation because a voltage offset is needed to constrain the reticle on the z-support.
- The magnitude of the measured collocated and non-collocated FRFs differ by approximately 45 dB. It corresponds to the magnitude difference that was calculated for the manipulator model in Section 5.4.1. The decoupling between the axes was analysed by comparing the Relative Gain Array (RGA) of the measured and modelled FRFs. They were calculated with Equation (5.3) and are provided in Figure

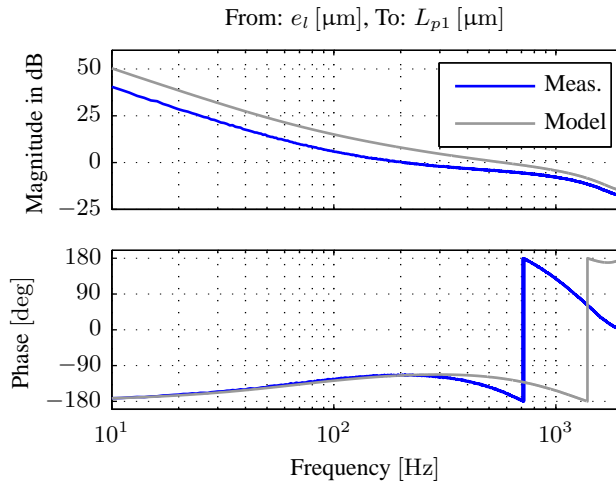


Figure 6.12: The open-loop FRF of a single piezoelectric actuator control loop of the curvature manipulator measurement setup and model after neglecting the interaction with the other axes. The model result is equal to that of Figure 5.12.

6.11. The RGAs approach the identity matrix for both the modelled and measured curvature manipulator across the whole frequency range. The RGA values of the measured FRFs show a slight increases above 1 [kHz] however. The values nevertheless confirm the decoupling between the axis.

The measured decoupling of the curvature manipulator confirms the possibility to apply decentralized control across the piezoelectric actuators. Details of the local feedback controller tuning is provided in Section 6.3.2.2.

6.3.2.2 Controller design

The design of the decentralized feedback controllers C_l across the piezoelectric actuators was performed in the same manner as for the curvature manipulator model in Section 5.4.2. A single robustly stable PI^2D -controller was tuned with manual loop shaping techniques and applied to all fourteen feedback loops. The single controller could be used because of the limited magnitude and phase variation of the measured collocated FRFs. Figure 6.12 provides the open-loop FRF of an actuator elongation control loop for the curvature manipulator measurement setup and the manipulator model of Section 5.4.2. The interaction with other plant dynamics was neglected because of the decoupling between the manipulator axes. The Bode plot shows that the unity-gain cross-over frequency for the measured open-loop FRF is located at 205 [Hz]. The achieved controller bandwidth for the measurement setup is more than a factor two lower than the 580 [Hz] bandwidth of the model. The difference is attributed to the larger phase lag in the measurement system. Higher bandwidths can be achieved for the actuator elongation control loops in the measurement setup but it comes at the cost of the 6 dB robustness margin that is normally used for industrial applications.

The closed loop stability of the curvature manipulator setup with the implemented decen-

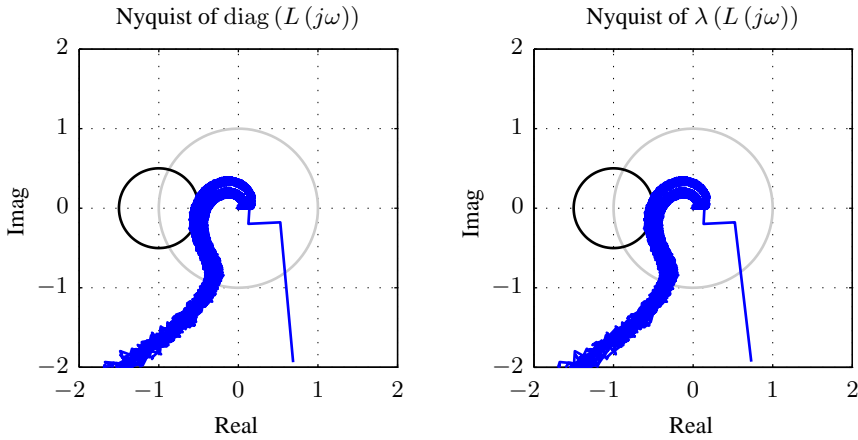


Figure 6.13: Nyquist diagrams of the fourteen diagonal loop gains $\text{diag}(L(j\omega))$ on the left and that of the characteristic loci $\lambda(L(j\omega))$ on the right. The graphs show that the system is robustly stable and that the manipulator axes are decoupled.

tralized controller across the piezoelectric actuators was also investigated. Section 5.4.2 mentioned that the stability of the closed loop system is guaranteed if the characteristic loci of the open-loop system satisfy the Generalized Nyquist Criterion [70?]. Figure 6.13 provides the Nyquist plots of the diagonal loop gains $\text{diag}(L(j\omega))$ and the characteristic loci of the curvature manipulator setup loop gain $L(j\omega)$. The characteristic loci do not enter the circle with radius 0.5. This proves that the controller satisfies the desired 6 dB robustness margin. Furthermore, the mechanical resonances that were visible in the non-collocated FRFs of Figure 6.10 do not affect the closed loop stability. These conclusions were also drawn from the modelling results of Section 5.4.2. The graphs have one branch that moves to the right of the Imaginary axis. This line is related to the axis with the broken strain gauge.

The sensitivity S and complementary sensitivity T of a single piezoelectric actuator feedback loop was also determined for the tuned controller. The results for the manipulator model of Section 5.4.2 and the measurement setup are respectively provided in Figure 6.14. Both graphs have the same trend and do not contain any mechanical resonances. The sensitivities have a 6 dB peak in order to ensure the desired robustness margin.

The sensitivity graphs of the modelled and measured manipulator highlight the difference in disturbance rejection between the measured and modelled system. The closed loop sensitivity of the measurement setup is equal to -33 dB at 16 [Hz] instead of the -42 dB for the modelled curvature manipulator. It highlights that the error by the piezoelectric actuator hysteresis is rejected by a factor of 44 instead of the factor 100 that was estimated in Section 4.3.3. The disturbance rejection could be improved by tuning a higher bandwidth controller. This results in larger sensitivity values and subsequently disturbance amplification at higher frequencies because of the *Waterbed effect* [79?].

The complementary sensitivity of the measured curvature manipulator is larger than the

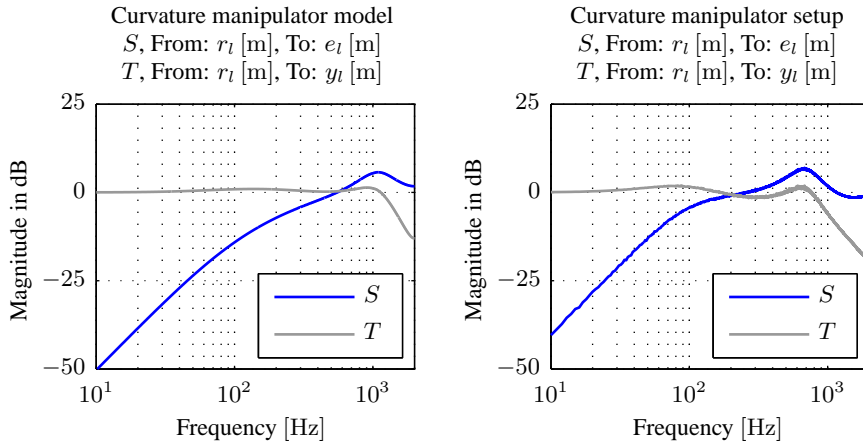


Figure 6.14: The sensitivity S and complementary sensitivity T of the decentralized control strategy in Figure 6.12 for one of the piezoelectric actuator feedback loops. The left and right plot provides the acquired results for the model in Section 5.4.2 and the measurement setup of Section 6.2. Both graphs were obtained without the inclusion of the feedforward path \mathbf{K}_l .

modelled system between 30 [Hz] and 100 [Hz]. It highlights that the amplification of the actuator elongation setpoints r_l and strain gauge sensor noise is larger for the measurement setup. Further insights into the control performance of the system are obtained in Sections 6.3.2.3 and 6.3.3 when the steady state error and the curvature control performance are presented.

6.3.2.3 Steady state error

The impact of the decentralized controller on the steady state performance of the curvature manipulator system was estimated by analysing the steady state error of the piezoelectric actuator elongation. The left graph in Figure 6.15 shows the elongation error of the first actuator in time domain with and without the applied feedback controller. The middle and right graphs respectively show the Power Spectral Density (PSD) and the Cumulative Power Spectrum (CPS) of the errors.

The results in Figure 6.15 demonstrate that the peak-to-peak actuator elongation error is approximately 36 [nm]. Furthermore, the PSD of the error before the applied feedback indicates that the error can be considered to have a flat spectrum of approximately 10^{-2} [$\text{nm}_{\text{rms}}^2/\text{Hz}$] with additional 50 [Hz] multiples. The latter contributions are attributed to the electrical design of the manipulator setup.

The application of the feedback controller results in a suppression of the elongation error below the 205 [Hz] controller bandwidth but an amplification of the error between 300 and 1000 [Hz]. The effects are especially clear in the PSD and CPS diagrams. The error suppression correlates to the trend of the closed loop sensitivity of Figure 6.14. The CPS shows that the error with the applied feedback controller is reduced from approximately 20 [nm_{rms}^2] to 4 [nm_{rms}^2] at 300 [Hz]. A specific disturbance that the controller counteracts is the noise from the actuator drive electronics.

The MA reticle curvature error was estimated from the MA error of the piezoelectric

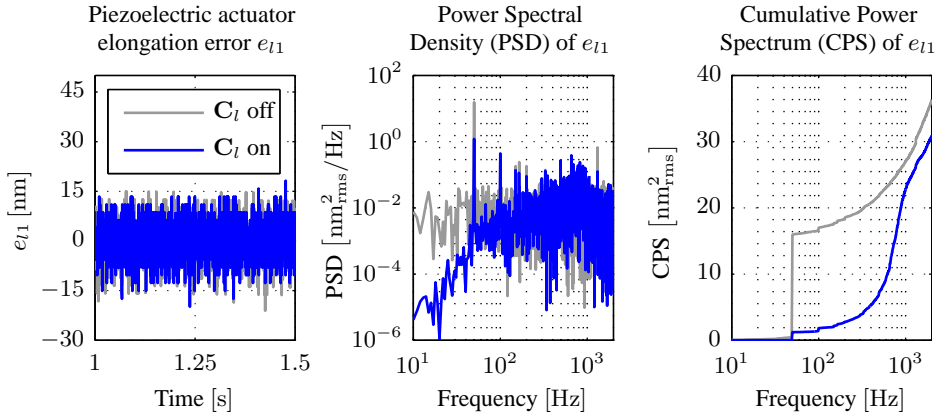


Figure 6.15: The steady state error of the first piezoelectric actuator elongation error e_{l1} with and without the applied actuator feedback control C_l . The left graph shows the error in time domain. The middle and right graphs provide the PSD and CPS of that error.

actuator elongation under the assumption that there are no external disturbances on the reticle. The latter are equal to 1.4 [nm] and 4.1 [nm] (1σ) with and without the applied feedback controller. They were derived from the CPS values of the actuator elongation error at the 145 [Hz] cut-off frequency of the MA-filter in Section 5.4.5. The resulting MA curvature errors were estimated at 1×10^{-7} [1/m] and 3×10^{-7} [1/m] by using the relation between the actuator elongation and reticle curvature of Section 6.3.1.1. The former value is approximately a factor 2 larger than the modelled MA curvature error in Section 5.4.5 which confirms the correlation between the modelled and measured disturbances. The estimated curvature error from the measurement also satisfies the curvature accuracy specification in Table 6.1 by a factor 20. This is considered an acceptable result for the first manipulator design.

6.3.3 Curvature control performance

The curvature control performance of the feedback controlled manipulator was investigated with the experimental setup of Section 6.2. This section explains the measurement results. Section 6.3.3.1 presents the photomask deflection results for a static curvature setpoint. The results for a dynamic curvature setpoint are provided in Section 6.3.3.2.

6.3.3.1 Static curvature setpoint

The curvature control performance of the manipulator was first identified for static curvature setpoints. The investigation was performed across the available actuator voltage range after preloading the reticle on the z-supports (see Section 6.2.3). The identified strain gauge sensor gains and control settings of 6.3.1.1 and Sections 6.3.2 were used for the measurement. The input decoupling vector \mathbf{T}_i consisted of the same gains for each actuator because of the calibration difficulties that were explained in Section 6.3.1.2.

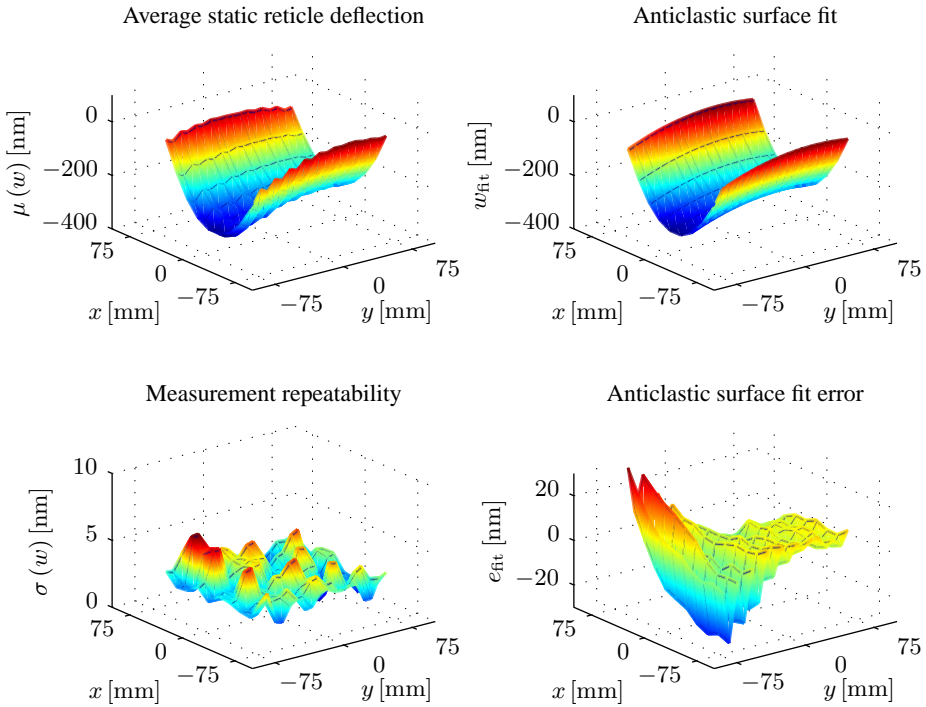


Figure 6.16: Results of the static deflection measurements of photomask bending. The top- and bottom-left graphs respectively show the average deflection and the measurement repeatability for eight measurement repetitions. The top- and bottom-right graphs respectively provide the results for the anticlastic curvature model fit through the deflection data and the fit error.

Description	Anticlastic curvature model coefficient					ν [-]
	T_z [nm]	α_x [μ rad]	α_y [μ rad]	κ_x [1/m]	κ_y [1/m]	
Measurements	-259	0.331	0.509	10.70×10^{-5}	1.68×10^{-5}	0.16
Model	-246	0.009	0	10.70×10^{-5}	1.71×10^{-5}	0.16
Difference	-13	0.322	0.509	0	-0.03×10^{-5}	≈ 0

Table 6.2: Comparison of the anticlastic curvature model coefficients that were derived from the measured photomask deflection with the values of the theoretical plate bending model of Section 3.3.1. The latter is defined by $w = \frac{1}{2} (\kappa_x x^2 - \kappa_y y^2) + \alpha_x x + \alpha_y y + T_z$.

Figure 6.16 provides the reticle deflection results for a static curvature setpoint and eight measurement repetitions. The top- and bottom-left graphs shows the average reticle deflection $\mu(w)$ and its repeatability $\sigma(w)$. The deflection results were compared to the analytical bending model of Section 3.3.1. The top-right and bottom-right graphs respectively provide the fitted anticlastic curvature shape through the measured average reticle deflection data and its fit error. The identified fit coefficients are provided in Table 6.2. The measurement and anticlastic surface fit results provide the following insights:

- The measured reticle deflection seems to correlate to the predicted anticlastic curvature shape even without an accurate calibration of the input decoupling vector \mathbf{T}_i . This is confirmed by Table 6.2 which shows agreement between the fitted and modelled anticlastic curvature model coefficients for the reticle curvature κ_x and κ_y , the out-of-plane translation T_z as well as the Poisson ratio ν . The latter value corresponds to the theoretical Poisson ratio of the Fused Silica material.
- The realized reticle curvature of $10.7 \times 10^{-5} [1/m]$ is approximately a factor 4 lower than the maximum curvature requirement of $40 \times 10^{-5} [1/m]$. This is attributed to the fact that 85% of the voltage range is used to preload the reticle onto the z-supports as was explained in Section 6.2.3.
- The measurement repeatability is equal to $\max(\sigma(w)) = 5.6 [nm]$. The repeatability is limited by the metrology setup or the curvature manipulator. It is recommended to investigate the specific limitation of the measurement repeatability.
- The identified reticle tilts from the measurement are larger than the expected tilts from the model. The parasitic tilts are probably caused by parasitic forces and moments that act on the reticle. One contributor to this error is the inability to close a feedback control loop across one of the piezoelectric actuator because it has a broken strain gauge. This is also highlighted by the anticlastic surface fit error which has a larger value at the location of the actuator without the applied feedback controller.

The linearity between the actuator command voltage U_c and the realized reticle curvature κ_x was also determined for the manipulator. The analysis consisted of conducting the above described static curvature measurement and fitting procedure for six different voltage setpoints. The identified reticle curvatures for those setpoints and the first order polynomial fit through the values are shown in Figure 6.17. The coefficient of determination of the fit is equal to $R^2 = 0.9993$ which confirms the linear relation between the applied voltage and reticle curvature. The identified relation was used to estimate the maximum achievable curvature across the full voltage range. A command voltage of $U_c = 10 [V]$ results in a predicted maximum curvature of $\kappa_x = 0.39 \times 10^{-3} [1/m]$. This is marginally lower than the $0.4 \times 10^{-3} [1/m]$ design specification.

The static measurement results have shown that the reticle acquires the expected anticlastic deformation shape and that the actuator behaves linearly across its actuation range. Additional parasitic rigid body motions and higher order deformations are also induced. These effects are undesired even though the reticle stage can correct for the the parasitic

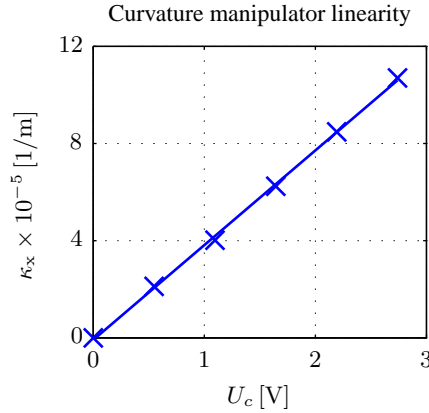


Figure 6.17: The linearity of the curvature manipulator between applied command voltage U_c and the identified reticle curvature κ_x from measurements. The linearity is described by $\kappa_x = 3.9 \times 10^{-5}U_c - 0.0829$ with a coefficient of determination of $R^2 = 0.9993$.

rigid body motions as was mentioned in Section 3.3.1. It is recommended to check if the parasitics are still present for an integrated z-support in the manipulator and closed loop control across all piezoelectric actuators.

6.3.3.2 Dynamic curvature setpoint

The dynamic curvature tracking performance of the feedback controlled manipulator was analysed for the wafer curvature setpoint of Section 5.4.4. The setpoint was scaled by a factor of six in order to ensure that the reticle was constrained on the z-supports. The tracking performance was thereafter quantified for the piezoelectric actuator elongation and the reticle curvature. Both results are explained below.

The tracking performance of the piezoelectric actuator to the actuator elongation setpoint r_l is provided in Figure 6.18. The left and right graphs respectively show the elongation setpoint to the first piezoelectric actuator and the MA tracking error of the piezoelectric actuator elongation. The right graph provides the error for a 205 [Hz] and 530 [Hz] controller bandwidth. It also shows the allowable MA elongation error in order to satisfy the curvature accuracy specification of 2.4×10^{-6} [1/m].

The results of the piezoelectric actuator elongation error demonstrate the following. The actuator elongation error for the 205 [Hz] controller bandwidth equals the error specification for the scaled curvature setpoint. The actuator elongation specification will therefore be exceeded by a factor of six for the original curvature setpoint if linear scaling is assumed to be valid. The error is reduced by a factor of two when the controller bandwidth is increased to 530 [Hz]. This demonstrates that a higher controller bandwidth is desired although it still does not satisfy the elongation accuracy requirement for a curvature of $\kappa_x = 0.4 \times 10^{-3}$ [1/m].

The absence of a curvature sensor in the external measurement setup of Figure 6.1 made it infeasible to directly measure the dynamic curvature tracking performance of the ret-

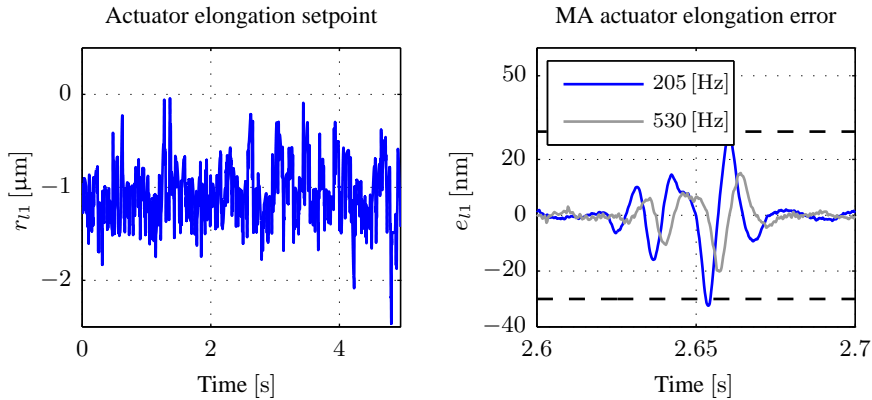


Figure 6.18: The piezoelectric actuator elongation tracking results for the scaled wafer curvature setpoint. The left graph provides the elongation setpoint as a function of time. The right graph shows the MA value of the actuator elongation tracking error. The dark and grey line are related to the tracking error for a 205 [Hz] and 530 [Hz] controller bandwidth. The dotted lines correspond to the allowable elongation error for a curvature accuracy of 2.4×10^{-6} [1/m].

icle. The performance was instead estimated by translating the deflection at the centre of the reticle into a curvature value. A constant relation between the reticle deflection and curvature was used for the estimation process. It was determined from the static curvature measurement results in Section 6.3.3.1. The relation was considered to be valid below the first resonance frequency of the manipulator and reticle assembly because of the quasi-static relation between the piezoelectric actuator elongation and reticle curvature.

Figure 6.19 provides the estimated curvature tracking performance of the curvature manipulator for both controller bandwidths. The top-left and top-right graphs respectively provide the curvature setpoint and curvature error. The bottom-left and bottom-right graph show the estimated MA and MSD results for the curvature tracking error.

The results in Figure 6.19 provide a number of insights. First, the original curvature error indicates the presence of high frequency reticle dynamics. This was also visible in the controller modelling results of Section 5.4.4 without an outer curvature feedback loop. That section showed that the error can be reduced by the presence of an outer curvature feedback loop. A possible source of the dynamic excitation is higher frequency content of the curvature setpoint signal in combination of the constant gain in the feedforward path. An inverse plant model in the feedforward path or shaped reference signal can potentially lead to lower excitation of the dynamics.

Analysis of the MA curvature tracking error shows that the curvature setting accuracy requirement is exceeded by more than a factor of three. Note that this is the case for the scaled wafer curvature setpoint in order to keep the reticle on the z-support. Visual inspection of the MA curvature error in Figure 6.19 also highlights that the trend of the error is different than the MA piezoelectric actuator elongation error in Figure 6.18. The difference between the MA curvature error for both feedback controller bandwidths is also negligible. This behaviour is not expected because the piezoelectric actuator error results indicated an improvement by a factor of two for the higher bandwidth. It is therefore

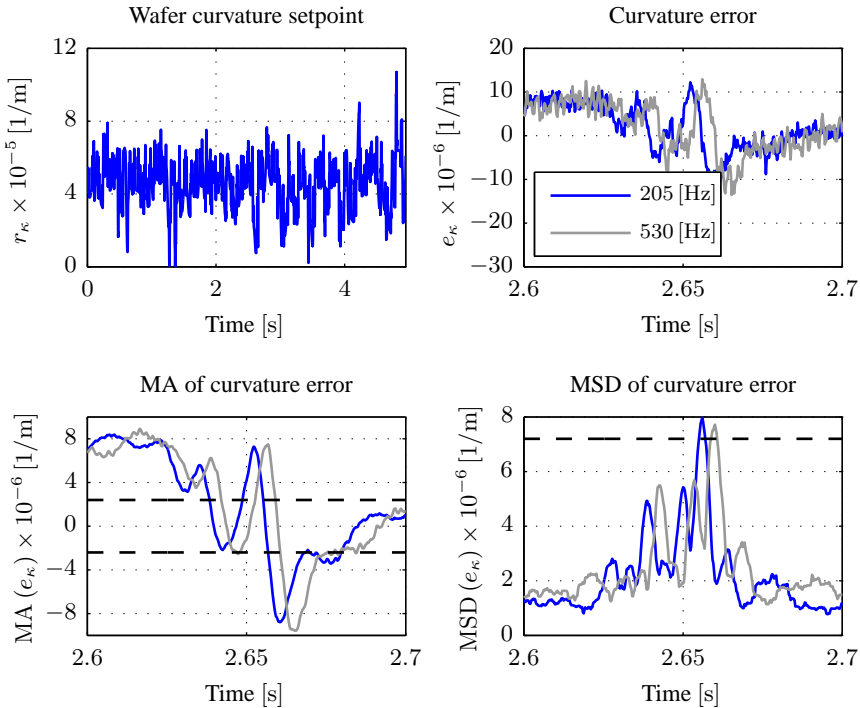


Figure 6.19: The estimated curvature tracking results for the scaled wafer curvature setpoint. The dark and grey line correspond to the tracking performance for a 205 [Hz] and 530 [Hz] controller bandwidth. The dotted lines shows the required tracking accuracy.

concluded that there is no constant relation between the applied piezoelectric actuator elongation and the reticle curvature below the 145 [Hz] cut-off frequency of the MA-filter. The error is potentially caused by hysteretic behaviour in the manipulator-clamp interface. This behaviour was also encountered in the Single-Axis curvature manipulator measurement results that are explained in Appendix E.

The above results highlight the necessity to further investigate the curvature manipulator performance in terms of the dynamic curvature setpoint tracking performance. The following recommendations are therefore proposed:

- Develop a real-time curvature measurement system. Such a measurement system makes it possible to quantify the reticle curvature tracking error. Furthermore, it can be used to investigate the curvature tracking improvement for the outer curvature feedback loop that was proposed in Section 5.4.3.
- Perform investigations into the presence of hysteresis in the manipulator-reticle interface.
- Investigate alternative feedforward control strategies such that the curvature tracking performance is enhanced.

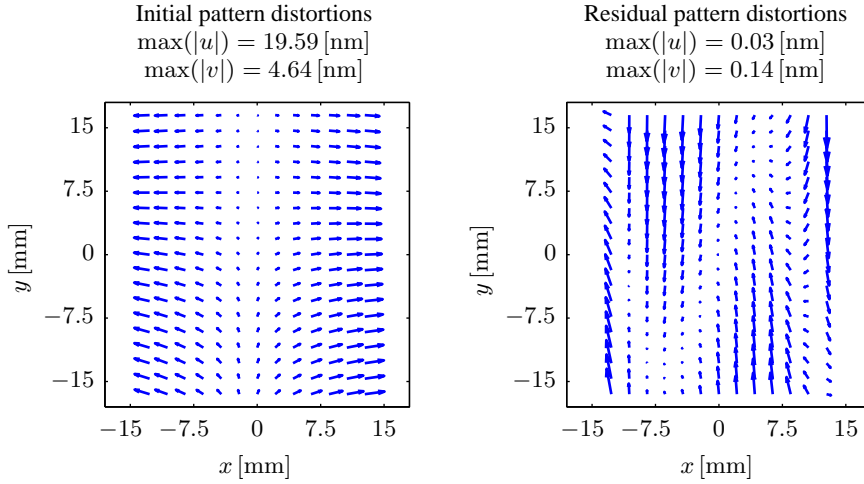


Figure 6.20: Estimated pattern distortions of the photomask for a curvature of $\kappa_x = 0.4 \times 10^{-3} \text{ [1/m]}$ that was derived from a fourth order polynomial fit through the out-of-plane deflection data of Figure 6.16. The left graph shows the initial pattern distortions and the right graph the residual pattern distortions after lens correction.

6.3.4 In-plane pattern distortion estimation

The feasibility of reticle bending depends on the achieved curvature tracking performance and the level of parasitics by bending. The distortions were estimated from the measured out-of-plane reticle deflection because they could not be measured with the external metrology setup. The estimates were obtained by multiplying the reticle local angles around the x - and y -axis by half the reticle thickness. Note that this method is unable to predict contributions of in-plane disturbance forces on the reticle.

The measured reticle deflection of Figure 6.16 was used to estimate the reticle pattern distortions with the above described procedure. The reticle local angles were first estimated by fitting a two-dimensional fourth order polynomial through the measured reticle deflection and taking the spatial derivative of the polynomial in x - and y -direction. The coefficient-of-regression was equal to $R^2 = 0.9944$ which indicated a good correlation between polynomial fit and measured reticle deflection. The pattern distortions were then evaluated across the pattern area using Equations (3.5) and (3.6). The results were scaled in order to obtain the pattern distortion estimated for a curvature of $\kappa_x = 0.4 \times 10^{-3} \text{ [1/m]}$.

Figure 6.20 provides the pattern distortion estimates from the measurement data. The left and right graphs respectively show the initial pattern distortions and the pattern distortions after corrections by the lithography system. The estimated pattern distortion before correction are in the same order of magnitude as the values that were determined in Chapter 3. Furthermore, the result also has a non-symmetry in the pattern distortion around the x - and y -axis. This is attributed to the parasitic tilt of the reticle around those axes as was mentioned in Section 6.3.3.1.

The results after the lithography system corrections shows that higher order residual pat-

tern distortions are present. This indicates that the lens and stage adaptations are not able to counteract the higher order residuals. It underlines that the manipulator was not able to introduce the desired pure asymmetric pattern magnification. Furthermore, the maximum value of the residual pattern distortions exceeds the overlay design specification of 0.1 [nm]. It highlights that further optimization of the curvature manipulator is needed in order to reduce the higher order reticle deformation and keep the residual pattern distortions below the overlay specification.

6.4 Summary & Conclusions

This chapter covered the validation experiments of the proposed photomask curvature manipulator in this thesis. The measurement results were compared to the specifications of Chapter 2 and simulated manipulator performance of Chapter 5.

The chapter started with an explanation of the measurement setup that was used for the experimental validation. The chosen differential measurement procedure made it possible to measure the out-of-plane reticle deflection by bending. The manipulator could not be validated with respect to reticle in-plane deformation, stress-birefringence and optical aberrations because these were not measurable with the setup.

The realized curvature manipulator setup also had limitations. One of the strain gauges on the piezoelectric actuators was broken which limited the application of local feedback control across that actuator. The other limitation was the absence of a mechanical preloading mechanism that keeps the reticle on the z -supports. This resulted in a parasitic z -translation of the reticle for an applied bending moment. A bias voltage had to be applied in order to keep the reticle on the z -supports during measurements. The validation measurements were therefore only possible across 15% of the initial actuation range.

The proposed manipulator control strategy in Figure 6.3 made it necessary to perform two calibration measurements. The first focussed on identifying the relation between the measured strain gauge voltages \mathbf{U}_s and piezoelectric actuator displacements \mathbf{y}_l which are needed for the implementation of the local feedback controllers. The measurements showed that the calibration error was lower than 10 [nm]. This satisfied the curvature setting accuracy specification by approximately a factor 3.

The second calibration measurement consisted of identifying the input decoupling vector \mathbf{T}_i that translates a reticle curvature setpoint r_κ to local piezoelectric actuator elongation setpoints \mathbf{r}_l . The calibration procedure consisted of measuring static reticle deformation shapes that are realized by a set of independent piezoelectric actuator setpoints. The shapes were then used to quantify the contribution of each actuator to the desired anti-clastic curvature shape. Theoretical analysis of the calibration procedure demonstrated that each shape had to be measured with a 0.1 [nm] (1σ) accuracy in order to satisfy the curvature setting accuracy requirement. The calibration measurements showed good correspondence between the modelled and measured static actuator deflection shapes. The input decoupling gains could not be identified however because of a 7.5 [nm] (1σ) variation on the measured deflection shapes.

The implementation of the controllers in the realized curvature manipulator setup provided the first opportunity to compare the measured and modelled system performance. System identification measurements showed that the modelled and measured curvature

manipulator had the same dynamic behaviour at piezoelectric actuator and strain gauge level. It confirmed the mechanical decoupling between the piezoelectric actuators and unobservability of the reticle dynamics by the strain gauge sensors. The larger phase lag in the measurement setup limited the bandwidth of the local actuator feedback controllers to 205 [Hz] instead of the 580 [Hz] in Chapter 5. The applied controller nevertheless reduced the steady-state MA elongation error of the piezoelectric actuator to 1.4 [nm] (1σ). This translates to an estimated curvature error of 1×10^{-7} [1/m] which satisfies the curvature accuracy by a factor 20.

The manipulator performance was first determined for static curvature setpoints. The measured reticle deflections corresponded to the modelled anticlastic curvature shape of $\kappa = 0.1 \times 10^{-3}$ [1/m]. The results also showed that the reticle curvature had a linear relationship with the applied actuator voltage. It is expected that larger curvature amplitudes can be realized if the issue of the reticle support is overcome in the design. A higher order deflection shape was also present in the photomask. This is attributed to uncalibrated input decoupling gains T_i and the inability to close one of the local actuator feedback loops due to the broken strain gauge. The focus error on the opposite side of the reticle was limited to sub-5 [nm] at reticle level however.

In-plane pattern deformations were finally predicted from the static curvature measurement results for a curvature of $\kappa_x = 0.4 \times 10^{-3}$ [1/m]. The initial distortions showed the expected asymmetric pattern magnification with an additional non-symmetry. The latter is attributed to a parasitic reticle tilt in the measurements. The distortions after correction were equal to 0.14 [nm] with an expected fading penalty if approximately 1.6 [nm]. Although this exceeds the 0.1 [nm] specification, it is probably still acceptable when the total overlay budget of the machine is considered. The conclusion from the static measurements is therefore that the desired curvature can statically be achieved with acceptable impact on the lithography process.

A first attempt was made to quantify the manipulator performance for dynamic curvature setpoints. The measurements were limited by the absence of a real-time curvature measurement system in the validation setup. This made it necessary to estimate the performance from the measured piezoelectric actuator elongations and the deflection at the centre of the reticle. Measurements showed that both the predicted MA curvature error from the piezoelectric actuator elongation error and the reticle centre exceeded the curvature setting accuracy specification. Furthermore, the measurements showed that the MA piezoelectric actuator elongation error was reduced by a factor 2 when the controller bandwidth was increased from 205 [Hz] to 530 [Hz] whilst the MA deflection of the photomask centre stayed the same. The difference indicates that there is no linear relation between the piezoelectric actuator elongation and the photomask deflection for dynamic setpoints up to the 145 [Hz] cut-off frequency of the MA filter. Mechanical hysteresis in the clamp-reticle interface is a possible cause for this behaviour. The unknowns in the dynamic validation experiments have led to another conclusion, namely that a curvature measurement system must be included in the design in order to be able to validate its dynamic curvature tracking performance.

The above has led to the following recommendations for future research:

- Eliminate the current limitations in the curvature manipulator setup. This consists of repairing the broken strain gauge sensor and adding a preloading mechanism to

Criteria		Specification	Measurements		Unit	Satisfies specification?
			Static ¹	Dynamic ²		
Imaging	Curvature	0.4×10^{-3}	0.4×10^{-3}	-	[1/m]	Yes
	Fading	2	1.6	-	[nm]	Yes
Overlay	DCO	0.1	0.14	-	[nm]	Yes ³

¹ Based on extrapolation of results for $\kappa = 0.1 \times 10^{-3}$ [1/m].

² Dynamic performance was not quantified in this thesis.

³ Can only be achieved with additional machine overlay corrections. The 0.14 [nm] is considered acceptable if the total overlay budget is considered.

Table 6.3: Comparison of the curvature manipulator specifications of Chapter 2 and the static and dynamic measurement results with the manipulator setup.

keep the reticle on its z -supports during actuation.

- Redesign or use a different the external measurement setup that is used for the manipulator validation measurements.
- Develop a real-time curvature measurement system. This system can be used to identify the dynamic curvature tracking performance. The measurement information also makes it possible to identify the presence of hysteresis in the mechanical interface between the reticle and photomask. It also enables the possibility to apply the outer curvature feedback loop as proposed in Chapter 5.
- Investigate the curvature manipulator performance with respect to other lithography performance specifications such as pattern distortions, stress-birefringence and optical aberrations. This probably requires other validation measurement setups.

Part III

Closing

Chapter 7

Conclusions and Recommendations

This chapter reflects on the thesis results. It presents the thesis conclusions and provides recommendations for future research.

7.1 Conclusions

The primary objective of this thesis was to investigate the benefit and feasibility of a photomask curvature manipulator as a focus improvement technology in immersion lithography systems. The manipulator facilitates active control of the aerial image curvature at wafer level. The resulting field curvature correction is a manner to improve focus control during the lithography exposure process.

The research question was investigated by the following approach. The first step consisted of identifying the focus improvement potential and theoretical feasibility of an ideal photomask curvature manipulator. A preferred manipulation concept was thereafter designed, modelled and experimentally validated. High level lithography specifications and boundary conditions were used to quantify the required performance of the manipulation concept. Results of the curvature manipulator investigation are summarized in Table 7.1.

The first conclusion from this thesis is:

"A field curvature correction of $\kappa = \pm 0.4 \times 10^{-3}$ [1/m] can enable the sub-70 [nm] focus budget requirement in DUV immersion lithography systems for the imaging of IC feature sizes below 20 [nm]."

The above conclusion can be drawn by considering the total focus budget as well as the focus improvement potential of a field curvature correction. Chapter 1 introduced the fact

Specification		Modeling		Validation		Unit
Description	Value	Ideal	Detailed	Static ¹	Dynamic	
Curvature amplitude ($\times 10^{-3}$)	± 0.4	± 0.4	± 0.4	± 0.4	-	[1/m]
Curvature accuracy ($\times 10^{-6}$)	± 2.4	-	± 1.0	-	-	[1/m]
Overlay (DCO)	0.1	0.02	0.05	0.14	-	[nm]
Overlay (MMO)	0.6	-	0.36	-	-	[nm]
Fading	2.0	1.6	1.6	1.6	-	[nm]
Birefringence	1.0	0.17	0.18	-	-	[nm/cm]
Aberrations	4.0	0.0	-	-	-	[m λ]
Reference		Chapter 3	Chapter 5	Chapter 6		[nm]

¹ Values based on extrapolation of measurement results for $\pm 0.4 \times 10^{-3}$ [1/m].

Table 7.1: Summary of the curvature manipulator performance results in this thesis.

that several technologies have been identified for a 70 [nm] focus control performance in immersion lithography machines [15]. This focus control is needed to manufacture IC feature sizes up to 20 [nm]. Chapter 2 demonstrated that a field curvature correction of $\kappa_x = \pm 0.4 \times 10^{-3}$ [1/m] can reduce lens heating and wafer non-flatness defocus by approximately 10 [nm] each. A field curvature correction can therefore reduce the 70 [nm] focus budget by more than 10 [nm] which is needed to manufacture IC feature sizes below 20 [nm].

The second conclusion that can be drawn from this thesis is:

“A field curvature correction of $\kappa = \pm 0.4 \times 10^{-3}$ [1/m] by ideal reticle bending is only feasible when the overlay correction mechanisms in the lithography system are used to correct the 16 [nm] overlay penalty below the 0.1 [nm] specification.”

This conclusion can be drawn from the derived system specifications and conceptual analysis results in Chapters 2 and 3 which are summarized in Table 7.1. The latter chapter demonstrated that the aerial image curvature at wafer level has a one-to-one dependency on the reticle curvature. Furthermore, it showed that the desired reticle curvature of $\kappa_x = 0.4 \times 10^{-3}$ [1/m] and a parasitic anticlastic curvature of $\kappa_y = -0.07 \times 10^{-3}$ [1/m] are obtained by the application of a 0.1 [Nm] bending moment to the reticle’s edges. The defocus effect by the anticlastic curvature can be neglected because of the small slit dimensions in y -direction. The parasitic pattern magnification of 16 [nm] that is induced by bending can theoretically be corrected down to 17 [pm] by existing lens manipulators in the lithography tool at the cost of a 1.6 [nm] fading penalty. Both the residual pattern distortions and fading penalty after correction are within the 50 [pm] overlay and 2 [nm] fading specifications. Other analyses demonstrated that the induced stress birefringence and optical aberrations were negligible. Reticle bending can therefore achieve the desired field curvature correction at wafer level and keep the bending parasitics (overlay, stress-birefringence and optical aberrations) within specifications as long as the correction potential of the lithographic lens is used.

The third conclusion of this thesis is:

“The integration of a curvature manipulator in the lithography tool requires a redesign of the reticle clamping configuration because the reticle bending and stage acceleration loads exceed the available in-plane reticle clamping force by a factor of 1.3.”

This conclusion can be drawn from considerations in Chapter 2 and 4. It showed that the present reticle clamping configuration has two frictional interfaces at the photomask bottom surface. Each interface has an available friction force of approximately 24 [N] to clamp the reticle. Acceleration of the reticle already consumes 22 [N] of the available friction force whilst a force of 7.5 [N] is needed in the clamping interface in order to follow the 100 [nm] contraction or expansion of the reticle's bottom surface at curvatures of $\kappa = \pm 0.4 \times 10^{-3}$ [1/m]. The combined loads exceed the available in-plane constraining force by a factor of 1.3 and therefore lead to reticle slip. The varying reticle curvature setpoint across wafers can lead to a changing reticle position error on the reticle clamp as well as varying local distortion forces at the reticle-to-clamp interface. Both effects introduce an overlay error.

Integration of the reticle bending manipulator in the current clamping configuration also has other disadvantages. First, the parasitic in-plane force that results from the 100 [nm] photomask deformation and the in-plane clamp stiffness leads to a stress-birefringence penalty of 0.4 [nm/cm]. Second, larger bending moments are needed for the current clamping membrane because it increases the bending stiffness of the reticle by approximately a factor of 2. The increase is caused by the membrane's in-plane stiffness which translates to a rotational stiffness due to the pitch between the reticle's bottom surface and its neutral bending axis. Finally, it is desired to introduce the bending moments into the reticle at the current clamping membrane location instead of its edge because it reduces the curvature manipulator stroke and stiffness requirements by three orders of magnitude. Alternative clamping configurations that accelerate the reticle by normal forces on the reticle edges are currently under investigation [4, 80, 103]. Such concepts free up the current clamping regions for the application of bending moments to the reticle. The final performance of the curvature manipulator in the lithography tool is therefore dependent on its own feasibility as well as that of an alternative clamping configuration.

The fourth conclusion from this thesis is:

"The manipulator design can theoretically realize static and dynamic reticle curvatures of $\kappa = \pm 0.4 \times 10^{-3}$ [1/m] whilst satisfying the lithography specifications."

This conclusion can be drawn from the values in Table 7.1. These were acquired in Chapters 4 and 5 which respectively presented the manipulator design and mechanical, control and thermal models of the manipulator. The models did not include non-linearities in the actuators, sensors or clamping interface. The proposed piezoelectrically driven curvature manipulator design satisfies the specifications for the following reasons. The mechanical modelling showed that the manipulator is able to realize the $\pm 0.4 \times 10^{-3}$ [1/m] curvature with a negligible higher order deformation in the reticle. It also demonstrated that the induced pattern distortions by bending were within the 50 [pm] specification after lens correction. Furthermore, the impact of the manipulator on the reticle clamping fingerprint satisfied the 0.6 [nm] MMO specification. Finally, the manipulator increased the reticle eigenfrequencies by a maximum of 18% and the stress-birefringence penalty was a factor 5 withinin specification.

The results of the control and thermal analysis also support the fourth conclusion. The control analysis demonstrated that the proposed local feedback across each piezoelectric actuator can satisfy the curvature tracking accuracy specification of 2.4×10^{-6} [1/m] for a characteristic wafer curvature setpoint. An error budgeting analysis proved that the ma-

nipulator disturbances were also not limiting the curvature setting accuracy specification. The thermal analysis highlighted that the power dissipation of the piezoelectric actuators was below the 4 [mW] specification.

There are nevertheless two items that challenge the above conclusion on manipulator performance. The first is the uncertainty about the allowed stresses in the ball-on-flat contacts between the reticle and manipulator. Although this requires further investigation, it is expected that the contact can be designed to accommodate the requirements. The second issue is the thermal load of the leaky seal and strain gauges which exceeds the 4 [mW] power dissipation specification near the reticle edge. The overlay penalty of the former is expected to be within the 90 [pm] specification but the latter exceeds this specification by a factor 7.6. It could be resolved however by a configuration change in strain gauge readout electronics. The linear mechanical, control and thermal analysis results of the curvature manipulator therefore satisfy the high-level lithography system specifications and boundary conditions.

The fifth conclusion of this thesis is:

“The curvature manipulator damps the 2nd reticle resonance mode by three orders of magnitude when a curvature sensor and outer curvature feedback loop are included in the manipulator design.”

This conclusion can be drawn from the manipulator control analysis in Chapter 5 which investigated two control strategies. The first employs decentralized or local feedback control across each collocated piezoelectric actuator and strain gauge sensor. Its main objective is to counteract the piezoelectric actuator hysteresis by feedback control. The second strategy has the same local actuator feedback with an additional outer curvature feedback loop. The control analysis showed that the second resonance mode of the reticle can only be counteracted by the second control strategy. This is attributed to the fact that this resonance is observed by a curvature sensor but not by the strain gauge on the piezoelectric actuator. The result demonstrated another potential use of the curvature manipulator namely that of an active damping mechanism for reticle resonances in the reticle stage. Sadly, this could not be experimentally validated because of the absence of a curvature sensor in the eventual measurement setup. Furthermore, the focus and fading gain by the damped reticle mode could not be determined because of lack of publicly available information on the reticle stage servo performance.

The sixth conclusion from this thesis is:

The manipulator can experimentally realize static photomask curvatures of $\kappa = 0.4 \times 10^{-3}$ [1/m] with a sub-1 [nm] focus error and 0.14 [nm] overlay penalty.

This conclusion is based on an extrapolation of the experimental validation results in Chapter 6. An extrapolation is needed because the results were acquired with a setup that had several limitations. First, validation measurements could only take place up to curvature of $\kappa = 0.1 \times 10^{-3}$ [1/m] because 85% of the piezoelectric actuator range was needed to constrain the reticle on its out-of-plane supports. It highlighted that correct integration of the out-of-plane supports in the mechanism are key in realizing the desired curvature amplitude. Furthermore, a broken strain gauge made it impossible to close one

of the local piezoelectric actuator elongation feedback loops. It showed up in measurements as an undesired higher order reticle deformation.

Even though the setup had flaws, the curvature manipulation measurements provided sufficient confidence that a static curvature of $\kappa = \pm 0.4 \times 10^{-3} [1/m]$ could be achieved. The measured static reticle deformation shape was in close agreement with the theoretically predicted anticlastic curvature shape of Chapter 3. They differed by less than 5 [nm] at the locations away from the broken strain gauge which translates to a sub-nanometre focus error at wafer level. Furthermore, the actuator linearity and expected steady state curvature error of the system also provided confidence. The latter satisfied the curvature accuracy specification by a factor of 20. Finally, the overlay penalty for a curvature of $\kappa = \pm 0.4 \times 10^{-3} [1/m]$ was predicted from scaled out-of-plane measurement results. It was equal to 0.14 [nm] after applying the lithography system correctables which is close to the 0.1 [nm] overlay requirement.

An attempt was made to validate the dynamic curvature tracking performance of the manipulator design. The measured and modelled transfer functions between the piezoelectric actuators and strain gauge sensors agreed between 1 to 7 dB up to 1 [kHz]. The absence of a real-time curvature measurement system in the external metrology setup limited further dynamic validation experiments however. First-order estimates of the curvature tracking performance were therefore obtained from the deflection measurements of the reticle centre and strain gauge sensor signals. Both values exceeded the curvature tracking error specification of $\kappa = 2.4 \times 10^{-6} [1/m]$ and also showed different trends. The difference highlighted that further investigation into the manipulator's dynamic curvature tracking performance is needed with the correct metrology system and that no conclusion could be drawn yet on the curvature tracking performance of the manipulator. The inability to directly measure curvature in the experimental setup has led to the seventh conclusion of this thesis:

"A curvature measurement system must be included in the manipulator design in order to be able to validate its dynamic curvature tracking performance."

The conclusion is based on the following argumentation. First, reticle curvature information is needed to be able to calibrate the input decoupling gains in the control strategy that translate the curvature setpoint to piezoelectric actuator elongation setpoints. Chapter 6 showed that errors in these gains can lead to unevenly applied bending moments by the actuator mechanisms and subsequently the wrong reticle deformation shape. Second, Chapter 5 demonstrated that the reticle deformations are largely unobservable by the strain gauge sensors on the piezoelectric actuators. This is attributed to the compliance that is placed in series with the piezoelectric actuator in the actuation mechanism. The deformed reticle shape results in the deformation of this compliance instead of the piezoelectric actuator. Third, the vacuum preloaded interface between the strain gauge and reticle is a mechanical contact with possibly hysteresis. Such a hysteretic interface can result in erroneous photomask deformations. Finally, disturbances might act on the reticle in the lithography environment. These disturbances cannot be counteracted by the piezoelectric actuators because they are unobservable by the strain gauge sensors. The above items confirm that it is necessary to have reticle curvature information either for calibration purposes or to implement the real-time outer curvature feedback loop. The sampling frequency that is required for the reticle curvature measurement depends on

the drifts, hysteresis and reticle disturbances in the system. These are currently not well characterized for the curvature manipulator.

The validation measurements in this thesis focussed on measuring the photomask curvature manipulation performance of the developed actuation system. The manipulation system was not validated with respect to other lithography specifications such as stress-birefringence, pattern deformations (overlay) and optical aberrations as is clear from Table 7.1. It is evident that this must be done before the system will be implemented in any HVM lithography tool.

To conclude, this thesis has proved the conceptual and practical feasibility of a reticle curvature manipulator at demonstrator level. Although improvements need to be made to the manipulator, the modelling results and experiments presented in this thesis have led to a main conclusion which can be summarized as follows:

"The use of a curvature manipulator in lithography tools is currently limited by the lack of validation measurement data of its dynamic curvature manipulation performance."

Future work should focus on further validation and evolution of the manipulator so that it can be used as a field curvature correction manipulator in immersion lithography systems. This integration step depends on the desire of the lithography industry to have the sub 70 [nm] focus control and the feasibility of a novel reticle clamping configuration in the lithography tool.

7.2 Recommendations

The work in this thesis has led to the following recommendations for the improvement of the manipulator and to facilitate machine integration.

- The z-support should be integrated into the curvature manipulator design in order to avoid the parasitic out-of-plane motion of the reticle that was predicted by the kinematic model in Chapter 4 and encountered in the experimental setup of the manipulator. The z-support should have the same out-of-plane stiffness as the current z-support but should be compliant in-plane to follow the reticle in-plane deformation during bending. The combined in-plane stiffness of the manipulator with z-support should not exceed the level of 4.7×10^5 [N/m] that was identified in Chapter 4 when it is kinematically constrained by another clamping mechanism.
- One of the current limitations in the realised measurement setup is the broken strain gauge sensor. The inability to close the local feedback loop between the piezoelectric actuator with the broken strain gauge is a potential cause for the higher order reticle deformation that was encountered in the static curvature measurement. It is advised to repair the strain gauge, close all local actuator feedback loops and redo the static curvature measurement to see if this indeed eliminates the higher order deformation.

- A detailed investigation of reticle damage and fracture at the ball-on-flat contact locations between the reticle and the interface rods has not been performed in this thesis. The high cost of customer photomasks (\$1,000 – \$100,000) makes it necessary to research this, both analytically and experimentally, in order to be confident that the manipulator design does not lead to reticle failure. The contacts should be changed if the contact stresses are an issue in the proposed manipulator design.
- A measurement setup and strategy should be developed in order to facilitate the accurate calibration of the input decoupling gains that translate the reticle curvature setpoint to the local piezoelectric actuator setpoints. This accuracy is limited in the current validation measurement setup which is a potential cause of the encountered higher order reticle deformations. Efforts should focus on calibration setups and strategies both for outside and inside the lithography scanner. A potential sensor which can facilitate the latter in an immersion lithography tool is a wavefront sensor as described in [120].
- A real-time curvature measurement system should be developed for future experimental validation of the manipulator. First, it allows the validation of its dynamic curvature control performance. Second, it provides information on the change of the manipulator performance in time by phenomena like strain gauge sensor drift or hysteresis in the reticle-to-manipulator interface. This information can then be used to identify the required frequency of system calibration. Finally, the sensor makes it possible to experimentally validate the performance of the outer curvature feedback loop in Chapter 5. Furthermore, it also provides the opportunity to test the manipulator as an active vibration damper for the suppression of reticle dynamics.
- The detailed control analysis in Chapter 5 provided performance estimates of an idealized manipulator. System non-linearities and delays were not taken into account. It is recommended to include these items and study their effect on the manipulator performance. Specific proposals are the inclusion of system delays, piezoelectric actuator hysteresis and drift as well as strain gauge sensor drifts and erroneous sensor gains. Specific models that can be used to describe the piezoelectric actuator drift and hysteresis are provided in [29, 54, 72].
- The investigated control strategies in this thesis consisted of conventional PID-control that were tuned using loop shaping techniques. Furthermore, a feedforward with constant gain was implemented. These methods are favourable because of their ease of implementation, but might not achieve the best performance. It is recommended to investigate if the system performance can be enhanced by more advanced control strategies like MIMO control [100]. Other possible enhancements that are interesting to investigate are inverse actuator hysteresis models similar to those applied for reluctance actuators [56, 57]. The extended manipulator model that was proposed in the previous recommendation can be used for the analysis of these control strategies.
- It is recommended to reconsider the choice of a strain gauge as local feedback sensor across the piezoelectric actuators. The sensor was largely chosen because of its

low mass and volume claim. Its main issues are the large thermal dissipation, possible sensor drift, the bridge offset and its sensitivity to parasitic stresses. Attempts should be made to minimize these effects if the strain gauge is indeed preferred. A full Wheatstone bridge configuration instead of the current quarter bridge should be used because it reduces the bridge sensitivity to temperature changes, bending strains and non-linearity. Furthermore, the driving voltage of the bridge must be reduced in order to satisfy the power dissipation specification at the reticle edge of 4 [mW] but still achieve the required signal-to-noise ratio.

- The feasibility of the curvature manipulator in the lithography tool depends on its ability to satisfy the overlay specifications. This holds both for the introduced Matched Machine Overlay error and the Dedicated Chuck Overlay. Section 6.2 explained that the validation of the manipulator in terms of its overlay performance requires a measurement of the in-plane pattern distortions with sub-nanometre accuracy. No off-the-shelf sensor was available for this measurement. A number of possibilities exist however. First, it is possible to perform the overlay validation experiment in the lithography tool using an overlay reticle as presented in [28]. It has the advantage that the lens correction functionality can be included in the measurements although this requires the complete integration of a curvature manipulator in a reticle stage. A second possibility is to cover the reticle with an encoder gratings. The encoders can then be used to measure the grid deformation due to bending. Finally, it is possible to get an estimate of the Matched Machine Overlay error by measuring the out-of-plane deformation of the reticle on the current reticle clamping configuration and on the reticle bending manipulator using a surface interferometer. The in-plane pattern distortions can thereafter be estimated from the out-of-plane deformation difference between the two cases using the technique in Section 6.3.4. It is proposed to investigate these proposals in greater detail.
- Closely related to the previous recommendation are validation experiments for the induced photomask stress-birefringence and optical aberrations by bending. These measurements are recommended even though Chapter 3 demonstrated that these are not introduced by bending. Stress-birefringence measurements can be performed outside the lithography system using commercially available hardware as was done in [22, 120]. A wavefront sensor is recommended for the measurement of the optical aberrations. One option is to use the wavefront sensor that is currently present in a state-of-the-art lithography system [120].
- The design of the curvature manipulator concept is based on predefined boundary conditions of the reticle stage. It is recommended to investigate the manipulator impact on the reticle stage design and its functionality. Reticle positioning and curvature manipulator performance must be investigated for the combined curvature manipulator and novel clamp design. Furthermore, the impact of the mechanism on chuck dynamics and stage positioning performance should be evaluated. Another proposal is to quantify the impact of chuck deformation that are introduced by the reaction moments of the curvature manipulator. Analysis should also be performed on the stresses in the chuck and manipulator at the maximum accelerations. These are currently equal to $150 \text{ [m/s}^2\text{]}$ at reticle stage [21].

- The final recommendation of this thesis is to place a reticle stage with curvature manipulator and novel reticle clamp in a lithography tool to test its performance under real scanner conditions.

To finalize, this thesis has presented initial results on how to obtain a focus improvement in lithography systems by actively controlling the photomask curvature. The theoretical analysis and the developed functional model have shown that the principle is conceptually feasible and that the desired shapes can be realized by the manipulator. Further optimization is needed however in order to satisfy the high level lithography requirements. The efforts should focus on the minimization of the parasitic deformations by the manipulator as well as enhancement of the curvature tracking performance by adding a reticle curvature sensor and corresponding feedback loop. Furthermore, the concept must prove its performance in a lithography scanner environment before it will be used for high-volume-manufacturing. The integration into high-volume-manufacturing tools is not only dependent on the manipulator performance but also on the need of the semiconductor industry to have an improved focus in DUV lithography machines for the manufacturing of sub-20 [nm] features. In that case, a field curvature correction by reticle bending is considered as an interesting focus improvement technology for which the results in this thesis can be used as a starting point.

Bibliography

- [1] A. Y. Abdo, P. L. Reu, M. P. Schlax, R. L. Engelstad, W. A. Beckman, J. W. Mitchell, and E. G. Lovell. Experimental model verification of the thermal response of optical reticles. In *Proceedings of SPIE, Optical Microlithography XIV*, volume 4346, September 2001.
- [2] H. J. M. T. A. Adriaens, W. L. De Koning, and Banning, R. Modelling piezo-electric actuators. *IEEE/ASME Transactions on Mechatronics*, 5(4):331 – 341, December 2000.
- [3] R. Albers. TAR Piezo Amplifier PI E-831. Technical report, ASML, 2009.
- [4] D. Amin-Shahidi. Patterning device support, October 2011. US Patent Application 2012/0140198.
- [5] Analog Devices Inc.. *AD620 Low Cost Low Power Instrumentation Amplifier specifications*, 1999. www.analog.com.
- [6] W. H. Arnold. Towards 3 [nm] overlay and critical dimension uniformity: an integrated error budget for double patterning lithography. In *Proceedings of SPIE, Optical Microlithography XXI*, volume 6924, February 2008.
- [7] J. Baselmans. Internal ASML discussion on defocus by lens heating, March 2011.
- [8] J. Bekaert, B. Laenens, S. Verhaegen, L. van Look, D. Trivkovic, F. Lazzarino, G. Vandenberghe, P. van Adrichem, R. Socha, S. Hsu, H.Y Liu, O. Mouraille, K. Schreel, M. Dusa, J. Zimmermann, P. Gräupner, and J.T. Neumann. Experimental verification of source-mask optimization and free-form illumination for 22-nm node static random access memory cells. *Journal of Micro/Nanolithography, MEMS, and MOEMS*, 10(1):013008, 2011.
- [9] J. Bekaert, L. van Look, G. Vandenberghe, P. van Adrichem, M.J. Maslow, J.W. Gemmink, H. Cao, S. Hunsche, J.T. Neumann, and A. Wolf. Characterization and control of dynamic lens heating effects under high volume manufacturing conditions. In *Proceedings of SPIE, Optical Microlithography XXIV*, volume 7973, February 2011.

- [10] J. Benschop. Innovation outside the box, ASML research review (public presentation), 15th October 2008. www.asml.com.
- [11] J.P. Bentley. *Principles of measurement systems*. Pearson Prentice Hall, 4th edition, 2005. ISBN 978-0-13-043028-1.
- [12] D.J. Bijvoet and A.A. Bijnagte. Lithographic apparatus and exposure method, October 2009. US Patent Application 2009/0073402.
- [13] M. Binnard, Y. Shibasaki, M. Hamatani, S. Wakamoto, Y. Shiba, Y. Uehara, and T. Fujiwara. Semiconductor lithography: enabling production beyond 22 [nm]. In *Proceedings of ASPE summer topical meeting, Precision Engineering and Mechanics Supporting the Semiconductor Industry*, June 2012.
- [14] M. Boonman, C. van de Vin, S. Tempelaars, R. van Doorn, J. Zimmerman, P. Teunissen, and A. Minnaert. The performance advantage of a dual stage system - Focus performance at high throughput. In *Proceedings of SPIE, Optical Microlithography XVII*, volume 5377, February 2004.
- [15] I. Bouchoms, M. Leenders, J.J. Kuit, R. Kazinczi, R. de Graaf, B. Paarhuis, P. Gunter, S. Weichselbaum, M. Beems, M. Verhoeven, and R. van Ballegoij. Extending 1.35 NA Immersion lithography down to 1x nm production nodes. In *Proceedings of SPIE, Optical Microlithography XXV*, volume 8326, February 2012.
- [16] W.E. Boyce and R.C. DiPrima. *Elementary differential equations and boundary value problems*. John Wiley & Sons Inc., 7th edition, 2001. ISBN 0-471-31999-6.
- [17] T. Brunner, D. Corliss, S. Butt, T. Wiltshire, C.P. Ausschnitt, and M. Smith. Laser bandwidth and other sources of focus blur in lithography. *Journal of Micro/Nanolithography, MEMS, and MOEMS*, 5(4):043003, November 2006.
- [18] T.A. Brunner. Impact of lens aberrations on optical lithography. *IBM Journal of Research and Development*, 41(1.2):57–67, 1997.
- [19] J.H. Burnett and S.G. Kaplan. Measurement of the refractive index and thermo-optic coefficient of water near 193 [nm]. *Journal of Micro/Nanolithography, MEMS, and MOEMS*, 3(1):68–72, 2004.
- [20] H. Butler. Position control in lithography equipment: an enabler for current-day chip manufacturing. *IEEE Control Systems Magazine*, 31(5):28–47, 2011.
- [21] T. Castenmiller, F. van de Mast, T. de Kort, C. van de Vin, M. de Wit, and S. van Cleef. Towards ultimate optical lithography with NXT : 1950i dual stage immersion platform. In *Proceedings of SPIE, Optical Microlithography XXIII*, volume 7640, February 2010.
- [22] E. Cotte, M. Selle, K. Bubke, and S. Teuber. Study of stress birefringence for 193-nm immersion photomasks. In *Proceedings of SPIE, Photomask and Next-Generation Lithography Mask Technology XII*, volume 5853, pages 10–19, April 2005.

- [23] E.P. Cotte, R.L. Engelstad, E.G. Lovell, D. Tanzil, O. Eschbach, and E.Y. Shu. Experimental and Numerical Studies of the Effects of Materials and Attachment Conditions on Pellicle-Induced Distortions in Advanced Photomasks. In *Proceedings of SPIE, Photomask and Next-Generation Lithography Mask Technology IX*, volume 4754, April 2002.
- [24] E.P. Cotte, R. Hässler, B. Utess, G. Antesberger, F. Kromer, and S. Teuber. Pellicle choice for 193 [nm] immersion lithography photomasks. In *Proceedings of SPIE, 24th BACUS Symposium on Photomask Technology*, volume 5567, pages 511–520, September 2004.
- [25] H. Cox, H. van der Schoot, and W. Simons. NXT SDS Mechatronic Specification for High Throughput and High Precision Stages. Technical report, ASML, 2008.
- [26] F. de Jong, B. van der Pasch, T. Castenmiller, B. Vleeming, R. Droste, and F. van de Mast. Enabling the lithography roadmap: an immersion tool based on a novel stage positioning system. In *Proceedings of SPIE, Optical Microlithography XXII*, volume 7274, February 2009.
- [27] D. de Klerk, D.J. Rixen, and S.N. Voormeeren. General framework for dynamic substructuring: history, review and classification of techniques. *AIAA Journal*, 46(5):1169–1181, 2008.
- [28] R. de Kruif, T. van Rhee, and E. van der Heijden. Reduced pellicle impact on overlay using higher order intra-field grid corrections. In *Proceedings of SPIE, the 25th European Mask and Lithography Conference*, volume 7470, January 2009.
- [29] S. Devasia, E. Eleftheriou, and S.O.R. Moheimani. A survey of control issues in nanopositioning. *IEEE/ASME Transactions on Control Systems Technology*, 15(5):802 – 823, September 2007.
- [30] S.N.L. Donders and T.A.R. van Empel. Lithographic apparatus with mask clamping apparatus, 2001. European Patent Application 2001/1107066.
- [31] D.J. Ewins. *Modal testing: theory, practice and application*. Research Studies Press Ltd., 2nd edition, 2000. ISBN 0-8638-0218-4.
- [32] J. Finders, M. Dusa, B. Vleeming, H. Megens, B. Hepp, M. Maenhoudt, S. Cheng, and T. Vandeweyer. Double patterning for 32 [nm] and below: an update. In *Proceedings of SPIE, Optical Microlithography XXI*, volume 6924, February 2008.
- [33] J. Finders, M. Dusa, B. Vleeming, B. Hepp, M. Maenhoudt, S. Cheng, and T. Vandeweyer. Double patterning lithography for 32 [nm]: critical dimension uniformity and overlay considerations. *Journal of Micro/Nanolithography, MEMS, and MOEMS*, 8(1):011002, 2009.
- [34] J. Finders, M. Dusa, J. Mulkens, Y. Cao, and M. Escalante. Solutions for 22 [nm] node patterning using ArFi technology. In *Proceedings of SPIE, Optical Microlithography XXIV*, volume 7973, February 2011.

- [35] G.F. Franklin, J.D. Powell, and A. Emami-Naeini. *Feedback control of dynamic systems*. Prentice Hall, 5th edition, 2008. ISBN 978-0-13-507181-6.
- [36] T. Fujisawa, M. Asano, T. Sutani, S. Inoue, H. Yamada, J. Sugamoto, K. Okumura, T. Hagiwara, and S. Oka. Analysis of Wafer Flatness for CD Control in Photolithography. In *Proceedings of SPIE, Optical Microlithography XV*, volume 4691, March 2002.
- [37] T. Fujiwara, T. Toki, D. Tanaka, J. Kosugi, T. Susa, N. Sakasai, and A. Tokui. Advanced CDU control for 22 [nm] and below. In *Proceedings of SPIE, Optical Microlithography XXIV*, volume 7973, February 2011.
- [38] Gartner Research, 2011. www.gartner.com.
- [39] W.K. Gawronski. *Advances Structural Dynamics and Active Control of Structures*. Springer-Verlag New York Inc., 1st edition, 2004. ISBN 0-387-40649-2.
- [40] P. Ge and M. Jouaneh. Tracking control of a piezoceramic actuator. *IEEE transactions on control systems technology*, 4(3):209 – 216, 1996.
- [41] B. Geh, G. Flagello, C. Proglar, P. Martin, L.H.A. Leunissen, S. Hansen, and W. de Boeij. The impact of mask birefringence on hyper-NA polarized imaging. In *Proceedings of SPIE, the 25th Annual BACUS Symposium on Photomask Technology*, volume 5992, October 2005.
- [42] M. Geradin and D.J. Rixen. *Theory and application to structural dynamics*. John Wiley & Sons Inc., 2nd edition, 1997. ISBN 0-471-93927-7.
- [43] J.M. Gere and S.P. Timoshenko. *Mechanics of materials*. Stanley Thornes Publishers Ltd., 4th edition, 1999. ISBN 0-7487-3998-X.
- [44] P. Graupner, R. Garreis, A. Göhnermeier, T. Heil, M. Lowisch, and D. Flagello. Impact of wavefront errors on low k_1 processes at extreme high NA. In *Proceedings of SPIE, Optical Microlithography XVI*, volume 5040, February 2003.
- [45] J.E. Grievenkamp. *Field Guide to Geometrical Optics*. SPIE Press, 1st edition, 2004. ISBN 0-819-45294-7.
- [46] H. Gross, F. Blechinger, and B. Achtner. *Handbook of optical systems: Survey of optical instruments*, volume 4. Wiley-VCH, 4th edition, 2008. ISBN 978-3-527-40380-6.
- [47] E. Hecht and A. Zajac. *Optics*. Addison Wesley, 4th edition, 2001. ISBN 0-321-18878-0.
- [48] C.Y. Huang, C.F. Chue, A.H. Liu, W.B. Wu, C.L. Shih, J. Chiou, T.B. Lee, O. Chen, and A. Chen. Using intra-field higher order correction to achieve overlay requirements beyond sub-40 [nm] node. In *Proceedings of SPIE, Metrology, Inspection, and Process Control for Microlithography XXIII*, volume 7272, February 2009.

- [49] International Technology Roadmap for Semiconductors (ITRS). ITRS Report, 2011 Edition. www.itrs.net.
- [50] J. Ishikawa, H. Kohno, S. Sato, J. Kosugi, and Y. Shibazaki. Practical performance and enabling technologies in immersion scanners for the double patterning generation. In *Proceedings of SPIE, Optical Microlithography XXIV*, volume 7973, February 2011.
- [51] L. Jabben. *Mechatronic Design of a Magnetically Suspended Rotating Platform*. PhD Thesis, Delft University of Technology, 2007. ISBN 978-90-9022523-4.
- [52] H. Jasper. Immersion lithography with an ultra-high-na in-line catadioptric lens and a high-transmission flexible polarization illumination system. In *Optical Microlithography XIX*, volume 6154. SPIE, 2006.
- [53] A.B. Jeunink, M.K.M. Baggen, D. Bijvoet, and T.J.M. Castenmiller. Lithographic apparatus with mask clamping apparatus, January 2008. US Patent Application 2008/013068.
- [54] A. Katalenic. *Control of reluctance actuators for high-precision positioning*. PhD Thesis, Eindhoven University of Technology, 2013. ISBN 978-90-9027450-8.
- [55] A. Katalenic, J. de Boeij, C.M.M. van Lierop, and P.P.J. van den Bosch. Linearisation of the reluctance force actuator based on the parametric hysteresis inverse and a 2D spline. In *Proceedings of the 8th International Symposium on Linear Drives for Industry Applications (LDIA 2011)*, July 2011.
- [56] A. Katalenic, C.M.M. Lierop, and P.P.J. van den Bosch. Smooth Parametric Hysteresis Operator for Control. In *Proceedings of the 18th International Federation of Automatic Control World Congress (IFAC)*, volume 18, pages 2388–2394, August 2011.
- [57] A. Katalenic, C.M.M. van Lierop, and P.P.J. van den Bosch. On hysteresis and air gap disturbance in current and voltage mode feed-forward control of variable reluctance actuators. In *Proceedings of the 50th IEEE Conference on Decision and Control and European Control Conference (CDC-ECC)*, pages 1608–1613, December 2011.
- [58] R. Kingslake, R.R. Shannon, and J.C. Wyant. *Applied Optics and Optical Engineering*, volume 11. Academic Press, 1992. ISBN 978-0-124-08611-1.
- [59] B. Kneer, P. Gräupner, R. Garreis, R. Kläsches, and H. Feldmann. Catadioptric lens design: the breakthrough to hyper-NA optics. In *Proceedings of SPIE, Optical Microlithography XIX*, volume 6154, February 2006.
- [60] C. Kohler, W. de Boeij, K. van Ingen-Schenau, M. van de Kerkhof, J. de Klerk, H. Kok, G. Swinkels, J. Finders, J. Mulkens, D. Fiolka, and T. Heil. Imaging Enhancements by Polarized Illumination: Theory and Experimental Verification. In *Proceedings of SPIE, Optical Microlithography XVIII*, volume 5754, February 2005.

- [61] H. Kok. Internal ASML discussion on induced optical aberrations by reticle bending, September 2010.
- [62] M.P. Koster. *Constructieprincipes voor het nauwkeurig bewegen en positioneren*. HB uitgevers, 5th edition, 2008. ISBN 978-90-5574-610-1.
- [63] I. Lalovic, A. Kroyan, J. Kye, H.Y. Liu, and H.J. Levinson. Image-blur tolerances for 65 [nm] and 45 [nm]-node IC manufacturing. In *Proceedings of SPIE, Optical Microlithography XVI*, volume 5040, February 2003.
- [64] D.A.H Laro. *Mechatronic Design of an Electromagnetically Levitated Linear Positioning System using Novel Multi-DoF Actuators*. PhD Thesis, Delft University of Technology, 2009. ISBN 978-90-9024255-2.
- [65] H.J. Levinson. *Principles of Lithography*. SPIE press, 3rd edition, 2011. ISBN 978-08-1948324-9.
- [66] B. Liegl, B. Sapp, K. Low, S. Greco, T. Brunner, N. Felix, I. Stobert, K. Nafisi, and C. Sarma. Predicting and reducing substrate induced focus error. In *Proceedings of SPIE, Optical Microlithography XXIII*, volume 7640, February 2010.
- [67] B.J. Lin. The k_3 coefficient in non-paraxial λ/NA scaling equations for resolution, depth of focus and immersion lithography. *Journal of Micro/Nanolithography, MEMS, and MOEMS*, 1(1):7–12, 2002.
- [68] B.J. Lin. *Optical lithography: here is why*. SPIE, 1st edition, 2010. ISBN 978-0-8194-7560-2.
- [69] P. Liu, M. Snajdr, Z. Zhang, Y. Cao, J. Ye, and Y. Zhang. A computational method for optimal application specific lens control in microlithography. In *Proceedings of SPIE, Optical Microlithography XXIII*, volume 7640, February 2010.
- [70] J.M. Maciejowski. *Multivariable Feedback Design*. Addison-Wesley, 1989. ISBN 978-0-201-18243-9.
- [71] C. Mack. *Fundamental principles of optical lithography - the science of micro-fabrication*. Wiley, 4th edition, 2007. ISBN 978-0-470-01893-4.
- [72] R.J.E. Merry. *Performance-driven control of nano-motion systems*. PhD Thesis, Eindhoven University of Technology, 2009. ISBN 978-90-386-2059-6.
- [73] A.F. Mills. *Basic heat and mass transfer*. Prentice Hall, 2nd edition, 1999. ISBN 0-13-096247-3.
- [74] S.O.R. Moheimani. Invited Review Article: Accurate and fast nanopositioning with piezoelectric tube scanners: Emerging trends and future challenges. *Review of Scientific Instruments*, 79:071101, July 2008.
- [75] G.E. Moore. Cramming more components onto integrated circuits. *Electronics*, 38(8):114–117, April 1965.

- [76] J. Mulkens, D. Flagello, B. Streefkerk, and P. Gräupner. Benefits and limitations of immersion lithography systems. *Journal of Micro/Nanolithography, MEMS, and MOEMS*, 3(1):104 – 114, January .
- [77] J. Mulkens, J. de Klerk, M. Leenders, F. de Jong, and J.W. Cromwijk. Latest developments on immersion exposure systems. In *Proceedings of SPIE, Optical Microlithography XXI*, volume 6924, February 2008.
- [78] J. Mulkens, J. Finders, H. van der Laan, P. Hinnen, M. Kubis, and M. Beems. Driving Imaging and Overlay Performance to the Limits with Advanced Lithography Optimization. In *Proceedings of SPIE, Optical Microlithography XXV*, volume 8326, February 2012.
- [79] R. Munnig Schmidt, G. Schitter, and J. van Eijk. *The design of high performance mechatronics: high-tech functionality by multidisciplinary system integration*. Delft University Press, 1st edition, 2011. ISBN 978-1-60750-825-0.
- [80] G.J. Naaijkens, N. Rosielle, and M. Steinbuch. Mask sidewall clamping. In *Proceedings of SPIE, Optical Microlithography XXVI*, volume 8683, February 2013.
- [81] T. Nakashima, Y. Ohmura, T. Ogata, Y. Uehara, H. Nishinaga, and T. Matsuyama. Thermal aberration control in projection lens. In *Proceedings of SPIE, Optical Microlithography XXI*, volume 6924, February 2008.
- [82] National Instruments. *NI 622x Specifications*, 2007. www.ni.com.
- [83] Y. Ohmura. The optical design for microlithographic lenses. In *Proceedings of SPIE, International Optical Design Conference 2006*, volume 6342, June 2006.
- [84] Y. Ohmura, T. Ogata, T. Hirayama, H. Nishinaga, T. Shiota, S. Ishiyama, S. Isago, H. Kawahara, and T. Matsuyama. An aberration control of projection optics for multi-patterning lithography. In *Proceedings of SPIE, Optical Microlithography XXIV*, volume 7973, February 2011.
- [85] Optical Society of America. *Handbook of Optics, Volume II - Devices, Measurements, and Properties*. McGraw-Hill, 2nd edition, September 1994. ISBN 978-0-07-047974-6.
- [86] J.J. Ottens. Lithographic apparatus, device manufacturing method, and device manufactured thereby, June 2005. US Patent Application 2005/134829.
- [87] Physik Instrumente (PI), GmbH & Co. *D-510 PISeca Capacitive Sensors Datasheet*, 2008. www.physikinstrumente.com.
- [88] Physik Instrumente (PI), GmbH & Co. *Piezo Actuators and Components: For Motion Control, Sensing, Energy Harvesting*, 2009. www.physikinstrumente.com.
- [89] Physik Instrumente (PI), GmbH & Co. *Piezoelectrics in Positioning: Tutorial on Piezotechnology in Nanopositioning Applications*, 2009. www.physikinstrumente.com.

- [90] Physik Instrumente (PI), GmbH & Co. *E-831 OEM Piezo driver datasheet*, 2012. www.physikinstrumente.com.
- [91] R. Pintelon and J. Schoukens. *System Identification - a frequency domain approach*. IEEE Press, 1st edition, 2001. ISBN 0-7803-6000-1.
- [92] A. Preumont. *Mechatronics: Dynamics of Electromechanical and Piezoelectric Systems*. Springer, 2006. ISBN 978-1-4020-4695-7.
- [93] R. Priestley. Birefringence dispersion in fused silica for DUV lithography. In *Proceedings of SPIE, Optical Microlithography XIV*, volume 4346, February 2001.
- [94] P. Rigolli, G. Capetti, E. De Chiara, L. Amato, U. Iessi, P. Canastrari, C. Llorens, S. Smit, L. Brige, and J. Plauth. High-order distortion effects induced by extreme off-axis illumination at hyper NA lithography. In *Proceedings of SPIE, Optical Microlithography XXII*, volume 7274, February 2009.
- [95] B. Roberts, M. McQuillan, N. Louka, T. Zavec, P. Reynolds, and M. Dusa. Critical evaluation of focus analysis methods. In *Proceedings of SPIE, Optical Microlithography XVII*, volume 5377, February 2004.
- [96] Semiconductor Equipment and Materials International. *SEMI P1-0708, Specification for hard surface photomask substrates*, 2008. www.semi.org.
- [97] W.N. Sharpe. *Handbook of Experimental Solid Mechanics*. Springer, 1st edition, 2008. ISBN 978-0-387-26883-5.
- [98] Shibazaka, Y. Movable body apparatus, exposure apparatus, exposure method and device manufacturing method, February 2011. US Patent Application 2011/0032496.
- [99] S. Shulepov. Flow and heat transfer in leaky seal. Technical report, Philips Research, November 2011.
- [100] S. Skogestad and I. Postlethwaite. *Multivariable feedback control*. John Wiley & Sons, Ltd., 2nd edition, 2007. ISBN 978-0-470-01168-3.
- [101] B. Sluijk, T. Castenmiller, R. du Croo de Jongh, H. Jasper, T. Modderman, L. Levasier, E. Loopstra, G. Savenije, M. Boonman, and H. Cox. Performance results of a new generation of 300 mm lithography systems. In *Proceedings of SPIE, Optical Microlithography XIV*, volume 4346, February 2001.
- [102] F. Staals, A. Andryzhyieuskaya, H. Bakker, M. Beems, J. Finders, T. Hollink, J. Mulkens, A. Nachtwein, R. Willekers, P. Engblom, T. Gruner, and Y. Zhang. Advanced Wavefront Engineering for Improved Imaging and Overlay Applications on a 1.35 NA Immersion Scanner. In *Proceedings of SPIE, Optical Microlithography XXIV*, volume 7963, February 2011.
- [103] STW perspective programme - Smart Optics Systems. Image Manipulation for Wafer Plane Conformity in Optical Lithography systems (IMWACOL), Oktober 2008.

- [104] T. Tamura, N. Onoda, M. Fujita, and T. Uchiyama. Focus, dynamics and defectivity performance at wafer edge in immersion lithography. In *Proceedings of SPIE, Optical Microlithography XXI*, volume 6924, February 2008.
- [105] Technobis Fibre Technologies - Fibre Optic Sensing. Lady Bug ISP850HR, 2011. www.technobis-fibre-technologies.nl.
- [106] N. Ten Kate. Internal ASML discussion on heat load by leaky seal in vacuum clamp design, January 2012.
- [107] M. Totzek, P. Gräupner, T. Heil, A. Göhnermeier, O. Dittmann, D. Krähmer, V. Kamenov, J. Ruoff, and D. Flagello. Polarization influence on imaging. *Journal of Micro/Nanolithography, MEMS, and MOEMS*, 4(3):031108, 2005.
- [108] K.T. Turner, S. Veeraraghavan, and J.K. Sinha. Predicting distortions and overlay errors due to wafer deformation during chucking on lithography scanners. *Journal of Micro/Nanolithography, MEMS, and MOEMS*, 8(4):043015, November 2009.
- [109] K.T. Turner, S. Veeraraghavan, and J.K. Sinha. Relationship between localized wafer shape changes induced by residual stress and overlay errors. *Journal of Micro/Nanolithography, MEMS, and MOEMS*, 11(1):013001, March 2012.
- [110] Uchino, K. and Hirose, S. Loss mechanisms in piezoelectrics: how to measure different losses separately. *IEEE Transactions on Ultrasonics, Ferroelectrics and Frequency Control*, 48(1):307 – 321, January 2001.
- [111] Y. Uehara, T. Matsuyama, T. Nakashima, Y. Ohmura, T. Ogata, K. Suzuki, and N. Tokuda. Thermal aberration control for low k_1 lithography. In *Proceedings of SPIE, Optical Microlithography XX*, volume 6520, February 2007.
- [112] W. Ulrich, H. Rostalski, and R. Hudyma. Development of dioptric projection lenses for deep ultraviolet lithography at Carl Zeiss. *Journal of Micro/Nanolithography, MEMS, and MOEMS*, 3(1):87 – 96, 2004.
- [113] United Electronic Industries. *PowerDAQ AO Series User Manual*, 2006. www.ueidaq.com.
- [114] C.L. Valentin, C.C. Ward, P. Graffeo, D. Burbank, M.J. Schuster, and E.R. Loopstra. Patterning device manipulating systems, lithographic apparatuses, and methods of manipulating a patterning device, 23 October 2012. Patent application.
- [115] C.L. Valentin, A.F.J. de Groot, R. Munnig Schmidt, J.P.M.B. Vermeulen, and B.C.T. van Bree. Lithographic apparatus and exposure method, September 2011. US Patent Application 2011/0222039.
- [116] J. Valley, N. Poduje, J. Sinha, N. Judell, J. Wu, M. Boonman, S. Tempelaars, Y. Dommelen, H. Kattouw, J. Hauschild, B. Hughes, A. Grabbe, and L. Stanton. Approaching new metrics for wafer flatness: an investigation of the lithographic consequences of wafer non-flatness. In *Proceedings of SPIE, Optical Microlithography XVIII*, volume 5375, February 2004.

- [117] A. van Beek. *Advanced engineering design - lifetime performance and reliability*. Delft University Press, 2009. ISBN 978-90-810406-1-7.
- [118] B. van Bree. EDS Reticle Bending FUMO. Technical report, ASML, 2009.
- [119] B. van Bree. EDS Single Axis Reticle Bender. Technical report, ASML Internal Report, 2010.
- [120] M. van de Kerkhof, W. de Boeij, H. Kok, M. Silova, J. Baselmans, and M. Hemerik. Full optical column characterization of DUV lithographic projection tools. In *Proceedings of SPIE, Optical Microlithography XVII*, volume 5377, February 2004.
- [121] M. van de Kerkhof, W. de Boeij, M. Demateau, B. Geh, L.H.A. Leunissen, P. Martin, and M. Cangemi. Mask substrate birefringence requirements for hyper-NA lithography. In *Proceedings of SPIE, Optical Microlithography XIX*, volume 6154, February 2006.
- [122] M. van den Brink. Step-and-scan and step-and-repeat, a technology comparison. In *Proceedings of SPIE, Optical Microlithography XXIII*, volume 2726, June 1996.
- [123] A.A. van Veggel. *The Basic Angle Monitoring system: picometre stability with Silicon Carbide optics*. PhD Thesis, Eindhoven University of Technology, 2007. ISBN 978-90-386-0874-7.
- [124] B. van Wuijckhuijse. *Dynamic Performance Modelling of Optical Element Curvature Manipulation*. M.Sc. Thesis, Delft University of Technology, 2003.
- [125] VDI-Gesellschaft Verfahrenstechnik und Chemieingenieurwesen. *VDI Heat atlas*. Springer, 2nd edition, 2010. ISBN 978-3-540-77876-9.
- [126] E.S. Ventsel and T. Krauthammer. *Thin plates and shells: theory, analysis and applications*. Marcel Dekker, New York, 1st edition, 2001. ISBN 978-08-2470-575-6.
- [127] N.H. Vrijsen, J.W. Jansen, and E.A. Lomonova. Comparison of linear voice coil and reluctance actuators for high-precision applications. In *Proceedings of the 14th International Power Electronics and Motion Control Conference (EPE/PEMC)*, pages S3–29 – S3–36, September 2010.
- [128] C. Wagner, W. Kaiser, J. Mulkens, and D.G. Flagello. Advanced technology for extending optical lithography. In *Proceedings of SPIE, Optical Microlithography XIII*, volume 4000, February 2000.
- [129] C.C. Ward, M.H.A. Leenders, C.L. Valentin, and M.J. Schuster. Real-time curvature sensing, 6 December 2012. Patent application.
- [130] G. Wenski, T. Altmann, W. Winkler, G. Heier, and G. Hölker. Doubleside polishing - a technology mandatory for 300 [mm] wafer manufacturing. *Materials Science in Semiconductor Processing* 5, 5(4):375 – 380, 2003.

-
- [131] J. Wesselingh. *Contactless positioning using an active air film*. PhD Thesis, Delft University of Technology, 2011. ISBN 978-90-9026437-0.
- [132] F.M. White. *Fluid mechanics*. McGraw Hill, 4th edition, 1999. ISBN 0-07-116848-6.
- [133] M. Yasuda, S. Wakamoto, H. Imagawa, S. Takubo, Y. Shiba, T. Kikuchi, Y. Shirata, and Y. Ishii. Stability and calibration of overlay and focus control for a double patterning immersion scanner. In *Proceedings of SPIE, Optical Microlithography XXIV*, volume 7973, February 2011.
- [134] Y.C. Yiu and A.R. Meyer. Computation of optical errors in transparent optical elements due to three dimensional photo-elastic effect. In *Proceedings of SPIE, Advances in Optical Structures*, volume 1303, April 1990.
- [135] G. Zhang, S. DeMoor, S. Jessen, Q. He, W. Yan, S. Chevacharoenkul, V. Vellanki, P. Reynolds, J. Ganeshan, J. Hauschild, and M. Pieters. Across wafer focus mapping and its application to advanced technology nodes. In *Proceedings of SPIE, Optical Microlithography XIX*, volume 6154, February 2006.
- [136] Q. Zhang, K. Poolla, and C.J. Spanos. Modelling of Mask Thermal Distortion and Its Dependency on Pattern Density. In *Proceedings of SPIE, Photomask and Next-Generation Lithography Mask Technology XII*, volume 5853, April 2005.

Appendix A

Lithographic lens correction model

This appendix provides an introduction to the simplified model of the lithographic lens. The model is used to determine lens manipulator settings that correct overlay, focus and imaging errors in the lithography tool. The appendix starts with an introduction to optical aberrations. The calculation procedure that is used to determine lens corrections is thereafter explained.

A.1 Optical aberrations

An imaging system is perfect when emitted waves from a point source in the object plane interfere in a single point at the image plane [47]. This is schematically shown in the left diagram of Figure A.1. The geometrical image formation in any imaging system can deviate from the ideal case however. In that case, not all waves from the point source at the object plane will interfere in the single point at the image plane. This is schematically shown in the right diagram of Figure A.1. The distortions in the image are known as *optical aberrations*. They are caused by lens design, lens construction and its use [71]. Optical aberrations are normally expressed in terms of the wavefront error [46]. A wavefront corresponds to a surface that is spanned by the ensemble of points that have the same *Optical Path Length (OPL)* from their mutual point source [47]. These wavefronts are a perfect sphere in an ideal imaging system but deviate from this in an aberrated imaging system as is schematically shown in Figure A.1. The wavefront error $\Delta W(\rho, \phi)$ is commonly expressed as the difference between the distorted and ideal spherical wavefront as a function of the position in the circular pupil plane (ρ, ϕ) of the lens. Pupil wavefront errors are normally quantified in an RMS value. It is obtained with the

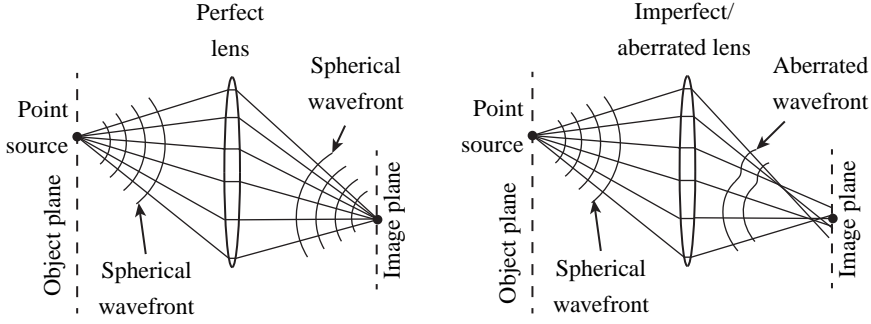


Figure A.1: Wavefronts in a perfect lens (left) and imperfect or aberrated lens (right).

following expression [58]:

$$\sigma_{\Delta W} = \sqrt{\frac{1}{\pi} \int_0^{2\pi} \int_0^1 (\Delta W(\rho, \phi) - \overline{\Delta W})^2 \rho d\rho d\phi} \quad (\text{A.1})$$

with $\sigma_{\Delta W}$ is the RMS wavefront error and (ρ, ϕ) the polar coordinates in the pupil plane. The term $\overline{\Delta W}$ is equal to the average wavefront error that is calculated with:

$$\overline{\Delta W} = \frac{1}{\pi} \int_0^{2\pi} \int_0^1 \Delta W(\rho, \phi) \rho d\rho d\phi. \quad (\text{A.2})$$

The above explanation focussed on the optical aberrations of a single point source from object to image plane. In imaging systems it is common that there are multiple point sources in the object and image plane. Each point source will have its own wavefront error in that case because the rays will pass through different parts of the imaging system.

A.2 Describing optical aberrations in Zernikes

It is common for imaging applications to express the pupil plane wavefront error in terms of a power series expansion. Zernike polynomials are used for this purpose because of their orthogonality and their correspondence to specific optical errors in imaging systems [71]. The power series expansion is mathematically described by:

$$\Delta W(\rho, \phi) = \sum_{i=1}^{\infty} A_i Z_i(\rho, \phi) \approx \sum_{i=1}^{37} A_i Z_i(\rho, \phi) \quad (\text{A.3})$$

where Z_i is the i^{th} Zernike polynomial and A_i is its amplitude. The first thirty-seven Zernike polynomials are normally used because they can describe the aberration be-

Number	Zernike polynomial	Common name
Z_1	1	Piston
Z_2	$\rho \cos(\phi)$	x-Tilt
Z_3	$\rho \sin(\phi)$	y-Tilt
Z_4	$2\rho^2 - 1$	Paraxial focus
Z_5	$\rho^2 \cos(2\phi)$	3 rd Order astigmatism
Z_6	$\rho^2 \sin(2\phi)$	3 rd Order 45° astigmatism
Z_7	$(3\rho^2 - 2) \rho \cos(\phi)$	3 rd Order x-coma
Z_8	$(3\rho^2 - 2) \rho \sin(\phi)$	3 rd Order y-coma
Z_9	$6\rho^4 - 6\rho^2 + 1$	3 rd Order spherical
Z_{10}	$\rho^3 \cos(3\phi)$	Trefoil
Z_{11}	$\rho^3 \sin(3\phi)$	45° Trefoil
Z_{12}	$(4\rho^2 - 3) \rho^2 \cos(2\phi)$	5 th Order astigmatism
Z_{13}	$(4\rho^2 - 3) \rho^2 \sin(2\phi)$	5 th Order 45° astigmatism
Z_{14}	$(10\rho^4 - 12\rho^2 + 3) \rho \cos(\phi)$	5 th Order x-coma
Z_{15}	$(10\rho^4 - 12\rho^2 + 3) \rho \sin(\phi)$	5 th Order y-coma
Z_{16}	$20\rho^6 - 30\rho^4 + 12\rho^2 - 1$	5 th Order spherical
Z_{17}	$\rho^4 \cos(4\phi)$	Quadrafoil
Z_{18}	$\rho^4 \sin(4\phi)$	45° Quadrafoil
Z_{19}	$(5\rho^2 - 4) \rho^3 \cos(3\phi)$	5 th Trefoil
Z_{20}	$(5\rho^2 - 4) \rho^3 \sin(3\phi)$	5 th Order 45° Trefoil
Z_{21}	$(15\rho^4 - 20\rho^2 + 6) \rho^2 \cos(2\phi)$	7 th Order astigmatism
Z_{22}	$(15\rho^4 - 20\rho^2 + 6) \rho^2 \sin(2\phi)$	7 th Order 45° astigmatism
Z_{23}	$(35\rho^6 - 60\rho^4 + 30\rho^2 - 4) \rho \cos(\phi)$	7 th Order x-coma
Z_{24}	$(35\rho^6 - 60\rho^4 + 30\rho^2 - 4) \rho \sin(\phi)$	7 th Order y-coma
Z_{25}	$70\rho^8 - 140\rho^6 + 90\rho^4 - 20\rho^2 + 1$	7 th Order spherical
Z_{26}	$\rho^5 \cos(5\phi)$	Pentafoil
Z_{27}	$\rho^5 \sin(5\phi)$	45° Pentafoil
Z_{28}	$(6\rho^2 - 5) \rho^4 \cos(4\phi)$	5 th Order Quadrafoil
Z_{29}	$(6\rho^2 - 5) \rho^4 \sin(4\phi)$	5 th Order 45° Quadrafoil
Z_{30}	$(21\rho^4 - 30\rho^2 + 10) \rho^3 \cos(3\phi)$	7 th Order Trefoil
Z_{31}	$(21\rho^4 - 30\rho^2 + 10) \rho^3 \sin(3\phi)$	7 th Order 45° Trefoil
Z_{32}	$(56\rho^6 - 105\rho^4 + 60\rho^2 - 10) \rho^2 \cos(2\phi)$	9 th Order Astigmatism
Z_{33}	$(56\rho^6 - 105\rho^4 + 60\rho^2 - 10) \rho^2 \sin(2\phi)$	9 th Order 45° Astigmatism
Z_{34}	$(126\rho^8 - 280\rho^6 + 210\rho^4 - 60\rho^2 + 5) \rho \cos(\phi)$	9 th Order x-coma
Z_{35}	$(126\rho^8 - 280\rho^6 + 210\rho^4 - 60\rho^2 + 5) \rho \sin(\phi)$	9 th Order y-coma
Z_{36}	$252\rho^{10} - 630\rho^8 + 560\rho^6 - 210\rho^4 + 30\rho^2 - 1$	9 th Order Spherical
Z_{37}	$924\rho^{12} - 2772\rho^{10} + 3150\rho^8 - 1680\rho^6 + \dots$ $420\rho^4 - 42\rho^2 + 1$	11 th Order Spherical

Table A.1: An overview of the Zernike polynomials as provided in [71].

haviour at a single field point with sufficient accuracy [71]. Table A.1 provides the mathematical expressions of the first 37 Zernike polynomials. The shapes of the first 64 Zernike polynomials are provided in Figure A.2. The table also provides the common names (spherical, coma, astigmatism, etc.) for each Zernike which relate to the azimuthal symmetry of the polynomials. Each group has a specific effect on the image at wafer level in lithography systems. RMS wavefront error specifications are therefore normally defined for each symmetry group [44, 46].

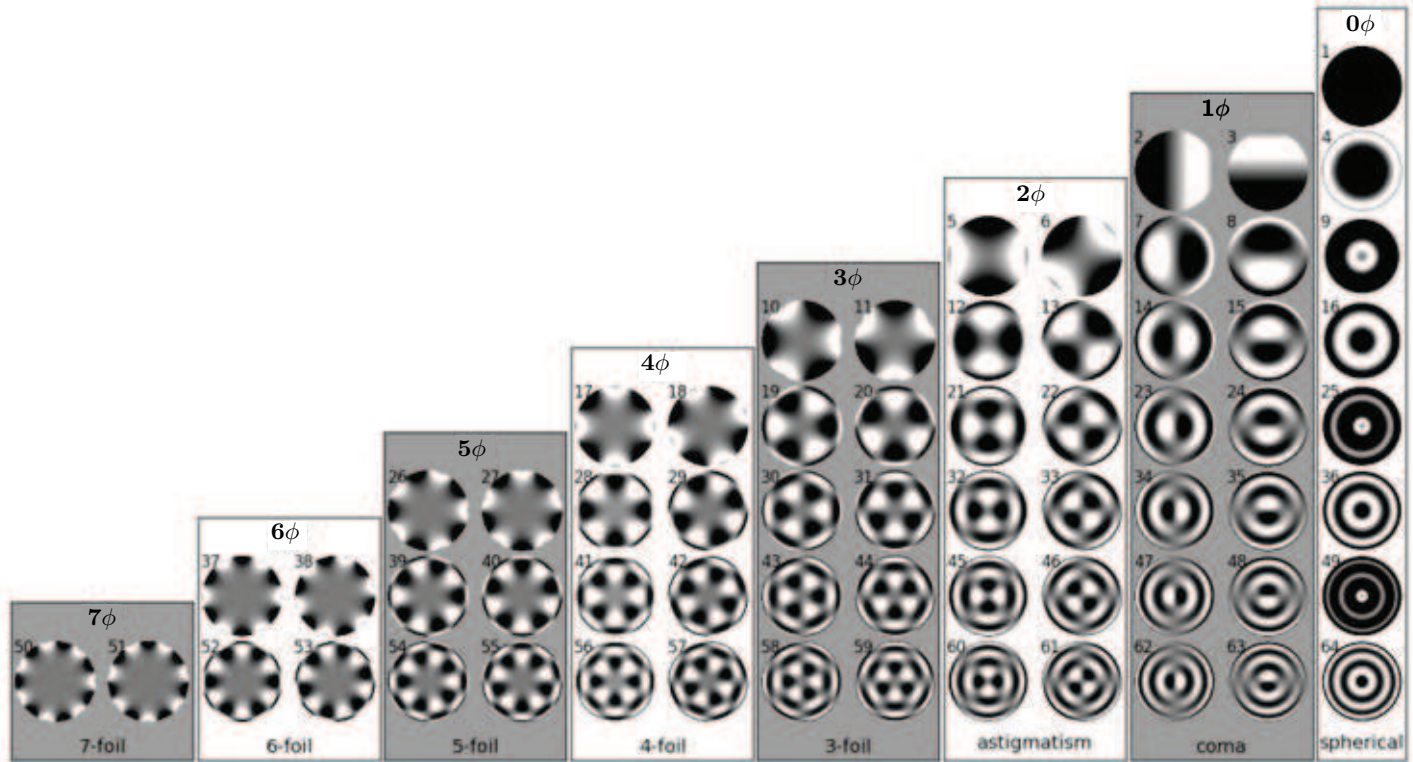


Figure A.2: An overview of the Zernike polynomial shapes. The categorization of the Zernikes are according to the Wyant Zernike expansion [58].

The effects of the second (Z_2) and third (Z_3) Zernike polynomial relate to image shifts for lithography applications. These shifts are equal to [71]:

$$u = -\frac{A_2}{\text{NA}}, \quad v = -\frac{A_3}{\text{NA}}. \quad (\text{A.4})$$

where u and v are the displacements of the image in x- and y-direction, A_2 and A_3 are the amplitudes of the second and third Zernike polynomial in the wavefront error of a specific field point whilst the NA relates to the Numerical Aperture of the lens.

A.3 Lens correction calculation procedure

The lithography system is able to counteract image errors at wafer level by stage and lens manipulator adaptations during the exposure process [71, 78, 133]. The required stage and lens manipulator settings for the correction can be determined a priori when the image errors are known beforehand. This section explains the calculation procedure that can be used to determine the lens manipulator settings when the wavefront sensitivities with respect to lens and stage adaptations are known. The results of the procedure also provide an estimate of the residual image errors after correction.

The calculation procedure is explained for the correction of in-plane image distortions. Such image errors are introduced by the reticle curvature manipulator as was explained in Section 3.4. The steps of the calculation procedure are explained in Sections A.3.1 to A.3.4.

A.3.1 Translation of pattern distortions to optical aberrations

The first step in the calculation procedure consists of translating the in-plane image distortions u and v at wafer level into Zernike aberration amplitudes A_2 and A_3 . This step is needed because the effect of a lens or stage manipulator change is described in terms of wavefront change. The equations of (A.4) can be used for this step. Note that the translation of the in-plane image distortions at wafer level has to be done for every field point (x, y) that falls within the exposure area of the lithographic lens.

A.3.2 Calculation of lens manipulator setpoints

The second step in the procedure consist of calculating the stage and lens adaptations \mathbf{m} that minimize the pattern distortions across the exposure area. They are obtained by solving the following equation:

$$\mathbf{A}(x, y) = \mathbf{S}(x, y) \mathbf{m} \quad (\text{A.5})$$

for \mathbf{m} using a least-squares procedure. In Equation (A.5), the vector \mathbf{A} is a vector which contains the derived image aberrations in the exposure area at wafer level that were obtained by the step in Section A.3.1. The matrix $\mathbf{S}(\mathbf{x}, \mathbf{y})$ contains the wavefront aberration sensitivities with respect to a stage or lens manipulator change for each (\mathbf{x}, \mathbf{y}) location in the exposure area. The vector \mathbf{m} represents the desired information, namely the stage and lens manipulator adaptations. The matrix and vectors in Equation (A.5) are organized in the following manner:

$$\begin{bmatrix} A_1(\mathbf{x}, \mathbf{y}) \\ \vdots \\ A_{37}(\mathbf{x}, \mathbf{y}) \end{bmatrix} = \begin{bmatrix} S_1(\mathbf{x}, \mathbf{y}, m_1) & \dots & S_1(\mathbf{x}, \mathbf{y}, m_N) \\ \vdots & \ddots & \vdots \\ S_{37}(\mathbf{x}, \mathbf{y}, m_1) & \dots & S_{37}(\mathbf{x}, \mathbf{y}, m_N) \end{bmatrix} \begin{bmatrix} m_1 \\ \vdots \\ m_N \end{bmatrix} \quad (\text{A.6})$$

where $S_i(\mathbf{x}, \mathbf{y}, m_n)$ is the lens sensitivity corresponding to the i^{th} Zernike polynomial and m_n is the n^{th} degree-of-freedom of the lithography tool (i.e. stage or lens manipulator). The vector containing the image aberrations A_i only has non-zero values for A_2 and A_3 because these relate to the values for the in-plane pattern distortions. All other aberration amplitudes are equal to zero.

The derived manipulator values \mathbf{m} need to be applied in order to correct the image distortions in the exposure area. It is necessary to check if these manipulator values fall within the available actuator range.

A.3.3 Calculation of residual pattern distortions

The third step in the analysis procedure is to calculate the residual aberrations after correction. These are obtained with the following equation:

$$\mathbf{R}(\mathbf{x}, \mathbf{y}) = \mathbf{A}(\mathbf{x}, \mathbf{y}) - \mathbf{S}(\mathbf{x}, \mathbf{y}) \mathbf{m} \quad (\text{A.7})$$

where $\mathbf{R}(\mathbf{x}, \mathbf{y})$ are the residual optical aberrations of all field positions after lens correction. These residual optical aberrations need to be translated back into image effects like pattern shift. This can be done with Equation (A.4) where the residual aberrations R_2 and R_3 replace the variables A_2 and A_3 .

A.3.4 Average distortions and fading penalty

The calculated distortion values in Section A.3.3 relate to the residual in-plane distortions in the exposure area at a specific moment in time. The exposure area scans across the wafer however. Each location on the wafer might therefore experience a varying image distortion during the time that it is exposed.

The final step of the calculation procedure therefore consists of calculating the Moving Average (MA) and Moving Standard Deviation (MSD) of pattern distortions for each location in the field. The MA value relates to the overlay penalty whilst the MSD value

represents the fading penalty. They can be calculated with the following equations:

$$\bar{u}(x, y) = \frac{1}{T} \int_{-T/2}^{T/2} u(x, y, t) dt \quad (\text{A.8})$$

$$\sigma_u(x, y) = \sqrt{\frac{1}{T} \int_{-T/2}^{T/2} [u(x, y, t) - \bar{u}(x, y)]^2 dt} \quad (\text{A.9})$$

where $\bar{u}(x, y)$ and $\sigma_u(x, y)$ are the MA and MSD pattern distortion values in x -direction whilst T is the time that a point on the wafer falls within the exposure area. Note that the expressions for the distortions in y -direction can be obtained by changing u to v in Equations (A.8) and (A.9).

A.4 Overview of correctable pattern distortions

Section (A.3) explained the calculation procedure that was used throughout this thesis to determine pattern distortions and the fading penalty after corrections. It did not give an idea about the correctable pattern distortions in a field however.

This section will provide an overview of the achievable pattern distortion corrections using an simplified correction model [15, 50, 78]. The correction model consists of the following third order polynomial regression model [28, 48]:

$$dx(x, y) = k_1 + k_3x + k_5y + k_7x^2 + k_9xy + k_{11}y^2 + k_{13}x^3 + \dots + k_{15}x^2y + k_{17}xy^2 + k_{19}y^3 \quad (\text{A.10})$$

$$dy(x, y) = k_2 + k_4y + k_6x + k_8y^2 + k_{10}yx + k_{12}x^2 + k_{14}y^3 + \dots + k_{16}y^2x + k_{18}yx^2 + k_{20}x^3 \quad (\text{A.11})$$

where $dx(x, y)$ and $dy(x, y)$ relate to the pattern distortions in respectively x - and y -direction whilst x and y relate to the *Qgrid* locations in one exposure field. This *Qgrid* corresponds to a grid of thirteen-by-nineteen overlay markers that are present on a standard qualification reticle [28]. The parameters k_i with $i = 1, \dots, 20$ are the amplitudes of specific grid distortion shapes. An overview of these shapes is shown in Figures A.3 to A.5 as a blue mesh. The dots in those figures relate to the original *Qgrid* locations in the field.

The shapes that are shown in Figures A.3 to A.5 are not all correctable by the stages or lens in the lithography system. The k_9 , k_{15} , k_{17} , k_{18} and k_{20} were recently uncorrectable in lithography tools [48]. Recent lens developments have made it possible to adapt the lens magnification during the exposure scan. This facilitates the correction of k_9 and k_{17} distortion shapes [15, 78, 133].

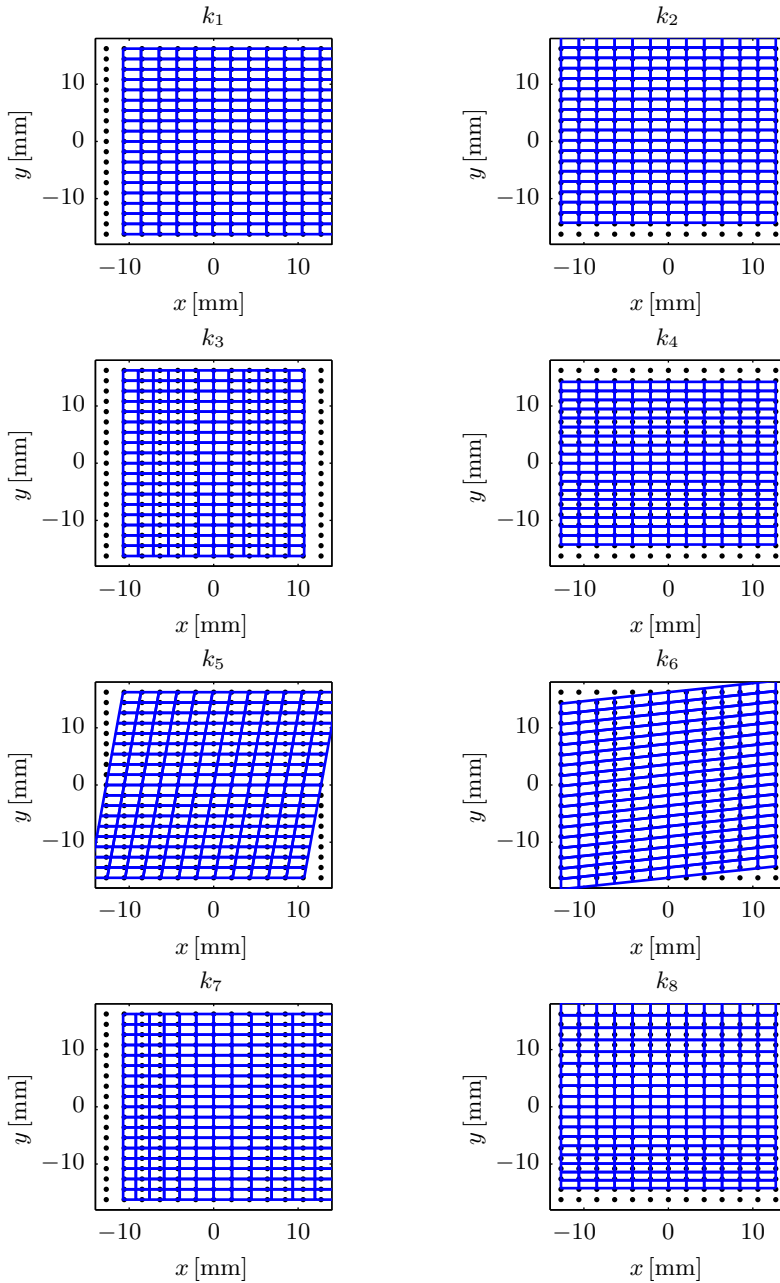


Figure A.3: The k_1 to k_8 pattern distortion shapes of the third order polynomial regression model of Equation (A.10) and (A.11).

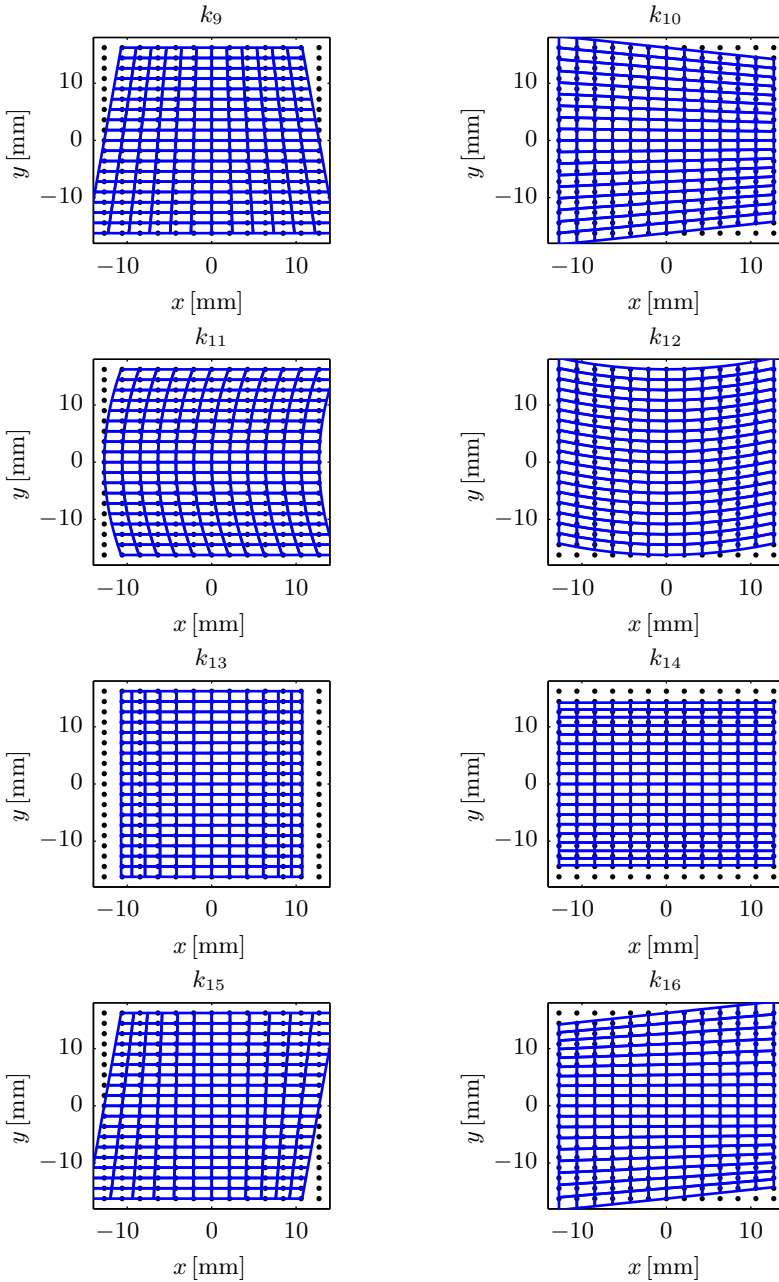


Figure A.4: The k_9 to k_{16} pattern distortion shapes of the third order polynomial regression model of Equation (A.10) and (A.11).

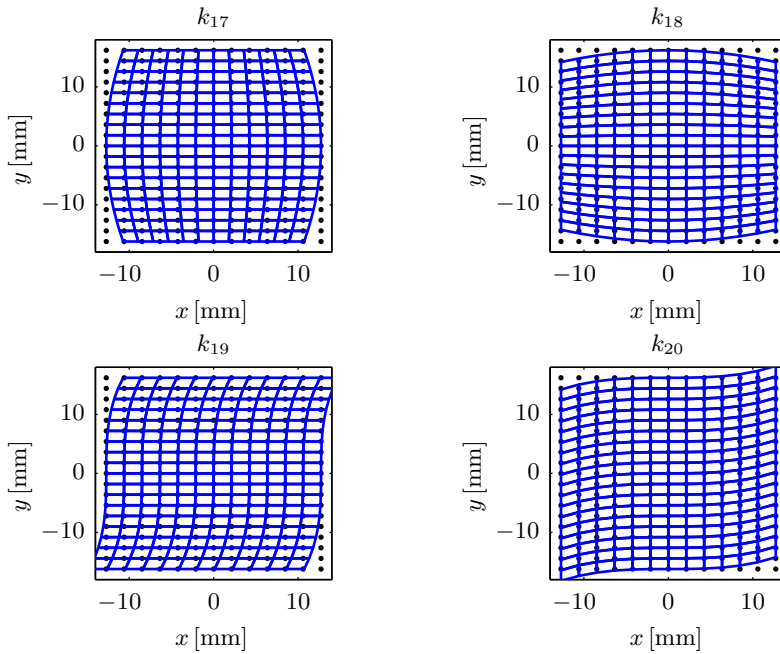


Figure A.5: The k_{16} to k_{20} pattern distortion shapes of the third order polynomial regression model of Equation (A.10) and (A.11).

Appendix B

Modelling the photomask as a Kirchhoff plate

This appendix introduces the Kirchhoff plate model. This analytical model is used to describe the behaviour of the photomask when it undergoes bending. It is first explained why the reticle can be modelled as a Kirchhoff plate. The plate model relations are thereafter introduced and reformulated for the photomask that is kinematically supported on three out-of-plane supports.

B.1 The Kirchhoff plate model assumptions

The Kirchhoff-Love plate model is used in this thesis to describe the photomask behaviour when it undergoes pure bending. This model is used because of its simplicity. Its assumptions are analogue to the Euler-Bernoulli beam theory with the difference that plates can bend in two directions as well as twist. This results in a two- instead of a three-dimensional model of the plate.

The Kirchhoff-Love plate model is based on a number of assumptions [42, 126]. They are explained with the help of Figure B.1 which provides a schematic representation of the plate deformation kinematics. The assumptions are the following:

- The material of the plate is elastic, homogeneous and isotropic.
- The plate is initially flat.
- The deflection of the plate's mid-plane w is small compared to the thickness h of the plate. The slope of the deflected surface is subsequently very small and the square of the slopes are therefore a negligible quantity with respect to unity.

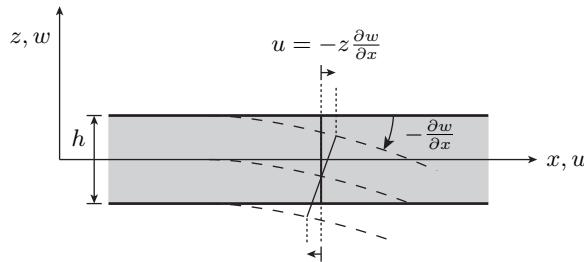


Figure B.1: The thin plate deformation kinematics where u and w represent the plate displacement in respectively the x - and z -direction.

- The straight lines that are initially normal to the middle plane of the plate before bending remain straight and normal to the middle surface during the deformation (see Figure B.1). Furthermore, their lengths are not altered. This means that the vertical shear strain γ_{xz} and γ_{yz} are negligible and the normal strain ε_z may also be omitted. This assumption is referred to as the *hypothesis of straight normals*.
- The stress normal to the middle plane, σ_z is small in comparison to the other stress components and may therefore be neglected in the stress-strain relations.
- Since the displacements of a plate are small, it is assumed that the middle surface remains unstrained after bending.

The Kirchhoff plate model is a valid description of the photomask for the following reasons. First, the photomask falls into the category of stiff thin plates because its length l over thickness h ratio is 24 whilst the ratio of the deflection w over thickness is below $1/1000$ [126]. Second, the reticle's bulk material¹ is Fused Silica which is an elastic, homogeneous and isotropic material. Furthermore, the reticle can be considered flat because they have a flatness specification of 0.5 [\mu m] over the pattern area. Its deformation due to gravity and machine constraints are in the same order of magnitude. This proves that the Kirchhoff plate model can be used to describe the photomask behaviour when it undergoes pure bending.

B.2 Strain-curvature relations

The Kirchhoff assumptions introduced in section B.1 are used to introduce the Kirchhoff plate bending equations. The equations are acquired by reviewing the elasticity equations that hold for a three-dimensional isotropic body in a Cartesian coordinate system (x, y, z) together with the Kirchhoff assumptions. The third assumption makes it possible to write

¹Note that the Chrome layer at the bottom of the photomask is not taken into consideration because of its negligible thickness with respect to that of the Fused Silica material.

the displacement field of the plate in the following manner:

$$\begin{aligned} u(x, y, z) &= u_0(x, y) - z \frac{\partial w(x, y)}{\partial x} \\ v(x, y, z) &= v_0(x, y) - z \frac{\partial w(x, y)}{\partial y} \\ w(x, y, z) &= w(x, y) \end{aligned} \quad (\text{B.1})$$

where z is the distance with respect to the plate's middle plane, $u(x, y, z)$ and $v(x, y, z)$ are the displacements in x - and y -direction whilst $w(x, y, z)$ is the deflection of the plate's middle surface in z -direction. The terms $u_0(x, y)$ and $v_0(x, y)$ are respectively the initial extension in x - and y -direction that result from a pre-stress in the middle plane. These terms are neglected in the remainder of this thesis because of the absence of an applied pre-stress in the reticle and the negligible stretching of the middle plane by bending. Coordinate dependencies are left out in the remainder of the text for simplicity. The relations of the photomask normal strains for the case of very small displacements and rotations are defined by [126]:

$$\varepsilon_x = \frac{\partial u}{\partial x}, \quad \varepsilon_y = \frac{\partial v}{\partial y}, \quad \varepsilon_z = \frac{\partial w}{\partial z} \quad (\text{B.2})$$

whilst the shear strains are equal to:

$$\gamma_{xy} = \frac{\partial v}{\partial x} + \frac{\partial u}{\partial y}, \quad \gamma_{xz} = \frac{\partial u}{\partial z} + \frac{\partial w}{\partial x}, \quad \gamma_{yz} = \frac{\partial v}{\partial z} + \frac{\partial w}{\partial y}. \quad (\text{B.3})$$

The fourth Kirchhoff assumption, i.e.:

$$\gamma_{xz} = \gamma_{yz} = \varepsilon_z = 0, \quad (\text{B.4})$$

makes it possible to reduce the number of strain relations into:

$$\varepsilon_x = \frac{\partial u}{\partial x}, \quad \varepsilon_y = \frac{\partial v}{\partial y}, \quad \gamma_{xy} = \frac{\partial v}{\partial x} + \frac{\partial u}{\partial y}. \quad (\text{B.5})$$

Equation (B.5) demonstrates that the Kirchhoff model reduces the three-dimensional plate problem into a two dimensional one. The final strain relations are obtained by substituting the displacements of (B.1) into Equation (B.5). This gives:

$$\varepsilon_x = -z \frac{\partial^2 w}{\partial x^2}, \quad \varepsilon_y = -z \frac{\partial^2 w}{\partial y^2}, \quad \gamma_{xy} = -2z \frac{\partial^2 w}{\partial x \partial y}. \quad (\text{B.6})$$

The relations for the photomask strain are dependent on the second derivative of the out-of-plane deflection. These derivatives have a geometrical meaning. The former two are related to the *bending curvature* along the x - and y -axis whilst the latter is equal to the *twisting curvature* with respect to the x - and y -axis. The mathematical expressions for the curvatures are:

$$\kappa_x = \frac{1}{\rho_x} = -\frac{\partial^2 w}{\partial x^2}, \quad \kappa_y = \frac{1}{\rho_y} = -\frac{\partial^2 w}{\partial y^2}, \quad \kappa_{xy} = \kappa_{yx} = \frac{1}{\rho_{xy}} = -\frac{\partial^2 w}{\partial x^2} \quad (\text{B.7})$$

where κ_x and κ_y are the bending curvatures, κ_{xy} is the twisting curvature and ρ_x , ρ_y and ρ_z are the radii of curvatures along the different directions. The strain-curvature relations of Equation (B.6) demonstrate that strains occur outside the photomask's middle plane. This is especially the case for the photomask pattern because it is located at the bottom surface of the reticle.

B.3 Stress-curvature relations

This section provides expressions of the photomask stresses as a function of curvature. The derivation uses the Hooke's law for linear isotropic materials which describes the relation between the photomask stresses and strains. These relations can be simplified using the fourth Kirchhoff assumption of Section B.1. It leads to the following expressions [126]:

$$\sigma_x = \frac{E}{1-\nu^2} (\varepsilon_x + \nu\varepsilon_y), \quad \sigma_y = \frac{E}{1-\nu^2} (\varepsilon_y + \nu\varepsilon_x), \quad \tau_{xy} = \frac{E}{2(1+\nu)} \gamma_{xy} \quad (\text{B.8})$$

where E is the elasticity modulus and ν is the poisson ratio of the material. Note that these stress expressions correspond to plane stress conditions. Expressions of the plate stresses as a function of curvature are obtained by substituting Equation (B.6) and (B.7) into Equation (B.8), i.e.:

$$\sigma_x = \frac{Ez}{1-\nu^2} (\kappa_x + \nu\kappa_y) = -\frac{Ez}{1-\nu^2} \left(\frac{\partial^2 w}{\partial x^2} + \nu \frac{\partial^2 w}{\partial y^2} \right) \quad (\text{B.9})$$

$$\sigma_y = \frac{Ez}{1-\nu^2} (\kappa_y + \nu\kappa_x) = -\frac{Ez}{1-\nu^2} \left(\frac{\partial^2 w}{\partial y^2} + \nu \frac{\partial^2 w}{\partial x^2} \right) \quad (\text{B.10})$$

$$\tau_{xy} = \frac{Ez}{1+\nu} \kappa_{yx} = -\frac{Ez}{1+\nu} \frac{\partial^2 w}{\partial x \partial y}. \quad (\text{B.11})$$

The equations show that the stresses vary linearly across the thickness of the reticle which was also the case for the photomask strains.

B.4 Internal bending moment relations

Expressions for the internal bending moments in the photomask are obtained by integrating the stresses over its thickness and length. The following results are obtained when Equations B.9 to (B.11) are used:

$$M_x = \int_0^L \int_{-h/2}^{h/2} z \sigma_x dz dy = D (\kappa_x + \nu \kappa_y) \quad (\text{B.12})$$

$$M_y = \int_0^L \int_{-h/2}^{h/2} z \sigma_y dz dx = D (\kappa_y + \nu \kappa_x) \quad (\text{B.13})$$

$$M_{xy} = \int_0^L \int_{-h/2}^{h/2} z \tau_{xy} dz dy = D (1 - \nu) \kappa_{xy} \quad (\text{B.14})$$

where D is the flexural rigidity of the plate. It is equal to:

$$D = \frac{ELh^3}{12(1 - \nu^2)} \quad (\text{B.15})$$

Equations (B.12) to (B.14) indicate that the plate curvature is directly related to the amount of internal bending moment in the photomask.

B.5 Governing equation of photomask deflection

The vertical displacement field of the photomask when it undergoes bending is governed by a partial differential equation. This differential equation can be derived by considering an element of the plate as is shown in Figure B.2. Three equilibrium equations must hold for that plate under static conditions [126]:

- Force equilibrium in the z -direction:

$$\frac{\partial Q_x}{\partial x} dx dy + \frac{\partial Q_y}{\partial y} dx dy + p dx dy = 0 \quad (\text{B.16})$$

- Moment equilibrium around the x -axis:

$$\frac{\partial M_{xy}}{\partial x} dx dy + \frac{\partial M_y}{\partial y} dx dy + Q_y dx dy = 0 \quad (\text{B.17})$$

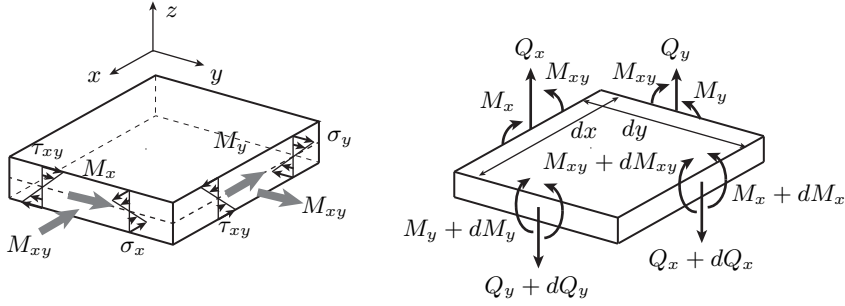


Figure B.2: The effects on a piece of plate that undergoes bending. The left diagram shows the internal bending moments and corresponding stresses. The right diagram shows its force and bending moment equilibrium [42].

- Moment equilibrium around the y -axis:

$$\frac{\partial M_{yx}}{\partial y} dx dy + \frac{\partial M_x}{\partial x} dx dy + Q_x dx dy = 0 \quad (\text{B.18})$$

where $M_{xy} = M_{yx}$ and Q_x and Q_y are respectively the vertical shear forces that act on the x - or y -face of the element. The shear forces can be expressed in terms of the bending moments by combining Equations (B.17) and (B.18):

$$Q_x = \frac{\partial M_x}{\partial x} + \frac{\partial M_{xy}}{\partial y}, \quad Q_y = \frac{\partial M_{xy}}{\partial x} + \frac{\partial M_y}{\partial y} \quad (\text{B.19})$$

The governing differential equation for the photomask deflection is obtained by substituting the shear force expressions into the vertical force equilibrium (B.16):

$$\frac{\partial^2 M_x}{\partial x^2} + 2 \frac{\partial^2 M_{xy}}{\partial x \partial y} + \frac{\partial^2 M_y}{\partial y^2} - p = 0 \quad (\text{B.20})$$

or

$$D \left(\frac{\partial^4 w}{\partial x^4} + 2 \frac{\partial^4 w}{\partial x^2 \partial y^2} + \frac{\partial^4 w}{\partial y^4} \right) - p = 0 \quad (\text{B.21})$$

when Equations (B.12) to (B.14) are used.

B.6 Photomask undergoing pure bending

Expressions for the photomask behaviour under bending can be obtained by solving the governing equation of Equation (B.21) for the specific photomask boundary conditions.

All reticle edges can be considered as free boundaries because of the kinematic mounting of the reticle in the chuck. Furthermore, it is assumed that only external bending moments are applied at the photomask edges. This configuration is known as *pure bending* which will result in a curvature of the reticle as will become clear below. This thesis will only consider the application of a uniform bending moment along the x -edge of the photomask because of the reasons explained in Section 3.2. Finally, no vertical distributed loads p are considered in the derivation. It is assumed that the gravitational deformation can be superpositioned on the bending moment induced deformations because of the linear nature of the model.

The derivation starts by assuming a solution form to the governing equation in (B.21). The following expression is proposed:

$$w = \frac{1}{2} (C_1 x^2 + C_2 y^2) + C_3 x + C_4 y + C_5. \quad (\text{B.22})$$

where the terms C_1 and C_2 correspond to the integration constants for the photomask curvatures whilst C_3 , C_4 and C_5 are the integration constants that correspond to the rigid body translations and rotations of the photomask. The former two constants are derived with the following boundary conditions:

$$M_x = M, \quad M_y = 0. \quad (\text{B.23})$$

Expressions for C_1 and C_2 are obtained by substituting Equation (B.22) into the internal bending moment Equations (B.12) to (B.13), i.e.:

$$C_1 = \kappa_x = -\frac{M}{D(1-\nu^2)}, \quad C_2 = \kappa_y = \frac{M\nu}{D(1-\nu^2)}. \quad (\text{B.24})$$

The expressions in (B.27) show that C_1 and C_2 are equal to the photomask curvatures κ_x and κ_y . Furthermore, they also show that the curvatures across and along the photomask are related to each other by:

$$\kappa_x = -\nu\kappa_y. \quad (\text{B.25})$$

Equation (B.25) demonstrates that the photomask will acquire a smaller opposite curvature in the y -direction for the case of $\nu < 1$. It will result in an *anticlastic curvature* or saddle shape deformation of the reticle.

The last three integration constants are found by considering the kinematic mounting assumption of the reticle on its three z -supports. In that case, the photomask deflection at those locations is equal to zero, i.e.:

$$w(x_{z1}, y_{z1}) = w(x_{z2}, y_{z2}) = w(x_{z3}, y_{z3}) = 0 \quad (\text{B.26})$$

with x_{zi} and y_{zi} the location of the i^{th} z-support for $i = 1, 2, 3$. The following values of the integration constants were acquired using the symbolic toolbox in MATLAB, the reticle's Poisson ratio and the locations of the z-supports:

$$C_3 \approx 0.0012\kappa_x, \quad C_4 = 0, \quad C_5 \approx -0.0023\kappa_x. \quad (\text{B.27})$$

Note that it is evident that the fourth integration constant is equal to zero because of model symmetry across the x-axis.

Substitution of all integration constants into Equation (B.22) gives the final relation for the photomask deflection:

$$w = \frac{1}{2}\kappa_x (x^2 - \nu y^2) + 0.0012\kappa_x x - 0.0023\kappa_x. \quad (\text{B.28})$$

The curvature κ_x of the photomask is described by:

$$\kappa_x = -\frac{M}{D(1-\nu^2)}. \quad (\text{B.29})$$

where M is the applied bending moment and D the photomask bending stiffness.

The relation for the photomask local angle around the x - and y -axis can be obtained by taking the partial derivative of Equation (B.28) with respect to y and x :

$$\theta_x = \frac{\partial w}{\partial y} = -\nu y \kappa_x \quad (\text{B.30})$$

$$\theta_y = \frac{\partial w}{\partial x} = (x + 0.0012) \kappa_x. \quad (\text{B.31})$$

The relations for the photomask pattern deformation in x - and y -direction are obtained by substituting Equations (B.30) and (B.31) into (B.1):

$$u = -\frac{1}{2}t \frac{\partial w}{\partial x} = -\frac{1}{2}t (x + 0.0012) \kappa_x \quad (\text{B.32})$$

$$v = -\frac{1}{2}t \frac{\partial w}{\partial y} = -\frac{1}{2}t \nu y \kappa_x \quad (\text{B.33})$$

where t is half the reticle thickness.

Appendix C

Number of discrete moments for photomask bending

This appendix explains the analysis to determine the required number of discrete bending moments to approach the case of uniform photomask bending. The analysis objective and the applied model are first introduced. The simulation results are thereafter explained.

C.1 Introduction

The first topic that was considered for the detailed design was the number of discrete bending moments that are needed in order to generate a sufficiently uniform internal bending moment in the photomask. The uniformness can be quantified by considering differences in photomask pattern distortions for a uniform bending moment and the case when the bending moment is generated by discrete actuators along the photomask edges. The model that was used for the analysis is explained in Section C.2. The analysis results are thereafter presented in Section C.3.

C.2 Model with discrete bending moments

The analysis was performed using the FE model of Section 3.3.2.2 in which several locations of force application were defined. They were located along the line of the distributed load that was used to generate the continuous bending moment, see Figure 3.4. Figure C.1 provides an example of the discrete actuation configuration when five pairs of local push/pull forces are used to generate the bending moment. Each pair generated

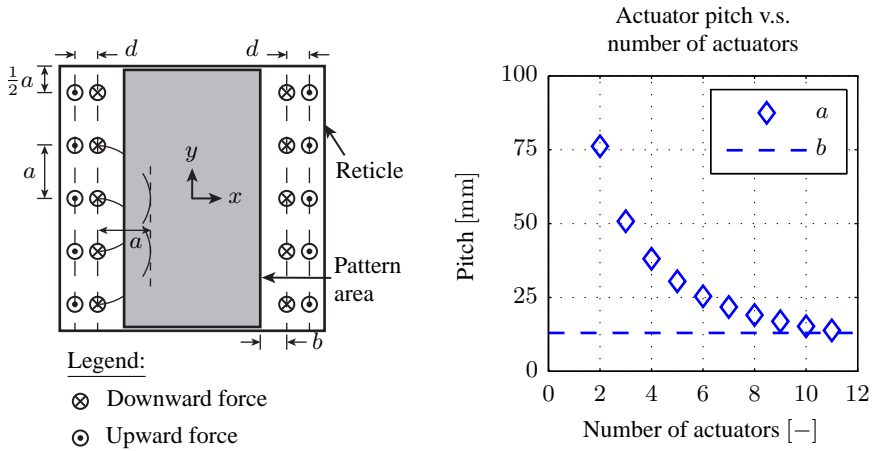


Figure C.1: Schematic representation of the model that was used to investigate the required number of discrete bending actuators. The left illustration provides a top view of the photomask where the bending moment is generated by locally applied push/pull forces. The right graph provides estimates of several distances that have been defined in the left illustration. It shows the relation of the actuator pitch a in y -direction as a function of the number of actuators as well as the distance s in x -direction between the inner local force and the edge of the pattern area.

the same bending moment and their sum corresponded to the total bending moment that is needed for a specific photomask curvature. The pitch in x -direction between two local opposing forces was kept at $d = 7$ [mm] which corresponds to the pitch used for the continuous bending moment (see Section 3.3.2.1). The forces were equally spaced in y -direction having a pitch a . Furthermore, they were placed such that the distance between the outer force and the photomask edge in y -direction corresponded to $1/2a$. This configuration was chosen such that each actuator would experience approximately the same volume of photomask material to bend.

cha:ConceptualAnalysis:PellicleEffect:PhotomaskNoPellicle). The forces were equally spaced in y -direction having a pitch a . Furthermore, they were placed such that the distance between the outer force and the photomask edge in y -direction corresponded to $1/2a$. This configuration was chosen such that each actuator would experience approximately the same volume of photomask material to bend.

The left graph of Figure C.1 shows the pitch a as a function of the number of actuators. A first-order-estimate of the minimum number of discrete bending moments can be obtained from the graph by comparing the pitch a with the distance b between the inner local force and the edge of the pattern area. Eleven discrete bending moments would be necessary in the ideal case if *Saint-Venant's principle* would be considered. The latter states that a non-uniform stress distribution which is caused by local concentrated loads becomes uniform at a sufficient distance from the point of application [43].

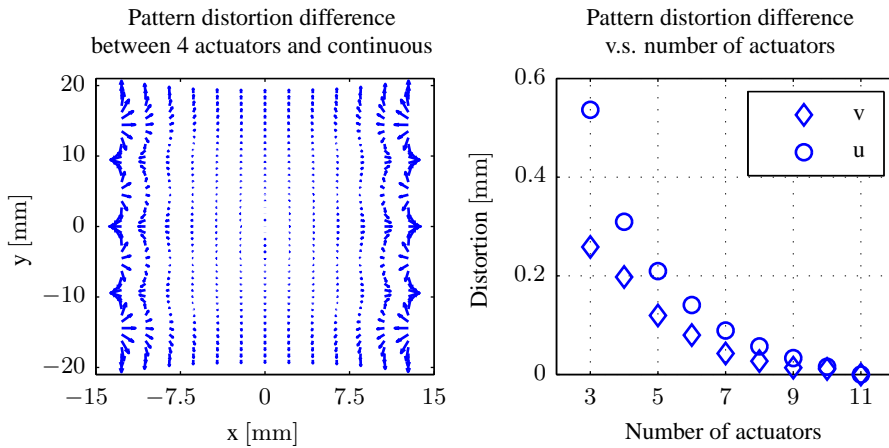


Figure C.2: Analysis results of the photomask pattern distortion difference between discrete and continuous bending moment application. The left figure shows a vector plot of the pattern distortion difference between the cases of a continuous bending moment application and the case where four discrete actuators are used. The right graph shows the pattern distortion difference between the discrete and continuous case in x - and y -direction versus the number of discrete bending actuators.

C.3 Analysis results for discrete actuation

FEM simulations were used to investigate the pattern distortion levels for the discrete bending moment application. Simulations were run for three to eleven bending actuators realizing a constant photomask curvature of $\kappa_x = 0.4 \times 10^{-3} [1/m]$ during scan. The extracted pattern distortions in x - and y -direction were compared to the pattern distortions for the continuous bending moment case. The vector plot on the left in Figure C.2 provides an example of the pattern distortion difference for the case of four discrete bending actuators. It clearly shows that local distortions are induced when discrete actuation is used. The figure also shows a graph of the maximum absolute value of the pattern distortion difference between discrete and continuous actuation as a function of the number of actuators. It confirms that the initial estimate of eleven discrete bending moments are needed to obtain the same pattern distortion levels as for the continuous bending moment case. It also shows that seven discrete bending moments will already ensure that the pattern distortions are below 0.1 [mm] and this is probably a sufficient number to achieve the desired performance.

An additional analysis was performed to identify the residual pattern distortions after the described lens correction in Section 3.4. The results are provided in Figure C.3. A vector plot of the residual pattern distortions when using four discrete bending moments is provided on the left. It shows that there are still edge effects visible that can be attributed to the four discrete actuators. The right graph provides results of the maximum absolute values of the x and y pattern distortions, respectively u_d and v_d , as a function of the number of actuators. The two dotted lines u_c and v_c indicate the maximum value of the absolute pattern distortions after lens correction for the continuous bending moment

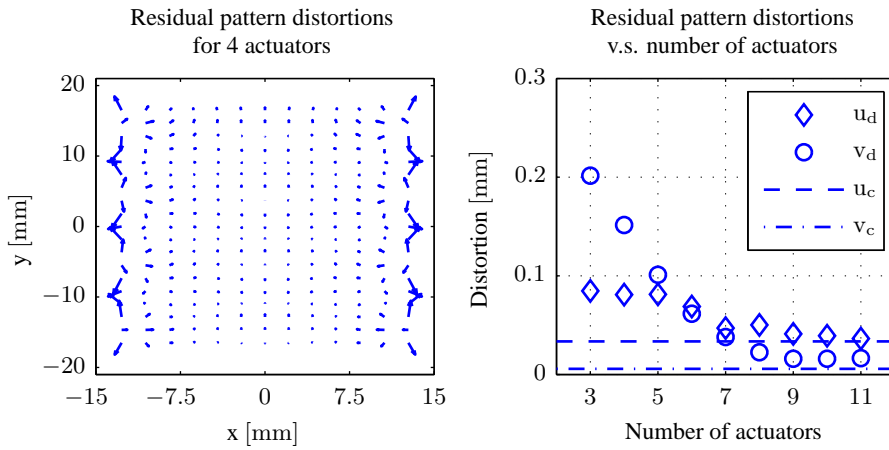


Figure C.3: Analysis results of the residual photomask pattern distortion for discrete bending moment application after lens correction. The left vector plot shows the residual pattern distortions when four discrete bending actuators are used whilst the right graph shows the maximum of the absolute values of the residual pattern distortions versus the number of actuators. The dotted lines in the graph provide the residual pattern distortion value when a continuous bending moment is applied.

case. From the graph it can be concluded that the pattern distortion levels have been reduced by the lens and that seven actuators will yield similar pattern distortion values as those obtained when applying a continuous bending moment.

Appendix D

Piezoelectric actuator power dissipation model

This appendix provides the derivation of the piezoelectric actuator power dissipation relation by its hysteresis. The relation is obtained by considering the linear model of a piezoelectric actuator and considering the hysteresis as a time delay operator. The relation is used in Chapter 5 to quantify the expected power dissipation by the curvature manipulator.

D.1 Introduction

In first order analysis in this thesis it was always assumed that a piezoelectric actuator does not have any electrical power dissipation because it can be approximated by an ideal capacitance. In reality, this is not necessarily the case. This appendix aims to derive an expression for the piezoelectric actuator power dissipation. Section D.2 introduces a linear model of the piezoelectric actuator. This model is thereafter used in Section D.3 to derive the relation of the actuator power dissipation that is caused by hysteresis. The derivation is based on the relations in [92, 110].

D.2 Linear model of a piezoelectric actuator

In most applications, piezoelectric actuator non-linearities such as drift and hysteresis are neglected such that they can be described in terms of their linear constitutive relations. The linear model for a piezoelectric stack actuator that consists of one-dimensional

piezoelectric material is equal to [92]:

$$\begin{bmatrix} \Delta L_p \\ q \end{bmatrix} = \begin{bmatrix} 1/k_p & d_p \\ d_p & C \end{bmatrix} \begin{bmatrix} F \\ U_p \end{bmatrix} \quad (\text{D.1})$$

where ΔL_p is the total extension of the actuator in [m], q is the total electric charge on the electrodes of the piezoelectric actuator in [C], F is the total force in [N] and U_p the applied voltage in [V]. The constants k_p is equal to the mechanical stiffness of the piezoelectric actuator in [N/m] whilst d_p and C are respectively the piezoelectric constant and capacitance of the piezoelectric actuator in [m/V] and [F]. Note that the top and bottom row in the matrix-vector relation of Equation (D.1) relate to the piezoelectric actuator description in the mechanical and electrical domain and that the piezoelectric constant defines the electromechanical coupling between the two.

D.3 Relation for actuator power dissipation

It is well known that piezoelectric actuators have an hysteretic relation between the applied electrical voltage U_p and electrical charge q [2]. This hysteresis is the main cause of the piezoelectric actuator power dissipation. The derivation for the piezoelectric actuator power dissipation relation starts by describing the hysteretic behaviour of the piezoelectric actuator as a perturbation on the linear model in Equation (D.1). In that case, complex physical constants (*) are used to mimic the hysteresis as a delay-time-related loss and the equation becomes [110]:

$$\begin{bmatrix} \Delta l \\ q \end{bmatrix} = \begin{bmatrix} 1/k_p^* & d_p^* \\ d_p^* & C^* \end{bmatrix} \begin{bmatrix} F \\ U_p \end{bmatrix}. \quad (\text{D.2})$$

For the derivation of the piezoelectric actuator power dissipation, it is assumed that there is no electromechanical coupling, i.e. $d_p^* = 0$ [m/V]. In that case, the piezoelectric actuator can be approximated by the complex capacitance C^* in the electrical domain with [110]:

$$C^* = \frac{\varepsilon^{T*} \varepsilon_0 A n^2}{l} \quad (\text{D.3})$$

where ε^{T*} is the complex dielectric constant that is defined as:

$$\varepsilon^{T*} = \varepsilon^{T'} (1 - j \tan \delta'). \quad (\text{D.4})$$

In equation (D.4), δ' is known as the *loss angle* which represents the phase delay of the electric displacement to an applied electric field for constant mechanical stress.

The electrical power dissipation of the actuator is dependent on its admittance. The admittance of the piezoelectric actuator is equal to:

$$Y = \frac{j\omega\varepsilon^{T*}\varepsilon_0An^2}{l} = \frac{j\omega\varepsilon^{T'}(1-j\tan\delta')\varepsilon_0An^2}{l} \quad (\text{D.5})$$

$$= j\omega C' + \frac{1}{R} \quad (\text{D.6})$$

with

$$C' = \frac{\varepsilon^{T'}\varepsilon_0An^2}{l} \quad \text{and} \quad \frac{1}{R} = \omega C' \tan\delta'. \quad (\text{D.7})$$

Equation (D.5) shows that the piezoelectric actuator can be described by an equivalent electric circuit consisting of an ideal capacitor C' that is placed in parallel to a resistance R . The electric power in the actuator when a voltage with amplitude U_n and frequency ω_n is applied to its electrodes is equal to:

$$P_{\text{av}} = \frac{U_n^2}{2}Y = j\omega_n C' \frac{U_n^2}{2} + \frac{1}{R} \frac{U_n^2}{2}. \quad (\text{D.8})$$

The imaginary part in Equation (D.8) represents the reactive power whilst the real part represents the power loss in the piezoelectric actuator. The latter is equal to:

$$P_{\text{loss}} = \frac{1}{2}\omega_n C' \tan\delta' U_n^2 = \pi f_n C' \tan\delta' U_n^2 \quad (\text{D.9})$$

where f_n is the excitation frequency in [Hz].

For the case where the piezoelectric actuator is excited by multiple frequencies, the cumulative power dissipation has to be considered. The expression is equal to [11]:

$$P_{\text{cum}} = \sum_{n=0}^N P_{\text{loss}} = \sum_{n=0}^N 2\pi f_n C' U_{\text{RMS}_n}^2 \tan\delta' \quad (\text{D.10})$$

where $U_{\text{RMS}_n}^2 = U_n^2/2$ is the value of the piezo voltage power spectrum at frequency f_n .

Appendix E

Experimental validation of a single actuator unit

This appendix summarizes the experimental validation measurements of a single actuator of the curvature manipulator assembly. The validation experiment consists of bending a beam by the single actuator unit and measuring the deflection with an external metrology system. The experimental setup is first explained. The measurement results are thereafter provided.

E.1 Experimental setup

The experimental setup that was used to validate the single bending actuator design of Chapter 4 is outlined in this section. Section E.1.1 introduces the objectives of the measurement setup. The design of the Single-Axis Functional Model (FUMO) is explained in Section E.1.2. The insights that were obtained during realization of the setup are provided in E.1.3.

E.1.1 Objectives

The validation measurements of the single actuator unit were performed for the following three objectives. The first objective was to identify the static and dynamic bending performance of a single actuator unit. Specific attention is given on the achievable curvature and the amount of parasitic motion of the beam. The second objective was to compare the manipulator performance for the control strategies of Chapter 5, namely one with only local feedback across the actuator and the other with an additional outer curvature feedback loop. The third objective was to test the assembly procedure for the full actuator array setup in order to reduce risks and component failure.

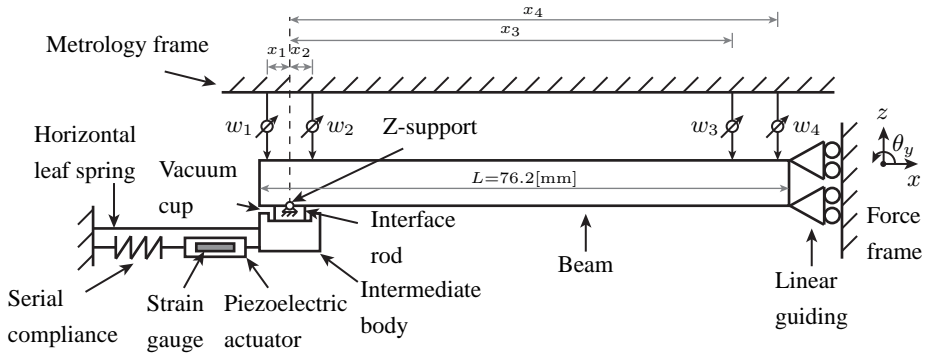


Figure E.1: Schematic representation of the Single-Axis FUMO.

E.1.2 Setup design

A conceptual drawing of the experimental setup that was used to validate a single actuator is provided in Figure E.1. It shows the bending manipulator, the bending beam and the beam deflection measurement locations. The following design choices were made [119]:

- *Number of actuators* - In order to achieve a beam curvature it is necessary to introduce two equal and opposite moments into the bending beam. It was chosen to achieve this with a single actuator unit and linear guiding because of the availability of one single piezoelectric actuator for the setup. Furthermore, it eliminated possible cross-talk with other actuators.
- *Beam properties* - The bending beam dimensions were $22.5 \times 76.2 \times 6.35$ [mm]. The width corresponds to one-seventh of the photomask dimension in y -direction. The length corresponds to half the reticle dimension in x -direction where the linear guidance resembles the reticle centre. The thickness is equal to that of the reticle. Finally, Aluminium was chosen as bulk material because its elasticity modulus approximates that of Fused Silica.
- *Beam constraints* - Two air bearings were used to realize a linear guiding at one beam end. It mimics the behaviour of the reticle centre during bending because it allows motion in z -direction but keeps θ_y constrained.
- *Application of a force and metrology frame* - The bending actuator was mounted to a force frame and the measurement system on a metrology frame in order to avoid deformations of the metrology frame by reaction forces [51].
- *Measurements on vibration isolated system* - The measurements are performed on a vibration isolation table which has a cut-off frequency at approximately 3 [Hz]. This reduces the transmission of external vibrations into setup.
- *In-plane beam deformation measurements* - The in-plane deformation measurement of the bending beam was omitted in the setup because no sensor was found that could achieve the in-plane measurement requirements of Table 6.1.

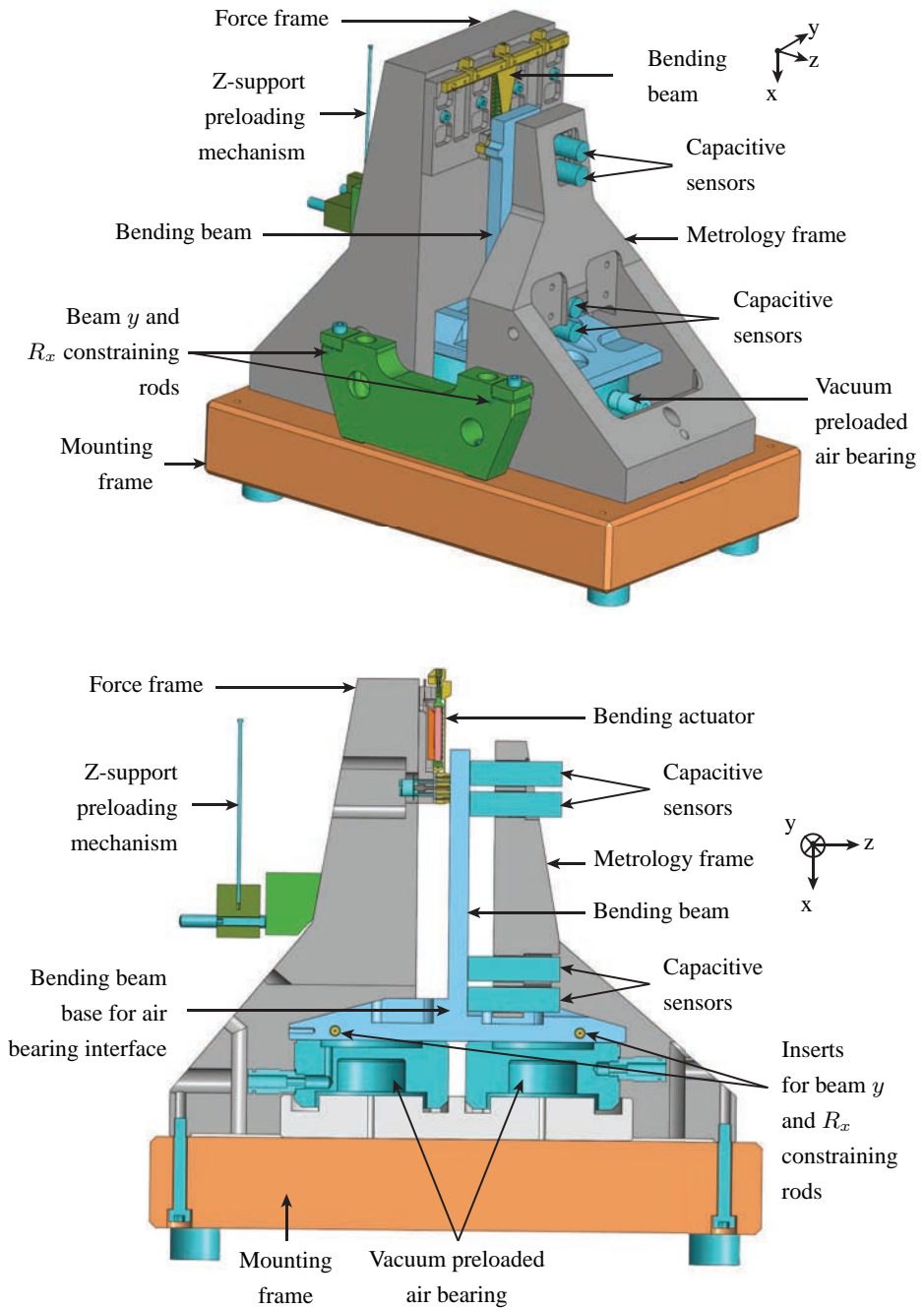


Figure E.2: CAD design of the Single-Axis Functional Model. The top picture provides a 3D view and the bottom picture a cross section of the design.

- *Out-of-plane beam deflection measurements* - The out-of-plane deflection of the bending beam is measured with four *D-510 PI-Seca* capacitive sensors and *E-852* signal conditioner electronics from Physik Instrumente [87]. The noise levels of the sensors are below 0.5 [nm] for a range of 50 [μm] range. This comes close to the measurement specifications of Table 6.1.

A value for the beam curvature and its parasitic motion is obtained by fitting a beam curvature model onto the measured deflection, i.e.:

$$\mathbf{c} = (\mathbf{X}^T \mathbf{X})^{-1} \mathbf{X}^T \mathbf{w} \quad (\text{E.1})$$

$$\mathbf{c} = \begin{bmatrix} T_z \\ \theta_y \\ \kappa_y \end{bmatrix}, \quad \mathbf{X} = \begin{bmatrix} 1 & x_1 & \frac{1}{2}x_1^2 \\ 1 & x_2 & \frac{1}{2}x_2^2 \\ 1 & x_3 & \frac{1}{2}x_3^2 \\ 1 & x_4 & \frac{1}{2}x_4^2 \end{bmatrix}, \quad \mathbf{w} = \begin{bmatrix} w_1 \\ w_2 \\ w_3 \\ w_4 \end{bmatrix}. \quad (\text{E.2})$$

where T_z , θ_x and κ_x respectively correspond to the beam translation, rotation and curvature whilst w_i and x_i correspond to the out-of-plane deflection and x-position of the i^{th} capacitive sensor across the beam. The sensors were placed at $x_1 = -5$ [mm], $x_2 = 5$ [mm], $x_3 = 58.6$ [mm] and $x_4 = 68.8$ [mm] in the setup.

The final design of the Single-Axis FUMO is provided in Figure E.2. It shows the four main subsystems which are the force frame, metrology configuration, bending beam and single curvature manipulator. The setup has been rotated by 90 [deg] in order to overcome the initial beam deformation due to gravity.

The bending beam in the setup has a large base at one end. The smaller beam end interfaces with the vacuum preload cup of the manipulator and is constrained on z -support by a preloading mechanism. The preloading mechanism consists of a thin flexible clamped beam that is attached to the vacuum clamp by a thin string. The amount of preload force can be tuned by positioning the clamped beam with respect to z -support.

The large base of the beam floats on two vacuum preloaded air bearings which act as the linear guiding [119]. The configuration is able to achieve a theoretical rotational stiffness of $k_{\theta_y} \approx 2 \times 10^4$ [Nm/rad] at the end of the beam when a 5 [μm] fly height is used. Finally, two constraining rods were included in the setup to constrain the beam y and R_x degrees-of-freedom [119]. A modal analysis was performed to identify the beam eigenfrequencies. The first resonance was expected at 221 [Hz] for the case of an ideal air bearing and z -support constraint. This is approximately a factor 2 smaller than the eigenfrequency in Table 6.1 which makes dynamic validation measurements less feasible. It was nevertheless chosen to pursue with this design.

The manipulator in the setup is essentially a single piezoelectrically driven mechanism with an adapted vacuum preload cup. The vacuum cup has four interface rods. Two are used to introduce the bending moment into the beam. The other two provide the R_x constraint between the beam and the vacuum cup. The vacuum surface area is equal to 130 [mm²] which relates to a total preload force of 9.75 [N] for vacuum pressure of -0.75 [barg]. This relates to a preload force of 2.4 [N] in each interface rod which marginally satisfies the required 2 [N] for the transfer of a 13.5 [mNm] bending moment.

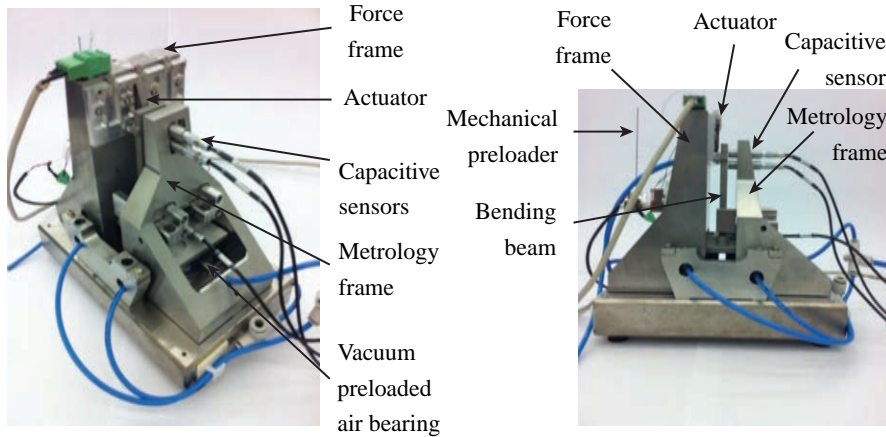


Figure E.3: The realized Single-Axis FUMO with its different components.

E.1.3 Realization

The realized Single-Axis measurement setup is shown in Figure E.3. The realization of the setup and initial testing provided a number of insights. These are explained below.

Beam mechanical constraints

The performance of the manipulator in the setup is dependent on the mechanical contact between the clamp and the beam as well as the beam's constraints. A sinusoidal voltage excitation was applied to the piezoelectric actuator in order to identify the manipulator behaviour. The left graph in Figure E.4 shows the strain gauge voltage reading versus the measured out-of-plane deformation of the bending beam. It clearly shows hysteresis between the actuator and the bending beam and a changing rate of beam deflection at larger actuator elongations. This could be caused by a loss of mechanical contact between the interface rods and bending beam and/or mechanical contact between the vacuum preloaded air bearings and the base of the bending beam.

Three actions were taken to overcome the hysteretic behaviour. First, the vacuum pressure in the clamp was increased to -0.88 [barg] which increased the vacuum preload in the interface rods. Second, the vacuum pressure of the vacuum preloaded air bearings was reduced to increase the fly height of the bending beam. This comes at the cost of a lower rotational stiffness at the air bearing interface and subsequently lower eigenfrequencies of the setup. Finally, the mechanical preloading that is applied by the z -support preloading mechanism in order to keep the beam on the supports was also increased.

The above described actions resulted in a more linear relation between the strain gauge and bending beam deflection as is visible in the right graph of Figure E.4. Note that the amplitude of the beam deflection has increased for the same strain gauge reading. These settings were used for the remainder of the Single-Axis measurements.

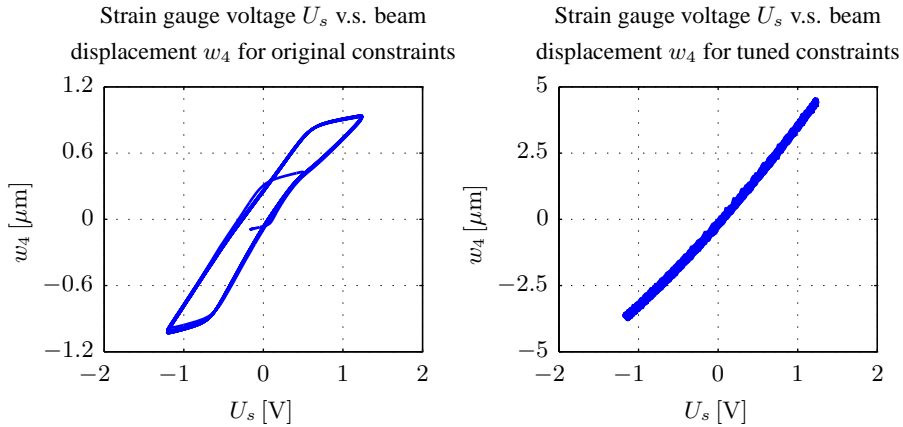


Figure E.4: The behaviour of the manipulator and the beam for an applied sinusoidal excitation voltage to the actuator. The left and right graph show the strain gauge voltage U_c and beam displacement w_4 for the original and tuned beam constraints. The hysteretic behaviour is removed after increasing the vacuum pressure in the clamp and the applied force by the z -support preloading mechanism.

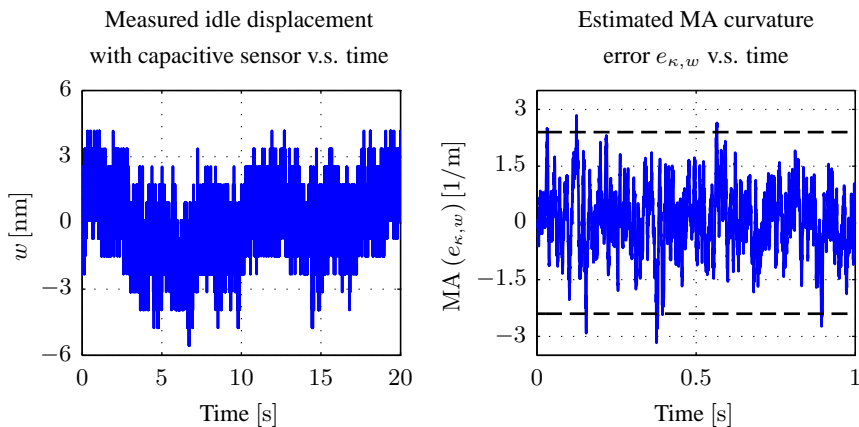


Figure E.5: The propagation of the capacitive sensor noise into the curvature estimate. The left graph shows measured capacitive sensor noise as a function of time. The right graph provides the resulting MA curvature error for those capacitive sensor noise levels. The dotted line corresponds to the required curvature accuracy of 2.4×10^{-6} [1/m].

Curvature error by capacitive sensor noise

An investigation was performed on the effect of capacitive sensor noise on the curvature estimate. The left graph of Figure E.5 shows the measured capacitive sensor noise in the setup. It had a standard deviation of $\sigma(w) = 1.4$ [nm]. The resulting curvature error was thereafter estimated with Equation (E.2) for four white noise signals w_1 to w_4 with $\sigma(w) = 1.4$ [nm]. The MA and MSD value of the curvature error was thereafter determined with Equations (5.4) and (5.5).

The calculated MA curvature error is shown in the right graph of Figure E.5. It has a 3σ value of 2.6×10^{-6} [1/m] which is already above the curvature setting accuracy specification of 2.4×10^{-6} [1/m]. The single axis measurement results will therefore not satisfy the curvature tracking accuracy requirements. Analysis showed that this can be improved in by increasing the distance between the sensor locations.

E.2 Measurements

The experimental validation measurements that were performed with the setup in Section E.1 are summarized in this section. Section E.2.1 explains the required actuator and sensor calibration measurements. The feedback controller implementation is provided in Section E.2.2. The curvature tracking results are finally presented in Section E.2.3.

E.2.1 Calibration

Figure E.6 shows two control strategies that were investigated with the Single-Axis setup. One strategy uses the estimated beam curvature by the capacitive sensors as feedback signal whilst the other uses the strain gauge measurement to reconstruct the beam curvature signal. The strategies are different to the proposed control configuration in Chapter 5 because the piezoelectric actuator and strain gauge calibration measurement of Section 6.3.1.1 did not take place for this setup. A local piezoelectric actuator elongation feedback loop could therefore not be applied.

The proposed control strategies in Figure E.6 has two grey blocks. The first corresponds to the relation between the measured strain gauge voltage and the beam curvature G_{sg} whilst the second is equal to the piezoelectric actuator gain G_m^{-1} . Both gains were identified by measurements. They results explained in Sections E.2.1.1 and E.2.1.2.

E.2.1.1 Strain Gauge curvature relation

The calibration measurement of the strain gauge to curvature gain G_{sg} was performed in open loop for a 1 [Hz] sinusoidal excitation voltage to the piezoelectric actuator. The top-left graph in Figure E.7 shows the measured strain gauge voltage U_s and the estimated beam curvature κ_{est} from the capacitive sensor signals after being filtered by a second-order 100 [Hz] low-pass Butterworth filter. The graph also contains a linear polynomial fit through the measurement data which seems to fit relatively well. The identified polynomial coefficients are summarized in Table E.1.

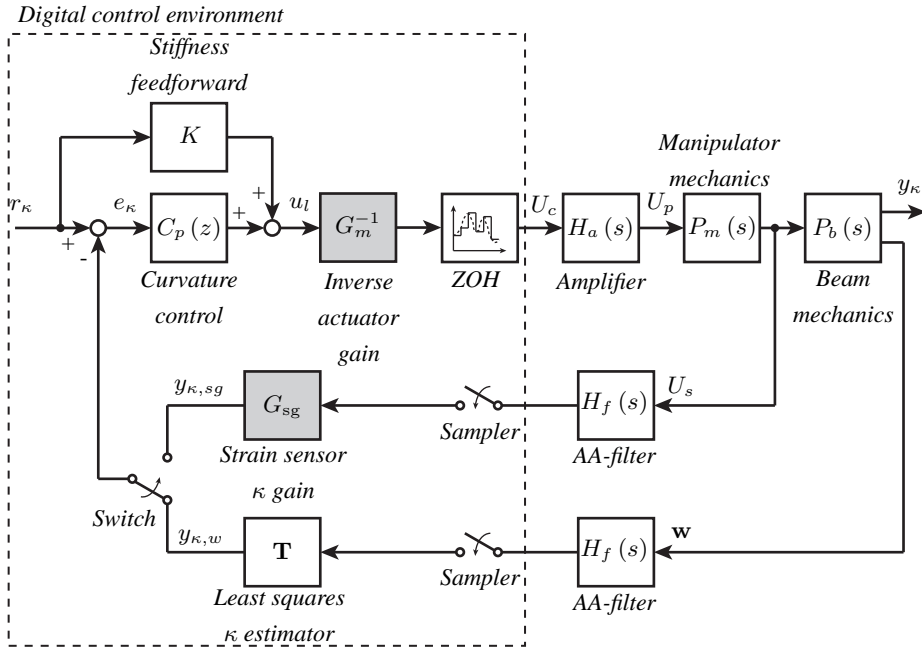


Figure E.6: The implemented control strategy for the Single-Axis measurement setup. The switch allows the use of the curvature estimated measurement signal from the strain gauge U_s or the beam deflection w . Different feedback controller settings were used for each measurement signal. The grey block G_{sg} corresponds to the strain gauge to curvature gain that has to be calibrated.

The top-right graph of Figure E.9 shows the error between the identified curvature and the linear fit. The fit error for a second order polynomial is provided in the bottom-left graph of Figure E.9. The graphs provide the following information:

- The fit error for a first and second order polynomial fit are equal to $\pm 15 \times 10^{-6}$ [1/m] and $\pm 7.5 \times 10^{-6}$ [1/m]. These errors are related to the beam curvature error via the complementary sensitivity which has a unity gain at frequencies below the controller bandwidth. The curvature errors are therefore expected to be a factor 6 and 3 larger than the curvature setting accuracy of 2.4×10^{-6} [1/m].
- Both fit errors show the presence of hysteresis. This could be caused by hysteresis at the curvature manipulator and beam interface, hysteretic behaviour of the strain gauge or hysteresis in the air bearing interface.

The calibration procedure was repeated after one month of testing. The bottom-right graph of Figure E.9 shows the error after fitting a second order polynomial. The identified coefficients are provided in Table E.1. The results highlight that the hysteresis loop has reduced and that the non-linearity error is equal to $\pm 5 \times 10^{-6}$ [1/m]. This change of hysteresis in time is common in contact mechanics. The error is still a factor two above the desired setting accuracy however. Further research must be conducted to identify the exact cause of the hysteresis and ways to reduce it.

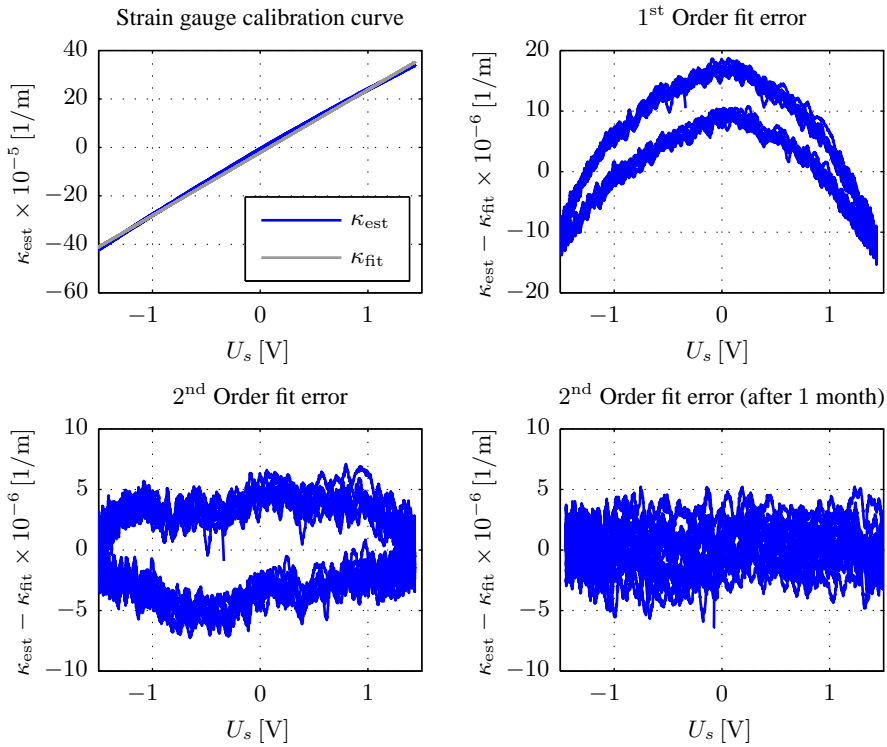


Figure E.7: Results of the strain gauge to curvature calibration process for a linear and quadratic fit. The two paths in the top-right and bottom-left graph represent hysteric behaviour.

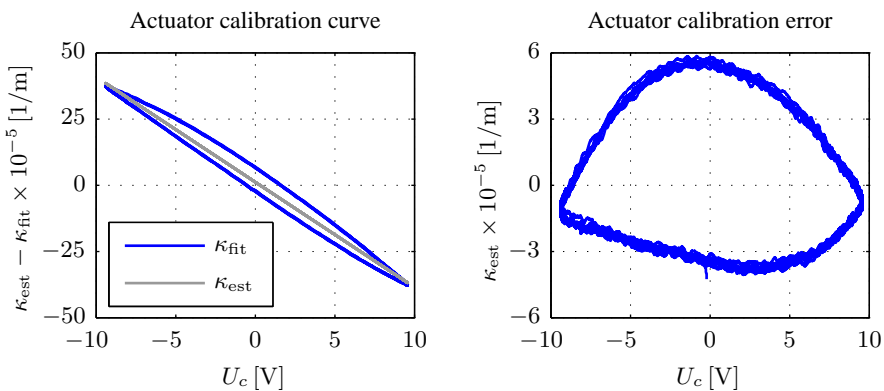


Figure E.8: Results of the actuator calibration process. The left graph shows the linear actuator model fit of $\kappa_{\text{fit}} = c_1 U_c + c_0$ with $c_1 = -3.97 \times 10^5$ [1/mV] and $c_0 = 1.19 \times 10^5$ [1/m]. The right graph provides the calibration error.

Polynomial coefficient	Initial calibration date		After one month	Unit
	1 st Order fit	2 nd Order fit	2 nd Order fit	
a_0	-0.2134×10^{-4}	-0.0907×10^{-4}	0.0401×10^{-4}	[1/mV ²]
a_1	2.5986×10^{-4}	2.5873×10^{-4}	2.4493×10^{-4}	[1/mV]
a_2	-	-0.1095×10^{-4}	-0.1244×10^{-4}	[1/m]

Table E.1: Identified coefficients for the strain gauge voltage to curvature polynomial relation $y_{\kappa,sg} = a_2 U_s^2 + a_1 U_s + a_0$. The variable U_s corresponds to the strain gauge measurement voltage and $y_{\kappa,sg}$ is the curvature estimate of the strain gauge signal.

E.2.1.2 Inverse actuator gain

The strain gauge calibration measurement data of Section E.2.1.1 was also used to calibrate the inverse actuator gains. The calibration procedure consisted of fitting a linear polynomial κ_{fit} through the command voltage U_c and beam curvature κ_{est} data as is shown in the left graph of Figure E.8. The graph clearly shows the hysteretic behaviour of the piezoelectric actuator because of the use of a voltage amplifier [2]. The right graph provides the actuator calibration error in which the hysteresis is still present. The feedback loop across the piezoelectric actuators will counteract this hysteresis below the controller bandwidth. The use of a charge amplifier or an inverse actuator hysteresis model are able to further linearise the actuator if needed [2, 55].

E.2.2 Controller implementation

The second step in the experimental validation of the single piezoelectric actuator unit is the implementation of the feedback controller C_p in Figure E.6 for the strategy that uses the estimated beam curvature from the strain gauge measurement signal or the capacitive sensor signals. Section E.2.2.1 presents the results of the system identification measurements. The feedback controller tuning is explained in Section E.2.2.2.

E.2.2.1 System identification

System identification measurements were performed on with the Single-Axis measurement setup to determine the FRFs between the piezoelectric actuator and the estimated curvature by the strain gauge and capacitive sensors. The results were used to tune the feedback controllers and identify the validity of the calibrated quasi-static curvature gain in Section E.2.1.1 across the measurement frequency range.

The system identification was performed by applying a multi-sine excitation to the piezoelectric actuator [91]. The identified curvature by the strain gauge sensor and the capacitive sensors were acquired during the excitation period with a sample frequency of 4 [kHz]. The identification were performed in open-loop because of the open-loop stability of the curvature manipulator. The FRFs were obtained by taking the average of ten measurement blocks. The contribution of stochastic noise is therefore reduced by a factor of $\sqrt{10}$, see [91].

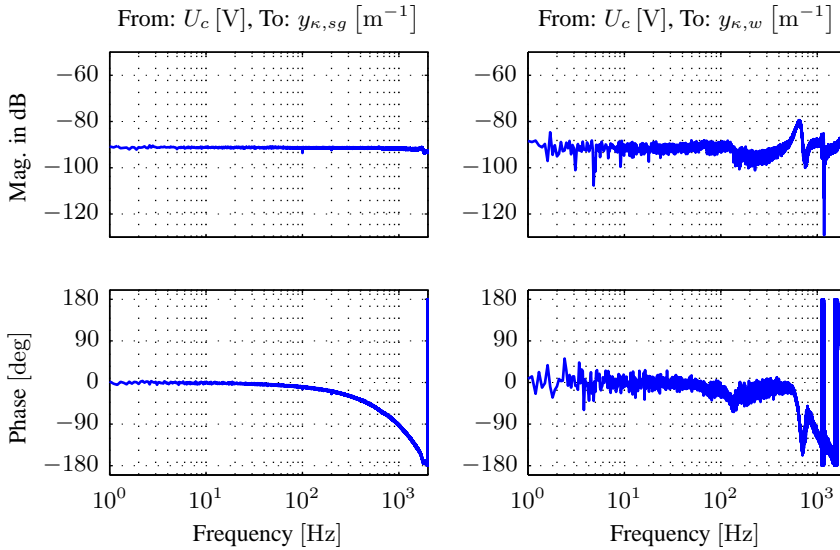


Figure E.9: Frequency response of the plant from the applied voltage to the piezoelectric actuator amplifier U_c to the identified beam curvature κ using the (left) strain gauge sensor and (right) capacitive sensors.

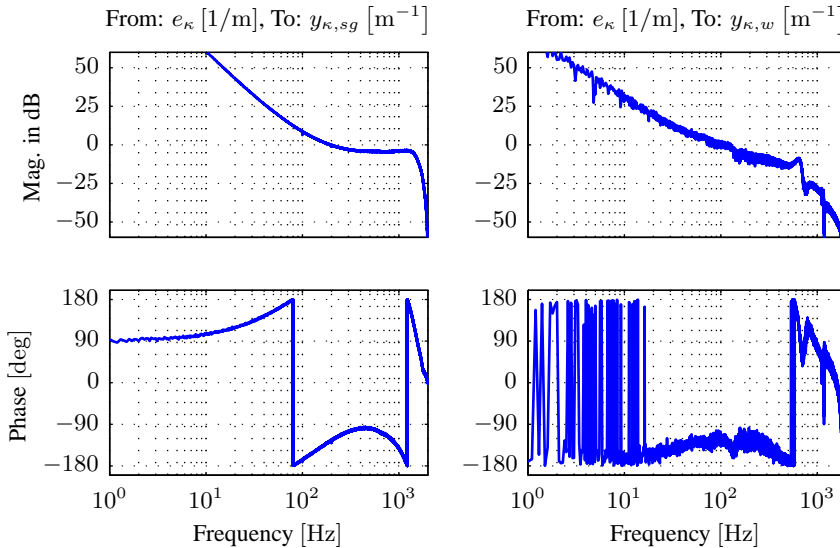


Figure E.10: The open-loop frequency response or loop gain of the curvature feedback loops in the Single Axis setup that uses a curvature estimate from the strain gauge sensor signal (left) and the capacitive sensor signals (right).

Figure E.9 shows Bode plots of the identified FRFs between the piezoelectric actuator command voltage U_c and the estimated beam curvature by the strain gauge sensor $y_{\kappa,sg}$ or by the capacitive sensors $y_{\kappa,w}$. The graphs highlight the following:

- Beam dynamics show up at 125, 645, 1150 and 1750 [Hz] in the estimated curvature signal by the capacitive sensors but not in the strain gauge sensor signal. It confirms the unobservability of the beam dynamics by the strain gauge as was shown in Chapter 5. The unobservability is attributed to the mechanical design of the manipulator and the strain gauge placement on the piezoelectric actuator.
- The magnitude of the measured FRF between the piezoelectric actuator command voltage U_c and the estimated beam curvature $y_{\kappa,sg}$ is 3.5 dB lower than that of the modelled manipulator in Figure 5.10. It demonstrates that the model has similar behaviour as the realized actuator at strain gauge level.
- Both FRFs in Figure E.9 have a magnitude of -43 dB up to 125 [Hz]. The calibrated gain between the strain gauge and curvature holds up to this frequency.
- The measured FRFs has a slightly larger phase drop as the modelled FRFs in chapter 5. This will limit the achievable bandwidth of the feedback controller.

The identification measurements were also performed around different actuator command voltage offsets. The identified FRFs were not different than those shown in Figure E.9. These FRFs were therefore used for the feedback controller design.

E.2.2.2 Controller design

A feedback controller C_p was designed for each of the measured plant FRFs in Figure E.9 using the manual loop shaping technique. The feedback controller across the piezoelectric actuator and strain gauge curvature signal $y_{\kappa,sg}$ consisted of a robustly stable PI³D-controller with low-pass filter. The latter was included to further suppress the sensor noise at higher frequencies.

The Bode plot and Nyquist diagram of the open-loop FRF between the curvature error and the estimated curvature with the strain gauge are respectively shown in the left graphs of Figure E.10 and E.11. The Bode plot shows that the unity-gain cross-over frequency for the measured open-loop FRF is located at 196 [Hz]. This is more than a factor two lower than the 580 [Hz] that was obtained with the manipulator model in Chapter 5.4.2. The Nyquist diagram highlights that the controller is robustly stable even though it just enters the circle with radius of 0.5. Further controller tuning attempts demonstrated that a bandwidth of 450 [Hz] could be achieved without a robustness loss by setting the cross-over frequency of the integral action at a higher frequency. No curvature tracking measurements were performed with this setting however.

The feedback controller across the piezoelectric actuator and the capacitive sensor curvature signal consisted of a robustly stable PI²D-controller. Its Bode and Nyquist diagrams are provided in the right graphs of respectively Figure E.10 and E.11. The unity-gain cross-over frequency is located at 110 [Hz] which could be increased by a higher controller gain. This was not done because of the uncertainty in the measured plant FRF.

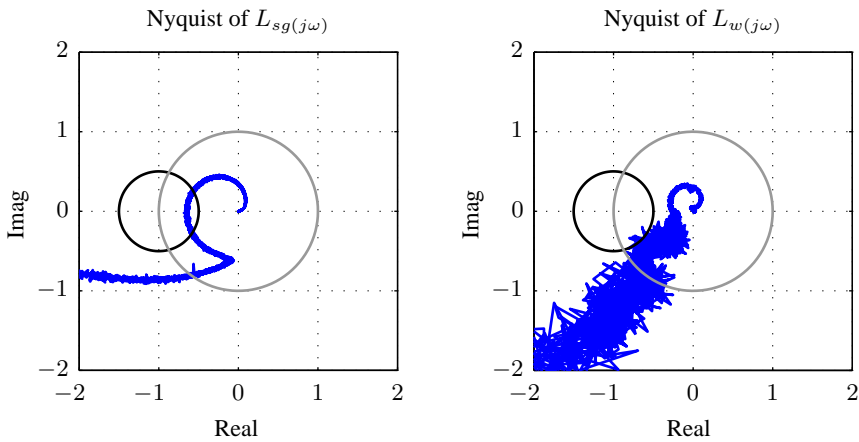


Figure E.11: Nyquist plot of the open-loop frequency responses that are shown in Figure E.10. The left graph shows the open-loop for the curvature feedback loop that uses strain gauge measurement information whilst the right graph shows the open-loop that uses the capacitive sensor signals.

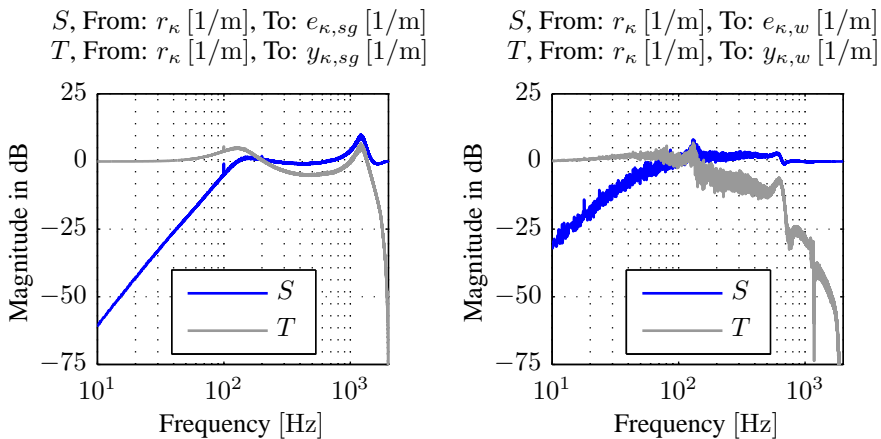


Figure E.12: The sensitivity S and complementary sensitivity T for the two curvature control strategies in Figure E.6.

The disturbance rejection and tracking performance of both curvature feedback control strategies in Figure E.6 are described by the sensitivities S and the complementary sensitivities T in Figure E.12. The left graph shows their values for the feedback loop that uses the strain gauge measurement information. The right graph shows the values when the capacitive sensors are used. The graphs provide the following insights:

- The strain gauge curvature feedback loop has better low frequency disturbance suppression than the capacitive sensor curvature feedback loop. This is attributed to the extra integrator in the feedback controller of the former configuration.
- The sensitivity functions of the strain gauge curvature and the capacitive sensor feedback loops have a 16 [Hz] disturbance suppression of respectively -48 dB and -20 dB. The strain gauge configuration is able to achieve the factor 100 reduction of the piezoelectric actuator errors that was identified in Section 4.3.3.
- The strain gauge curvature feedback loop has a sensitivity peak of 9 dB which is 2 dB larger than the sensitivity peak of the capacitive sensor feedback loop.

The above provided insights into the expected control performance of both feedback loops. Sections E.2.3 provides further details on the curvature tracking performance of both control strategies for the Single-Axis setup.

E.2.3 Curvature tracking performance

The curvature tracking performance was investigated for the feedback controllers of Section E.2.2. Wafer curvature setpoints were used as reference signal for the analyses. Section E.2.3.1 presents the tracking results for the strain gauge curvature feedback loop. The results for the capacitive sensor curvature feedback loop are given in Section E.2.3.2.

E.2.3.1 Strain-gauge curvature feedback

The curvature tracking results for the strain gauge curvature feedback are provided in Figure E.13. The top-left graph shows the wafer curvature setpoint as a function of time. The top-right graph of Figure E.13 shows the curvature errors that are estimated by the strain gauge sensor $e_{\kappa,sg}$ and the capacitive sensors $e_{\kappa,w}$ for a specific time interval. The bottom-left and bottom-right graphs of Figure E.13 provide the MA and MSD values of the curvature error that have been determined with Equations (5.4) and (5.5). The dotted lines show the MA and MSD curvature error specifications. Inspection of the graphs in Figure E.13 provide the following insights:

- The estimated MA curvature error by the strain gauge and the capacitive sensor are different in amplitude and phase. It highlights that the strain gauge curvature estimate is erroneous when the derived curvature error from the capacitive sensors

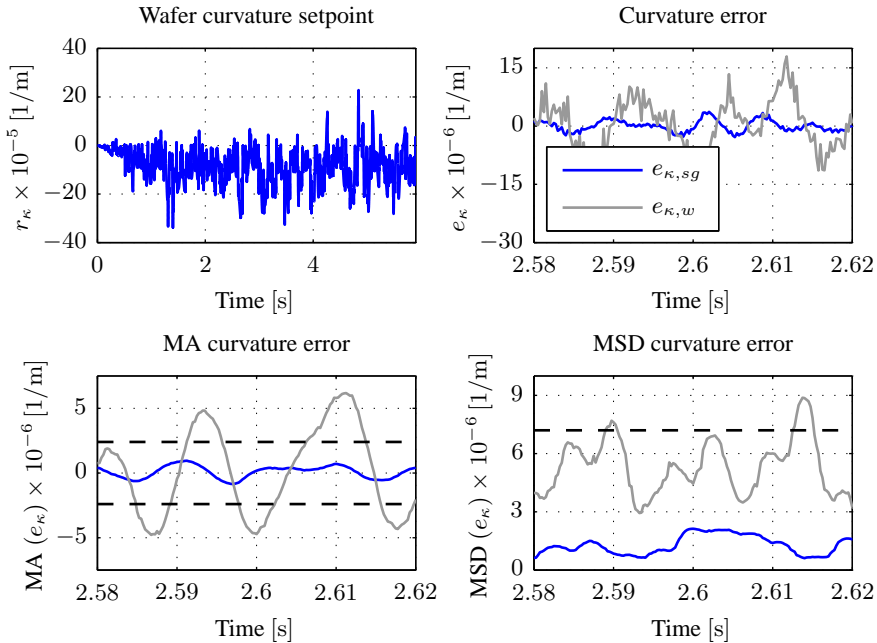


Figure E.13: Results of the curvature tracking measurements when feedback is applied across the curvature estimate of the strain gauge.

is assumed correct. Potential causes are system dynamics that are unobservable by the strain gauge or hysteresis in the interface between the manipulator and beam.

- The estimated MA error by the strain gauge is within specifications which is not the case for the value that is estimated by the capacitive sensors. This demonstrates that the local feedback control across the actuator and strain gauge does not guarantee the desired tracking accuracy. This is largely caused by the erroneous curvature error estimate by the strain gauge.
- The MSD curvature error shows that the capacitive sensor signal has more high frequency content than the strain gauge. This can have two causes. First, beam dynamics are largely unobservable by the strain gauge. Second, the capacitive sensor noise and the least-squares curvature estimation procedure can introduce high frequency content as was shown in Section E.1.2.

The above results for the strain gauge curvature feedback loop demonstrates that an indirect curvature measurement will lead to erroneous tracking performance in terms of the performance variable. The tracking performance for a more direct curvature estimate are therefore investigated in Section E.2.3.2.

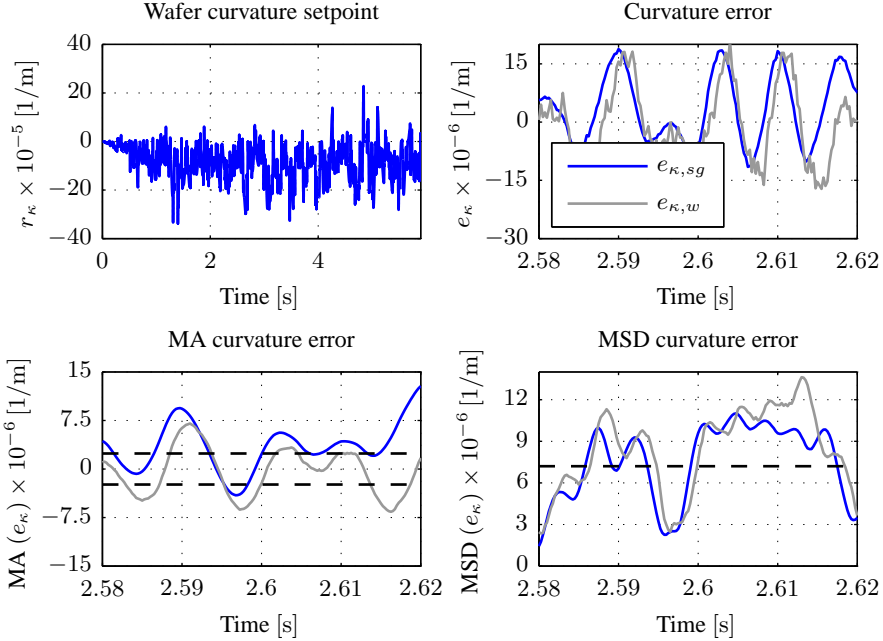


Figure E.14: Results of the curvature tracking measurements when feedback is applied across the curvature estimate of the capacitive sensors.

E.2.3.2 Capacitive sensor curvature feedback

The curvature tracking results for the capacitive sensor curvature feedback are provided in Figure E.14. The top-left graph shows the curvature setpoint and the top-right graph the estimated curvature tracking error by the strain gauge $e_{\kappa,sg}$ and capacitive sensors $e_{\kappa,w}$. The MA and MSD values of both curvature estimated signals are respectively shown in the bottom-left and bottom-right graphs. The results provide the following insights:

- The estimated MA curvature error by the stain gauge and the capacitive sensor show similar behaviour in terms of magnitude and phase. This is attributed to the fact that a direct beam curvature measurement is used as feedback signal. The feedback loop can therefore counteract the mechanical hysteresis in the manipulator to beam contact interface
- The curvature error signal has a dominant contribution of 130 [Hz]. This corresponds to the location of the sensitivity peak for the capacitive sensor feedback controlled system in Figure E.12.
- The estimated MA curvature error by the strain gauge and capacitive sensor exceed the curvature tracking accuracy specification by approximately a factor of 4.

The above results for the curvature feedback across the capacitive sensors and piezoelectric actuator have shown that a direct measurement of the beam curvature will result in a better correlation between the curvature that is estimated from the strain gauge and capacitive sensor signals. The result also emphasizes that the tracking performance needs to be improved. Potential solution directions are the use of charge instead of a voltage amplifier [2, 74], a higher feedback controller bandwidth or the use of an inverse hysteresis model in the feedforward path [57].

Samenvatting

De halfgeleider industrie verbetert continu geïntegreerde schakelingen om de samenleving te voorzien van de nieuwste betaalbare informatie technologie. De verbeteringen worden verkregen door het verkleinen van de componenten in een chip. De afmetingen worden bepaald door een lithografisch proces waarbij een geometrisch patroon van een masker op een halfgeleidend substraat afgebeeld wordt met behulp van licht.

De focus diepte tijdens het lithografische proces beïnvloedt de scherpte van de afgebeelde structuren op het substraat. Een 65 – 70 [nm] focus diepte en 2 [nm] overlay fout is gewenst in de huidige immersielithografiemachines voor het afbeelden van 20 [nm] structuren. De focus diepte en overlay fout zullen nog kritischer worden wanneer deze machines gebruikt worden voor het vervaardigen van nog kleinere structuren.

Dit proefschrift onderzoekt de haalbaarheid van een manipulator die de kromming van het masker aanpast om zodoende een focus verbetering te verkrijgen in immersielithografiesystemen. De kromming van het masker kan tijdens het belichtingsproces worden geregeld door aanbrengen van buigende momenten op de randen van het masker. Dit resulteert in een gekromde afbeelding op substraat niveau. Analyses hebben aangetoond dat een kromming van $\kappa = \pm 0.4 \times 10^{-3}$ [1/m] nodig is om focus fouten door lens opwarming en wafer onvlakheid ieder met 10 [nm] te reduceren. Alternatieve technieken zoals een lens manipulator of het actief vervormen van het substraat zijn ongeschikt omdat deze te complex zijn of negatieve effecten hebben op het lithografisch proces.

De eerste stap in het onderzoek richt zich op het identificeren van de randvoorwaarden en specificaties van de manipulator. Het gebruik van een transmissief masker tijdens het lithografisch proces maakt het noodzakelijk om de buigende momenten aan de randen van het masker aan te brengen. Daarnaast zal de huidige masker inklemming aangepast moeten worden omdat de stijfheid van de constructie de buigstijfheid van het masker verhoogt. Ook zal er waarschijnlijk slip optreden tussen de inklemming en het masker wanneer deze verbogen wordt. Parasitaire effecten die verder geminimaliseerd moeten worden zijn optische aberraties, dubbele breking ten gevolge van mechanische spanningen in het masker en overlay fout. De laatste mag niet groter zijn dan 0.1 [nm].

De conceptuele haalbaarheid van de manipulator is onderzocht met vereenvoudigde optomechanische modellen van het masker en lithografische systeem. Analytische en numerieke modellen zijn gebruikt om het buigingsgedrag van het masker te quantificeren. Een buigend moment van ± 0.1 [Nm] is nodig om de gewenste kromming van $\pm 0.4 \times 10^{-3}$ [1/m] te realiseren. Er kan voldaan worden aan de 0.1 [nm] overlay specificatie

indien het verstoorde masker patroon ten gevolge van buiging gecorrigeerd wordt met de lithografische lens. Analyses hebben aangetoond dat de veroorzaakte dubbele breking en optische aberraties verwaarloosbaar klein zijn. Er kan daarom geconcludeerd worden dat het verbuigen van een masker haalbaar is op conceptueel niveau.

De volgende stappen in het onderzoek bestaan uit het ontwerpen, modelleren en experimenteel valideren van een masker manipulator. Ontwerp specificaties zijn allereerst afgeleid van de lithografische systeem specificaties en vervolgens gebruikt om een manipulator concept te kiezen. Het concept bestaat uit twee rijen van piezoelectrisch aangedreven mechanismen die zich door middel van een lekkende vacuümkamer vasthouden aan het masker. Deze mechanismen zijn gekozen vanwege hun lage vermogensdissipatie, volume en massa. Ze voldoen ook aan de parasitaire stijfheid en kracht specificaties zodat de gewenste kromming gerealiseerd wordt met acceptabele patroon verstoringen. De piezoelectrische actuatoren zijn allen uitgerust met een rekstrookje. Hiermee kan een lokale regelaar over de actuator verlenging gesloten worden om zo actuator hysteresis en kruip tegen te gaan. De mechanische ontkoppeling tussen de piezoelectrische actuatoren maakt de implementatie van lokale regelars mogelijk.

De prestaties van het ontwerp zijn verder onderzocht met lineaire mechanische, regeltechnische en thermische modellen. Het mechanische model laat zien dat het ontwerp voldoet aan de specificaties voor mechanische eigenfrequenties, maskervervorming, patroon verstoringen en dubbele breking. Het regeltechnische model is gebruikt om de dynamische prestaties van het ontwerp te onderzoeken voor verschillende regelstrategieën. De analyse heeft aangetoond dat het ontwerp een 100 [Hz] krommingsreferentiesignaal kan volgen binnen de toegestane fout. Een additionele krommingsregeling wordt wel voorgesteld omdat de masker kromming niet observeerbaar is door het rekstrookje. Het thermische model toont aan dat de warmte last van de piezoelectrische actuatoren en de lekkende vacuümkamer niet leiden tot een onacceptabele thermische uitzetting van het masker. De configuratie van de rekstrookjes zal geoptimaliseerd moeten worden om aan de thermische specificaties te voldoen.

De prestaties van de manipulator zijn uiteindelijk experimenteel gevalideerd. De uit-het-vlak masker vervormingen ten gevolge van de manipulator zijn bepaald met een extern meetsysteem. In-het-vlak vervormingen konden echter niet gemeten worden. Metingen met een statisch referentiesignaal hebben laten zien dat de gerealiseerde masker vervormingen overeenkomen met de theoretische modellen. Het masker had echter ook een hogere order vervorming waar fouten in de gerealiseerde manipulator opstelling en het externe meetsysteem verantwoordelijk voor zijn. De gerealiseerde krommingsamplitude was ook gelimiteerd tot 0.11×10^{-3} [1/m] omdat de uit-het-vlak ondersteuning van het masker niet goed geïntegreerd waren in de manipulator. De manipulator heeft echter wel een lineair gedrag over het gemeten krommingsbereik. Metingen met een dynamisch referentiesignaal zijn ook nog uitgevoerd. De systeemprestaties konden echter slecht gekwantificeerd worden door de afwezigheid van een krommingssensor.

De gesimuleerde en gemeten resultaten die verkregen zijn in dit proefschrift hebben de conceptuele haalbaarheid van een masker manipulator aangetoond. Het concept is echter niet volledig gevalideerd met betrekking tot alle lithografie specificaties. Eventueel vervolgonderzoek zal zich moeten richten op de verdere validatie en optimalisatie van de manipulator zodat deze gebruikt kan worden als een veldkrommingsmanipulator in immersielithografiesystemen.

Curriculum Vitae

Christiaan (Chris) Valentin was born on August 13th, 1982 in Seria, Brunei. After finishing his secondary education at the Interconfessionele Scholengroep Westland (ISW) in 's-Gravenzande in 2000, he started at Delft University of Technology. He received his propaedeutics degree in Mathematical Engineering in 2001 as well as his B.Sc and M.Sc. degree (Cum Laude) in Mechanical Engineering in 2004 and 2006. He specialized in the field of Engineering Dynamics and conducted his internship and master thesis work at Bayerische Motor Werke (BMW) in respectively Dingolfing and Munich, Germany. The subject of his M.Sc. thesis focussed on the development of a gear noise identification procedure for operational rear axle differentials. The work was rewarded with the CORUS Young Talent Award by the Koninklijke Nederlandse Academie van Wetenschappen (KNAW) in 2007.

After graduating from university at the end of 2006, Chris worked as a researcher at the European Space Research and Technology Centre (ESTEC) in Noordwijk where he conducted research on the dynamics and control of a large multi-DoF hydraulic shaker facility for satellite testing. At the start of 2008, he began his PhD. research in the field of Mechatronics at Delft University of Technology and ASML. It focussed on active curvature manipulation of lithography photomasks which resulted in this thesis. Since 2011 he is employed by ASML. He currently has the role of System Architect/Project Lead in the Mechatronic Research Department where he works on the next generation lithography machines.

